

# Energetics and thermodynamics of $\alpha$ -iron from first-principles and machine-learning potentials

THÈSE N° 6952 (2016)

PRÉSENTÉE LE 22 FÉVRIER 2016

À LA FACULTÉ DES SCIENCES ET TECHNIQUES DE L'INGÉNIEUR  
LABORATOIRE DE THÉORIE ET SIMULATION DES MATÉRIAUX  
PROGRAMME DOCTORAL EN SCIENCE ET GÉNIE DES MATÉRIAUX

ÉCOLE POLYTECHNIQUE FÉDÉRALE DE LAUSANNE

POUR L'OBTENTION DU GRADE DE DOCTEUR ÈS SCIENCES

PAR

Daniele DRAGONI

acceptée sur proposition du jury:

Prof. D. Damjanovic, président du jury  
Prof. N. Marzari, directeur de thèse  
Prof. M. Bernasconi, rapporteur  
Prof. G. Csányi, rapporteur  
Prof. M. Ceriotti, rapporteur



ÉCOLE POLYTECHNIQUE  
FÉDÉRALE DE LAUSANNE

Suisse  
2016



*Everything should be as simple as it can be, but not simpler.*  
— Albert Einstein

To my parents...



# Acknowledgements

I wish to express my sincere thanks to all the people who contributed in different ways to the work described in this thesis.

First and foremost, let me thank my academic advisor, Prof. Nicola Marzari, who provided me an opportunity for a very formative experience. During these years he gave me the chance to work in a vibrant and intellectually stimulating environment, demanding a high quality of work in all my endeavors, giving me access to the super-computing facilities, and supporting my attendance at various conferences.

I would like also to acknowledge Prof. Gábor Csányi who donated me his precious times and the opportunity to work on Gaussian approximation potentials sharing codes, ideas, and hosting me in his group in Cambridge. I thank Dr. Tom Daff, Dr. Albert Bartok-Partay, and Dr. Wojciech Szlachta for helping me in the compilation of the QUIP code, for sharing data, for generating and testing the GAP potential models.

My genuine thanks go to Dr. Davide Ceresoli who assisted me especially at the beginning of this research, sharing his vast knowledge of the QUANTUM-ESPRESSO code and of density-functional theory. Thanks for the many useful discussions and for hosting me in Milano in various occasions.

Thanks to all my current and former fellow THEOS lab-mates for the stimulating discussions, for sharing their opinions and for all the nice moments in and out office, I really enjoyed hiking on the beautiful Swiss Alps. In particular, I am in debt with my room-mate and friend Anand Chandrasekaran, who contributed to make the days at office more interesting with his knowledge and his tips about the Indian culture and *cuisine*. Thanks for being such a nice person, for all the time spent together, for all the interesting and entertaining discussions, for the walks at the lake-side and for lending an ear to me every time I needed. I want to acknowledge Dr. Matteo Cococcioni who was always available and happy to discuss with me about everything, and for correcting different part of this thesis despite all the pressing deadlines. I cannot forget Dr. Giovanni Borghi, Dr. Ivano Castelli and Dr. Nicola Colonna, who volunteered to read this manuscript helping me with the corrections. Thanks to all of them also for sharing many happy moments here in Lausanne.

I am grateful to my old friend Dr. Daniele Brunetti for his unconditioned friendship, for being always present when needed, and for all the long peaceful walks around Lausanne.

Let me thank Aurora, for being always a good sister and being present when needed. I wish to thank my parents, Rosella and Domenico who always supported and encouraged me with their guidance and love throughout my entire life, they made me who I am today and to them

## **Acknowledgements**

---

I owe everything. I miss you dad. Last but not least, thanks to Francesca for the enthusiastic support during this journey, for the every-day presence and for all the rest.

*Lausanne, 7 Décembre 2015*

D. F. D.

# Preface

In the past few decades, the study and simulation of materials by means of computers has proved to be extremely fruitful and successful. The Moore-like steady increase in computational power, along with the development of state-of-the-art schemes to model the fundamental interactions that govern atoms dynamics, provided the tools to describe materials properties with an increasingly high accuracy, and allowed to design new materials which were not known in nature. Today, we are at the birth of a new era for materials science in which learning-machines are trained to screen over a vast class of new candidate compounds, sampling the enorums space of compositional and structural configurations, in order to deliver innovative materials for next generation devices in times that are reduced by orders of magnitude with respect to the past. In this perspective, computers will play a key role, but human intelligence and creativity will be still central in the whole process for at least the near future. What will happen afterwards is hard to foresee, humanity is, and will be, responsible for its own fate.

*Lausanne, 31 Mai 2015*

D. F. D.





# Abstract

Iron is a material of fundamental importance in the industrial and economic processes of our society as it is the major constituent of steels. With advances in computational science, much progress has been made in the understanding of the microscopic mechanisms that determine the macroscopic properties of such material at ordinary or extreme conditions. Ab initio quantum mechanical calculations based on density-functional theory (DFT), in particular, proved to be a unique tool for this purpose. Nevertheless, in order to study large enough systems up to length- and time-scales comparable with those accessible in experiments, interatomic potentials are needed. These are typically based on functional forms driven by physical intuition and fitted on experimental data at zero/low temperature and/or on available first-principles data. Despite their vast success, however, their low flexibility limits their systematic improvement upon database extension. Moreover, their accuracy at intermediate and high temperature remains questionable.

In this thesis, we first survey a selection of embedded atom method (EAM) potentials to understand their strengths and limitations in reproducing experimental thermodynamic, vibrational and elastic properties of bcc iron at finite temperature. Our calculations show that, on average, all the potentials rapidly deviate from experiments as temperature is increased. At the same time, they suggest that, despite an anomalous rapid softening of its  $C_{44}$  shear constant, the Mendeleev03 parameterization is the most accurate among those considered in this work.

As a second step, we compute the same finite-temperature properties from DFT. We verify our plane-wave spin-polarized pseudopotential implementation against selected zero temperature all-electron calculations, thus highlighting the difficulties of the semi-local generalized gradient approximation exchange and correlation functional in describing the electronic properties of iron. On the other hand, we demonstrate that after accounting for the vibrational degrees of freedom, DFT provides a good description of the thermal behavior of thermodynamic and elastic properties of  $\alpha$ -iron up to a good fraction of the Curie temperature without the explicit inclusion of magnetic transverse degrees of freedom. Electronic entropy effects are also analyzed and shown to be of secondary importance.

Finally, we attempt at generating a set of highly flexible Gaussian approximation potentials (GAP) for bcc iron that retain ab initio accuracy both at zero and finite temperature. To this end, we use a non-linear, non-parametric Gaussian-process regression, and construct a training database of total energies, stresses and forces taken from first-principles molecular dynamics simulations. We cover approximately  $10^5$  local atomic environments including

## **Preface**

---

pristine and defected bulk systems, and surfaces with different crystallographic orientations. We then validate the different GAP models against DFT data not directly included in the dataset, focusing on the prediction of thermodynamic, vibrational, and elastic properties and of the energetics of bulk defects.

Key words: Gaussian approximation potentials, density-functional theory, embedded atom method potentials, iron, body centered cubic, thermodynamics, thermoelasticity, machine learning, magnetism

# Résumé

Le fer, principal constituant de l'acier, est un matériau d'une importance fondamentale dans les processus industriels et économiques de notre société. Les progrès récents de la physique numérique ont permis une meilleure compréhension des mécanismes microscopiques à l'origine des propriétés macroscopiques de ce matériau, que ce soit en conditions ordinaires ou extrêmes. En particulier, la simulation des lois de la mécanique quantique par des méthodes ab initio fondées sur la théorie de la fonctionnelle de la densité (density-functional theory, DFT) ont démontré leur efficacité dans ce domaine. Cependant, afin d'étudier des systèmes à des échelles de taille et de temps comparables à celles de l'expérience, des potentiels interatomiques sont nécessaires. Typiquement, ces derniers sont construits avec des formes fonctionnelles inspirées par l'intuition physique dans lesquelles on insère des paramètres ajustés aux données expérimentales à température nulle/basse, et/ou aux données ab initio disponibles. Cependant, malgré leur grand succès, leur faible flexibilité limite l'amélioration systématique de ces potentiels lorsqu'on étend la base de données. De plus, leur précision aux températures intermédiaires et élevées reste incertaine.

Dans ce travail de thèse, nous commençons par examiner une sélection de potentiels selon le modèle de l'atome entouré (embedded atom method, EAM). Le but est de comprendre leurs points forts et leurs limites dans la reproduction des propriétés thermodynamiques, vibrationnelles et élastiques expérimentales du fer cubique centré (bcc) à température finie. Nos calculs suggèrent que tous les potentiels ne reproduisent pas les expériences à haute température, où l'on sait que les fluctuations magnétiques, qui ne sont pas explicitement prises en compte dans la dynamique moléculaire (MD) classique, deviennent de plus en plus importantes. De plus, ils donnent à penser que, malgré une rapide et anormale diminution de la constante élastique de cisaillement  $C_{44}$ , le paramétrage Mendeleev03 est en moyenne le plus précis parmi tous ceux pris en compte dans ce travail.

Dans une deuxième étape, nous calculons les mêmes propriétés à température finie en utilisant la théorie de la fonctionnelle de la densité. Nous vérifions notre implementation utilisant des pseudopotentiels, des ondes planes et prenant en compte la polarisation du spin, en la comparant à une sélection de calculs "tous électrons" à température nulle. Nous mettons ainsi en évidence les limites de la fonctionnelle d'échange et de corrélation semi-locale avec approximation de gradient généralisé pour la description des propriétés électroniques du fer. En revanche, nous démontrons que, si l'on tient compte des degrés de liberté vibrationnels, la DFT fournit une bonne description du comportement thermique des propriétés thermodynamiques et élastiques du fer- $\alpha$  jusqu'à une température relativement

## Preface

---

proche de la température de Curie, sans explicitement inclure des degrés de liberté magnétiques transversaux. Les effets d'entropie électronique sont également analysés et on montre qu'ils sont d'une importance secondaire.

Enfin, dans une tentative de créer de nouveaux modèles interatomiques flexibles et systématiquement améliorables lorsqu'on étend la base de données, nous générons une sélection de potentiels d'approximation Gaussienne (Gaussian approximation potentials, GAP) sur la base d'une régression par processus Gaussien non-linéaire et non-paramétrique. À cette fin, nous construisons une base de données d'énergies totales, de contraintes et de forces obtenues à partir de simulations de dynamique moléculaire *ab initio* effectuées sur des structures pures ou avec défauts et sur des surfaces avec diverses orientations cristallographiques. Cette base de données contient approximativement  $10^5$  environnements atomiques locaux différents. Nous validons ensuite les différents modèles GAP en les comparant à des données DFT non directement incluses dans le jeu de données initial, en se focalisant sur la prédiction des propriétés thermodynamiques, vibrationnelles et élastiques ainsi que sur celle des énergies de formation des défauts du solide.

Mots clefs: Potentiels d'approximation Gaussienne, théorie de la fonctionnelle de la densité, modèle de l'atome entouré, fer, cubique centré, thermodynamique, thermoélasticité, apprentissage automatique, magnétisme

# Contents

<b>Acknowledgements</b>	<b>i</b>
<b>Preface</b>	<b>iii</b>
<b>Abstract (English/Français)</b>	<b>v</b>
<b>List of figures</b>	<b>xiii</b>
<b>List of tables</b>	<b>xv</b>
<b>1 Introduction</b>	<b>1</b>
1.1 Why iron? . . . . .	3
1.2 Outline . . . . .	6
<b>2 Theoretical tools: Quantum energy models</b>	<b>9</b>
2.1 Born-Oppenheimer approximation . . . . .	9
2.2 Density-functional theory . . . . .	11
2.2.1 Exchange and correlation functionals . . . . .	13
2.2.2 Spin-polarized DFT . . . . .	14
2.2.3 Bloch theorem and plane-wave formulation . . . . .	15
2.2.4 Pseudopotentials . . . . .	17
2.3 Finite-temperature extension of DFT . . . . .	18
2.4 Crystal vibrations . . . . .	22
2.4.1 Hellmann-Feynman forces . . . . .	22
2.4.2 Normal modes – Phonons . . . . .	23
2.4.3 Dynamical-matrix calculation . . . . .	25
<b>3 Theoretical tools: Classical energy models</b>	<b>29</b>
3.1 Interatomic potentials and linear scaling . . . . .	29
3.1.1 Local environments . . . . .	31
3.1.2 Pairwise Lennard-Jones model . . . . .	32
3.1.3 Embedded-atom method . . . . .	33
3.1.4 Bond-order potentials . . . . .	34
3.1.5 Artificial neural networks . . . . .	36

## Contents

---

<b>4</b>	<b>Elasticity</b>	<b>39</b>
4.1	Strain . . . . .	39
4.2	Stress . . . . .	40
4.3	Elastic constants . . . . .	41
4.3.1	Elastic constants and sound velocities relations . . . . .	42
4.4	Long wavelength limit of acoustic phonons . . . . .	43
<b>5</b>	<b>Statistical sampling</b>	<b>45</b>
5.1	Quasi-harmonic approximation (QHA) . . . . .	46
5.2	Useful thermodynamic relations . . . . .	47
5.3	Molecular dynamics . . . . .	48
<b>6</b>	<b>Gaussian approximation potentials (GAP)</b>	<b>49</b>
6.1	Gaussian process regression . . . . .	49
6.1.1	Function-space view . . . . .	50
6.1.2	Weights-space view . . . . .	51
6.1.3	Mean and error prediction: equivalence of the two methods . . . . .	52
6.2	Covariance functions and hyper-parameters . . . . .	53
6.3	Training interatomic potentials from total energies, forces and stresses . . . . .	54
6.4	Sparsification . . . . .	55
6.5	GAP kernel: smooth overlap of atomic positions (SOAP) . . . . .	56
6.5.1	SOAP GAP parameters . . . . .	58
6.6	Database generation . . . . .	58
6.6.1	Equilibrium geometry and elastic constants . . . . .	59
6.6.2	Bulk vibrations . . . . .	60
6.6.3	Vacancies . . . . .	62
6.6.4	Surfaces . . . . .	65
6.6.5	Gamma surfaces . . . . .	68
6.6.6	Convergence of first-principles calculations for GAP database . . . . .	70
<b>7</b>	<b>Thermodynamic and thermoelastic properties of <math>\alpha</math>-iron</b>	<b>75</b>
7.1	EAM results . . . . .	75
7.1.1	Thermodynamic results . . . . .	76
7.1.2	Phonons and elastic constants . . . . .	77
7.1.3	Computational details . . . . .	84
7.2	DFT results . . . . .	86
7.2.1	Thermodynamics and thermoelasticity . . . . .	86
7.2.2	Volumetric strain . . . . .	87
7.2.3	Tetragonal and trigonal strains – $C_{11}$ , $C_{44}$ . . . . .	88
7.2.4	Finite temperature electrons . . . . .	101
7.2.5	Defects . . . . .	107
7.2.6	Computational details and pseudopotential selection . . . . .	110
7.3	GAP results . . . . .	115

7.3.1	Setting of the hyper-parameteres and verification . . . . .	115
7.3.2	Validation . . . . .	117
<b>8</b>	<b>Conclusions and future directions</b>	<b>133</b>
<b>A</b>	<b>Gaussian processes for EOS fitting: a basic 1D Python implementation</b>	<b>137</b>
<b>B</b>	<b>Supplemental material</b>	<b>143</b>
	<b>Bibliography</b>	<b>163</b>
	<b>Curriculum Vitae</b>	<b>165</b>





# List of Figures

1.1	Experimental phase diagram of iron . . . . .	3
2.1	Mesh-smearing convergence: total energy . . . . .	21
2.2	Mesh-smearing convergence: pressure . . . . .	22
3.1	Neural network scheme . . . . .	36
6.1	Phonon BO AIMD trajectories . . . . .	62
6.2	Selected di-vacancies . . . . .	64
6.3	Mono- and di-vacancy BO AIMD trajectories . . . . .	65
6.4	Selected self-interstitials . . . . .	66
6.5	Surface BO AIMD trajectories . . . . .	67
6.6	Surface geometries . . . . .	68
6.7	Supercell for the (211) $\gamma$ surfaces . . . . .	69
6.8	$k$ -mesh convergence of physical properties . . . . .	71
6.9	Cutoff convergence of physical properties . . . . .	72
6.10	Absolute average force convergence in supercell . . . . .	73
7.1	Thermal expansion and linear coefficient: EAM . . . . .	78
7.2	Heat capacity: EAM . . . . .	79
7.3	Phonon dispersions: EAM . . . . .	79
7.4	Phonons: EAM . . . . .	80
7.5	$C_{11}$ elastic constant: EAM . . . . .	81
7.6	$C'$ and $C_{44}$ elastic constant: EAM . . . . .	82
7.7	$B$ and $C_{12}$ elastic constant: EAM . . . . .	83
7.8	$B$ from the finite deformations and virial: EAM . . . . .	84
7.9	Phase velocity convergence as a function of the cell size . . . . .	86
7.10	Phonon dispersion and Grüneisen from DFT QHA . . . . .	89
7.11	Phase diagram and thermal expansion from DFT QHA . . . . .	90
7.12	Thermal expansion coefficient and heat capacity from DFT QHA . . . . .	91
7.13	Adiabatic bulk modulus from DFT QHA . . . . .	92
7.14	Static energy landscape from DFT QHA . . . . .	94
7.15	Vibrational energy landscape from DFT QHA . . . . .	96
7.16	Free energy landscape from DFT QHA . . . . .	97

## List of Figures

---

7.17 $C_{11}$ and $C_{44}$ elastic constant from DFT QHA . . . . .	99
7.18 $C'$ elastic constant from DFT QHA . . . . .	100
7.19 DOS for electronic excitations: example . . . . .	102
7.20 DOS integration step . . . . .	102
7.21 Chemical potential . . . . .	103
7.22 Electronic entropy, Helmholtz free energy and magnetization . . . . .	104
7.23 Total heat capacities: electrons + QHA . . . . .	105
7.24 Total thermal expansion and adiabatic bulk modulus: electrons + QHA . . . . .	106
7.25 $\gamma$ surface (110) . . . . .	108
7.26 $\gamma$ surface (112) . . . . .	109
7.27 Equilibrium lattice parameter: pseudopotentials . . . . .	111
7.28 Equilibrium bulk modulus: pseudopotentials . . . . .	112
7.29 Equation of state and magnetization from DFT . . . . .	113
7.30 Density of states: shift with volume . . . . .	114
7.31 Equations of state GAP_3/5 and DFT . . . . .	118
7.32 Mono-vacancy formation energy as a function of volume . . . . .	119
7.33 Vacancy formation enthalpy as a function of pressure . . . . .	119
7.34 Minimum energy path from NEB: GAP_6 . . . . .	120
7.35 Self-interstitial formation energies: GAP_6 . . . . .	120
7.36 Phonon dispersions: GAP_3 . . . . .	122
7.37 Phonon dispersions: GAP_5 . . . . .	123
7.38 Phonon dispersions: GAP_6 . . . . .	124
7.39 Phonon softening: GAPS . . . . .	125
7.40 Thermal expansion: GAP_3/5 . . . . .	127
7.41 Thermal expansion: GAP_6 . . . . .	128
7.42 Thermal expansion coefficient: GAPS . . . . .	129
7.43 Heat capacity: GAPS . . . . .	130
7.44 Bulk modulus: GAP_6 . . . . .	131
B.1 Full trigonal strain tensor . . . . .	143
B.2 Ultrasoft and PAW pseudopotential comparison: phonons . . . . .	144
B.3 Bulk modulus from DFT QHA: polynomial fit comparison . . . . .	144
B.4 $C_{11}$ from DFT QHA: polynomial fit comparison . . . . .	145
B.5 $C_{44}$ from DFT QHA: polynomial fit comparison . . . . .	145

## List of Tables

6.1	Common covariance functions . . . . .	54
6.2	Hyper-parameters for a SOAP kernel . . . . .	58
6.3	Experimental lattice constants for bcc tungsten and $\alpha$ -iron . . . . .	60
6.4	Calculation details primitive distorted cells: electrons . . . . .	60
6.5	Calculation details bulk phonons: electrons . . . . .	61
6.6	Calculation details bulk phonons: ions . . . . .	61
6.7	Temperatures and volumes for the bulk phonon database . . . . .	61
6.8	Calculation details of $\gamma$ surfaces: electrons . . . . .	70
6.9	Calculation details of $\gamma$ surfaces: ions . . . . .	70
6.10	DFT database: $k$ -mesh information . . . . .	71
6.11	GAP training database: summary . . . . .	74
7.1	Thermoelasticity from EAM potentials . . . . .	77
7.2	Deformation tensors . . . . .	87
7.3	Average absolute error and coefficient of determination static landscape from DFT QHA . . . . .	94
7.4	Equilibrium lattice parameter and elastic constants from DFT QHA . . . . .	98
7.5	Extra equilibrium elastic constants from DFT QHA . . . . .	98
7.6	DFT vacancy formation and binding energies . . . . .	107
7.7	Radial cutoff, angular and radial resolution convergence . . . . .	116
7.8	GAPs generation details . . . . .	116
7.9	DFT and GAP elastic constants . . . . .	117
7.10	DFT and GAP properties . . . . .	132



# 1 Introduction

Since its theoretical foundation by Kohn and Sham in the mid-1960's [1–3], density-functional theory (DFT) has proved to be one of the most successful tools in the study of materials properties. The theory addresses the fundamental problem of solving the Schrödinger equation of a many-body system of interacting electrons via a Kohn-Sham mapping onto an auxiliary fictitious system of non-interacting electrons moving in a self-consistent external potential and generating the same electronic density of the real system. The formalism provides a method to compute the ground-state energy  $E_0$  for any given position of the atoms' nuclei, the so called potential energy surface (PES). The configuration in which each atom occupies its equilibrium position is the one that minimizes  $E_0$ . Furthermore,  $E_0$  allows one to compute the forces acting on atoms, which opens the way for first-principles simulations of the vibrational spectra, chemical reactions, first-principles molecular dynamics, and so on. Although exact in principle, this theoretical scheme requires some approximations to describe the unknown exchange and correlation contribution to the self-consistent potential stemming from the quantum fermionic nature of the interacting electrons. The development of simple local and semi-local exchange and correlation functionals such as the local density approximation [3] (LDA) and the generalized gradient approximation [4] (GGA), though relaxing the important requirement of non-locality of the exchange-correlation interactions, has proved to be reliable in a number of practical cases, although performing poorly in special classes of materials. Thanks to a steady increase of the available computational resources, the extension of the method to metallic and magnetic systems, and recent improvements in the description of the exchange and correlation interaction fixing part of the deficiencies suffered by LDA and GGA functionals (self-interaction [5–7], piece-wise linearity [8, 9], van der Waals dispersion forces [10–12]), this first-principles method is today routinely used in the study of many fundamental electronic, vibrational and optical properties and a broad range of applications, achieving in its plane-waves implementation (the leading workhorse for DFT calculations), an accuracy comparable to the one of real-life experiments and a predictive power well beyond that of any empirical model. However, the computational cost associated to solving the self-consistent set of equations by keeping the orthonormality condition in plane-wave approaches, is intrinsically cubic in the number  $N$  of Kohn-Sham orbitals explicitly treated

in the calculation. As a consequence, while relatively benign compared to other correlated wavefunction methods, this  $N^3$  scaling poses a severe limitation on the domain of applicability of DFT calculations that, with the current state-of-the-art implementations, are restricted to systems containing at most a few hundreds of atoms. The introduction of the concept of pseudopotentials [13–16], based on the idea of replacing the core electrons that do not participate to the chemistry of the atoms and the atomic nuclei with an effective potential, as well as the technological rush towards faster and faster supercomputers, have shown to be extremely useful in making DFT calculations faster. Nonetheless, they couldn't solve the underlying scaling problem which simply does not catch Moore's linear prediction for the increase of processing units performance with time.

For this reason, in the years, there has been considerable interest in the development of alternative or complementary approaches displaying an improved scaling. Recently, order- $N$  first-principles methods based on localized basis-set [17, 18] have been proposed and proved to achieve an accuracy comparable to the one of traditional plane-wave cubic-scaling methods. These offer potential to enlarging the size-scale of first-principles DFT calculations to include entire biological molecules and nanostructures containing a few thousands of atoms. However, the computational cost is still dominated by the explicit self-consistent treatment of the electronic problem which, if on the one hand provides a reasonably accurate and transferable description of the atomic interactions, on the other hand represents the actual bottleneck of this kind of first-principles methods to be used to study large systems.

Commonly, the gap between sizes affordable in first-principles DFT calculations and those necessary for describing realistic systems is bridged by removing *in toto* the electronic degrees of freedom and describing the interactions between atoms with approximated interatomic potentials. These achieve a linear scaling, similarly to order- $N$  DFT schemes, by relying on the concept of *locality* of the atomic energies, i.e., assuming the energy of any atom to depend just on the local environment within a given cutoff value. The main advantage of this approach over order- $N$  DFT schemes is however that the linear prefactors are orders of magnitude smaller than their first-principles counterparts. Interatomic potentials are commonly modeled with semi-empirical functional forms driven by physical intuition and fitted to experimental or computational data. The moderate flexibility of these functional forms limits their ability to be systematically improved by increasing the fitting datasets; on the other hand, their qualitative description of the essential physical interactions ensures a modicum degree of transferability. Recently, a novel trend has emerged where potential-energy surfaces are represented by neural networks [19–22] fitted on large numbers of first-principles calculations, thus maximizing flexibility but requiring extensive datasets to ensure transferability. Gaussian Approximation Potentials [23] (GAP) in particular are a novel class of potentials based on non-linear, non-parametric Gaussian-process regression. In this thesis we apply the GAP method to the case of  $\alpha$ -iron, training potential models from energies, stresses and forces taken from accurate first-principles DFT simulations of pristine and defected bulk and surface systems.

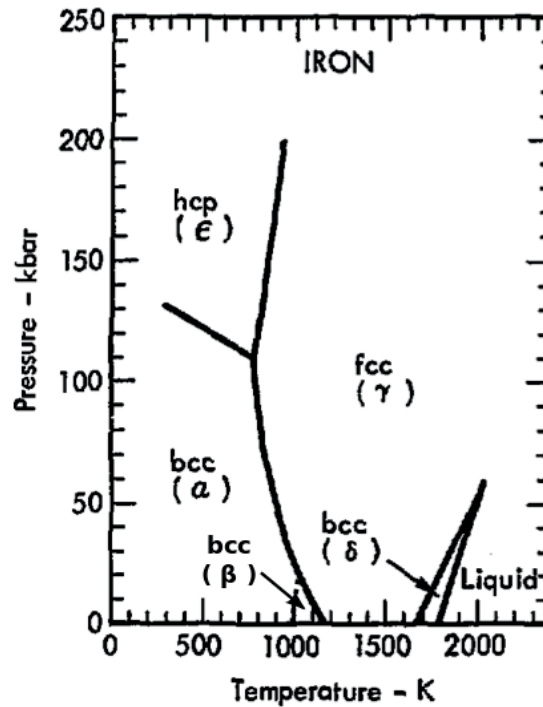


Figure 1.1: Phase diagram of elemental iron with the relevant thermodynamic phases. The image, taken originally from Ref. [24], is modified to display the  $\beta$ -phase.

## 1.1 Why iron?

To date, iron is a material of primary importance in the industrial and economic processes of our society as it is the major constituent of steels. A detailed knowledge of its thermo-mechanical properties from a microscopic scale is crucial for the understanding of all those phenomena related to steel production and processing like melting/solidification dynamics, grains/dendrites nucleation and growth [25–27], cracking [28], embrittlement [29–33], radiation damage [34, 35], just to cite a few. Other domains of relevant scientific interest and active research where iron is important are geophysics [36–38], due to the abundance of this element at the earth core, and biology, where iron is studied for its pivotal role in hemoproteins [39–42]. Elemental crystalline iron has a complex phase diagram (see Fig. 1.1) which has been studied experimentally for a long time. Its ground state, also called  $\alpha$ -ferrite, is a bcc ferromagnetic structure that turns into a paramagnetic bcc phase, the so-called  $\beta$ -phase, at the Curie temperature ( $T_C$ ) of  $\sim 1043$  K experiencing a second order transition. This magnetic transition is then followed at higher temperature by two other structural transformations, namely a  $\beta$ -bcc  $\rightarrow$   $\gamma$ -fcc and a  $\gamma$ -fcc  $\rightarrow$   $\delta$ -bcc, before melting at  $\sim 1810$  K. On the other hand, by application of pressure at sufficiently low temperature, the bcc ground state transforms into the hcp  $\epsilon$ -phase.

After the advent of DFT, many atomistic studies have been performed in order to shed light on the origin of the complexity of this phase diagram and to understand the driving mechanisms of the phase transformations. Nevertheless, standard DFT schemes turned out to have some

difficulties in describing the combined metallic and magnetic nature of iron. DFT-GGA proved to be able to correctly predict the bcc structure as the ground state of the system, explaining its stabilization over the closed-packed fcc and hcp ones in terms of the magnetic energy associated to the ferromagnetic ordering [43, 44]. However, the agreement between experimental and calculated lattice parameter and elastic constants is not as good as for other materials and, contrarily to what is typically found in the literature, the GGA lattice parameter of iron is systematically underestimated while the bulk modulus is overestimated [43, 45]. At the same time, LDA functionals would wrongly predict a non-magnetic hcp structure as the lowest energy state [43]. Only introducing gradient corrections, able to better describe density inhomogeneities typically associated to open structures like the bcc one, one recovers the expected experimental ground state structure.

Upon compression, GGA predicts a decreasing of the bcc atomic magnetic moments and, eventually, a stabilization of the hcp  $\epsilon$ -phase at sufficiently high pressure. Various DFT studies [46–48] suggest a collinear or non-collinear antiferromagnetic ordering for the ground state of the hcp structure rather than a non-magnetic configuration as was first proposed in Refs. [44, 49]. In fact, GGA predicts  $\alpha \rightarrow$  nonmagnetic hcp critical pressures in good agreement with experiments [50–52] but largely overestimates the bulk modulus and underestimates the equilibrium volume compared to the experimental values [46]. The agreement with experimental equation of state is improved assuming antiferromagnetic ordering for the hcp structure [53]. From the experimental point of view the situation is not clear since Mössbauer spectroscopy [54, 55], x-ray emission spectroscopy [56] and x-ray magnetic circular dichroism [57] provide no evidence of magnetism in the hcp phase. Nonetheless, at sufficiently low pressures, the possibility of weak remnant magnetism in the hcp phase has been invoked through indirect measurements of structural variation [58] or Raman mode splitting [59] and supported by more recent x-ray emission spectroscopy data [60], which however are in conflict with the large magnetic moments predicted theoretically in Refs. [46–48]. Recently, a high-pressure super-conductive state, whose nature is still debated, has been observed experimentally [61] in hcp iron. On the one hand, the possible disappearing of magnetism in going from the  $\alpha \rightarrow \epsilon$ -phase has been proposed as the trigger for such super-conductive state that, according to the BCS theory [62], is expected for any non-magnetic metal at sufficiently low temperature. On the other hand, several authors [46, 63, 64] have discussed the possible presence of remnant antiferromagnetic fluctuations in proximity of the super-conductive state as an indication of the exotic origin of the super-conductivity. To the best of my knowledge, only recently *ab initio* studies [65] have been carried out in this direction.

One of the first electronic structure works studying the high temperature phases of iron was carried out by Hasegawa and Pettifor [66]. The authors were especially interested in the effect of temperature on the magnetic degrees of freedom and, using a single-site spin-fluctuation theory of band magnetism (tight binding), were able to model the relative thermodynamic stability of the  $\alpha$ ,  $\gamma$ ,  $\delta$  phases invoking the thermal magnetic excitations as unique driving force for the transitions. However, because their model neglected the short-range magnetic correlations, the authors were unable to predict correctly the fact that the observed Curie



temperature for bcc  $\alpha$  iron is lower than the temperature of the  $\alpha \rightarrow \gamma$  transition and they didn't address the  $\alpha \rightarrow \beta$  transition. More recently, Körmann et al. [67] were able to compute fully ab initio the Helmholtz free energy up to the Curie point, including all the (uncoupled) thermal excitations that are thought to be the most relevant for magnetic metals, namely phonons, magnons, and thermal electrons. This approach was extended also to iron alloys like cementite [68] and clearly showed the relative importance of each of these contributions to the free energy and, consequently, to the description of selected thermodynamic quantities. In Ref. [67, 69], the same authors were also able to predict the divergence of the specific heat experimentally observed at the Curie point. More recently Körmann et al. and Ikeda et al. succeeded in modeling the paramagnetic bcc phase of iron in a fashion similar to Hasegawa and Pettifor, assuming a local picture for the magnetic moments without short-range order through the use of magnetic special quasi-random structures [70] and performing ensemble averages over supercells with disordered collinear magnetic moments. This approach relies on the separation of the fast and the slow dynamics of the magnetic- and vibrational degrees of freedom and completely neglects local magnetic correlations that have been observed experimentally at intermediate temperature above  $T_C$  [71]. The ability of calculating paramagnetic forces [72] and phonon dispersions [72, 73] allowed them to analyze magnetic disorder effects on phonons thus explaining the experimentally observed high temperature softening of transversal phonon modes (between  $H$  and  $P$  and between  $\Gamma$  and  $N$ ) that could not be described simply accounting for the thermal expansion effects of the ferromagnetic configuration [74, 75]. The softening in the  $\Gamma \rightarrow N$  direction in particular is associated to a strong decrease in the elastic constant  $C_{11}$ ,  $C' = \frac{C_{11}-C_{12}}{2}$  that is considered as a precursor of martensitic transformation through a Bain path from a bcc to a fcc structure, thus being critical for understanding the mechanical failure of ferritic steels at high temperature. Also, the authors of Ref. [72] were able to demonstrate the stabilization of high temperature fcc phonons, that turn out to be unstable both in a ferromagnetic and non-magnetic configurations. Very recently, they introduced a semi-empirical model to connect the ferromagnetic low temperature and paramagnetic high temperature regimes that were able to describe in a pure DFT fashion and managed to reproduce to a good extent the experimental temperature softening of the bcc phonon dispersion across the  $\alpha/\beta$  temperature range of stability. In order to describe temperature effects and magnetic disorder in  $\alpha$ -iron from an ab initio point of view, dynamical mean-field theory in combination with DFT has also been used [76, 77]. Leonov [77] managed to compute the high temperature paramagnetic phonons of the bcc and fcc structures with results similar to Ref. [72] in terms of mechanical stability of the two structures and also demonstrating the relative thermodynamic stability of the two phases across the Curie point. Another state-of-the-art ab initio method that has been developed to study magnetically disordered systems is the coherent potential approximation (CPA), in combination with the so-called disordered local moment (DML) model [78, 79]. An inherent limitation of this method is the impossibility of calculating forces and force constants, thus impeding the study of structural relaxation or mechanical instabilities. Beyond ab initio, other approaches that have been used to study magnetic disorder rely on semi-classical Heisenberg- or Ising-like model Hamiltonian, including magnetic cluster expansion and post Heisenberg

models [80, 81]. In these cases the exchange parameters of the models are typically fitted on DFT data and might be considered explicit functions of the local environment. Two problems at least may arise here. First, these models are fitted typically on non-collinear DFT configurations close to collinearity and their use for the description of disordered highly non-collinear conditions remains questionable. A more fundamental problem arises from the current implementation of non-collinearity available in most of the DFT codes. Non-collinear calculations are indeed generally performed through LSDA and GGA functionals. However, as pointed out by H. Gross [82], these functionals lack in providing a proper full non-collinear description of a magnetic system. A step towards more reliable non-collinear calculations is done by constructing functionals that allow for a Kohn-Sham exchange magnetic field that is not forced to be parallel to the local spin magnetization.

It is clear from this short review that elemental iron is not easily describable through standard ab initio methods even in its ground state. At finite temperature, different efforts have been made in order to study the effects of magnetic fluctuations. However, despite the encouraging results mentioned above, no standard ab initio approaches are available that can provide a reliable quantitative description of the thermodynamic properties of the different paramagnetic phases. To this end, one should first find ways of dealing with the short range magnetic correlations, and of including the coupling of magnetic fluctuations with other relevant thermal excitations such as vibrations (harmonic and anharmonic). Nonetheless, as shown in Ref. [45, 75, 83], standard DFT alone can describe ferromagnetic bcc iron and its thermodynamical and mechanical properties fairly well up to a large fraction of the Curie point. In this work, we prove also the ability of DFT in describing thermoelastic properties of the  $\alpha$ -phase and we consider this phase for the generation of reliable GAP interatomic potentials fitted entirely on DFT data. We think the creation of interatomic potentials able to achieve DFT accuracy within the entire temperature range of stability of the  $\alpha$ -phase is of paramount interest both for the scientific community and industry.

## 1.2 Outline

This thesis is organized as follows:

- **Chapter 2** contains a basic and succinct description of the quantum theoretical tools used in this thesis to compute materials properties from first-principles. Density-functional theory (DFT) for total energy calculations and density-functional perturbation theory (DFPT) for the phonon calculations are briefly reviewed. For more details the interested reader can look at a number of books and review articles [84–87].
- **Chapter 3** contains a short description of the most used classical energy models, i.e. the (semi-empirical) interatomic potentials, for metallic systems. For more details the reader is addressed to the review articles of the different models that are cited in the main body of this work.

- **Chapter 4** provides those relations from elasticity theory that are relevant for this work.
- **Chapter 5** deals with the statistical approaches used in this work to compute thermodynamic properties. Large emphasis is given to the description of the so-called quasi-harmonic approximation (QHA) for the analysis of the vibrational contributions to the Helmholtz free energy. Molecular dynamics (MD) techniques instead, although largely used throughout this work, will not be covered here, see rather Refs. [88–90] for an extended discussion. The chapter also provides useful thermodynamic relations used throughout the thesis.
- **Chapter 6** focuses on the theoretical framework of the Gaussian approximation potentials (GAP), thereby providing a description of the stochastic approach that allows for prediction starting from some reference data. The similarity kernel used in this work for representing and discriminating truly inequivalent local atomic environments is also introduced. Finally, the generation of the DFT database used for the training of GAP models is presented along with all the computational details.
- **Chapter 7** is devoted to the presentation of the results:
  - Sec. 7.1: the thermodynamic, vibrational and thermoelastic properties are calculated from four widely known embedded atom semi-empirical potentials available in the literature [91–94]. The results are obtained from classical MD that fully include phonon-phonon anharmonicity through a renormalization of the dynamical matrix and its eigenvalues. The thermoelastic response of the different potentials is obtained from the long-wavelength limit of the temperature dependent phonon dispersions. A manuscript with the results of this section is in preparation for publication in a peer-reviewed journal.
  - Sec. 7.2: the thermodynamic, thermoelastic properties of iron are also calculated from DFT. In this context the thermodynamic analysis is performed making use of the QHA described in chapter 5 allowing the longitudinal relaxation of the non-zero magnetic moments obtained from spin-polarized calculations. The results show that despite the missing transverse magnetic moment degrees of freedom, DFT predict good thermal trends for the elastic moduli up to a large fraction of the Curie point. The mismatch with experiments is attributable to the zero Kelvin description of the ferromagnetic system provided by the GGA functionals. The main results of this analysis have been reported in the following journal publication: [ D. Dragoni et al., “Thermoelastic properties of  $\alpha$ -iron from first-principles”, *Phys. Rev. B*, vol. 91, p. 104105, 2015 ] In addition, the effects on the thermodynamic properties due to the thermally activated electronic excitation in a band-theory formalism are considered.
  - Sec 7.3: this section is dedicated to the verification and validation of different versions of GAP models. The validation part is achieved comparing the GAP prediction for the structural, vibrational, thermodynamic properties obtained

## Chapter 1. Introduction

---

from classical MD and also of the energetics of defects against first-principles data. These results will be possibly made available via publication in a peer-reviewed journal.

- **Chapter 8** contains the conclusions and a discussion on possible future applications.

In Appendix A, we also report a code <sup>1</sup> for fitting one dimensional equation of states (or other one dimensional functions) through a Gaussian process regression, similarly to what is done in a higher dimensional space for Gaussian approximation potentials.

---

<sup>1</sup>Python Language Reference, version 2.7. Available at <http://www.python.org>

## 2 Theoretical tools: Quantum energy models

In this chapter we provide a brief description of the theoretical tools used in this thesis for the modeling of materials at a quantum level. The density-functional theory formalism and the Kohn-Sham scheme used to find electronic ground state energies is first introduced. The assumptions and approximations used in the theory, as well as the role of temperature as introduced by N. D. Mermin, are also discussed. In the second part of the chapter we address the theory of harmonic vibrations as obtained from a quadratic expansion of the potential energy surface around the equilibrium atomic positions, thus introducing the concept of collective vibrational modes, i.e. phonons. We finally give a brief overview on the methods available in the literature and adopted in this work to compute the phonon dispersion in solids.

### 2.1 Born-Oppenheimer approximation

A completely quantum mechanical description (also known as *first-principles* or *ab initio*) of a system and of its properties requires the full account of the elementary constituents of matter, atomic nuclei and electrons, and of all the electromagnetic interactions they mutually exchange. According to the rules of quantum mechanics, the state of a system is then described by a single wavefunction which includes both the nuclear and electronic degrees of freedom. If we knew the form of this wavefunction we could in principle solve the associated Schrödinger equation and calculate many equilibrium properties of materials. The trouble is that the solution for all but the simplest systems (e.g. small molecules) is very challenging, and in most cases still practically impossible even with the most powerful computers at hand. In the realm of solid state physics a useful approximation generally introduced to tackle the coupled nuclear-electronic problem is known as *adiabatic Born-Oppenheimer* (BO) approximation. It invokes a separation between the energy and time scales for ionic and electronic motions based on the different inertia of the two species. Indeed, being much lighter than ions (the proton and neutron/electron mass ratios are approximately 1836.152 and 1838.683 [95]), the electrons are considered as delocalized quantum particles which can move in solids much faster than the nuclei. Hence, the BO approximation assumes the electronic configuration

## Chapter 2. Theoretical tools: Quantum energy models

---

instantaneously relaxes to its ground state at each position the ions assume during their motion. In this “decoupled” approach, the ground state energy of the electrons can then be calculated fully quantum mechanically and the dynamical evolution of the nuclei takes place on the energy landscape, the BO potential energy surface (PES), that is determined by the electronic ground state at each atomic configuration.

In mathematical language, the BO approximation relies on the factorization of the global nuclear-electronic wavefunction into a wavefunction for the nuclei only and a wavefunction for the electrons depending parametrically upon the ionic positions as:

$$\Psi(\mathbf{R}, \mathbf{r}) = \Phi(\mathbf{R})\psi_{\mathbf{R}}(\mathbf{r}), \quad (2.1)$$

where  $\mathbf{R} = \{\mathbf{R}_I\}$  is the set of all the nuclear coordinates of the system, and  $\mathbf{r} = \{\mathbf{r}_i\}$  is its electronic counterpart (the spin degrees of freedom are not explicitly indicated). Assuming this factorization in the general Schrödinger equation of the coupled system and neglecting the *non-adiabatic* terms coming from the kinetic operator for the nuclei acting on the electronic wavefunction  $\psi_{\mathbf{R}}(\mathbf{r})$  (which depends parametrically on the nuclei coordinates), it is possible to split the initial complicated problem into two subproblems for the two degrees of freedom. This is expected to be a good approximation for most materials since the neglected terms are of the order of  $m/M$  between the (effective) electronic mass and the ionic one, but is known to perform poorly in those cases where non-adiabatic electron-vibron/phonon coupling become important. When adopted, the nuclear/ionic problem is then recast in the form of a Schrödinger equation for the nuclear/ionic wavefunction  $\Phi(\mathbf{R})$  only:

$$\left( -\sum_I \frac{\hbar^2}{2M_I} \frac{\partial^2}{\partial \mathbf{R}_I^2} + E(\mathbf{R}) \right) \Phi(\mathbf{R}) = \epsilon \Phi(\mathbf{R}), \quad (2.2)$$

where  $M_I$  is the mass of the  $I^{th}$  nucleus and  $E(\mathbf{R})$  is the Born-Oppenheimer PES corresponding to the energy of the electronic system with the nuclei clamped at configuration  $\mathbf{R}$ , obtained by solving a Schrödinger equation for the many-body electronic wavefunction  $\psi_{\mathbf{R}}(\mathbf{r})$ :

$$\left( -\sum_i \frac{\hbar^2}{2m} \frac{\partial^2}{\partial \mathbf{r}_i^2} + \frac{e^2}{2} \sum_{i \neq j} \frac{1}{|\mathbf{r}_i - \mathbf{r}_j|} - \sum_{iI} \frac{Z_I e^2}{|\mathbf{r}_i - \mathbf{R}_I|} + \frac{e^2}{2} \sum_{I \neq J} \frac{Z_I Z_J}{|\mathbf{R}_I - \mathbf{R}_J|} \right) \psi_{\mathbf{R}}^{\alpha}(\mathbf{r}) = E_{\alpha}(\mathbf{R}) \psi_{\mathbf{R}}^{\alpha}(\mathbf{r}), \quad (2.3)$$

where  $eZ_I$  is the charge of the  $I^{th}$  nucleus,  $-e$  and  $m$  are the electronic charge and mass, and  $\alpha$  is an index for the electronic state. Eq. 2.3 suggests that the BO PES is not unique. In fact, there is a different PES (and a different nuclear wavefunction) for each electronic state. In general (and in this work we comply with this point of view) the ground state PES is considered as the reference one.

This separation of the electronic and ionic degrees of freedom is also a very useful simplification that allows to perform (classical or quantum-mechanical) molecular dynamics calculations once the reference PES is known. The calculation of the PES however remains a formidably hard task. In fact, the wavefunction of a system of interacting electrons cannot

be factorized in single-electron terms and the direct solution of the many-body Schrödinger equation becomes a prohibitive task for almost all the systems. As result, in order to perform electronic structure calculations on materials of realistic complexity, an alternative approach is highly needed that, while maintaining all correlations between all the electronic degrees of freedom, is based on a more tractable quantity than the many-body wavefunction. The *density-functional theory* (DFT) proved to be the most successful of such methods.

## 2.2 Density-functional theory

Density-functional theory allows one to reformulate the interacting electronic many-body problem, shifting the attention from the many-body wavefunction  $\psi_{\mathbf{R}}(\mathbf{r})$  (depending explicitly on  $3N$  electronic Cartesian coordinates for a system of  $N$  electrons) to the electronic charge density  $n(\mathbf{r})$  (depending on three spatial coordinates only) as the key quantity to calculate.

The total energy  $E$  of an interacting electronic system can be generally written as the expectation value of the Hamiltonian  $\hat{H}$  on the many-body wavefunction:

$$E = E(\mathbf{R}) = \langle \psi_{\mathbf{R}} | \hat{H} | \psi_{\mathbf{R}} \rangle = \int d\mathbf{r}_1 \dots d\mathbf{r}_N \psi_{\mathbf{R}}^*(d\mathbf{r}_1, \dots, d\mathbf{r}_N) \hat{H} \psi_{\mathbf{R}}(d\mathbf{r}_1, \dots, d\mathbf{r}_N), \quad (2.4)$$

where the structure of  $\hat{H}$ , defined in left-hand side of eq. (2.3), does not depend on the particular system under consideration. This simple fact suggests that, at each ionic configuration, any variation of  $E$  must result from changes in the electronic many-body wavefunction,  $\psi_{\mathbf{R}}$ . In other words, eq. (2.4) shows that the total energy is a *functional*  $E[\psi]$  of the electronic wavefunction (the subscript  $\mathbf{R}$  is dropped for sake of clarity from now on). Its ground state value  $E_0 = E[\psi_0]$  can be obtained in principle through the Rayleigh-Ritz variational principle. In practice, this minimization approach hides the same complexity of the Schrödinger problem and, as such, becomes soon intractable with exact methods as the number of the degrees of freedom increases.

The quite remarkable result that Hohenberg and Kohn [1] were able to demonstrate and which lies at the core of density-functional theory, is a one to one correspondence between the ground state electronic charge density and the external potential. The non trivial part of the theorem shows that two or more external potentials differing from more than a constant from each other cannot result in the same ground state charge density  $n(\mathbf{r})$ . Being dependent on the external potential, all the ground state properties can thus be seen as functionals of the electronic density and, in particular, it is possible to express the total energy as:

$$E[n] = \int d\mathbf{r} V_{ext}(\mathbf{r}) n(\mathbf{r}) + F[n]. \quad (2.5)$$

The first term of the functional, explicitly dependent on  $n(\mathbf{r})$ , contains the interaction with fixed nuclei, while the second, implicitly dependent on  $n(\mathbf{r})$ , is a universal functional that contributes the kinetic and Coulomb electron-electron interaction terms of the energy. The

nuclear-nuclear Coulomb term can be added as a constant shift at any fixed nuclear configuration. The total energy functional (2.5) is also shown to be variational with respect to the electronic density and has an absolute minimum  $E_0$  at the ground state density  $n_0(\mathbf{r})$  corresponding to  $V_{ext}$ . It follows that the problem of minimizing the expectation value of eq. (2.4) through the Variational Principle on  $\psi_R$  is formally reduced to a much simpler problem of minimizing the functional (2.5) with respect to  $n(\mathbf{r})$ . It is important to notice that, following the original HK theorem, the functional  $E[n]$  has physical meaning only on the domain of real, integrable, positive definite functions  $n(\mathbf{r})$  which are ground state densities of some external potential ( $\nu$ -representability). Referring to Gunnarsson and Lundquist [96] “*As pointed out by Hohenberg and Kohn ... it has not been proved that an arbitrary density distribution containing an integer number of electrons can be realized by some external potential. When applying the variational principle ... one might therefore go outside ... range of definition*”, it is clear this restriction can be source of problems. In practice, this limitation to  $\nu$ -representable densities was formally solved by Levy who demonstrated through a constrained search approach how the total energy functional remains variational on an extended domain of  $N$ -representable densities [86, 97] realized by those antisymmetric functions that minimize the expectation value of kinetic plus electron-electron Coulomb interaction:

$$F[n] = \min_{\Psi \rightarrow n} \langle \Psi | \hat{K} + \hat{W} | \Psi \rangle. \quad (2.6)$$

The theoretical framework introduced to this point is formally exact and a minimization of eq. (2.5) (with a constraint to fix the total number of electrons  $N$ ) would lead to the solution of the problem. Unfortunately, the exact form of the functional  $F[n]$  is not known. The successful idea of Kohn and Sham to deal with this problem was to solve for the ground state an auxiliary system of non-interacting electrons constrained to have the same ground state electronic density of the interacting one. This constraint is imposed by assuming that the electrons of the auxiliary non interacting system move in the effective (so-called Kohn-Sham) potential resulting from the external potential and the interaction with other electrons. The problem can be recast into a series of single-particle Schrödinger-like equations:

$$\left[ -\frac{1}{2}\nabla^2 + V_{KS}(\mathbf{r}) \right] \phi_i(\mathbf{r}) = \epsilon_i \phi_i(\mathbf{r}), \quad (2.7)$$

called Kohn-Sham equations from which the ground state charge density can be computed as:

$$n(\mathbf{r}) = \sum_i^N |\phi_i(\mathbf{r})|^2, \quad (2.8)$$

where the sum is over the lowest possible single-particle eigenstates filled according to the Pauli exclusion principle.

In order to understand how Kohn-Sham equations can be obtained, it is convenient to rewrite eq. (2.6) using the expression of the ground state charge density in eq. (2.8). Separating a single-particle kinetic term and a classical density-density Coulomb interaction one easily



obtains;

$$E[n] = \int d\mathbf{r} V_{ext}(\mathbf{r})n(\mathbf{r}) - \sum_i \int d\mathbf{r} \phi_i^*(\mathbf{r}) \frac{\nabla^2}{2} \phi_i(\mathbf{r}) + \frac{e^2}{2} \int \int d\mathbf{r} d\mathbf{r}' \frac{n(\mathbf{r})n(\mathbf{r}')}{|\mathbf{r} - \mathbf{r}'|} + E_{xc}[n]. \quad (2.9)$$

The last term, corresponding to the difference between the unknown functional  $F[n]$  and the explicit single-particle kinetic and Hartree terms, is the so-called exchange-correlation (XC) functional and contains all the many-body terms of the energy. Minimizing this expression with respect to  $\phi_i^*(\mathbf{r})$  (or equivalently with respect to  $\phi_i(\mathbf{r})$ ) with the constraint  $\lambda_{ij}(\int d\mathbf{r} \phi_i^*(\mathbf{r})\phi_j(\mathbf{r}) - \delta_{ij})$ , it is easy to obtain the KS equations where the eigenvalues formally result from the diagonalization of the Lagrange multipliers matrix. This derivation highlights the meaning of the  $V_{KS}$  corresponding to:

$$V_{KS}(\mathbf{r}) = V_{ext}(\mathbf{r}) + e^2 \int d\mathbf{r}' \frac{n(\mathbf{r}')}{|\mathbf{r} - \mathbf{r}'|} + v_{xc}; \quad v_{xc} = \frac{\delta E_{xc}[n]}{\delta n(\mathbf{r})}. \quad (2.10)$$

$v_{xc}$  is called the exchange and correlation potential and is the derivative of the  $E_{xc}$  with respect to  $n$ . The price to be paid for the simplified picture is the dependence of  $V_{KS}$  in the solution  $n$ . That imposes a self-consistent iterative technique. It is important to remark also that  $\phi_i$  do not have any precise physical meaning except that sum of the squared moduli is the charge density of the system according to (2.8). At this level the theory is still exact. However, in order to make DFT a practical tool it is necessary to introduce approximations for the unknown XC energy term.

### 2.2.1 Exchange and correlation functionals

The simplest approximation is the local density approximation [3] (LDA) in which the exchange and correlation ( $xc$ ) energy functional is assumed to be a functional of the density only and to locally correspond to that of the homogeneous electron gas (HEG) having the same density,

$$E_{xc}^{LDA}[n] = \int d\mathbf{r} \epsilon_{xc}^{HEG}(n(\mathbf{r}))n(\mathbf{r}). \quad (2.11)$$

This approximation was designed to work with slowly varying electronic charge densities but it gives indeed quite good results also with non homogeneous systems like molecules, covalently bonded materials and (some) transition metals. It typically produces good agreement with experiments about structural and vibrational properties, but usually overestimates bonding energies and predicts shorter equilibrium bond lengths than found in experiments. In order to overcome these and other difficulties of LDA, some extensions of the original approximation were introduced; among those, the generalized gradient approximation [4] (GGA) family is the most successful. Within GGA the  $xc$  energy density is a functional of the local density and its

gradient:

$$E_{xc}^{GGA}[n] = \int d\mathbf{r} \epsilon_{xc}^{GGA}(n(\mathbf{r}), |\nabla n(\mathbf{r})|) n(\mathbf{r}) = \int d\mathbf{r} \epsilon_{xc}^{LDA}(n(\mathbf{r})) F_{xc}(n(\mathbf{r}), |\nabla n(\mathbf{r})|) n(\mathbf{r}). \quad (2.12)$$

In the literature two types of GGA functionals can be found: (i) the empirical functionals, whose parameters were determined by fitting to experimental or first-principles data, and (ii) the parameter free functionals, e.g. Perdew-Burke-Ernzhehorf [98] (PBE) and Perdew-Wang [98] (PW91), whose parameters were determined in order to satisfy mathematical relations which are known to hold for the exact functional. Within this context it should be mentioned that the parameter free functionals contain arbitrary choices such as the analytical form chosen to represent the function  $F_{xc}$  or the choice of constraints to be satisfied. The PBE approximation is the most used in the literature and is generally able to cure some inaccuracies of LDA (although the improvement is not systematic) most notably the of structural properties of materials. PBE improves in particular the results about the binding energy of real systems. It is also expected to give a better description of non homogeneous systems, like transition metals, producing correct results in some cases where LDA completely fails. A very important example is bulk iron for which it correctly predicts a ferromagnetic BCC ground state as opposed to LDA; this is also the main reason why it has been chosen as the reference functional parametrization in a large part of the calculations performed in this work.

### 2.2.2 Spin-polarized DFT

Since this work is focused on the ferromagnetic  $\alpha$ -phase of iron, it is necessary to discuss briefly how DFT incorporates spin degrees of freedom, leading to spin-density-functional theory (spin-DFT). The extension of the Hohenberg-Kohn theorem to spin-DFT implies that the total energy is a functional of the electron density (as in the non-magnetic case), and of the spin density, or in other terms, of the more general density matrix defined as :

$$n_{\alpha,\beta} = \sum_i \phi_i^*(\mathbf{r}; \alpha) \phi_i(\mathbf{r}; \beta), \quad (2.13)$$

with  $\alpha$  and  $\beta$ , taking the values up or down, to designate the two spinor components. As shown by von Barth and Hedin [99] one can derive the analog of the Kohn-Sham equations (2.7) for the generalized spin-DFT case. The effective Kohn-Sham potential then becomes:

$$V_{KS}(\mathbf{r}) = V_{ext}(\mathbf{r}) + e^2 \int d\mathbf{r}' \frac{n(\mathbf{r}')}{|\mathbf{r} - \mathbf{r}'|} + v_{xc} + \mu_B \boldsymbol{\sigma} \cdot \mathbf{B}_{xc}(\mathbf{r}), \quad (2.14)$$

where the effective magnetic field  $\mathbf{B}_{xc}(\mathbf{r})$  results from the functional derivative of the XC energy with respect to the various components of the density matrix. In most spin-DFT calculations performed, a ‘‘collinear’’ approximation is adopted in which spin is treated as a scalar quantity that can take only two possible values corresponding to the two eigenstates of the Pauli matrix  $\sigma_z$ . Within this approximation, the density matrix (2.13) is diagonal with only two components,

the up and down electronic densities

$$n^\uparrow(\mathbf{r}) = \sum_i |\phi_i^\uparrow(\mathbf{r})|^2, \quad n^\downarrow(\mathbf{r}) = \sum_i |\phi_i^\downarrow(\mathbf{r})|^2. \quad (2.15)$$

The total density  $n(\mathbf{r})$  and the magnetization  $m(\mathbf{r})$  can be obtained as:

$$n(\mathbf{r}) = n^\uparrow(\mathbf{r}) + n^\downarrow(\mathbf{r}), \quad (2.16)$$

$$m(\mathbf{r}) = \mu_B(n^\uparrow(\mathbf{r}) - n^\downarrow(\mathbf{r})), \quad (2.17)$$

and the Kohn-Sham equations can be rewritten independently for the two electron densities:

$$V_{KS}^\sigma(\mathbf{r}) = V_{ext}(\mathbf{r}) + e^2 \int d\mathbf{r}' \frac{n(\mathbf{r}')}{|\mathbf{r} - \mathbf{r}'|} + v_{xc}^\sigma; \quad v_{xc}^\sigma = \frac{\delta E_{xc}[n^\uparrow, n^\downarrow]}{\delta n^\sigma(\mathbf{r})}, \quad (2.18)$$

where  $\sigma$  runs over up and down spins.

In this collinear spin-polarized approach a generalization of the LDA and GGA approximations for the exchange and correlation functionals, known as local spin density approximation (LSDA), is typically used. The new expressions for the  $xc$  energies now reads:

$$E_{xc}^{LSDA}[n^\uparrow, n^\downarrow] = \int d\mathbf{r} \epsilon_{xc}^{HEG}(n^\uparrow(\mathbf{r}), n^\downarrow(\mathbf{r})) n(\mathbf{r}) \quad (2.19)$$

$$E_{xc}^{GGA}[n^\uparrow, n^\downarrow] = \int d\mathbf{r} \epsilon_{xc}^{GGA}(n^\uparrow(\mathbf{r}), n^\downarrow(\mathbf{r}), |\nabla n^\uparrow(\mathbf{r})|, |\nabla n^\downarrow(\mathbf{r})|) n(\mathbf{r}). \quad (2.20)$$

It is worth to mention that the two spins populations ( $\uparrow, \downarrow$ ) interact with each other through the Hartree and  $xc$  terms of the effective potential since the latter depends on both spin charge densities simultaneously. However, the Coulomb part of the potential has the same expression found in (2.10) and depending on the total charge density has the same value on both spins. The possible imbalance between the two spin populations (which produce a finite magnetization density  $m(\mathbf{r})$ ) is thus stabilized by the XC energy term.

### 2.2.3 Bloch theorem and plane-wave formulation

Crystalline solids are described as infinite repeated structures. The smallest repeated unit is the primitive unit cell, identified by three so-called Bravais vectors  $\{\mathbf{a}_1, \mathbf{a}_2, \mathbf{a}_3\}$  designating its edges, and by the positions of the atoms inside it. Because of periodicity any observable  $A$  is invariant with respect to translations by a multiple of the lattice vectors, i.e.  $A(\mathbf{r}) = A(\mathbf{r} + \mathbf{R})$ , where  $\mathbf{R} = n_1 \mathbf{a}_1 + n_2 \mathbf{a}_2 + n_3 \mathbf{a}_3$ . In particular this property is satisfied by the density  $n(\mathbf{r})$  and  $V_{ext}(\mathbf{r})$ .

The Bloch theorem states that single-particle wavefunction obeying a one-electron Schrödinger equation with a periodic potential can be written as:

$$\phi_{\mathbf{k},\nu}(\mathbf{r}) = e^{i\mathbf{k}\cdot\mathbf{r}} u_{\mathbf{k},\nu}(\mathbf{r}), \quad (2.21)$$

## Chapter 2. Theoretical tools: Quantum energy models

---

where  $u_{\mathbf{k},\nu}(\mathbf{r}) = u_{\mathbf{k},\nu}(\mathbf{r} + \mathbf{R})$  has the same periodicity of the crystal,  $\mathbf{k}$  is the so-called crystal momentum of the electrons, and  $\nu$  is a discrete band index classifying states of the same  $\mathbf{k}$ -vector. The  $\mathbf{k}$ -vectors can always be confined to the so-called first Brillouin Zone (BZ) of the reciprocal space. In turn, the first BZ is the reciprocal space counterpart of the primitive cell and, as the primitive cell in direct space, it is defined by means of three fundamental lattice vectors  $\mathbf{b}_i$  which are related to the primitive vectors  $\mathbf{a}_i$  in direct space according to  $\mathbf{b}_i \cdot \mathbf{a}_j = 2\pi\delta_{ij}$ ,  $i, j = 1, 2, 3$ . Imposing periodic boundary conditions on the wave functions it is possible to demonstrate that the wave vector  $\mathbf{k}$  must be real, and also restricted to the values  $\mathbf{k} = \sum_{i=1}^3 \frac{m_i}{N_i} \mathbf{b}_i$ , with  $m_i$  integer and  $N_i$  the number of repeated primitive cells in the crystal along the  $\mathbf{b}_i$  direction. As a consequence, in the limit of infinite (macroscopic) crystals, the spacing between consecutive  $\mathbf{k}$  points goes to zero and  $\mathbf{k}$  can be considered as a continuous variable. The dependence (dispersion) of  $\epsilon_{\mathbf{k},\nu}$  over  $\mathbf{k}$  along high symmetry paths of the BZ gives rise to the so-called band structure of the crystal.

In order to solve the KS equations in practice, it is useful to transform the original integro-differential problem into a more tractable algebraic one. This is obtained by expanding the Bloch electronic wavefunction on a basis set. The periodicity of the (ideal) crystal makes the plane wave (PW) basis set particularly suitable. This basis set also allows to exploit efficient algorithms, like the Fast Fourier Transform [100] (FFT), to move back and forth from real to reciprocal space. The Bloch single-particle wavefunction in eq.(2.21) can then be represented in the form:

$$\phi_{\mathbf{k},\nu}(\mathbf{r}) = \frac{1}{(N_c\Omega)^{\frac{1}{2}}} \sum_{\mathbf{G}} e^{i(\mathbf{k}+\mathbf{G})\cdot\mathbf{r}} c_{\nu}(\mathbf{k} + \mathbf{G}), \quad (2.22)$$

where  $\Omega$  is the volume of the unit cell,  $N_c$  the number of cells in the crystal, the  $\mathbf{G}$  vectors are the reciprocal lattice vectors, and the  $c_{\nu}(\mathbf{k} + \mathbf{G})$  coefficients are normalized in such a way that:

$$\sum_{\mathbf{G}} |c_{\nu}(\mathbf{k} + \mathbf{G})|^2 = 1. \quad (2.23)$$

Using this expansion, the KS equations can be written in reciprocal space as:

$$\sum_{\mathbf{G}'} \left[ \frac{\hbar^2}{2m} |\mathbf{k} + \mathbf{G}|^2 \delta_{\mathbf{G}\mathbf{G}'} + v_h(\mathbf{G} - \mathbf{G}') + v_{xc}(\mathbf{G} - \mathbf{G}') + v_{ext}(\mathbf{G} - \mathbf{G}') \right] c_{\nu}(\mathbf{k} + \mathbf{G}') = \epsilon_{\mathbf{k},\nu} c_{\nu}(\mathbf{k} + \mathbf{G}). \quad (2.24)$$

This equation illustrates how the periodicity of the potential makes the Hamiltonian block diagonal with respect to  $\mathbf{k}$  vectors and allows the diagonalization to be performed within each of these block separately, i.e. it is possible to solve the KS equations for each  $\mathbf{k}$  separately. Such expansion is clearly exact in the limit of an infinite number of plane waves but, in practical calculations, one can deal with a finite number of  $\mathbf{G}$  vectors only. Typically, they are chosen to

correspond to a kinetic energy up to a maximum (cutoff) value  $E_{cut}$

$$\frac{\hbar^2}{2m} |\mathbf{k} + \mathbf{G}|^2 \leq E_{cut}. \quad (2.25)$$

As a consequence, all the quantities of interest calculated in plane-wave DFT approaches need to be tested and converged with respect to this cutoff value. Fixing  $E_{cut}$  corresponds to being able to resolve real space features of KS wavefunction and other quantities down to a length of  $2\pi\hbar/\sqrt{2mE_{cut}}$ .

### 2.2.4 Pseudopotentials

The cost of solving the self-consistent set of Kohn-Sham equations for a given  $k$ -vector is known to scale as the cube of the number of electrons explicitly included in the system. As a consequence, the reduction of such a number can be beneficial for practical calculations and can be achieved by noting that electrons of each atom can be subdivided ideally in valence and core electrons. While the former tend to be delocalized, or partially localized around their atomic nuclei, and to participate to the chemistry of the system, the latter are much more localized and tend to have a strong atomic like character with deep energy levels. It seems therefore a natural choice to solve explicitly the KS problem for the valence orbitals only, while leaving internal electrons “frozen” in the cores they belong to. The resulting effective external potential that models the interaction of the reactive valence electrons with the nuclei dressed by core electrons is the so-called *pseudopotential* (PP). In practice, there exist different procedures for building a pseudopotential but they rely basically on the same general idea of replacing the original wavefunction of the valence electrons in the core region (defined by a core radius) with a nodeless and smooth pseudo-wavefunction. Once the pseudo-wavefunctions are generated with given shape and core-radius, the effective external potential is constructed by inverting the Schrödinger-like KS equation for the considered electronic state under the condition it reproduces the scattering properties of the "real" valence states of the reference atomic configuration in an energy range which has to be as large as possible to ensure good transferability of the pseudopotential when used in different chemical environments.

The position of the core-radius, the mathematical structure of the PP, the shape and the conditions enforced on the pseudo-wavefunction determine different possible families of pseudopotentials. For the norm-conserving [101] pseudopotentials a pseudo-wavefunction is built with the condition that the norm of the original full-potential wavefunction is preserved. This condition is relaxed in the case of Ultrasoft (US) PPs and Plane-Augmented Waves (PAW) PPs in order to reduce the number of  $\mathbf{G}$ -vectors required to describe the variation of the pseudo-wavefunctions in the core region thus making practical calculations less expensive. In this work thus we will make use mainly of these two types of PPs; the interested reader can refer to Ref. [102, 103] for detailed information about US and PAW pseudopotentials.

### 2.3 Finite-temperature extension of DFT

The theoretical infrastructure described so far is restricted to the calculation of ground state properties. N. D. Mermin [104] showed that it is possible to generalize the formalism of DFT to the finite temperature case. If we consider a system embedded in an external bath with which it is possible to exchange energy and particles (grand-canonical ensemble), a quantum state is generally described by a probability distribution over all the accessible pure states in the form of density operators  $\hat{\Gamma} = \sum_{N,i} p_{N,i} |\psi_{N,i}\rangle \langle \psi_{N,i}|$ , where  $p_{N,i}$  represents the probability to access to a pure state  $|\psi_{N,i}\rangle$  with  $N$  particles (under the constraints of  $\sum_{N,i} p_{N,i} = 1$ ,  $p_{N,i} \geq 0$ ). The expectation value of a generic physical observable, represented by an operator  $\hat{A}$ , can then be accessed by means of statistical averages over this mixture of states as the  $A[\hat{\Gamma}] = Tr\{\hat{\Gamma} \hat{A}\}$ .

The essential result shown by Mermin is that for a grand-canonical system at finite temperature a grand-canonical thermodynamic potential does exist (the analog of the total energy functional of eq.(2.5)) which is a variational functional on the domain of  $N$ -representable electronic densities and is minimum at the equilibrium density for that temperature. This functional is defined as the statistical average of the grand-canonical operator  $\hat{\Omega} = \hat{H} - T\hat{S} - \mu\hat{N}$ , and can be written as

$$\Omega[n] = \int d\mathbf{r} n(\mathbf{r})(v(\mathbf{r}) - \mu) + G[n], \quad (2.26)$$

$$G[n] = \min_{\hat{\Gamma} \rightarrow n} F[\hat{\Gamma}] = \min_{\hat{\Gamma} \rightarrow n} \{T[\hat{\Gamma}] + W[\hat{\Gamma}] - TS[\hat{\Gamma}]\}, \quad (2.27)$$

where  $\hat{H}$ ,  $\hat{S}$ ,  $\hat{N}$ ,  $T$  and  $\mu$  are the Hamiltonian, entropy, particle-number operators, temperature, and chemical potential, respectively, while  $G[n]$  is the finite temperature analog of the universal Hohenberg-Kohn functional of Sec. 2.2, defined by a constrained minimization (*à la* Levy [97]) of  $F[\hat{\Gamma}]$  in the space of density operators that realize the density  $n(\mathbf{r})$ .

Our ignorance on the functional form of  $G[n]$  prevents us from a direct minimization in the space of  $N$ -representable densities of the thermodynamic functional  $\Omega[n]$ . However, adopting a KS approach as developed for the ground state, as described in Sec. 2.2, it is possible to rewrite the grand-canonical potential functional using an auxiliary non-interacting system constrained to have the same density of the interacting one. In strict analogy to the  $T=0$  case,

our ignorance on  $G[n]$  is confined into a single exchange-correlation term  $F_{xc}[n]$  as

$$\Omega[n] = \int d\mathbf{r} n(\mathbf{r})(v_{ext}(\mathbf{r}) - \mu) + K_s[n] + J_s[n] - TS_s[n] + F_{xc}[n], \quad (2.28)$$

$$K_s[n] = \sum_i^\infty f_i \int d\mathbf{r} \phi_i(\mathbf{r}) \left( -\frac{1}{2} \nabla^2 \right) \phi_i(\mathbf{r}), \quad (2.29)$$

$$J_s[n] = \frac{e^2}{2} \int \int d\mathbf{r} d\mathbf{r}' \frac{n(\mathbf{r})n(\mathbf{r}')}{|\mathbf{r} - \mathbf{r}'|}, \quad (2.30)$$

$$S_s[n] = -k_B \sum_i^\infty \{f_i \ln f_i + (1 - f_i) \ln (1 - f_i)\}, \quad (2.31)$$

$$n(\mathbf{r}) = \sum_i^\infty f_i |\phi_i(\mathbf{r})|^2, \quad (2.32)$$

where  $f_i = (1 + e^{\beta(\epsilon_i - \mu)})^{-1}$  is the Fermi-Dirac occupation number,  $\beta = 1/(k_B T)$ , and  $S_s$  the Fermi-Dirac entropy of the non-interacting Kohn-Sham electrons. The exact  $xc$  free energy functional is not known but, as before, is supposed to be small compared to the other terms so that approximations in its expression can be expected to have a moderate impact on the results of calculations. In practice, in most cases where temperature conditions are not severe, either LDA or GGA approximations are assumed to be adequate to describe a system at finite temperature. As in the zero temperature case, the problem of minimizing the thermodynamic functional is reduced to finding the minimum free energy of an auxiliary system of non-interacting particles in an effective external potential able to enforce the same charge density. The following finite temperature KS equations result:

$$\left[ -\frac{1}{2} \nabla^2 + v_{KS}(\mathbf{r}) \right] \phi_i(\mathbf{r}) = \epsilon_i \phi_i(\mathbf{r}), \quad (2.33)$$

$$v_{KS}(\mathbf{r}) = v_{ext}(\mathbf{r}) + e^2 \int d\mathbf{r}' \frac{n(\mathbf{r}')}{|\mathbf{r} - \mathbf{r}'|} + v_{xc}; \quad v_{xc} = \frac{\delta F_{xc}[n]}{\delta n(\mathbf{r})}, \quad (2.34)$$

which can be solved self-consistently remembering that the population of the KS states is determined by the Fermi-Dirac statistics.

It is worth to mention that in actual total energy calculations one deals with canonical systems with fixed number of particles  $N$ ; the reference thermodynamic potential in this case is the *Helmholtz* free energy which can be calculated as  $F[n] = \Omega[n] + \mu N[n]$  from eq. 2.28. The chemical potential now is considered as an adjustable parameter which can be tuned in order to satisfy (at self-consistency) the condition  $N = \sum_i^\infty f_i$  for the conservation of the non-interacting particle number.

### Non self-consistent finite-temperature DFT

In this work, calculations of finite temperature electronic properties have been carried out with an approximated method that has been discussed in the literature [83, 105]. This method provides finite temperature information at the cost of a single run performed at zero tem-

perature. The temperature dependence of the physical quantities of interest is introduced *a posteriori*, by assuming the occupation of the KS eigenstates to change with temperature only through the Fermi-Dirac statistics. No self-consistency is performed, the KS eigenvalues and the total electronic density are calculated once and are assumed to be in their ground-state values. In mathematical language, if we consider also a volume dependence of the free energy, this is equivalent to rewriting the Helmholtz free energy as

$$F_{el}(V, T) = E_{stat}(V) + \sum_i \epsilon_i^0 [f_i^{FD}(V, T) - f_i^{FD}(V, 0)] - TS(V, T), \quad (2.35)$$

$$f_i^{FD} = (1 + e^{\beta(\epsilon_i - \mu)})^{-1} \quad (2.36)$$

with  $S(V, T)$  given in eq. (2.31). Exploiting this definition of the entropy is then possible to get an analytic expression for the non-interacting electronic specific heat contribution

$$C_V(V, T) = T \left. \frac{\partial S}{\partial T} \right|_V = T \sum_i \frac{\partial f_i}{\partial T} \ln \left[ \frac{f_i}{1 - f_i} \right], \quad (2.37)$$

being

$$\frac{\partial f_i(V, T)}{\partial T} = (1 - f_i) f_i \left[ \frac{\epsilon - \mu}{k_B T^2} - \frac{1}{k_B T} \frac{\partial \mu}{\partial T} \right], \quad (2.38)$$

$$\frac{\partial \mu(V, T)}{\partial T} = \frac{\sum_i (1 - f_i) f_i (\epsilon_i - \mu)}{\sum_i (1 - f_i) f_i} \frac{1}{k_B T^2}. \quad (2.39)$$

It is important to note that the entropic term of eq. (2.35) is the entropy of the fictitious system of non interacting KS particles. The difference between the entropy of the interacting system and the one computed from the FD occupation of the KS energies is contained in  $F_{xc}[n]$  of eq.(2.28). The derivative  $-\left. \frac{\partial F_{el}}{\partial T} \right|_V$ , where  $F_{el}$  is calculated self-consistently, corresponds to the total (approximated) entropy of the interacting system.

### Smearing

Finally, it is important to note that finite temperature approaches are exploited to improve the convergence with respect to the  $k$ -points BZ sampling in metals. At zero temperature, the Fermi-Dirac occupations drop abruptly from 1 (or 2, if spin unpolarized) to 0 as the corresponding KS eigenvalues become larger than the Fermi energy. As a consequence many key physical quantities, like the total energy or the charge density, that are obtained as integrals over the BZ and sums over bands, require very dense  $k$ -point meshes to be accurately represented with accuracy. Furthermore, even with dense meshes, self-consistent calculations could be affected by numerical instability due to the possible shift of the position of the eigenstate from above to below the Fermi energy  $\epsilon_F$  and viceversa. A way to circumvent this problem, is to introduce an electronic temperature that makes the occupation function smooth around the Fermi level. As stated by de Gironcoli [106], this is formally equivalent to introducing a smearing function on the density of states. Although Fermi-Dirac is the most



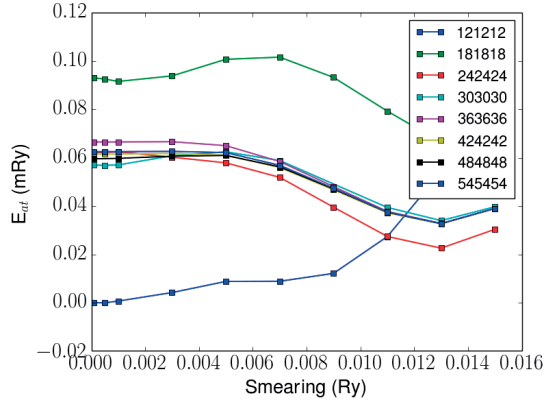


Figure 2.1: Convergence of the cold-smearing free energy per atom with respect to the  $k$ -point mesh and smearing temperature  $\sigma$ . Note that for large enough smearing values (out of the range reported in this figure) the different curves would coincide.  $\alpha$ -iron with the Fe.pbe-spn-kjpaw.UPF (PAW GGA-PBE) functional from the pslibrary 0.3.1. [112]

natural choice to smear the occupation function, it is possible to show that the convergence of the Mermin free energy with respect to the electronic temperature  $T$  (for  $T$  low enough) to the zero temperature total energy  $E_{tot}$  is only quadratic. In practice, due to computational limitations, one is forced to use coarse meshes and smearing widths corresponding to very high temperature and the quadratic convergence may introduce large errors in the calculation. It is then useful to define alternative smearing schemes that display an improved convergence rate by making the occupation function artificially smoother.

Examples of smearing schemes/occupation functions that are generally used in practical calculations are the Gaussian [107] scheme, the Methfessel and Paxton generalized Gaussians [108] scheme and the Marzari-Vanderbilt [109] scheme. These show a convergence of the free energy which is either cubic or quartic with respect to a smearing temperature  $\sigma$ . The price to pay is that the fictitious temperature parameter  $\sigma$  loses any direct relation with the real FD electronic temperature  $T$  and that the free energy functional to be minimized is not the “natural” finite temperature Mermin functional anymore. In fact, as discussed by De Vita and Gillan [110], each smearing scheme is associated to its own free energy functional. In this thesis we will mainly stick to the Marzari-Vanderbilt scheme, also called cold-smearing, which is cubic in  $\sigma$  at the leading order and is forced to have always positive occupations, thus solving the unphysical negative occupations that the Gaussian scheme can have. More recently Verstraete and Gonze developed a generalized cold-smearing technique [111] to construct smearing schemes that target not just the zero-temperature occupation function, but any other choice like, for instance, a finite-temperature Fermi-Dirac one.

A practice example of the convergence of the total energy and other quantities with respect to the interdependent  $k$ -mesh and fictitious temperature  $\sigma$  is provided in Figs. 2.1, 2.2.

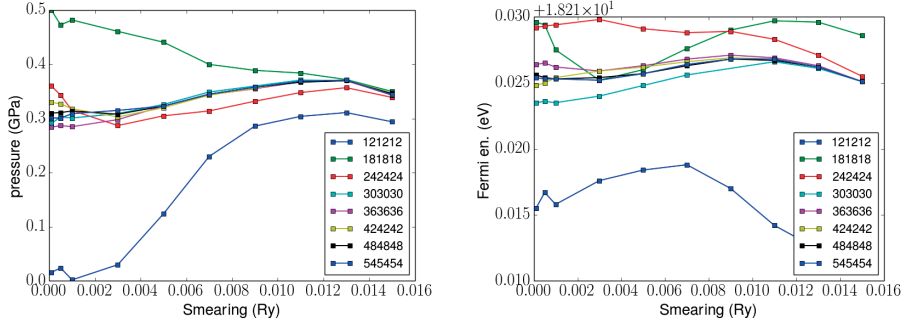


Figure 2.2: Convergence of the pressure and Fermi energy with respect to the  $k$ -point mesh and cold smearing temperature  $\sigma$ . Note that for large enough smearing values (out of the range reported in this figure) the different curves would coincide.  $\alpha$ -iron with the Fe.pbe-spn-kjpaw.UPF (PAW GGA-PBE) functional from the pslibrary 0.3.1. [112]

## 2.4 Crystal vibrations

As we have seen above, DFT is essentially a theory to describe the electronic structure of materials without any external parameter. The theory is formally exact within the BO approximation for any ionic configuration although approximations are needed for the  $xc$  term. In practice, a wide variety of physical properties of solids depend on their lattice vibrations. In this section a concise review of the method to extract them from DFT calculations will be presented. The precise evaluation of the BO PES  $E(\mathbf{R})$  will be the starting point of this discussion that will mainly concern calculation of the energy derivative with respect to atomic positions.

### 2.4.1 Hellmann-Feynman forces

The first quantity necessary for studying dynamics and/or equilibrium conditions of a system are ionic forces. The force acting on any atom  $I$  is defined as the negative derivative of the total energy with respect to the position of the considered atom:

$$F_I = - \frac{dE(\mathbf{R})}{d\mathbf{R}_I}. \quad (2.40)$$

Although a finite difference approach is possible, it results largely impractical due to the large number of total energy calculations needed. A more elegant and efficient way to compute forces is based on the Hellmann-Feynman theorem [113]. This theorem states that the first derivative of the energy eigenvalues of an Hamiltonian  $H_\lambda$ , depending on a parameter  $\lambda$  (a set of nuclear positions in a solid for instance), is given by the expectation value of the derivative of the Hamiltonian:

$$\frac{dE_\lambda}{d\lambda} = \frac{d}{d\lambda} \langle \psi_\lambda | H_\lambda | \psi_\lambda \rangle = \left\langle \psi_\lambda \left| \frac{\partial H_\lambda}{\partial \lambda} \right| \psi_\lambda \right\rangle, \quad (2.41)$$

where  $\psi_\lambda$  is the eigenfunction of the parametric Hamiltonian  $H_\lambda$  corresponding to the eigenvalue  $E_\lambda$ . This theorem leads to a considerable simplification in the task of calculating atomic forces. In fact, combining eqs. (2.2, 2.5), we find that the Hellmann-Feynman force acting on an atom  $I$  is:

$$\mathbf{F}_I = \int d\mathbf{r} n_{\mathbf{R}}(\mathbf{r}) \frac{\partial V_{\mathbf{R}}(\mathbf{r})}{\partial \mathbf{R}_I} + \frac{\partial E_N(\mathbf{R})}{\partial \mathbf{R}_I}, \quad (2.42)$$

$V_{\mathbf{R}}(\mathbf{r})$  being the electron-nuclei interaction (external potential) and  $E_N(\mathbf{R})$  the electrostatic interaction between nuclei (whose derivative is known analytically). This relation shows that the calculation of the forces for all  $M$  atoms in a specific configuration in the system only requires the electronic ground state density,  $n_{\mathbf{R}}(\mathbf{r})$  for the same nuclear configuration, which can be obtained from a single total energy calculation, as opposed to  $3M + 1$  calculations required by eq. (2.40).

### 2.4.2 Normal modes – Phonons

The potential energy surface is also a critical quantity for calculating the vibrational properties of solids. The theory of vibrations in crystals (see Refs. [114,115]) is generally addressed starting from the limit of small oscillations of the atoms around the equilibrium crystal positions. In fact, in this limit the potential energy surface can be Taylor expanded up to the second order in the atomic displacements  $\{\mathbf{u}\}$  around the equilibrium position  $\{\mathbf{R}^0\}$ . To this end it is useful to exploit the periodicity of the crystal, which is also assumed from now on to have  $P$  atoms per unit cell. Then the position of the  $b$ th atom in the  $l$ th unit cell can be written as:

$$\mathbf{R}(\mathbf{l}\mathbf{b}) = \mathbf{l} + \mathbf{b} + \mathbf{u}(\mathbf{l}\mathbf{b}), \quad (2.43)$$

where  $\mathbf{l}$  is the position of the  $l$ th unit cell in the Bravais lattice,  $\mathbf{b}$  the equilibrium position of the atom in that unit cell while  $\mathbf{u}(\mathbf{l}\mathbf{b})$  is the atomic displacement. The Taylor expanded PES (around the equilibrium configuration) truncated at the second order then writes:

$$E(\mathbf{R}_1, \dots, \mathbf{R}_M) = \frac{1}{2} \sum_{\mathbf{l}, \mathbf{b}, \mathbf{l}', \mathbf{b}', \alpha, \beta} K_{\alpha\beta}(\mathbf{l}\mathbf{b}; \mathbf{l}'\mathbf{b}') u_\alpha(\mathbf{l}\mathbf{b}) u_\beta(\mathbf{l}'\mathbf{b}'), \quad (2.44)$$

with  $\alpha, \beta$  being Cartesian components and,

$$K_{\alpha\beta}(\mathbf{l}\mathbf{b}; \mathbf{l}'\mathbf{b}') = \left. \frac{\partial^2 E}{\partial \mathbf{R}_\alpha(\mathbf{l}\mathbf{b}) \partial \mathbf{R}_\beta(\mathbf{l}'\mathbf{b}')} \right|_{\{\mathbf{R}^0\}}. \quad (2.45)$$

In eq. (2.44) we have taken advantage of the fact that the first constant term of the expansion is unimportant for the dynamical problem and is set to zero, while the linear term vanishes at the equilibrium configuration  $\{\mathbf{R}^0\}$ .

This is known as the *harmonic* approximation and it is equivalent to having a set of atoms interconnected by forces that are linear in the displacement (like in classical springs) with

## Chapter 2. Theoretical tools: Quantum energy models

---

force constants that are given by the quadratic (non-zero lowest order) coefficients of the PES expansion, i.e. the Hessian components of the the BO energy surface. Higher order anharmonic terms in the expansion, especially cubic and quartic terms, are typically important when the atomic oscillations around the equilibrium become a relevant fraction of the inter-atomic distance and are responsible for a variety of phenomena such as thermal expansion (or contraction) and thermal conductivity. The harmonic approximation is not justified in all those cases in which the system under consideration is far from the equilibrium condition with respect to the atomic positions (i.e. a minimum of the potential energy surface) and in those cases where anharmonic effects are non-negligible (bulk materials [116, 117], atoms close to surfaces, vacancies [118] or defects in general).

In the harmonic approximation, the dynamics of the system is described by a set of coupled Newton's equations of motion for the atomic displacements

$$m_b \ddot{u}_\alpha(\mathbf{l}\mathbf{b}) = \sum_{\mathbf{l}'\mathbf{b}',\beta} K_{\alpha\beta}(\mathbf{0}\mathbf{b}; \mathbf{l}'\mathbf{b}') u_\beta(\mathbf{l}'\mathbf{b}'), \quad (2.46)$$

where we have used the lattice translational symmetry ( $K_{\alpha\beta}(\mathbf{l}\mathbf{b}; \mathbf{l}'\mathbf{b}') = K_{\alpha\beta}(\mathbf{0}\mathbf{b}; (\mathbf{l}' - \mathbf{l})\mathbf{b}')$ ) for which a wave-like solution exist of the form:

$$u_\alpha(\mathbf{l}\mathbf{b}) = \frac{1}{\sqrt{m_b}} \sum_{\mathbf{q},\nu} U(\mathbf{q}\nu; \mathbf{b}) e^{i[\mathbf{q}\cdot\mathbf{l} - \omega t]}. \quad (2.47)$$

The normal frequencies  $\omega$  and displacement patterns  $\mathbf{u}(\mathbf{l}\mathbf{b})$  for atom  $b$  in the unit cell  $l$  at atomic position  $\mathbf{R}(\mathbf{l}\mathbf{b})$  are determined from the secular equation:

$$\det |\tilde{D}_{\alpha\beta}(\mathbf{b}\mathbf{b}'; \mathbf{q}) - \omega^2(\mathbf{q}) \delta_{\alpha\beta} \delta_{\mathbf{b}\mathbf{b}'}| = 0, \quad (2.48)$$

where  $\tilde{D}$  is known as the (reciprocal) *dynamical matrix* ( $3P \times 3P$  matrix with  $3P$  modes at each  $\mathbf{q}$  for a system of  $P$  atoms) and its components are the Fourier transform of the force constants scaled by the square root of the nuclear masses as:

$$\tilde{D}_{\alpha\beta}(\mathbf{b}\mathbf{b}'; \mathbf{q}) = \frac{1}{\sqrt{m_b m_{b'}}} \sum_{\mathbf{l}'} e^{i\mathbf{q}\cdot\mathbf{l}'} K_{\alpha\beta}(\mathbf{0}\mathbf{b}; \mathbf{l}'\mathbf{b}') = \frac{1}{\sqrt{m_b m_{b'}}} \tilde{K}_{\alpha\beta}(\mathbf{b}\mathbf{b}'; \mathbf{q}). \quad (2.49)$$

Eq. 2.48 produces  $3P$  eigenvalues  $\omega^2(\mathbf{q}, \nu)$ , where  $\nu = 1, 2, \dots, 3P$ . Two remarks are in order: first the dynamical matrix is Hermitian and its eigenvalues real (a negative eigenvalue corresponds to imaginary frequencies and usually suggests that the system is mechanically unstable); second from the property of translational invariance a lattice distortion of wave vector  $\mathbf{q}$  does not induce force response in the crystal at wave vector  $\mathbf{q}' \neq \mathbf{q}$ .

The wave-packets into which an atomic displacement is decomposed are the so-called normal vibrational modes, or simply *phonons*. These are (thermally excited) collective modes of the periodic crystal lattice each with its own characteristic frequency  $\omega(\mathbf{q}, \nu)$ , wavelength  $\mathbf{q}$  (restricted to the first BZ) and band index  $\nu$  (as the KS electrons described in the section above)

that, at each instant of time  $t$ , describe the apparently disordered motion of the nuclei around the crystal equilibrium positions. They can also be considered as non-interacting quasi-particle obeying a Bose-Einstein statistics and are characterized by energy levels  $\hbar\omega(n + \frac{1}{2})$ , with  $n$  integer number enumerating the accessible discrete states for a given mode  $\mathbf{q}\nu$ .

### 2.4.3 Dynamical-matrix calculation

From the discussion above it is clear that the first step to solve the secular equation is the calculation of the dynamical matrix. The approaches available in the literature that we have used to achieve this goal throughout this thesis are linear-response, frozen phonons and a new method developed by T. Kong based on molecular dynamics ensemble averages.

#### Density-functional perturbation theory

In the linear-response approach [87, 119], the dynamical matrix is computed directly in reciprocal space by means of a perturbation of the equilibrium configuration with monochromatic displacements. In this case the Fourier transformed force constant  $\tilde{K}_{\alpha\beta}(\mathbf{b}\mathbf{b}'; \mathbf{q})$  is split in a ionic  $^{ion}\tilde{K}_{\alpha\beta}(\mathbf{b}\mathbf{b}'; \mathbf{q})$  and in an electronic contribution  $^{el}\tilde{K}_{\alpha\beta}(\mathbf{b}\mathbf{b}'; \mathbf{q})$ . The ionic contribution comes from the ion-ion interaction, does not depend on the electronic structure and can be calculated quite easily. The electronic part instead is more complex to compute and is given by:

$$^{el}\tilde{K}_{\alpha\beta}(\mathbf{b}\mathbf{b}'; \mathbf{q}) = \frac{1}{N_c} \left[ \int d\mathbf{r} \left( \frac{\partial n_{\mathbf{R}}(\mathbf{r})}{\partial u_{\alpha}(\mathbf{l}\mathbf{b}; \mathbf{q})} \right)^* \frac{\partial V_{\mathbf{R}}(\mathbf{r})}{\partial u_{\beta}(\mathbf{l}'\mathbf{b}'; \mathbf{q})} + \int d\mathbf{r} n_{\mathbf{R}}(\mathbf{r}) \frac{\partial^2 V_{\mathbf{R}}(\mathbf{r})}{\partial u_{\alpha}^*(\mathbf{l}\mathbf{b}; \mathbf{q}) \partial u_{\beta}(\mathbf{l}'\mathbf{b}'; \mathbf{q})} \right], \quad (2.50)$$

where  $N_c$  is the number of unit cells in the crystal,  $V_{\mathbf{R}}(\mathbf{r})$  the external potential (obtained as the sum of all the ionic pseudopotentials), and all the derivatives must be evaluated at zero displacement. This expression is obtained differentiating the Hellmann-Feynman forces in eq. (2.42) with respect to monochromatic displacements about the equilibrium positions and suggests that the calculation of the force constants for a given  $\mathbf{q}$  vector can be obtained by the knowledge of the first derivative of the DFT electronic density with respect to such displacements. The calculation of this derivative can be done very efficiently using *density-functional perturbation theory* [87] (DFPT), which is *linear-response theory* applied to DFT. DFPT solves the Sternheimer equation of perturbation theory treating the (linear) variation of the KS wavefunction (or of the charge density) as the main unknown. Since the corresponding variation of the effective KS potential depends on charge density variation these equations need to be solved self-consistently, starting from a well converged ground state calculation.

In DFPT one can calculate phonon frequencies at arbitrary wave vectors  $\mathbf{q}$  avoiding the use of supercells and with a workload that is essentially independent of the phonon wavelength. Although in principle it is possible to compute the entire phonon dispersion by sampling the first BZ with many different DFPT calculations, suitable interpolation techniques that

reduce the overall workload can be used when complete dispersions are needed. Simple concepts from discrete Fourier analysis show that the smoother the phonon dispersions, (i.e., the smoother the matrix elements  $\tilde{K}_{\alpha\beta}(\mathbf{b}\mathbf{b}'; \mathbf{q})$ ), the shorter is the range of real space interatomic force constants:

$$K_{\alpha\beta}(\mathbf{0}\mathbf{b}; \mathbf{l}'\mathbf{b}') = \frac{1}{N_c} \sum_{\mathbf{q}} e^{-i\mathbf{q}\cdot\mathbf{l}'} \tilde{K}_{\alpha\beta}(\mathbf{b}\mathbf{b}'; \mathbf{q}), \quad (2.51)$$

i.e., the smaller the number of their nonvanishing values (to any given accuracy). Real space interatomic force constants can thus be readily obtained by Fourier analyzing a set of force constant matrices calculated and tabulated over a uniform grid of points in reciprocal space. The most efficient way of calculating all these Fourier transforms numerically is the *fast Fourier transform* (FFT) technique [100]. Once real space interatomic force constants have been thus obtained, dynamical matrices in reciprocal space and vibrational frequencies can be obtained at any wave vector (not necessarily contained in the original grid) by FFT. The shorter the range of real space force constants, the coarser will be the reciprocal space grid needed for such Fourier interpolation. In practice, the size of the reciprocal space grid will be assessed a posteriori by verifying that it yields vanishing real space constants (to within a given accuracy) beyond some cutoff radius. A simple rule of thumb is to include in the FFT grid enough points in the BZ so as to reach neighbor interactions extending up to 2-3 bond lengths, and to check the accuracy of the interpolation against the full calculation on some points not included in the grid. The above considerations apply to metals, away from Kohn anomalies, and to nonpolar insulators. The presence of Kohn anomalies in metals is associated with long-range interatomic force constants propagating along the direction of the wave vector of the anomaly. Catching the details of the anomaly with a regular grid of wave vectors in the Brillouin zone would be very impractical. In these cases, once the position of the anomaly has been located, it is much simpler to refine the grid locally, in the neighborhood of the anomaly.

### Frozen phonons

In the frozen phonons approach [120, 121] the force constant matrix is calculated in real space by means of finite atomic displacements around their equilibrium positions and numerical derivative of the resulting Hellmann-Feynman forces. The force constant matrix is then converted to reciprocal space and its eigenvalues are then computed. At variance with the DFPT case, the phonon frequencies can be computed only for those  $\mathbf{q}$  wave-vectors that are commensurate with the chosen supercell. This approach is based on the assumption that force constants decay fast in real space so that the influence of those between atoms in different unit cells (always present with PBCs) to the reciprocal space dynamical matrix and phonon frequencies also decays rapidly as the unit cell size increases. In practice, the convergence of the phonon dispersion with respect to the size of the supercell needs always to be checked. The requirement of supercells can make this approach relatively time consuming. The advantage of this approach is that it can be used for any interatomic potentials capable to provide atomic forces since no knowledge of the electronic density is required.

### Averaged second moment of atomic displacements

The method developed by Kong [122] is based on Green's function and molecular dynamics simulations and the reciprocal force constant matrix is computed from real space atomic displacements as:

$$\tilde{K}_{\alpha\beta}(\mathbf{b}\mathbf{b}'; \mathbf{q}) = k_B T [\tilde{\mathbf{G}}^{-1}]_{\alpha\beta}(\mathbf{b}\mathbf{b}'; \mathbf{q}) \quad (2.52)$$

$$\tilde{\mathbf{G}}_{\alpha\beta}(\mathbf{b}\mathbf{b}'; \mathbf{q}) = \langle \tilde{u}_\alpha(\mathbf{b}; \mathbf{q}) \tilde{u}_\beta^*(\mathbf{b}'; \mathbf{q}) \rangle \quad (2.53)$$

where  $k_B$  is the Boltzmann constant,  $T$  the temperature and  $\langle \dots \rangle$  denotes the ensemble average, and  $\tilde{u}_\alpha(\mathbf{b}; \mathbf{q}) = \frac{1}{N_c} \sum_l u_\alpha(\mathbf{l}\mathbf{b}) e^{-i\mathbf{q}\mathbf{l}}$ . Like in the frozen phonon method, the dynamical matrices are calculated at  $\mathbf{q} = (\frac{h_1}{N_1} \mathbf{b}_1, \frac{h_2}{N_2} \mathbf{b}_2, \frac{h_3}{N_3} \mathbf{b}_3)$ , where  $h_i = 0, \dots, N_i - 1$ ;  $N_i$  is the number of unit cell in the  $i^{th}$  dimension,  $\mathbf{b}_i$  the basis vector of the corresponding reciprocal lattice. Remarkably this method accounts for anharmonic effects that are naturally present in MD via temperature effects; these are recast into a standard dynamical matrix whose eigenvalues depend explicitly on the temperature. The advantage over other methods based on velocity-velocity autocorrelation function is that the calculation provides directly the phonon dispersion besides the phonon density of states.





## 3 Theoretical tools: Classical energy models

This Chapter is dedicated to classical energy models. In the following I introduce the concept of interatomic potential used to provide an approximate description of the interactions between atomic nuclei, treated as classical point-like particles, without the need of an explicit treatment of the electronic degrees of freedom. I show the computational advantages of such method compared to first-principles quantum mechanical calculations. I then concisely discuss the role of improved ways to represent atomic environments and their beneficial impact on training and use of the potentials. Finally, I expand the discussion on a selection of classical energy models that are relevant for metallic systems, starting from the historical, widely known 2-body Lennard-Jones to end up with sophisticated state-of-the-art models that are used in the literature.

### 3.1 Interatomic potentials and linear scaling

The predictive power and the level of accuracy of quantum-mechanical calculations are inherently associated to the explicit treatment of the electrons and of their mutual interactions. The price to pay for this is a high computational cost that generally shows a power-law scaling with respect to the number of electrons in the system (roughly proportional to the number of atomic nuclei). DFT approaches display a cubic scaling which is relatively good compared to higher order scalings typical of Hartree-Fock or other wavefunction-based approaches typical of quantum chemistry. Nonetheless, the study of those classes of problems requiring the simulation of large supercells, such as extended defects, defects interactions or phase transformations are largely off-reach for DFT. This is the main reason for the development of methods with improved scaling like interatomic potentials.

The concept of interatomic potential is based on the assumption that the total energy  $E$  of a system, a point on the BO PES, can be approximated as a *separable* function of atomic

contributions as:

$$E = \sum_i^N \epsilon(\mathbf{R}_i - \mathbf{R}_1, \dots, \mathbf{R}_i - \mathbf{R}_N) = \sum_i^N \epsilon(\{\mathbf{R}_i - \mathbf{R}_j\}_j^N) = \sum_i^N \epsilon_i. \quad (3.1)$$

The sum is over all  $N$  atoms in the system, which are represented as classical point-like masses, and the function  $\epsilon_i$  describes the many-body energy of an atom  $i$  as a function of the relative position of all the other atoms in the system. The approximated mathematical function that is used to model the unknown  $\epsilon_i$ , and ultimately the unknown PES, without any explicit treatment of electronic degrees of freedom is called a classical *interatomic potential*. Classes of potentials sharing common functional forms or similar approximations to  $\epsilon_i$  are called potential models.

Typically, given a potential model, the details of the interatomic potential are tuned to reproduce the PES of various materials. The way this is done can vary but the most common strategy is to model  $\epsilon_i$  as a parametric function which has to be optimized. The optimization consists in a minimization of a cost function, i.e. the problem of generating a working reliable interatomic potential is reduced to a fitting procedure. In practice, the parameters of the mathematical functions are varied in a way to reproduce target physical quantities such as bulk lattice parameter, cohesive energies, vacancy formation energies, elastic constants, melting temperature coming from experiments. The ensemble of these target values is called a *training set* or *training database* while the ensemble of values used to test the predictive power of a potential is called *test set* or *test database*. In the last few decades people started also to take advantage of data from quantum-mechanical calculations. In fact, these are able to provide valuable information like accurate energies and stresses for a number of different atomic configurations and microscopic information like forces that can be included in the fitting procedure via Force matching methods [123]. Although in the literature are available many examples of potentials fitted on mixed experimental and computational databases, in this work only purely computational (DFT) training set will be considered. This is done firstly in order to have complete control on the internal consistency of the data and of their associated errors and second to avoid to deal with possible mismatches between measurements and calculations (that for iron are proved to be non negligible).

Given an approximated functional form for  $\epsilon_i$ , the force acting on atom  $i$  is then computed as the gradient of the approximated PES with respect to a change in the position of atom  $i$ :

$$\mathbf{f}_i = -\nabla_i E = -\nabla_i \sum_k^N \epsilon(\{\mathbf{R}_k - \mathbf{R}_j\}_j^N), \quad (3.2)$$

which reduces to be  $-\nabla_i \epsilon(\{\mathbf{R}_i - \mathbf{R}_j\}_j^N)$  only in the case of  $\epsilon_i$  depending on the relative distance between pairs of atoms. A further important approximation to be introduced is to assume the interatomic potential to be short-ranged. This approximation assumes that long range electrostatic effects are not relevant and is generally justified recalling the screening properties

of metals. In mathematical terms this is described by the following equation:

$$\lim_{|\mathbf{R}_i - \mathbf{R}_j| \rightarrow \infty} \nabla_j \epsilon_i = 0. \quad (3.3)$$

This condition is enforced by forcing the approximated potential function  $\epsilon_i$  to go smoothly zero as the distance between the atom  $i$  and the surrounding atoms goes beyond a radial cutoff of value  $r_{cut}$ . The requirement of smoothness is necessary to avoid unphysical discontinuities in the forces of the atoms when jumping from one side to the other of the cutoff. The concept of cutoff  $r_{cut}$ , is also useful to introduce the concept of *local atomic environment*, i.e. the collection of positions of the  $M \leq N$  atoms within the sphere of radius  $r_{cut}$  around a given atom  $i$ .

The two approximations that have been introduced at this point, namely the decomposability of the PES into a sum of atomic contributions and the short range nature of the atomic interactions, result in linear scaling. In fact, for these short ranged classical energy models, the evaluation of the total energy is linear in the number of atoms explicitly treated in a calculation. This linear scaling is extremely useful to study large systems that cannot be tackled with quantum-mechanical approaches displaying non-linear scaling. On the other hand, a limited accuracy and transferability are to be expected. These are related to the choice (and the parametrization) of the functional forms that are used to approximate the atomic energy functions  $\epsilon_i$ . In some cases [124] the short-range nature of the interatomic potential is not justified. In these cases it is possible to write the many-body atomic energy function as the sum of a short range term (with the characteristics described above) plus a long range electrostatic term treated with Ewald summation methods [125].

#### 3.1.1 Local environments

Above we have introduced the concept of atomic environment as the collection of atoms around a chosen atom  $i$  within a cutoff radius  $r_{cut}$ . The problem of effectively representing such environments is crucial in the fields of structural search, phase transition analysis (looking for suitable order parameters), and in the generation and use of interatomic potentials as well. In this last case, a carefully chosen representation of the atomic environment helps in defining interatomic models with simple functional forms. The most traditional and direct way of describing a local atomic environment made of  $M$  atoms around atom  $i$  is a  $3M$ -dimensional vector of Cartesian coordinates  $\{\mathbf{R}_i - \mathbf{R}_j\}_{j=1}^M$ . Cartesian coordinates provide an unequivocal description of the atomic environment. However, they are not the best suited representation for detecting and discriminating configurations which are related by symmetry transformations such as translations, rotations, reflections or permutation of atoms of the same species. In fact, it is easy to see how Cartesian coordinates are shuffled by any of these symmetry operations. Alternative representations can be used that have a built-in *invariance* with respect to the mentioned symmetry operations, thus being able to accurately discriminate genuinely different atomic environments (i.e. atomic environments

not related by symmetry operations). In practice, a generic representation of the atomic environment of an atom  $i$  is provided by a tuple of real valued functions of the atomic positions,  $q_1^{(i)}, q_2^{(i)}, \dots, q_K^{(i)} = \mathbf{q}_i$  known as *descriptors*. If the mapping between the set of descriptors and the genuinely different local atomic environments is a bijection, i.e., it has the ability to discriminate between any two structures differing by more than symmetry transformations, the representation is said to be *complete*. It is instead said to be *over-complete* if it contains a subset of descriptors that is, by itself, complete. A practical example of the usefulness of non-Cartesian invariant descriptors is the following. Let's consider a generic atomic environment that has to be taught to a potential and the (infinite) subset of all iso-energetic structures related to it by symmetry transformations. It is clear that, thanks to the property of invariance of the representation, the inclusion of one of these configurations in the training set would result in a potential that already knows the energy of all the others in the subset, without the need for their explicit inclusion in the training database. Oppositely, for an efficient training, a Cartesian representation would require many of them. The net result of invariant (and complete) descriptors is a dimensionality reduction of the training-set through the exclusion of the redundant configurations that are useless to a systematic improvement of the potential.

In order to have smooth change in the descriptors it would be also useful to ask for a continuous and differentiable mapping between them and the atomic positions.

There are multiple methods of constructing atomic representation invariants. In the following sections it will be clear how typical examples of descriptors are atomic pair distances. In fact, their use allows to write interatomic models in simple closed functional forms, although they are not invariant with respect to permutations of atoms of the same species. Recently, a number of descriptors have been proposed that satisfy some of the criteria mentioned above. Some examples are the widely known bond-order parameters [126], the symmetry functions by Behler and Parrinello [22] and the power-spectrum or the bispectrum [23, 127, 128] by Bartók. In Sec. 6.5 we will briefly discuss the Smooth Overlap of Atomic Functions (SOAP) invariants used within the Gaussian Approximation Potential formalism adopted in this work.

#### 3.1.2 Pairwise Lennard-Jones model

Typically the approximations to the many-body  $e_i$  are based on physical intuition and justified by semi-empirical arguments so that, in these cases, it is common to talk about semi-empirical interatomic potentials. One of the simplest semi-empirical approximations is provided by the class of pairwise potentials. In this case,  $e_i$  is assumed to be decomposed into the sum of 2-body energy terms. These 2-body terms depend on the bond length  $r_{ij}$  between the particle  $i$  and the neighboring particle  $j$  (within a cutoff  $r_{cut}$ ). The most popular pair-potential is the Lennard-Jones (LJ) potential. This potential was initially developed to model neutral noble gases and consists of a short ranged repulsion and a long ranged attractive tail with two

adjustable parameters as:

$$\epsilon_i(\{\mathbf{R}_i - \mathbf{R}_j\}_j^N) = \sum_j^N 4\epsilon \left[ \left( \frac{\sigma}{r_{ij}} \right)^{12} - \left( \frac{\sigma}{r_{ij}} \right)^6 \right]. \quad (3.4)$$

The  $r^{-6}$  cohesion term is meant to model the van der Waals interactions, while the repulsive term is introduced *ad hoc* with the aim of modeling the Pauli repulsion at short distance due to overlapping electron orbitals. In this classical energy model, the total energy of the system can be written as:

$$E = \sum_i^N \epsilon_i = \sum_i^N \sum_{j<i}^N 4\epsilon \left[ \left( \frac{\sigma}{r_{ij}} \right)^{12} - \left( \frac{\sigma}{r_{ij}} \right)^6 \right], \quad (3.5)$$

where the conditional sum avoids double counting of bonds. This kind of potential has been studied extensively and is known to suffer of many drawbacks. For instance, independently of the parameters, it predicts outward surface relaxation when in (almost) all metals surface atoms relax towards the bulk. The vacancy formation energy is equal to the cohesive energy by construction, while in metals their ratio is typically one third. The elastic constants are also constrained such that the  $C_{12} = C_{66}$  when experimentally this relation in metals is largely violated. This limitations are inherently related to the strong approximation introduced to model the many-body atomic energy function  $\epsilon_i$ .

### 3.1.3 Embedded-atom method

In order to overcome the deficiencies associated to the pairwise potentials mentioned above it is necessary to use improved approximated functional forms that retain the many-body character of  $\epsilon_i$ . One of the most successful examples of such approximations is the embedded-atom method [129] (EAM). This class of semi-empirical potentials was originally derived from the DFT-LDA idea that the total energy of the system depend on the electronic density. The concept was then revisited in a classical fashion to provide an interatomic potential depending on the local electronic density of the form:

$$\epsilon_i = F_i(\bar{\rho}_i) + \frac{1}{2} \sum_{j \neq i}^N \phi(r_{ij}), \quad (3.6)$$

$$\bar{\rho}_i = \sum_{j \neq i}^N \rho(r_{ij}), \quad (3.7)$$

The total energy of the system is then given by:

$$E = \sum_i^N F_i(\bar{\rho}_i) + \frac{1}{2} \sum_i^N \sum_{j \neq i}^N \phi(r_{ij}). \quad (3.8)$$

where the sums run over the atoms  $i$  and  $j$  and  $\phi(r_{ij})$  is a short-range pair interatomic term depending on the atomic separation only describing the screened nuclear electrostatic

interaction. The embedding function  $F_i$  instead is the energy to embed an atom of type  $i$  into the background electron density  $\bar{\rho}_i$  at site  $i$ , built as a linear superposition of spherically averaged atomic electron densities  $\rho(r_{ij})$  generated by the surrounding atoms. The use of this function reflects the fact the the bond strength depends on the local environment, differently from a simple pairwise potential. It is interesting to note that eq. (3.8) is invariant with respect to the transformation:

$$\hat{\phi}(r) = \phi(r) + 2\lambda\rho(r), \quad (3.9)$$

$$\hat{F}(\bar{\rho}) = F(\bar{\rho}) - \lambda\bar{\rho}, \quad (3.10)$$

for any value of  $\lambda$ . This implies that there is no unique choice for  $\phi(r)$  and  $F(\bar{\rho})$ . In order to fix this Gauge invariance, one can arbitrarily impose a condition such as  $F'(\bar{\rho}_0) = 0$  to define a  $\bar{\rho}_0$  value of reference (for example the bulk atom density at 0 K). Fixed the Gauge, possible choices for the analytical form of the functions  $F_i$ ,  $\rho(r_{ij})$ , and  $\phi(r_{ij})$  can be considered. Eqs. 3.9 also show that if  $F(\bar{\rho})$  is a linear function of  $\bar{\rho}$ , then the whole scheme reduces to a 2-body potential: many-body effects are related to the curvature of  $F(\bar{\rho})$ , which is typically taken as positive. In fact,  $F''(\bar{\rho})$  is invariant with respect to (3.9). Noticeably, in this model, only interparticle distances  $r_{ij}$  are needed to get energy and forces so that their calculation is nearly as simple and efficient as with pair potentials.

In this work we will consider only EAM potentials but, for sake of completeness, it is worth to mention that similar models sharing the form eq. (3.6) were developed independently by other groups in the same period. The Glue model [130] by Ercolessi et. al and the Finnis-Sinclair [131] (FS) model are a few examples (see Ref. [132] for a more detailed list). The FS model in particular was derived from a second-moment approximation to tight binding and by construction  $F_i = \sqrt{\bar{\rho}_{ij}}$  with the function  $\bar{\rho}_{ij}$ , differently from the EAM case, specific to the atomic types of both atoms  $i$  and  $j$ . Furthermore,  $\bar{\rho}_{ij}$  was originally derived as a superposition of overlap integrals and represents here the atomic coordination of the atom  $i$ . For a monoatomic system the EAM and FS potentials are formally identical when the embedding function is chosen to have a square-root form.

Also, the EAM potentials were originally developed to describe nearly filled  $d$ -band transition metals where the delocalized  $s$ ,  $p$  character of the bond is assumed to dominate. However, for metallic systems more covalently  $d$ -bonded, the introduction of explicit 3-body terms depending on the angles between the atoms might be important. This physical consideration lead Baskes to developed the modified embedded atom model [133] (MEAM), where the electronic density  $\rho_i$  at site  $i$  is now corrected to include a angular dependences.

#### 3.1.4 Bond-order potentials

Bond-order potentials [134, 135] (BOP), formulated by Pettifor and Oleinik are a further generalization of the ideas used in the EAM, FS potentials to describe the total binding energy of a system as a sum over individual bonds, the energy of the each bond comprising a repulsive

pairwise contribution and an attractive contribution depending on the bond environment. In the BOP, the entire formulation was derived as an approximation to the exact many-atom expansion of the bond energy within the two-center, orthogonal tight binding representation of the electronic structure. The original formulation has been successfully extended to nonmagnetic transition metals and also to magnetic materials like iron [136], by describing the magnetic interactions via a Stoner theory of itinerant magnetism. Recently, Drautz and Pettifor derived a framework for calculating the binding energy and forces for a collection of atoms as analytic functions of the moments of the local DOS [137, 138], thus overcoming the inaccuracies in the Hellman-Feynman forces that afflicted the numerical BOP.

Without going into too much mathematical detail, the total energy of the system can be expressed as:

$$E = E_{bond} + E_X + E_C + E_{rep} + E_{emb}. \quad (3.11)$$

The bond energy  $E_{bond}$ , and the local charges and magnetic moments required for the calculation of the Coulomb and exchange energies are determined from the solutions to the tight-binding matrix formulation of Schrödinger equation,

$$\sum_{i\alpha\mu} [H_{j\beta\nu i\alpha\mu} - E^{(n)}] c_{i\alpha\mu}^{(n)}, \quad (3.12)$$

where  $H_{j\beta\nu i\alpha\mu}$  are the parameterized (explicitly spin dependent) Hamiltonian matrix elements connecting atoms  $i$  and  $j$ , orbitals  $\alpha$  and  $\beta$  and spin indexes  $\mu$  and  $\nu$ .  $E^{(n)}$  are the eigenvalues of the equation and  $c_{i\alpha\mu}^{(n)}$  are the expansion coefficients of the eigenvectors on a basis of atomic like orbital functions. Once the eigenvalues are found, it is possible to calculate the local density of states (DOS) and, in turn, the bond energy as:

$$\sum_{i\alpha\mu} \int^{E_f} (E - E_{i\alpha\mu}) n_{i\alpha\mu}(E) dE, \quad (3.13)$$

with  $E_f$  the Fermi energy. The exchange energy and the Coulomb energy are then also computed. An additional pairwise repulsive function,  $E_{rep}$ , is then added that accounts for other energy contributions (such overlap repulsion, exchange-correlation and crystal fields effects), as well as the nuclear-nuclear electrostatic contribution. Finally, the embedding energy,  $E_{emb}$ , accounts for the neglected contributions from  $s-d$  hybridization in the transition metals.

BOP potentials represent one of the best potential models to date in terms of accuracy, as far as conventional interatomic potentials are concerned. They provide an efficient  $\mathcal{O}(N)$  method for performing large scale simulations, although computationally they are significantly more complex and expensive than FS or EAM methods.

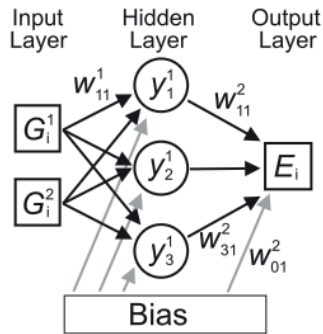


Figure 3.1: Standard Neural Network scheme employed for fitting potential energy surfaces. Fig. taken from [22].

### 3.1.5 Artificial neural networks

We have seen that for semi-empirical potentials like Lennard-Jones and EAM the choice of the local atomic energy functional forms is typically dictated by physical intuition and simplicity. This typically results in a very crude approximation to the “true”  $e_i$  that makes such models poorly flexible and, as a consequence, unable to be systematically optimized as the training database is increased. In fact, these models are thought and trained to describe reasonably well bulk properties of metals but tend to perform poorly when used to describe defective structures or far-from-equilibrium atomic environments.

A possible approach to tackle this problem is to increase the complexity and, consequently, the flexibility of the model. As we have seen above, in BOP potentials this is achieved by decomposing  $E$  as a sum over bond energies (as opposed to atomic energies) whose complex functional form is motivated by a tight binding analysis. An alternative “orthogonal” approach is the one exploited by Neural Networks [21, 22, 124] (NN). In NN potentials the total energy of the system  $E$  is described as a sum over the atomic energy functions  $e_i$ . However these are assumed not to have any predetermined, physically motivated functional form. Instead, the exact functional form has to be determined through NN algorithms.

Neural networks are biology-inspired algorithms that provide an accurate tool for the representation of arbitrary functions. They are defined by means of an input layer, containing the input data of the function of interest, and an output layer, providing the value of the same function evaluated at the input points. In between there are several hidden layers, each of which contains a number of artificial interconnected neurons, the so-called nodes (a schematic example is reported in Fig. 3.1). Each node is associated to a numerical value which is determined by the neighboring nodes. The output layer is then obtained as a complicated nested combination of the node values. The higher the number of hidden layers and nodes per layer, the higher the flexibility of the NN model.

In a feed-forward algorithm the value of node  $j$  in layer  $k$  is determined as follows: first a linear combination of the node values of the preceding neighboring layer is calculated, its value



being defined  $x_j^k$ . Then, a non-linear function  $f_j^k$  is applied to  $x_j^k$  thus yielding the numerical value  $y_j^k = f_j^k(x_j^k)$  of the node under consideration. Once all values of all nodes in a hidden layer have been determined, the values of the subsequent layer can be calculated and so forth until the output of the NN is obtained. In the simple case of one hidden layer with three nodes it reads:

$$\epsilon_i = f_j^2 \left[ w_{01}^2 + \sum_{j=1}^3 w_{j1}^2 f_j^1 \left( w_{0j}^1 + \sum_{\mu=1}^2 G_i^\mu \right) \right], \quad (3.14)$$

where  $w_{jl}^k$  is the weight parameter connecting node  $l$  in layer  $k$  with node  $j$  in layer  $k-1$ ,  $w_{0l}$  is a bias weight that is used as an adjustable offset for the activation function  $f_j^k$ , and  $G_i^\mu$  are generalized coordinates describing the local environment of atom  $i$  (the sum is over all the generalized coordinates of the local environment). The linear coefficients, or weights,  $w_{jl}^k$  are the fitting parameters of the NN. Since the weight parameters initially are chosen randomly, the output of the NN does not correspond to the correct total energy, but since the latter is known for a set of input points from DFT calculations, an error function can be constructed and minimized to optimize the weight parameters in an iterative way. The optimized set of weights can then be used to calculate the potential energy for a new set of coordinates. The function  $f_j^k$  is the so-called activation function or transfer function of the NN. Activation functions are typically nonlinear functions that introduce the capability to fit nonlinear functions into the NN. Commonly, they are shaped like the sigmoid function  $1/[1 + \exp(-x)]$  or the hyperbolic tangent  $\tanh(x)$ , although other functions have also been proposed.

As generalized coordinates for high-dimensional NN potentials, for the reasons discussed in Sec. 3.1.1, Behler and Parrinello used a set of descriptors  $\{G_i^\mu\}$  called symmetry functions. The symmetry functions are typically taken to be invariant with respect to rotations and translations, and independent on the coordination of the atom they refer to, although they do not form a complete representation of the atomic environment. Commonly, to characterize the local environment a set of radial and angular symmetry function are used of the form:

$$G_i^1 = \sum_{j \neq i} \exp[-\eta(R_{ij} - R_s)^2] f_c(R_{ij}), \quad (3.15)$$

$$G_i^2 = 2^{1-\zeta} \sum_{j,k \neq i} (1 + \lambda \cos \theta_{ijk})^\zeta \exp[-\eta(R_{ij}^2 + R_{ik}^2 + R_{jk}^2)] f_c(R_{ij}) f_c(R_{ik}) f_c(R_{jk}), \quad (3.16)$$

where  $\lambda = (+1, -1)$ ,  $\eta$ ,  $\zeta$  are adjustable parameters which can assume different values,  $f_c$  is a suitable smooth cutoff function of the interatomic separation  $R_{ij}$  between atom  $i$  and  $j$ , which goes smoothly to zero at  $r_{cut}$  thus defining the local atomic environments,  $\theta_{ijk}$  the angle between atoms  $i$ ,  $j$  and  $k$  centered in  $i$ . It is worth to note that the  $\{G_i^\mu\}$  above depend on all atomic positions inside the cutoff radius and thus represent ‘‘many-body’’ terms. Several functions of each type with different parameter values are used since the choice of symmetry functions and their parameters is not unique.



## 4 Elasticity

In this chapter, the theory and the constitutive equation of linear elasticity of crystals are presented. In fact, when a crystal is deformed due to an external load, the internal stresses oppose the deformation that takes place until a new equilibrium condition between internal and external stresses is reached. The connection between internal stresses and the degree of deformation can be described by general fundamental relations called constitutive equations. For small deformations, when the external force is no longer applied, the original state is fully recovered and the constitutive equation is linear. This linear relation is known as generalized Hooke's law, or constitutive equation of linear elasticity, and the elastic coefficient is called stiffness. In three dimensions, it is a tensor whose components are thermodynamic quantities that fully determine the elasto-mechanical response of the different materials. In the case of large deformations instead, non-linearity arises due to both elastic and plastic effects.

### 4.1 Strain

For thermodynamic calculations, the crystal is considered to be a homogeneous, anisotropic elastic medium. The applied load/stresses are uniform, i.e. constant on a given crystal surface, and the associated deformation is homogeneous, i.e. uniform throughout the crystal. The uniform deformation (in three dimensions) can then be described through a  $3 \times 3$  second-order tensor  $\mathbf{J}$  that transforms a position vectors  $\mathbf{X}$ , locating an arbitrary element of mass of the medium in the initial configuration, into a final position vector  $\mathbf{x} = \mathbf{J}\mathbf{X}$ . The tensor  $\mathbf{J}$  is known as Jacobian tensor and can be rewritten in terms of the identity matrix  $\mathbf{1}$  and the matrix of the displacement gradients  $\mathbf{u}$  as  $\mathbf{J} = \mathbf{1} + \mathbf{u}$ . The matrix of the displacement gradients is defined so that its components  $u_{ij} = \frac{\partial u_i}{\partial X_j}$ , and  $x_i = \sum_j (\delta_{ij} + u_{ij})X_j$ ,  $u_i = x_i - X_i$  being the displacement components and  $\delta_{ij}$  being the Kronecker delta. The Jacobian tensor includes information about stretching and rigid motion of a continuum body. In order to define a suitable measure for the stretching of the crystal independently of rotations and/or translations (rigid body motions) it is possible to introduce the so-called Lagrangian strain  $\boldsymbol{\eta}$ . This type of strain is typically used to describe deformations of crystals with respect to the initial frame of reference

and is defined from the matrix of the displacement gradients as:

$$\boldsymbol{\eta} = \frac{1}{2}(\mathbf{u} + \mathbf{u}^T + \mathbf{u}^T \mathbf{u}), \quad (4.1)$$

$$\eta_{ij} = \frac{1}{2}(u_{ij} + u_{ji} + \sum_k u_{ki} u_{kj}). \quad (4.2)$$

If the initial configuration  $\mathbf{X}$  of a crystal subjected to a uniform deformation  $\mathbf{J}$  is known, the Lagrangian strain completely determines the final one up to the rigid body motions and can be used as a good descriptor for the thermodynamic state of the system so that thermodynamic state functions as the Helmholtz free energy  $F$  or internal energy  $U$  can be written as  $F/U(\mathbf{x}, T) = F/U(\mathbf{X}, \boldsymbol{\eta}, T)$ .

In the case of (infinitely) small deformations,  $\mathbf{J}$  is close to unity, the deformation gradients are (infinitely) small and the Lagrangian strain defined in eq. (4.1, 4.2) can be truncated to the first order in  $\mathbf{u}$  to give the so-called infinitesimal Cauchy strain  $\boldsymbol{\varepsilon}$ :

$$\boldsymbol{\eta} \approx \boldsymbol{\varepsilon} = \frac{1}{2}(\mathbf{u} + \mathbf{u}^T), \quad (4.3)$$

$$\eta_{ij} \approx \varepsilon_{ij} = \frac{1}{2}(u_{ij} + u_{ji}). \quad (4.4)$$

It corresponds to the symmetric part of the deformation gradients matrix and describes the strain of a body, while the antisymmetric counterpart  $\boldsymbol{\omega} = 1/2(\mathbf{u} - \mathbf{u}^T)$  describes pure rotations. As such, it can also be used as a descriptor of the thermodynamic state of the system so that  $F/U(\mathbf{x}, T) = F/U(\mathbf{X}, \boldsymbol{\varepsilon}, T)$ . Note also that it is always possible to define a Jacobian matrix and, consequently, a displacement gradient matrix which are symmetric by construction ( $\mathbf{u} = \mathbf{u}^T = \boldsymbol{\varepsilon}$ ) so that  $\mathbf{u}$  itself is a measure of strain. If the deformation is finite,  $\boldsymbol{\varepsilon}$  and  $\boldsymbol{\omega}$  represent only approximately the strain and rotational part of the deformation, loosing progressively this meaning as the deformation gets bigger.

## 4.2 Stress

The conjugate variable of the Lagrange strain is known as the second Piola-Kirchoff stress [139], which is defined from the Helmholtz free energy or from the Internal energy as [140, 141]:

$$\tau_{ij} = \frac{1}{V} \frac{\partial F}{\partial \eta_{ij}} \Big|_{T\eta'} = \frac{1}{V} \frac{\partial U}{\partial \eta_{ij}} \Big|_{S\eta'}, \quad (4.5)$$

where  $V$  is the volume of the undistorted crystal, the subscript  $\eta'$  means that all the other  $\eta_{kl}$  are to be held constant while differentiating with respect to  $\eta_{ij}$ , and constant temperature/entropy  $T/S$ . As its conjugate strain, in three dimensions it is a symmetric  $3 \times 3$  tensor with, therefore, only six independent component. Note that this is not equivalent to the so-called Cauchy stress [140] (the conjugate of the Euler-Almansi strain [139]), also known as physical stress, i.e. the true measure of the force per unit area in the current/deformed

configuration, and cannot be straightforwardly interpreted in terms of forces acting on surface elements. Note however that, in the limit of (infinitely) small deformations, both the second Piola-Kirchoff stress and the Cauchy stress reduce to the infinitesimal Cauchy stress whose components, analogously to eq. (4.5), can then be obtained as:

$$\sigma_{ij} = \frac{1}{V} \frac{\partial F}{\partial \varepsilon_{ij}} \Big|_{T\varepsilon'} = \frac{1}{V} \frac{\partial U}{\partial \varepsilon_{ij}} \Big|_{S\varepsilon'}. \quad (4.6)$$

### 4.3 Elastic constants

Since rotational and translational invariance requires that the state functions depend on a final configuration  $\mathbf{x}$  only through  $\mathbf{X}$  and, in the limit of (infinitely) small deformations, through  $\boldsymbol{\varepsilon}$  as described above, then  $F$  and  $U$  may be expanded in powers of strain components:

$$F(\mathbf{X}, \boldsymbol{\varepsilon}, T) = F(\mathbf{X}, T) + V \sum_{ij} \sigma_{ij} \varepsilon_{ij} + \frac{1}{2} V \sum_{ijkl} C_{ijkl}^{(T)} \varepsilon_{ij} \varepsilon_{kl} + \dots, \quad (4.7)$$

$$U(\mathbf{X}, \boldsymbol{\varepsilon}, S) = U(\mathbf{X}, S) + V \sum_{ij} \sigma_{ij} \varepsilon_{ij} + \frac{1}{2} V \sum_{ijkl} C_{ijkl}^{(S)} \varepsilon_{ij} \varepsilon_{kl} + \dots. \quad (4.8)$$

In this expansion we have used eqs. (4.6) evaluated at the reference configuration and we have introduced the elastic constants of the second order as the coefficient of proportionality of the quadratic terms in the expansion. In particular, we have defined the isothermal elastic constants from the Helmholtz free energy

$$C_{ijkl}^{(T)} = \frac{1}{V} \frac{\partial^2 F}{\partial \varepsilon_{ij} \partial \varepsilon_{kl}} \Big|_{T\varepsilon'}, \quad (4.9)$$

and the adiabatic elastic constants from the internal energy:

$$C_{ijkl}^{(S)} = \frac{1}{V} \frac{\partial^2 U}{\partial \varepsilon_{ij} \partial \varepsilon_{kl}} \Big|_{S\varepsilon'}. \quad (4.10)$$

The elastic constants are the elements of the so-called fourth-order stiffness tensor, are a thermodynamic quantities and are a property of the specific material under consideration.

Since we have assumed the case of small deformations, the expansions (4.7,4.8) above can be safely truncated at the second order in  $\varepsilon_{ij}$ , thus recovering (if the reference configuration is assumed to be at zero stress) the *constitutive equation of linear elasticity* also known as *Generalized Hooke's law*:

$$\boldsymbol{\sigma} = \mathbf{C} : \boldsymbol{\varepsilon}, \quad (4.11)$$

where  $\mathbf{C}$  is the stiffness tensor (either isothermal or adiabatic) and the symbol  $:$  indicates a double product [139]. As mentioned above, it is found experimentally that most crystals follow this linear stress-strain relation up to a limit value, above which non-linear effects arise

## Chapter 4. Elasticity

and also plastic effects start to be important. Since for a generic material the stiffness tensor has to reflect the symmetries of the second-order strain and stress tensors, the number of its independent components reduces from 81 to 21. Exploiting the symmetries and the reduced number of independent components of the strain, stress and stiffness tensors, eq. (4.11) can be rewritten using the Voigt notation:

$$\boldsymbol{\sigma}_V = \mathbf{C}_V \boldsymbol{\varepsilon}_V, \quad (4.12)$$

with strain, stress and stiffness in the Voigt form:

$$\boldsymbol{\sigma}_V = [\sigma_1, \sigma_2, \sigma_3, \sigma_4, \sigma_5, \sigma_6] = [\sigma_{11}, \sigma_{22}, \sigma_{33}, \sigma_{23}, \sigma_{13}, \sigma_{12}], \quad (4.13)$$

$$\boldsymbol{\varepsilon}_V = [\varepsilon_1, \varepsilon_2, \varepsilon_3, \varepsilon_4, \varepsilon_5, \varepsilon_6] = [\varepsilon_{11}, \varepsilon_{22}, \varepsilon_{33}, 2\varepsilon_{23}, 2\varepsilon_{13}, 2\varepsilon_{12}], \quad (4.14)$$

$$\mathbf{C}_V = \begin{pmatrix} C_{11} & C_{12} & C_{13} & C_{14} & C_{15} & C_{16} \\ C_{21} & C_{22} & C_{23} & C_{24} & C_{25} & C_{26} \\ C_{31} & C_{32} & C_{33} & C_{34} & C_{35} & C_{36} \\ C_{41} & C_{42} & C_{43} & C_{44} & C_{45} & C_{46} \\ C_{51} & C_{52} & C_{53} & C_{54} & C_{55} & C_{56} \\ C_{61} & C_{62} & C_{63} & C_{64} & C_{65} & C_{66} \end{pmatrix}, \quad (4.15)$$

being  $C_{ij} = C_{ji}$ . Furthermore, if the material under consideration is a crystal with extra symmetries, the number of independent elastic constants is reduced. For example, a cubic crystal has only 3 independent elastic constants (with the stiffness matrix given by eq. (4.16)), while a isotropic material only 2.

$$\mathbf{C}_V^{cubic} = \begin{pmatrix} C_{11} & C_{12} & C_{12} & & & \\ C_{12} & C_{11} & C_{12} & & & \mathbf{0} \\ C_{12} & C_{12} & C_{11} & & & \\ & & & C_{44} & 0 & 0 \\ & \mathbf{0} & & 0 & C_{44} & 0 \\ & & & 0 & 0 & C_{44} \end{pmatrix}. \quad (4.16)$$

### 4.3.1 Elastic constants and sound velocities relations

Let's now assume that for any initial configuration of a element of mass in the crystal, its final position  $\mathbf{x}$  is a function of time and the strain descriptors should be constants of time as well. Then the Lagrange's equations of motion in the absence of body forces and linearized (see Wallace [140]) can be written as:

$$\rho(\mathbf{X}) \ddot{x}_i = \sum_{jkl} [\tau_{jl} \delta_{ik} + C_{ijkl}^T] \left( \frac{\partial^2 x_k}{\partial X_i \partial X_j} \right), \quad (4.17)$$

where  $\tau_{jl}$  is the stress component defined as  $(\partial F / \partial \eta_{ij})_{T\eta'} V^{-1}$  with respect to the initial configuration while  $C_{ijkl}^T = (\partial^2 F / \partial \eta_{ij} \partial \eta_{kl})_{T\eta'} V^{-1}$  is the definition of isothermal elastic constant

#### 4.4. Long wavelength limit of acoustic phonons

with respect to the initial configuration at zero strain (a similar equation containing the adiabatic elastic constants holds), and  $\rho$  the density of mass at  $\mathbf{X}$ .

This is a harmonic equation and the solutions are plane elastic waves of the form  $\mathbf{X} + \mathbf{w} \sin(\mathbf{q} \cdot \mathbf{X} - \omega t)$ . We then have the following equation of motion (for isothermal propagation) of the mass evaluated at  $\mathbf{X}$ :

$$\rho v^2 w_i = \sum_{jkl} [\tau_{jl} \delta_{ik} + C_{ijkl}^T] \hat{q}_j \hat{q}_l w_k, \quad (4.18)$$

where  $v = \omega/|\mathbf{q}|$ . To note that this eigenvalue/eigenvector equation in the case of cubic crystal at zero initial pressure has eigenvalues that can be written as usual to give the sound velocities of the elastic waves in the various directions of the crystal. Some examples that will be used in this work (valid for either isothermal and adiabatic cases) are:

$$v_L [100] = \sqrt{\frac{C_{11}}{\rho}}, \quad (4.19)$$

$$v_{T_1} [100] = \sqrt{\frac{C_{44}}{\rho}}, \quad (4.20)$$

$$v_{T_2} [110] = \sqrt{\frac{C'}{\rho}}, \quad (4.21)$$

#### 4.4 Long wavelength limit of acoustic phonons

In complete analogy with the elastic theory of the sections above, the propagation of long-wavelength waves in the crystal can be discussed in terms of equations for the elastic waves in a continuous medium, provided the wavelengths are long compared to the (finite) effective range of interactions among the ions in the crystals. It is worth to highlight that here we rely specifically on Wallace [140] argumentations claiming that, contrarily to what is reported in some textbooks like Refs. [114, 142], this analogy between mechanical and thermodynamic equations is not a strict equivalence. In fact, this analogy becomes an exact equivalence only within what is referred to as *potential approximation*, where the potential energy surface of a system is considered to be an approximation to the thermodynamic state functions:

$$E(\mathbf{R}) \approx F, \quad (4.22)$$

$$E(\mathbf{R}) \approx U, \quad (4.23)$$

and the stresses and elastic constants are given by strain derivatives of  $E(\mathbf{R})$ , with  $E(\mathbf{R})$  actually interpreted as a function of the cell vectors alone since the atomic equilibrium positions are assumed at the equilibrium. Citing D. C. Wallace <sup>1</sup> “*One should always keep in mind that the quantities so calculated are only the mechanical approximations to the corresponding*

<sup>1</sup>Ref. [140], Chapter 7, Page 73

*thermodynamic quantities*". In fact, even at 0 K the approximations above do not become equivalences due to the missing zero point terms in  $E(\mathbf{R})$ .

Starting from the equation of motion for the ions, e.q. (2.46), it is possible to show after some lengthy math, that for plane wave solutions in the limit of long wavelengths one recovers the mechanical analog of eq. (4.18), i.e.

$$\rho v_s^2 w_{is} = \sum_{jkl} [\tilde{C}_{jl} \delta_{ik} + \tilde{C}_{ijkl}] \hat{q}_j \hat{q}_l w_{ks}, \quad (4.24)$$

with  $\mathbf{q}$  the phonon wave-vector,  $v_s$  and  $\mathbf{w}_s$  the velocity and eigenvector of the three independent polarized waves for each  $\mathbf{q}$  and  $\rho$  the density of the crystal in the initial configuration, while  $\tilde{C}_{jl} = (\partial E(\mathbf{R}) / \partial \varepsilon_{ij})_{\varepsilon'} V^{-1}$  is the mechanical stress and  $\tilde{C}_{ijkl} = (\partial^2 E(\mathbf{R}) / \partial \varepsilon_{ij} \partial \varepsilon_{kl})_{\varepsilon'} V^{-1}$  the mechanical elastic constants. Eq. (4.24) can be used also at finite temperature with renormalized phonon frequencies and dynamical matrix due to inclusion of anharmonic effects (see for instance Sec. 2.4.3). The net result is that even eqs. 4.19 are still valid but display a temperature dependence. However, it is important to stress once again that according to D. C. Wallace<sup>2</sup>, when anharmonicity is included, long-wavelength acoustic phonons, isothermal elastic sound waves and adiabatic elastic sound waves "*are generally different and do propagate as phonons, isothermal waves and adiabatic waves respectively*". In details it can be shown that at finite temperature adiabatic velocity is greater than the isothermal velocity (they are the same at zero temperature) while long-wavelength acoustic renormalized velocities are likely to be greater than the isothermal waves (there might be cases for which this qualitative prediction drops).

---

<sup>2</sup>Ref. [140], Chapter 17, Page 195



## 5 Statistical sampling

In order to characterize the thermodynamics of crystals from a theoretical point of view, it would be necessary to have access to the configurational space of all the possible states associated with all the degrees of freedom of the system so that a partition function can be constructed. However, for realistic systems, this approach of building the complete partition function is typically impractical due to the difficulty of exploring such a highly dimensional configurational space. Some simplifications are therefore needed. The first simplification we introduce consists in considering only those excited states that are typically thermally activated (in a temperature range generally of the order of  $10^3$  K) in crystalline structures, while the second one, corresponds to assuming these excitations are completely decoupled (their coupling is assumed as a second order effect). For magnetic metals such thermal excitations are known to be the phonons, the electronic excitations and the magnons, so that the total energy and the total partition function can be written as:

$$E_{tot} = E_0 + \Delta E_{ph} + \Delta E_{el} + \Delta E_{mag}, \quad (5.1)$$

$$Z_{tot} = Z_0 \cdot Z_{ph} \cdot Z_{el} \cdot Z_{mag}, \quad (5.2)$$

where  $E_0$  is the ground state energy with respect to the vibrational, electronic and spin degrees of freedom,  $\Delta E$  are the extra energy cost due to the excitations associated to the same degrees of freedom, and  $Z_{tot} = \exp[-E_{tot}/k_B T]$ .

- The phonons, discussed in Sec. 2.3, are collective vibrations of the atoms that can be described as non interacting mechanical waves propagating in the crystal with different possible polarizations  $\nu$ , different possible wavevectors  $\mathbf{q}$  and frequencies  $\omega(\mathbf{q}, \nu)$ , and carry an energy  $\epsilon(\mathbf{q}, \nu) = \hbar\omega(\mathbf{q}, \nu)$  each. This description is valid under the assumption of an harmonic approximation for the BO PES.
- The electronic excitations, in a band theory picture, correspond to jumps of the electrons from a state characterized by a band index  $n$  and a wavevector  $\mathbf{k}$  to a new empty state  $(n', \mathbf{k})$ . In DFT, as explained in Sec. 2.3, the band picture of non-interacting KS particles can be used to evaluate the energy cost of an excited state in a system of interacting

electrons.

- As for the phonons, the magnons can be described as collective oscillations of the total electronic spins of an atom or, alternatively, as collective oscillations of the atomic magnetic moments. They obey a Bose-Einstein statistics and can be described in terms of non-interacting spin waves with polarization, wavevector and characteristic frequency. In the case of iron, these excitations have been shown [67, 69] to be increasingly important as the temperature is raised in order to explain the specific heat divergence at the Curie point ( $\sim 1043$  K). In this work we do not calculate them explicitly but we will discuss their relative importance in the different thermodynamic quantities of interest.

## 5.1 Quasi-harmonic approximation (QHA)

In the harmonic limit it is possible to calculate the equilibrium properties of a solid (at low temperatures) by calculating the partition function  $Z_{ph}$  for an appropriate gas of phonons. The energy of a state in which there are  $n(\mathbf{q}, \nu)$  phonons of polarization index  $\nu$  and wavevector  $\mathbf{q}$  is:

$$E\{n(\mathbf{q}, \nu)\} = \sum_{\mathbf{q}, \nu} \hbar\omega(\mathbf{q}, \nu) \left( n(\mathbf{q}, \nu) + \frac{1}{2} \right). \quad (5.3)$$

Following the derivation in Refs. [143, 144] it is possible to end up with a purely harmonic free energy. A pure harmonic approximation assumes vibrational frequencies do not depend on interatomic distances, so that the vibrational contribution to the crystal internal energy does not depend on the volume. As a consequence, constant-pressure and constant-volume specific heats from vibrations coincide and the equilibrium volume of a crystal does not depend on temperature. To overcome this shortcoming, the harmonic approximation can be generalized to the quasi harmonic approximation [145] (QHA), where the vibrational frequencies are assumed volume/cell dependent. In the QHA, the crystal Helmholtz free energy is assumed to be determined by the vibrational spectrum via the standard harmonic expression:

$$F(X, T) = F_0(X) + \frac{1}{2} \sum_{\mathbf{q}, \nu} \hbar\omega(\mathbf{q}, \nu, X) + k_B T \sum_{\mathbf{q}, \nu} \ln \left( 1 - e^{-\frac{\hbar\omega(\mathbf{q}, \nu, X)}{k_B T}} \right), \quad (5.4)$$

where  $X$  indicates any global static constraint upon which vibrational frequencies may depend (most commonly the volume  $V$ , components of the strain tensor  $\epsilon$  as from eq. 4.7, or some externally applied field), and  $F_0(X)$  is the zero temperature energy of the crystal as a function of  $X$ . Note that the second term in the righthand side equations is the so-called zero-point energy correction while the third term, depending explicitly on the temperature, is the so-called thermal contribution. Similarly to eq. 4.6, if  $X = V$ , differentiation of eq. 5.4 with respect to the volume gives the pressure  $P$

$$P(V, T) = -\frac{\partial F(V, T)}{\partial V}. \quad (5.5)$$

Other useful quantities like the entropy  $S$ , the internal energy  $U$ , the specific heat at constant volume  $C_V$ , the average occupation number  $n(\mathbf{q}, \nu, X)$ , the mean square displacement  $\langle |u_s(X)|^2 \rangle$  of atom  $s$  in the cell  $l$  that can be obtained [140] from a quasiharmonic treatment of the vibrational contributions to the thermodynamics of a crystal follow:

$$S(X, T) = -k_B \sum_{\mathbf{q}, \nu} \ln [1 - \exp(-\hbar\omega(\mathbf{q}, \nu, X)/k_B T)] + \sum_{\mathbf{q}, \nu} \frac{\hbar\omega(\mathbf{q}, \nu, X)}{\exp(\hbar\omega(\mathbf{q}, \nu, X)/k_B T) - 1}, \quad (5.6)$$

$$U(X, T) = \sum_{\mathbf{q}, \nu} \hbar\omega(\mathbf{q}, \nu, X) \left[ \frac{1}{\exp(\hbar\omega(\mathbf{q}, \nu, X)/k_B T) - 1} + \frac{1}{2} \right], \quad (5.7)$$

$$C_V(X, T) = k_B \sum_{\mathbf{q}, \nu} \left[ \frac{\hbar\omega(\mathbf{q}, \nu, X)}{k_B T} \right]^2 \frac{\exp(\hbar\omega(\mathbf{q}, \nu, X)/k_B T)}{[\exp(\hbar\omega(\mathbf{q}, \nu, X)/k_B T) - 1]^2}, \quad (5.8)$$

$$n(\mathbf{q}, \nu, X) = \frac{1}{\exp(\hbar\omega(\mathbf{q}, \nu, X)/k_B T) - 1}, \quad (5.9)$$

$$\langle |u_s(X, T)|^2 \rangle = \frac{\hbar}{2Nm_s} \sum_{\mathbf{q}, \nu} \frac{1 + 2n(\mathbf{q}, \nu, X) |\hat{\mathbf{n}} \cdot \mathbf{e}_s(\mathbf{q}, \nu, X)|^2}{\omega(\mathbf{q}, \nu, X)}, \quad (5.10)$$

where  $m_s$ , is the mass of atom  $s$ ,  $N$  is the number of atom in the considered cell,  $\hat{\mathbf{n}}$  is an arbitrary unit direction and  $\mathbf{e}_s(\mathbf{q}, \nu, X)$  is the eigenvector of the mode  $(\mathbf{q}, \nu)$  fixed the constraint  $X$ .

## 5.2 Useful thermodynamic relations

Contrarily to a pure harmonic theory, focusing our attention to the case of cubic systems, in the QHA the specific heats at constant pressure and volume deviate. In fact, by imposing the total differentials of the entropy as a function of pressure and temperature and the entropy as a function of volume and temperature coincide, and by using Maxwell identities, one can show that [140]:

$$C_P - C_V = TV\beta^2 B^{(T)}, \quad (5.11)$$

$$\beta = \frac{1}{V} \left. \frac{\partial V(T)}{\partial T} \right|_P. \quad (5.12)$$

where  $\beta$  is the volumetric thermal expansion and  $B^{(T)}$  is the isothermal bulk modulus. The (adiabatic/isothermal) bulk modulus is the inverse of the (adiabatic/isothermal) compressibility and can be obtained from the (adiabatic/isothermal) elastic constants as  $B^{(S/T)} = \frac{1}{3}(C_{11}^{(S/T)} + 2C_{12}^{(S/T)})$  or from the curvature of the Internal/Helmholtz free energy as  $B^{(S/T)} = V \left. \frac{\partial^2 U/F}{\partial V^2} \right|_{S/T}$ . Another useful relation that can be obtained equating the differentials of the volume as a function of pressure/temperature and pressure/entropy brings to:

$$\frac{C_P}{C_V} = \frac{B^{(S)}}{B^{(T)}}, \quad (5.13)$$

or equivalently to:

$$B^{(S)} - B^{(T)} = \frac{TV\beta^2 B^{(T)2}}{C_V}, \quad (5.14)$$

where the difference between the adiabatic and the isothermal bulk moduli are related to the heat capacities. This relation can also be extended to describe the difference between adiabatic and isothermal elastic constants in cubic systems (in an equilibrium condition):

$$C_{ijkl}^{(S)} - C_{ijkl}^{(T)} = \delta_{ij}\delta_{kl}(B^{(S)} - B^{(T)}), \quad (5.15)$$

which in Voigt notation reads:

$$C_{11}^{(S)} - C_{11}^{(T)} = C_{12}^{(S)} - C_{12}^{(T)} = B^{(S)} - B^{(T)}, \quad (5.16)$$

$$C_{44}^{(S)} - C_{44}^{(T)} = 0. \quad (5.17)$$

### 5.3 Molecular dynamics

Molecular dynamics is an extremely important approach to study materials from a statistical point of view, like Monte Carlo, computing time averages (equivalent to ensemble averages in the ergodic limit) over configurations distributed according to a certain statistical ensemble, and also to study real time dynamics of a material in different conditions by integration of Newton's equations of motion for the atoms. In contrast with the Monte Carlo method, molecular dynamics is a deterministic technique: given an initial set of positions and velocities, the subsequent time evolution is *in principle* completely determined. Many good books and reviews [88–90, 146] on the subject are available and we refer to those for a exhaustive description of the technical aspects of the approach.

# 6 Gaussian approximation potentials (GAP)

The chapter is dedicated to the theoretical framework on which the Gaussian Approximation Potentials (GAP) is based. It is divided in three main parts. In the first part, a Bayesian approach to non-linear regression, the so-called Gaussian process (GP) regression, is introduced that explain how to infer functions underlying some reference data. It follows a discussion on how to adapt this formalism to train atomic energy functions from first-principles total energies, forces and stresses and, reversely, how to predict these same quantities from optimized atomic energy functions exactly, without the need of finite differences. The second part is devoted to the descriptors that are best suited to represent atomic environments within the Gaussian process regression framework. The last, instead, is specific to the case of  $\alpha$ -iron, and deals with the generation of an extended training set from DFT calculations.

## 6.1 Gaussian process regression

Gaussian approximation potentials are developed to learn and reproduce smooth highly dimensional BO PESs interpolating available quantum-mechanical data. As discussed in Chapter 3 for other potential models, this task is achieved by first decomposing each point of the PES in a sum of local atomic energy functions  $\epsilon_i$  and, second, providing suitable functional forms for the  $\epsilon_i$ . However, differently from all the other approaches encountered so far, in Gaussian approximation potentials the  $\epsilon_i$  are assumed to be *non-linear, non-parametric* functions that are optimized through a stochastic approach known as *Gaussian process regression*. This is ultimately equivalent to a two-layer NN model with an infinite number of hidden nodes. As it will be clear in a moment, this approach allows for a very high flexibility of the model and hence, a high interpolative power, which are not achievable with fixed parametrized functional forms and which make possible a systematic improvement of the potential as new configurations are included in the training set. On the other hand, such a high flexibility is responsible for a limited extrapolative power of the model when used to predict environments and situations out of the configurational space on which it has been previously trained.

In order to understand how a Gaussian process regression works let us consider the problem

## Chapter 6. Gaussian approximation potentials (GAP)

---

of predicting the values of a continuous (well-behaved) function  $f : \mathbb{R}^n \rightarrow \mathbb{R}$  that is assumed to underly some observations (training data). If the observed data  $\mathbf{t}_N = \{t_i\}_{i=1}^N$  are known at the points  $\mathbf{X}_N = \{\mathbf{x}_i\}_{i=1}^N$  with some error  $\varepsilon_i$  (i.e. it is possible to write  $t_i = f(\mathbf{x}_i) + \varepsilon_i$ ), the prediction of the values  $f(\mathbf{x})$  taken by the *unknown* function  $f$  at any new point  $\mathbf{x}$  can be formulated as a Bayesian regression problem [147, 148]. Following this approach, any  $f(\mathbf{x})$  is obtained as the most probable value of the conditional probability distribution of the values  $f(\mathbf{x})$ ,  $P(f(\mathbf{x})|\mathbf{t}_N, \mathbf{X}_N)$ , given the knowledge of the observed data. This is also called the *posterior* distribution and, according to Bayes' rule, it can be written as

$$P(f(\mathbf{x})|\mathbf{t}_N, \mathbf{X}_N) = \frac{P(\mathbf{t}_N|f(\mathbf{x}), \mathbf{X}_N)P(f(\mathbf{x}))}{P(\mathbf{t}_N|\mathbf{X}_N)}, \quad (6.1)$$

where:

- The first term at the numerator of the right-hand side of the equation,  $P(\mathbf{t}_N|f(\mathbf{x}), \mathbf{X}_N)$ , is called *likelihood*, and represents the probability density of the observed data given the output value  $f(\mathbf{x})$ .
- The second term at the numerator,  $P(f(\mathbf{x}))$ , is called *prior* distribution and plays a central role in the theory. It expresses our beliefs about the type of functions that underlie the observations before any observation of the data themselves.
- The last term in the right-hand side of eq. (6.1),  $P(\mathbf{t}_N|\mathbf{X}_N)$ , is known as the *marginal likelihood*.

Since the marginal likelihood can be considered a normalization factor, all that is relevant to the posterior are the prior  $P(f(\mathbf{x}))$  and likelihood  $P(\mathbf{t}_N|f(\mathbf{x}), \mathbf{X}_N)$  which also encodes the information about the noise assumed on the observations.

### 6.1.1 Function-space view

In practice, to find  $P(f(\mathbf{x})|\mathbf{t}_N, \mathbf{X}_N)$  it is necessary to make assumptions on the probability distributions on the right-hand side of eq. (6.1). A general way of proceeding is to assume the infinite set of function evaluations  $f(\mathbf{x})$  (that the function  $f$  assumed to underly the data takes at every  $\mathbf{x}$ ) as a collection of random variables, any finite number of which have a joint Gaussian distribution. Such a collection is called a *Gaussian process*. A Gaussian process can be thought as a distribution over the space of functions  $\mathbb{R}^n \rightarrow \mathbb{R}$  and, as a Gaussian distribution is determined by its mean  $m$  and covariance  $\Sigma_C$ , it is fully specified by a mean function  $m(\mathbf{x})$  and a covariance function  $C(\mathbf{x}, \mathbf{x}')$ . The mean defines the most probable function of the process/distribution and, although it can be any well-behaved function, in what follows will be considered to be identically zero for simplicity. The covariance instead is a kernel function that expresses the expected correlation between any two random variables of the process, i.e., in this case, between the output values of the function  $f$  at two points  $\mathbf{x}$  and  $\mathbf{x}'$ . The specification of the kernel is of primary importance in the regression procedure and, as such

is discussed in details in Sec. 6.2. As a consequence of the Gaussian process assumption, the prior is a joint Gaussian distribution of function evaluation vectors. If then it is also assumed an independent, identically distributed<sup>1</sup> Gaussian noise with zero mean and variance  $\sigma_v^2$  on the observations, it is possible to show (see below and Ref. [147, 148]) that the posterior is a joint Gaussian distribution for any vector of function evaluations, whose mean and kernel function depend directly on the prior mean and kernel function, and on the Gaussian noise of the data.

### 6.1.2 Weights-space view

A more pedagogic, but formally equivalent, way to determine the posterior probability distribution of eq. (6.1), and to interpret a Gaussian process regression, is based on the so-called weight-space view (as opposed to the function-space view described above). In the weight-space view the unknown function  $f(\mathbf{x})$  that is assumed to underlie the observed data is expressed as a linear combination of non-linear basis-functions  $\{\phi_h(\mathbf{x})\}_{h=1}^H$  with coefficients/weights  $\mathbf{w}$ :

$$f(\mathbf{x}; \mathbf{w}) = \sum_{h=1}^H \phi_h(\mathbf{x}) w_h = \boldsymbol{\phi}(\mathbf{x})^T \mathbf{w}. \quad (6.2)$$

In neural network terms, this model for the function  $f$  is like a multilayer network whose connections from the input layer to the non-linear hidden layer are fixed; only the output weights are adaptive. For a specific choice of the basis functions, it is possible to infer the function value  $f(\mathbf{x})$  either optimizing the parameters  $\mathbf{w}$  in a deterministic way (using for example a traditional force matching approach in the case of a finite number of parameters) or adopting a Bayesian approach. In the latter case, it is possible to write the posterior probability of the parameters using Bayes' rule:

$$P(\mathbf{w} | \mathbf{t}_N, \mathbf{X}_N) = \frac{P(\mathbf{t}_N | \mathbf{w}, \mathbf{X}_N) P(\mathbf{w})}{P(\mathbf{t}_N | \mathbf{X}_N)}. \quad (6.3)$$

The prediction for a new value of  $t_{N+1}$  of the function  $f$  evaluated at any new input point  $\mathbf{x}_{N+1}$  can then be written by marginalizing over all the possible parameter values. i.e. by weighting all possible models with a fixed set of parameters with the posterior probability of the weights of eq. above: :

$$P(t_{N+1} | \mathbf{t}_N, \mathbf{X}_N) = \int d^H \mathbf{w} P(t_{N+1} | \mathbf{w}, \mathbf{x}_{N+1}) P(\mathbf{w} | \mathbf{t}_N, \mathbf{X}_N). \quad (6.4)$$

In a Gaussian process regression the probability distributions of eqs. (6.3,6.4) are taken to be Gaussians such that the integral of eq. (6.4) can be solved exactly. For the case of generic probability distributions one can solve eq. (6.4) numerically relying on Monte Carlo approaches.

<sup>1</sup>i.e. the random variables of the collection have the same probability distribution and are mutually independent

### 6.1.3 Mean and error prediction: equivalence of the two methods

After some lengthy math discussed exhaustively in Refs. [127, 147–149], it is possible to show that the prediction of a new value  $t_{N+1}$  of the function  $f$  evaluated at the input point  $\mathbf{x}_{N+1}$  is normally distributed as:

$$P(t_{N+1} | \mathbf{t}_N, \mathbf{X}_N) \propto \exp\left(-\frac{(t_{N+1} - \bar{t}_{N+1})^2}{2\sigma_{\bar{t}_{N+1}}^2}\right). \quad (6.5)$$

In the weights-space view the mean value of the prediction and its variance take the form:

$$\bar{t}_{N+1} = \sigma_w^2 \boldsymbol{\phi}(\mathbf{x}_{N+1}) \Phi^T \cdot (\sigma_w^2 \Phi \Phi^T + \sigma_v^2 \mathbf{I})^{-1} \cdot \mathbf{t}_N, \quad (6.6)$$

$$\sigma_{\bar{t}_{N+1}}^2 = \sigma_w^2 \boldsymbol{\phi}(\mathbf{x}_{N+1}) \boldsymbol{\phi}^T(\mathbf{x}_{N+1}) - \sigma_w^2 \boldsymbol{\phi}(\mathbf{x}_{N+1}) \Phi^T \cdot (\sigma_w^2 \Phi \Phi^T + \sigma_v^2 \mathbf{I})^{-1} \cdot \sigma_w^2 \Phi \boldsymbol{\phi}^T(\mathbf{x}_{N+1}), \quad (6.7)$$

where, in the case of  $N$  training points and  $M$  target points,  $\Phi = \Phi(\mathbf{X}_N)$  is a  $N \times H$  matrix whose elements are the  $H$  basis-functions evaluated at the  $N$  training inputs  $\mathbf{X}_N$ ,  $\boldsymbol{\phi}$  is defined above as the  $M \times H$  matrix of basis-functions evaluated at the  $M$  target point(s)  $\mathbf{x}_{N+1}$ , and  $\sigma_v^2$  is the noise assumed on the observations and  $\sigma_w^2$  the noise assumed on the weights.

Similarly, in the function-space view, mean and covariance of eq.(6.5) quantities can be written as:

$$\bar{t}_{N+1} = \mathbf{k}^T (\mathbf{C}_N + \sigma_v^2 \mathbf{I})^{-1} \mathbf{t}_N, \quad (6.8)$$

$$\sigma_{\bar{t}_{N+1}}^2 = \kappa - \mathbf{k}^T (\mathbf{C}_N + \sigma_v^2 \mathbf{I})^{-1} \mathbf{k}, \quad (6.9)$$

where  $\mathbf{C}_N = C(\mathbf{X}_N, \mathbf{X}_N)$ ,  $\mathbf{k} = C(\mathbf{x}_{N+1}, \mathbf{X}_N)$ , and  $\kappa = C(\mathbf{x}_{N+1}, \mathbf{x}_{N+1})$  are covariance functions evaluated between the input training points  $\mathbf{X}_N$ , between the test points  $\mathbf{x}_{N+1}$  and the training points  $\mathbf{X}_N$ , and between the test points  $\mathbf{x}_{N+1}$  respectively. If there are available  $N$  training points and a prediction of  $M$  new points  $t_{N+1}$  evaluated at  $\mathbf{x}_{N+1} = \{\mathbf{x}_i^*\}_{i=1}^M$  is required, then  $\mathbf{C}_N$  is a  $N \times N$  matrix,  $\mathbf{k}$  is  $M \times N$  while  $\kappa$  is a  $M \times M$  matrix.

Since the two methods are equivalent, as rigorously proved in Refs. [127, 147–149], then the equivalences  $\mathbf{C}_N = \sigma_w^2 \Phi \Phi^T$ ,  $\mathbf{k} = \sigma_w^2 \boldsymbol{\phi}(\mathbf{x}_{N+1}) \Phi^T$ , and  $\kappa = \sigma_w^2 \boldsymbol{\phi}(\mathbf{x}_{N+1}) \boldsymbol{\phi}^T(\mathbf{x}_{N+1})$  have also to be true, and it follows that any specific choice of the covariance function  $C(\mathbf{x}, \mathbf{x}')$  corresponds to a particular choice of basis-function  $\boldsymbol{\phi}(\mathbf{x})$  (without the need of determining the weights  $\mathbf{w}$ ). Remarkably, this holds also in the case of an infinite basis-set thus unveiling the origin of the (ideally) infinite flexibility of the model achievable with finite computational resources.

It is interesting to point out that the most time consuming operation for making predictions out of eqs. (6.6,6.8) is the inversion of the matrix  $\mathbf{C}_N + \sigma_v^2 \mathbf{I}$ . This mathematical operation scales as the cube of the training data and corresponds to the *training* or *teaching* part of a Gaussian process regression. If the database of observations is fixed, however, it can be performed just once without the need of being repeated each time a new prediction point is calculated. The



only term that explicitly depends on the input values  $\mathbf{x}_{N+1}$  at which we seek a new function value prediction is  $\kappa = C(\mathbf{x}_{N+1}, \mathbf{x}_{N+1})$ . As a consequence, in eqs. (6.6,6.8), it is possible isolate this term thus rewriting the predictive mean as a linear combination of  $N$  kernel functions, each one centered on a training point:

$$\bar{t}_{N+1} = \sum_{i=1}^N \alpha_i C(\mathbf{x}_i, \mathbf{x}_{N+1}), \quad (6.10)$$

where the linear coefficients  $\boldsymbol{\alpha} = (\mathbf{C}_N + \sigma_v^2 \mathbf{I})^{-1} \mathbf{t}_N$  are taught once and stored for prediction.

## 6.2 Covariance functions and hyper-parameters

The Gaussian process regression is sensitive to the choice and the details of the covariance function or, equivalently, of the basis-set. In fact, the covariance function determines the properties of the functions samples and predictive mean function from the posterior distributions. A multitude of covariance function families for regression are possible. These are required to be symmetric, semi-positive definite and, for the purpose of generating interatomic potentials, mean square continuous, mean square differentiable and smooth. The most common example is the squared exponential kernel, which is reported for reference along other examples from the literature Tab. 6.1. Although the choice of the kernel class seems to be arbitrary in general, as discussed in Sec. 6.5, for the generation of interatomic potentials, such a choice is instead inherently related to the type of descriptors of the local atomic environment.

As evident from Tab. 6.1, each kernel class depends on a limited number of parameters, the so-called *hyper-parameters*, denoted here as  $\mathbf{h}$ . As a consequence, the posterior distribution of the Gaussian process regression would also depend on these hyper-parameters, i.e.  $P(t_{N+1} | \mathbf{t}_N, \mathbf{X}_N, \mathbf{h})$ . In principle, this dependence can be removed by marginalizing over such hyper-parameters, that is evaluating the integral:

$$P(t_{N+1} | \mathbf{t}_N, \mathbf{X}_N) = \int d\mathbf{h} P(t_{N+1} | \mathbf{t}_N, \mathbf{X}_N, \mathbf{h}) P(\mathbf{h} | \mathbf{t}_N, \mathbf{X}_N). \quad (6.11)$$

Although depending to the assumed distribution models, analytical or numerical integration by means of Markov chain Monte Carlo or Nested Sampling [150] would be possible, it is more practical finding the optimal hyper-parameters through a maximization of the likelihood (or equivalently its logarithm) with respect to the hyper-parameters themselves. Noticeably, the log likelihood is typically multimodal thus having different maxima points corresponding to a different optimal interpretation of the data. As such, the solution to a Gaussian process regression is not guaranteed to be unique. Alternatively, it is possible to tune some of them by hand from an *a priori* knowledge of the training data. Those that cannot be tuned in this way can be regarded as convergence parameters to be varied *a posteriori*. In practical cases, the accuracy is tested on data that are not included explicitly in the training set, the so-called test database.

Constant	$\theta$
Squared Exponential	$\exp -\frac{(x_i-x_j)^2}{2\theta^2}$
$\gamma$ -exponential	$\exp -\left(\frac{x_i-x_j}{\theta}\right)^\gamma$
Matérn	$\frac{2^{1-\nu}}{\Gamma(\nu)} \left(\frac{\sqrt{2\nu}}{l}(x_i-x_j)\right)^\nu K_\nu \left(\frac{\sqrt{2\nu}}{l}(x_i-x_j)\right)$
Rational Quadratic	$\left(1 + \frac{(x_i-x_j)^2}{2\alpha\theta^2}\right)^{-\alpha}$
Dot Product	$\theta + \mathbf{x}_i \cdot \mathbf{x}_j$
Polynomial	$(\theta + \mathbf{x}_i \cdot \mathbf{x}_j)^p$

Table 6.1: Some of the most commonly used covariance function classes.

### 6.3 Training interatomic potentials from total energies, forces and stresses

The Gaussian process regression scheme can be generalized for predicting atomic energy functions,  $\epsilon : \mathbb{Q} \rightarrow \mathbb{R}$ , defined on the space  $\mathbb{Q}$  of generalized coordinates (the descriptors). In this case, however, teaching data-points for the atomic energy function are not readily available since quantum-mechanical codes typically provide total energies (that are not easily decomposable in atomic contributions), atomic forces and stresses of an atomic positions' configuration. Nonetheless, the formalism described above can be adapted to use directly this kind of data to train the atomic energy function in a way similar to eqs. (6.6, 6.7). The derivation of the modified equations is straightforward but lengthy and, since it has been previously discussed in details in Refs. [127, 149, 151], we report here only the final relations. In particular, the equation for the mean atomic energy prediction and its associated error from total energies (in a weights approach) are:

$$\bar{\epsilon}(\mathbf{q}_i) = \sigma_w^2 \boldsymbol{\phi}(\mathbf{q}_i) \Phi^T \cdot (\sigma_w^2 \Phi \Phi^T + \sigma_{v_E}^2 \mathbf{I})^{-1} \cdot \mathbf{E}^{train}, \quad (6.12)$$

$$\sigma_{\bar{\epsilon}}^2(\mathbf{q}_i) = \sigma_w^2 \boldsymbol{\phi}(\mathbf{q}_i) \boldsymbol{\phi}^T(\mathbf{q}_i) - \sigma_w^2 \boldsymbol{\phi}(\mathbf{q}_i) \Phi^T \cdot (\sigma_w^2 \Phi \Phi^T + \sigma_{v_E}^2 \mathbf{I})^{-1} \cdot \sigma_w^2 \Phi \boldsymbol{\phi}^T(\mathbf{q}_i), \quad (6.13)$$

where  $\mathbf{E}^{train}$  is the total energy  $K \times 1$  training vector of  $K$  configurations containing  $N$  atoms each (here  $N$  is assumed constant for all configurations for simplicity of the notation),  $\boldsymbol{\phi}$  is the vector of basis-functions evaluated at the atomic environment  $\mathbf{q}_i$ , while

$$\Phi = \begin{bmatrix} \sum_{j_1=1}^N \boldsymbol{\phi}(\mathbf{q}_{j_1}) \\ \vdots \\ \sum_{j_k=1}^N \boldsymbol{\phi}(\mathbf{q}_{j_k}) \end{bmatrix} \quad (6.14)$$

with  $j_k$  indexes running on the number of atoms in the configuration  $k$ . From the definition of atomic forces given in eq. (3.2), and following Refs. [127, 149, 151], the atomic energy functions

is trainable also from atomic forces as follows:

$$\bar{\epsilon}(\mathbf{q}_i) = \sigma_w^2 \boldsymbol{\phi}(\mathbf{q}_i) \Psi^T \cdot (\sigma_w^2 \Psi \Psi^T + \sigma_{v_f}^2 \mathbf{I})^{-1} \cdot (-\mathbf{f}^{train}), \quad (6.15)$$

$$\sigma_{\bar{\epsilon}(\mathbf{q}_i)}^2 = \sigma_w^2 \boldsymbol{\phi}(\mathbf{q}_i) \boldsymbol{\phi}^T(\mathbf{q}_i) - \sigma_w^2 \boldsymbol{\phi}(\mathbf{q}_i) \Psi^T \cdot (\sigma_w^2 \Psi \Psi^T + \sigma_{v_f}^2 \mathbf{I})^{-1} \cdot \sigma_w^2 \Psi \boldsymbol{\phi}^T(\mathbf{q}_i), \quad (6.16)$$

where  $\mathbf{f}^{train}$  is the vector of the quantum-mechanical three force components for each of the  $N$  atoms in each of the  $K$  configurations. In this case, the matrix  $\Psi$  is defined as

$$\Psi = \begin{bmatrix} \sum_{j_1=1}^N \boldsymbol{\psi}_{x,l_1}(\mathbf{q}_{j_1}) \\ \sum_{j_1=1}^N \boldsymbol{\psi}_{y,l_1}(\mathbf{q}_{j_1}) \\ \sum_{j_1=1}^N \boldsymbol{\psi}_{z,l_1}(\mathbf{q}_{j_1}) \\ \vdots \end{bmatrix}, \quad \boldsymbol{\psi}_{\alpha,l_1}(\mathbf{q}_{j_1}) = \frac{\partial \phi(\mathbf{q}_{j_1})}{\partial x_{\alpha,l_1}}, \quad (6.17)$$

where  $\alpha = \{x, y, z\}$  is the Cartesian index,  $l_k$  the index of an atom in configuration  $k$ . Analogously to eqs. (6.12,6.15), also the virial stress tensor (a linear combination of forces) can be used to teach the atomic potential energy. In practice, however, since teaching is typically performed from total energies, forces and stresses at the same time, it is useful to provide a generalized relation for the prediction of the atomic energy function  $\bar{\epsilon}$  as:

$$\bar{\epsilon}(\mathbf{q}_i) = \sum_j \alpha_j C(\mathbf{q}_j, \mathbf{q}_i) \equiv \mathbf{k}(\mathbf{q}_i)^T \boldsymbol{\alpha}, \quad (6.18)$$

where the sum over  $j$  includes (some or all of) the local environments of the configurations in the database, and the meaning of the covariance kernel  $C$  is that of a similarity measure between different neighbor environments (see next section). This relation is similar to eq. (6.10) even though, in this case, the expression for the coefficients  $\boldsymbol{\alpha}$  is more complicated because the quantum mechanical input data are total energies, forces and stresses together rather than values of the atomic energy function itself. The exact expression is given by linear algebra relations and can be found in Ref. [152].

Finally, the GP regression allows also for the prediction of total energies, total energy derivatives, i.e. atomic force, and consequently virial stress. The equations for the prediction of these quantities are based on the summation, differentiation (or a combination of the two operations) of eq. (6.18) with respect to the proper degrees of freedom and are reported in Refs. [127, 149, 151].

## 6.4 Sparsification

A price to pay for a high flexibility is an explicit dependence of the method on the amount of information taught to the model, i.e. on the size of the training-set. The Gaussian process regression allows to compute predictions at  $M$  new points starting from  $N$  teaching points with a computational cost that scales as  $\mathcal{O}(NM)$  for the predictive mean,  $\mathcal{O}(N^2M)$  for the corresponding error and  $\mathcal{O}(N^3)$  for training part. While this method remains computationally

tractable for training sets consisting of several thousands of input points, this limit can be exceeded if one needs to train the atomic energy function from total energies, forces and stresses of a wide variety of inequivalent atomic configurations (because of the resultant cross terms). However, the size of the training set can be reduced by noting that many training data are correlated. In order to remove redundant information, thus minimizing the computational load, one can rely on sparsification methods. Among the many sparsification schemes that have been invented in the past recent years (more details in Ref. [153]), the one proposed by Snelson and Ghahramani in Ref. [154] turned out to be useful for GAP. In fact, adopting this approach, where  $S \ll N$  sparse points are selected from the full training set, the computational resources required for the training GAP scale as  $\mathcal{O}(NS^2)$ , while the cost of the prediction of mean function values scales as  $\mathcal{O}(S)$ .

### 6.5 GAP kernel: smooth overlap of atomic positions (SOAP)

As mentioned in Sec. 3.1.1, there are possible ways of constructing reliable descriptors for local atomic environments that could be considered in a GAP framework. However, it has been shown in the previous sections that what really matters in a Gaussian process regression framework is not the descriptors *per se*, but the covariance function  $C(\mathbf{q}, \mathbf{q}')$  that is constructed from the descriptors. In this context, therefore, one can bypass altogether the concept of descriptor for representing and discriminating atomic environments by constructing a kernel function which is itself as a *similarity measure* between two atomic neighborhoods. To this end, such a similarity kernel should satisfy the condition of invariance to symmetry operations required for the descriptors on top of those required for generic kernel functions of a Gaussian process. Additional useful properties that one might seek, are the existence of well-defined limit values (like 1 and 0) when comparing two identical or two very different environments, and the smoothness with respect to changes of Cartesian coordinates. The so-called *smooth overlap of atomic positions* (SOAP) similarity kernel developed by Bartók *et al.* [128] complies with all these requirements. It is currently the state-of-the-art kernel available for GAP and, since proved to perform reliably for the purposes of generating potentials for bcc metals [152], it has been chosen as reference kernel for this work.

The SOAP kernel  $C(\rho_i, \rho_j)$  is constructed starting from a similarity kernel  $k(\rho_i, \rho_j)$  defined as follows:

$$k(\rho_i, \rho_j) = \int |S(\rho_i, \hat{R}\rho_j)|^t d\hat{R}, \quad (6.19)$$

$$S(\rho_i, \hat{R}\rho_j) = \int \rho_i(\mathbf{r})\rho_j(\hat{R}\mathbf{r}) d\mathbf{r}, \quad (6.20)$$

where the atomic neighbor density of the atom  $i$  is  $\rho_i(\mathbf{r}) = \sum_j w_{Z_j} \delta(\mathbf{r} - \mathbf{r}_{ij})$ , with  $\mathbf{r}_{ij}$  being the vectors pointing to the neighboring atoms, and  $w_{Z_j}$  the weight factors assigned according to the atomic species. The similarity function  $k(\rho, \rho')$  is built from  $S(\rho, \rho')$ , defined as the inner product of two atomic neighbor densities, and integrated over all possible rotations  $\hat{R}$

## 6.5. GAP kernel: smooth overlap of atomic positions (SOAP)

in order to satisfy rotational invariance on top of the permutational invariance satisfied by construction. In the GAP framework,  $t \geq 2$  so that the kernel retains the angular information of the original environments. Moreover,  $k$  is typically normalized dividing by  $\sqrt{k(\rho_i, \rho_i)k(\rho_j, \rho_j)}$ , and raised to some power  $\zeta \geq 2$  thus to accentuate the sensitivity of the kernel to changing the atomic positions in a local environment. Considering all these modifications, it is possible to define the general form of the SOAP kernel as:

$$C(\rho_i, \rho_j) = \left( \frac{k(\rho_i, \rho_j)}{\sqrt{k(\rho_i, \rho_i)k(\rho_j, \rho_j)}} \right)^\zeta. \quad (6.21)$$

In practice, however, the SOAP kernel is evaluated numerically by first approximating the Dirac-delta functions of the original atomic density as Gaussians to ensure smoothness of the kernel, and then expanding such a new atomic density in a radial and spherical harmonic basis [155],

$$\rho_i(\mathbf{r}) = \sum_j e^{-|\mathbf{r}-\mathbf{r}_{ij}|^2/2\sigma_{atom}^2} f_{cut}(|\mathbf{r}_{ij}|), \quad (6.22)$$

$$= \sum_{n < n_{max}} \sum_{l < l_{max}} \sum_{|m| \leq l} c_{nlm}^i g_n(|\mathbf{r}|) Y_{lm}(\hat{\mathbf{r}}), \quad (6.23)$$

where  $\sigma_{atom}$  is a parameter corresponding to the "size" of the atoms,  $g_n$  and  $Y_{lm}$  orthonormal radial basis functions and spherical harmonics with the usual indexes, while  $f_{cut}$  is a smooth cutoff function with compact support defining the extension of the local environment that, for the specific GAP implementation used in this work, is chosen of the form

$$f_{cut}(|\mathbf{r}_{ij}|) = f_{cut}(r) = \begin{cases} 1, & 0 < r \leq (r_{cut} - r_\Delta) \\ \frac{1}{2}(1 + \cos(\pi \frac{r - r_{cut} + r_\Delta}{r_\Delta})), & (r_{cut} - r_\Delta) < r \leq r_{cut} \\ 0, & r_{cut} < r \end{cases}. \quad (6.24)$$

The truncation of the atomic local environment (and of the atomic interactions) at a finite value is a strong approximation that, although qualitatively justified in metallic systems with screening arguments, should be always analyzed case-by-case from a quantitative point of view. In fact, the values of  $r_{cut}$  and of  $r_\Delta$  are strongly system dependent and might affect the prediction of atomic energies and of atomic forces differently.

Following the derivation in Ref. [128], exploiting eqs. (6.21,6.22,6.24) it is therefore possible to show that in the case of  $t = 2$  the SOAP kernel can be equivalently rewritten as a dot-product kernel

$$C_{ij} = \sigma_w^2 |\hat{\mathbf{q}}_i \cdot \hat{\mathbf{q}}_j|^\zeta, \quad (6.25)$$

## Chapter 6. Gaussian approximation potentials (GAP)

---

$r_{cut}$	$r_{\Delta}$	$\zeta$	$\sigma_{atom}$
$n_{max}$	$l_{max}$	$\sigma_w$	$\sigma_{vE/f/\sigma}$

Table 6.2: List of parameters to specify during a GAP generation with a SOAP kernel.  $\sigma_{vE/f/\sigma}$  refers to the different errors assumed on the total energy, the atomic forces and the stresses respectively.

where

$$\mathbf{q}_i = \left\{ \sum_m (c_{nlm}^i * c_{n'lm}^i) \right\}_{nn'l}, \quad \hat{\mathbf{q}}_i = \mathbf{q}_i / |\mathbf{q}_i|. \quad (6.26)$$

with  $n, n', \leq n_{max}$  and  $l \leq l_{max}$ . Noticeably, this reformulation means that a Gaussian process regression with a  $t = 2$  SOAP kernel is equivalent to a Gaussian process regression with a dot-product covariance kernel (see also Tab. 6.1) SOAP and *power spectrum* descriptors [23, 128]. Note also that, since the basis-set truncation limits the ability of discrimination between genuinely different environments,  $n_{max}, l_{max}$  have to be considered as convergence parameters.

### 6.5.1 SOAP GAP parameters

The SOAP-GAP framework has been designed to generate potentials that are relatively stable against oscillations of hyper-parameters [23, 152]. These are listed in Tab. 6.2 for the sake of completeness. The SOAP-GAP computational cost for the prediction of total energies  $E$  scales as  $\mathcal{O}(N_{at} S n_{max}^2 l_{max})$ , while for atomic forces  $\mathbf{f}$  scales as  $\mathcal{O}(N_{r_{cut}} 3 S n_{max}^2 l_{max})$ , with  $S$  number of sparse training points,  $N_{at}$  number of atoms in a cell under consideration,  $N_{r_{cut}}$  number of atoms in the neighborhood defined by  $r_{cut}$  around a given atom, and  $n_{max}, l_{max}$  defined above. By construction, the scaling of the virial stress, is also dominated by the one associated to the atomic forces.

## 6.6 Database generation

The GAP potentials are constructed to interpolate the atomic energy function in the space of neighbor environments. To this end, a good coverage of the *relevant* environments that can provide information about the physical properties that are to be reproduced is necessary. In this work, for each property of interest, a set of minimal representative unit cell configurations amenable to accurate first-principles calculations is considered. The energies, forces and stresses of such configurations are stored in specific databases and used selectively for training.

Since the focus of this work are thermodynamic, thermo-mechanical and defects properties of  $\alpha$ -iron, following Ref. [152], we generate the following set of training databases:

- **DB1** Equilibrium geometry & Elastic constants

- **DB2** Bulk vibrational properties
- **DB3** Vacancies
- **DB4** Free surfaces
- **DB5**  $\gamma$  surfaces

The motivations for the generation of the different databases are discussed in the following sections along with the generation details, which are also summarized in Tab. 6.11.

### 6.6.1 Equilibrium geometry and elastic constants

The first basic physical property that a potential should be able to reproduce is the total energy versus volume curve, i.e. the equation of state, since it provides information about the equilibrium geometry (lattice constant, volume), and about the compressibility of the material. In addition, it provides information about the stiffness tensor of the material, i.e. about the material response under small deformations. The ability of reproducing the elastic constants is the first necessary condition to properly reproduce the energetics of point or extended defects, such as dislocations or stacking faults. In fact, it is known [156, 157] that such defects come along with long range elastic residual stresses which can directly influence structure and dynamics of the core-defect region, where anelasticity typically dominates. A reliable potential should then be capable at least to reproduce such elastic (and ideally also the anelastic) response.

In order to train GAP in terms of the mentioned properties we calculate DFT energies and stresses from primitive randomly distorted cells, so to sample and interpolate the BO PES region associated to cell distortions of a bcc structure around two reference volumes. These volumes correspond roughly to the equilibrium volume at 300 K and 1000 K obtained from quasi-harmonic theory respectively (see Ref. [45]). The relevant deformed cells are obtained from a Monte Carlo (MC) slice-sampling algorithm [158] at a temperature of 300 K. Unlike Molecular Dynamics, in MC a new geometry is generated through non-uniform, pseudo-random sampling of relevant phase-space dimensions, provided that the samples are distributed according to Boltzmann statistics for the canonical ensemble, with Boltzmann factors given by  $P(E) \propto \exp(-\beta E)$ . MC is preferred to variable cell MD due to its ability of generating less correlated samples at a similar computational cost [159]. In practice however, instead of performing MC calculations, we recycle those configurations generated in Ref. [149] for bcc tungsten, properly rescaling them to account for the different equilibrium lattice parameter and elastic properties of iron. This procedure is approximated as follows. First we define an average elastic constant  $C = \frac{C_{11}+C_{12}+C_{44}}{3}$ ; second we search for the effective strain values at which the effective elastic (free) energy  $\Delta E^{eff} = \frac{1}{2} V_{eq}(T) C(T) \varepsilon^2$  for the two systems satisfies the condition  $\Delta E_{Fe}^{eff} = \Delta E_W^{eff}$ , being  $V_{eq}(T)$  the equilibrium volume of a material at finite temperature. From experimental values for the equilibrium volumes and elastic constants

## Chapter 6. Gaussian approximation potentials (GAP)

(see also Tab. 6.3), and from the imposed equality of the elastic energies, one gets:

$$\frac{\varepsilon_{Fe}}{\varepsilon_W} = \sqrt{\frac{V_{eq}^W(T)C^W(T)}{V_{eq}^{Fe}(T)C^{Fe}(T)}} \approx \sqrt{\frac{V_{eq}^W(0)C^W(0)}{V_{eq}^{Fe}(0)C^{Fe}(0)}} \varepsilon_W \approx 1.56. \quad (6.27)$$

This result, along with the correct equilibrium volume and the tungsten deformation matrices, provides the scaling ratio to get the relevant deformed iron cells.

	$a(T=0)$ (Bohr)	$B(0)$ (GPa)	$C_{11}(0)$	$C_{12}(0)$	$C_{44}(0)$	$C(0)$
<i>W</i> [160, 161]	5.97	314	532	204	163	300
<i>Fe</i> [162–164]	5.42	171	240	136	121	166
<i>W/Fe</i>	1.10	1.84	2.22	1.50	1.35	1.81

Table 6.3: Experimental lattice parameter and elastic constants of bcc tungsten and  $\alpha$ -iron at 0 K. The elastic constant  $C$  is defined in the text as the arithmetic average between  $C_{11}$ ,  $C_{12}$  and  $C_{44}$ .

Given the shape of the primitive distorted cells for iron, we performed DFT calculations (see Tab. 6.4) computing and storing stresses and total energies in the database. Note that in order to ensure a good convergence of the stresses (see Sec. 6.6.6) we use a higher wavefunction and charge density kinetic-energy cutoff compared to that use for total energies. The total number of atomic environments calculated in this database is 4000.

$N_{atoms}$	1
cell size	$1 \times 1 \times 1$
$k$ -points	$20 \times 20 \times 20$
ecutwfc (Ry)	90 (1080) / 144 (1728)
smearing (Ry)	0.01 Marzari-Vanderbilt
$\beta_{mix}$ (Ry)	0.2
conv_thr (Ry)	1-e10

Table 6.4: Parameters of the calculations for sampling primitive distorted cells.

**Future work DB1:** sampling to be performed at contracted volumes to study also bcc iron under pressure.

### 6.6.2 Bulk vibrations

In order to train the thermal expansion and the phonon spectrum of the system, we generate supercell atomic configurations obtained from MD runs. The dynamics is performed in a BO ab initio framework rather than using pre-existing interatomic potentials in order to generate trajectories fully consistent with an ab initio description of the system. However, since generating ab initio MD trajectories is costly, the integration of the equations of motion is done with a cheap, non-fully converged, set of ab initio parameters (see Tab. 6.5). The



cheap trajectories are initialized with atoms arranged in a perfect bcc structure and an initial temperature which is twice the target temperature. Thermalization and equilibration are performed in a NVE ensemble using a time-step of 4 fs (Tab. 6.6). This procedure is followed for different volumes and different target temperatures as reported in Tab. 6.7 to span the entire  $\alpha$  region of iron phase-space. Two different cell sizes, namely a  $3 \times 3 \times 3$  and a  $4 \times 4 \times 4$  cubic supercell with a cubic unit cell contains 2 atoms, are chosen to guarantee a reasonable trade-off between computational cost and appropriate sampling of the vibrational spectrum. In fact, although the atomic forces converge pretty fast with the size of the simulation supercell [127], the phonons that can be sampled in MD in presence of supercells with boundary conditions, are only those with a wavevector commensurate with the cell edges. Each volume-temperature trajectory is run for at least 9 ps for the small supercells, and 2.5 ps for the large one. From each of them are then extracted a number of snapshots that are equally spaced in time (an initial arbitrary shift is also introduced). Fig. 6.1 shows the total energy associated to given trajectory and displays selected snapshots. Finally, the total energies and forces of these snapshots are re-computed with fully converged ab initio parameters (see tab. 6.6.6) and stored in the database.

$N_{atoms}$	54/128
cell size	$3 \times 3 \times 3 / 4 \times 4 \times 4$
$k$ -points	$1/4 \times 1/4 \times 1/4$
ecutwfc (Ry)	64 (576)
smearing (Ry)	0.01 Marzari-Vanderbilt
$\beta_{mix}$ (Ry)	0.05
conv_thr (Ry)	1-e7

Table 6.5: Parameters of the electronic calculation for sampling of bulk phonons.

$\Delta t$ (fs)	4
ensemble	NVE

Table 6.6: Parameters of the ionic calculation for sampling of bulk phonons.

Supercell	$3 \times 3 \times 3$	$4 \times 4 \times 4$
Temperature (K)	400 / 600 / 1000 / 1400	800
Lattice (Å)	2.8137, 2.8336, 2.8534, <b>2.8668</b> (-0.7,0,+0.7,+1.17%)	2.8137, 2.8336, 2.8534, 2.8668 (-0.7,0,+0.7,+1.17%)

Table 6.7: Temperatures and volumes considered for sampling bulk phonons in the case of  $3 \times 3 \times 3$  and  $4 \times 4 \times 4$  supercells. The volumes considered correspond to 0.0%,  $\pm 0.7\%$ , and  $+1.17\%$  of the DFT electronic equilibrium; the  $+0.7\%$  and  $+1.17\%$  also correspond to the quasi-harmonic equilibrium volume at 600 K and 1000 K respectively (see Ref. [45]). In the  $3 \times 3 \times 3$  case the blue color indicates that the considered configurations are obtained from a  $+0.7\%$  volume trajectory after rescaling the volume per atom and the atomic positions to the value of interest.

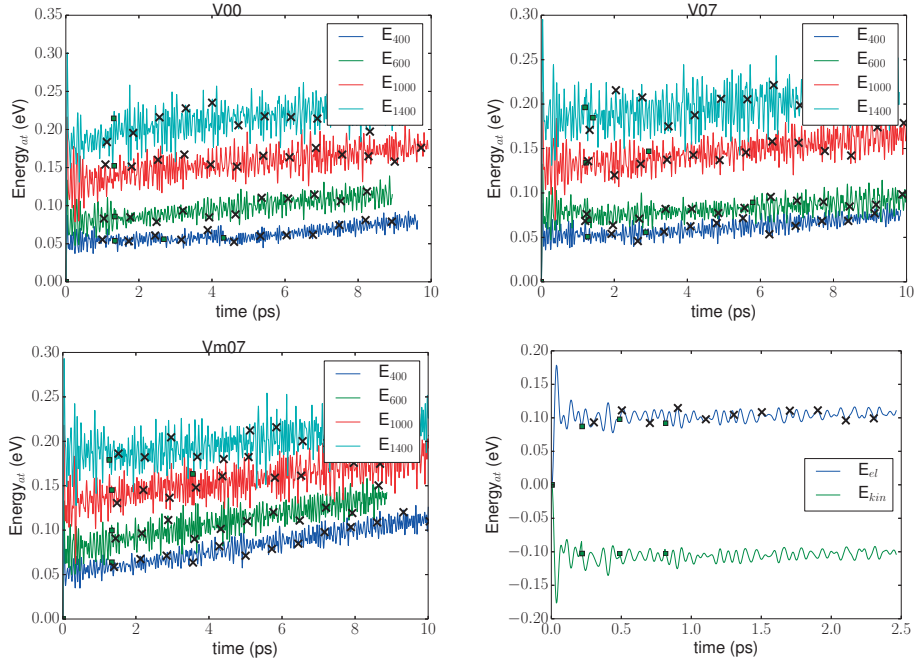


Figure 6.1: Top left, top right and bottom left panels show total energies (per atom) of bulk iron as a function of time during MD trajectories and refer to a  $3 \times 3 \times 3$  supercell with three different volumes and different temperatures (see Tab. 6.7). Bottom right panel displays total potential plus kinetic energy (per atom) of the same system and refers to a  $4 \times 4 \times 4$  supercell at the electronic equilibrium volume and a temperature of 800 K. The curves are rigidly shifted for the sake of clarity. The black crosses along the total energy curves highlight the snapshots that have been extracted for training GAP. Squares correspond to points in which the trajectories have been interrupted and reinitialized with randomized atomic velocities due to hardware/software failure.

The total number of atomic environments generated and stored to train GAP (from total energies and forces) is 13126. These are distributed as 167+50 [no MD] configurations from a  $3 \times 3 \times 3$  supercell with 54 atoms, i.e. 9018 atomic environments, and 90 configurations from a  $4 \times 4 \times 4$  supercell with 128 atoms, i.e. 11520 environments.

**Future work DB2:** sampling to be performed at contracted volumes to study also bcc iron under pressure.

### 6.6.3 Vacancies

The simplest lattice defect one can simulate in crystals is an isolated vacancy. It is a type of point defect that consist in a missing atom from the regular crystalline lattice. Vacancies occur naturally in crystals at any given temperature and are known to have a strong impact on mechanical strength and ductility, e.g., by enabling material transport, acting as a pinning centers for dislocations, or enabling a dislocation climb. They have an equilibrium concentration

which, in the dilute limit, is proportional to  $\exp -G_f^{vac}/k_B T$ , where  $G_f^{vac}(T, P)$  is the Gibbs energy of formation. Although there are methods to compute Gibbs formation energies from DFT [118], here we focus on the zero pressure and zero temperature limit. In this limit the key quantity to characterize a vacancy is its formation energy  $G_f^{vac}(T = 0, P = 0) = E_f^{vac}$  that, in first approximation (for examples neglecting the zero thermal motion of atoms), can be obtained from total energy calculations as the change in the energy of the system with ( $N - 1$  atoms) and without ( $N$  atoms) the vacancy including the optimization of the positions of all the surrounding atoms:

$$E_f^{vac} = \min_{\mathbf{x}_1, \dots, \mathbf{x}_{N-1}} (E^{vac}(N - 1)) - \frac{N - 1}{N} E_0(N), \quad (6.28)$$

where  $E_0$  is the ground state energy of the perfect crystal at the equilibrium. In practice, calculations are done at fixed volume and one should converge the first term in the right-hand side of equation above in terms of the supercell size in order to ensure the mono-vacancy does not interact with its images in the other cells thus getting a reliable formation energy value. In fact, the stress field associated to the mono-vacancy is typically long range (with a spherical symmetry), and one should consider very large supercells in order to be sure to have conditions of zero stress at the cell boundaries. However, since in DFT large supercells are hardly affordable, one is typically left with unbalanced stresses. In order to improve the convergence rate [149] fulfilling the requirement of zero pressure, it is possible (when affordable) to perform variable cell relaxations, optimizing the cell vectors along with the atomic positions. In this case, the formula for the vacancy formation energy is modified as:

$$E_f^{vac} = \min_{\mathbf{x}_1, \dots, \mathbf{x}_{N-1}, V} (E^{vac}(N - 1)) - \frac{N - 1}{N} E_0(N). \quad (6.29)$$

This formula can be readily generalized to compute formation energies of multi-vacancies or (self-)interstitials. Note also that from a technical point of view, it is better to compute  $E_0$  with same supercell and convergence parameters used for  $E^{vac}(N - 1)$  rather than computing it as  $N$  times ( $N$  being the number of atoms in the pristine supercell) the ground state energy per atom. This ensures the same level of accuracy in the two calculations.

In order to train mono-vacancy formation energies (and diffusion pathways) from DFT, we rely on the same strategy outlined in the section above. We perform a set of MD trajectories at a reduced cost for sampling the configurational space and, afterwards, we recalculate accurate total energies and atomic forces of selected snapshots along these trajectories. All the trajectories are obtained in a NVE ensemble with controlled average temperature (rescaled one every 100 steps roughly). The initial configurations of the trajectories correspond to the last snapshots of the cheap MD runs of Sec. 6.6.2 at same temperatures (avoiding 1400 K), volumes, supercell sizes and  $N - 1$  atoms. The parameters for the electronic and ionic parts of the calculations are the same reported in Tab. 6.5 and Tab. 6.6 respectively with the exception that now we deal with 53 and 127 atoms for the  $3 \times 3 \times 3$  and  $4 \times 4 \times 4$  supercells. We run the trajectories for at least 30 ps for the  $3 \times 3 \times 3$  supercell and about 12 ps for the  $4 \times 4 \times 4$

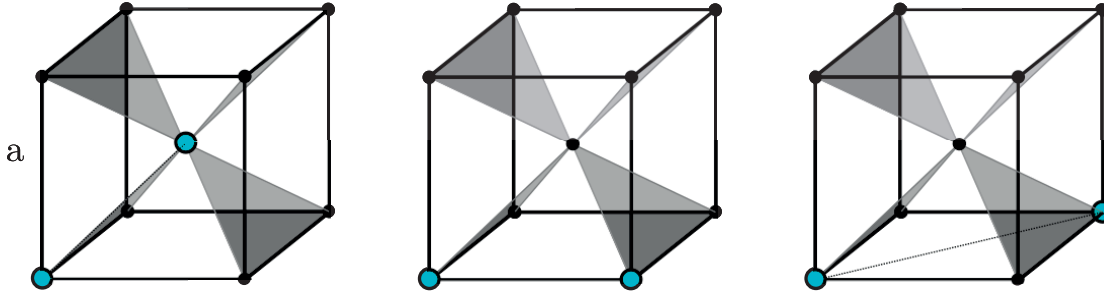


Figure 6.2: From left to right, schematics of first, second, and third nearest-neighbors di-vacancies.

one as visible from Figs. 6.3. We extract the snapshots to be recalculated at higher accuracy that are equidistant in time space along each MD trajectory (excluding the re-equilibration part, and with a relative initial shift chosen arbitrarily). We have also generated trajectories of about 8 ps containing a di-vacancy in a  $4 \times 4 \times 4$  supercell with 126 atoms at electronic bulk equilibrium volume and 800 K (same electronic and ionic parameters of the cases above). More specifically, we consider a third nearest-neighbors di-vacancy (see Fig. 6.2) which results to be stable during the trajectory, in the sense that no diffusion or hopping is observed. In the case of two interacting vacancies, their binding energy can also be computed using the following definition:

$$E_f^b = 2 \min_{\mathbf{x}_1, \dots, \mathbf{x}_{N-1}} (E^{vac}(N-1)) - \left[ \min_{\mathbf{x}_1, \dots, \mathbf{x}_{N-2}} (E^{vac}(N-2)) + E_0(N) \right]. \quad (6.30)$$

The total number of atomic environments generated and recalculated with high accuracy (see Sec. 6.6.6) to train GAP (from total energies and forces) is 27432. These are distributed as 381 mono-vacancy configurations from a  $3 \times 3 \times 3$  supercell with 53 atoms, i.e. 20193 environments, and 57 mono-vacancy configurations from a  $4 \times 4 \times 4$  supercell with 127 atoms, i.e. 7239 environments, and 39 di-vacancy configurations from a  $4 \times 4 \times 4$  supercell with 126 atoms, i.e. 4914 environments.

**Future work DB3:** as the equilibrium concentration of vacancies in the crystal increases, multi-vacancy interactions become increasingly relevant. For this reason one might also think at training GAP on an extensive set of various di-vacancies (first- and second-nearest neighbor to start with), tri-vacancies, and vacancy cluster configurations. In order to train activation barriers for vacancy diffusion one should consider to generate high temperatures MD trajectories. Metadynamics [165] might also be considered for finding diffusion pathways. Furthermore the inclusion of self-interstitial defects is also important. Although such a type of defects is unlikely to be thermally activated, the ability of reproducing they energetics is relevant for radiation damage studies. Some examples that should be considered in the future are the 111 dumbbell (crowdion), the 110 dumbbell, the 100 dumbbell, the tetrahedral and

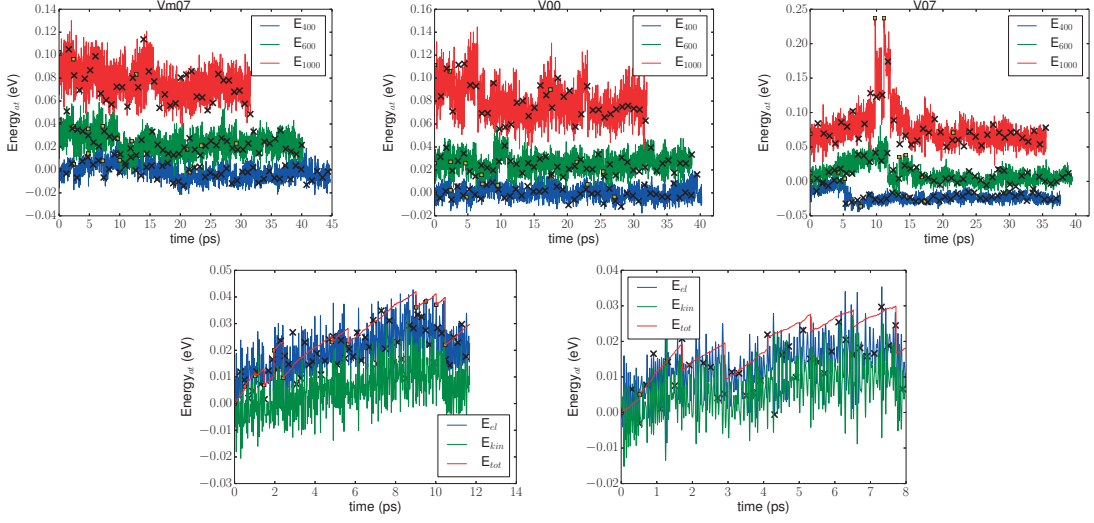


Figure 6.3: In the first row are reported the total energies (per atom) of mono-vacancies MD trajectories as a function of time calculated with a  $3 \times 3 \times 3$  supercell. In a single panel are reported the trajectories associated to the three temperatures of interest while the different panels, moving from left to right panel, are associated to the different volumes (see Tab. 6.7 for temperature and volume details). These curves are rigidly shifted for the sake of clarity. In the second row, the left panel shows total potential and kinetic energy (per atom) of a mono-vacancy in a  $4 \times 4 \times 4$  supercell at the electronic equilibrium volume and a temperature of 800 K. The right panel shows the same thing at same thermodynamic conditions for a di-vacancy. The black crosses on top of the total energy curves highlight the snapshots selected for training GAP while the squares correspond to points in which the trajectories have been interrupted and reinitialized with randomized atomic velocities due to hardware/software failure.

octahedral self-interstitials (see Fig. 6.4 for a schematic representation).

#### 6.6.4 Surfaces

Free surfaces can be regarded as a type of extended defect. These can be created cutting a crystal through a plane and separating macroscopically the two halves. The energy cost of a bulk terminated surface and its dependence on crystallographic orientation can determine the equilibrium shape of the crystal and its growth. As for the vacancies it is possible to calculate their (free) energy cost. This will be a function of the considered crystallographic orientation. The formula to calculate it (neglecting thermal and pressure contributions) is the following:

$$E_f^{surf} = \frac{1}{2A} \left( \min_{\mathbf{x}_1, \dots, \mathbf{x}_N} (E^{surf}) - E_0 \right), \quad (6.31)$$

where the minimization performed over the atomic positions, and the factor 1/2 indicating that two surfaces are created out of a bulk configuration. The surface energy is given per

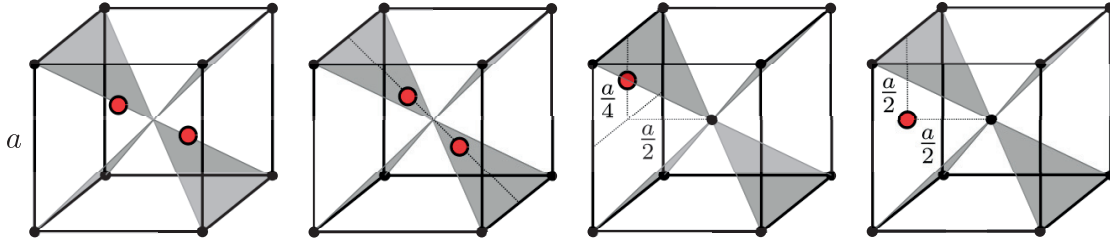


Figure 6.4: Schematic of relevant self-interstitial defects to include in the training database. From left to right the 111 dumbbell (crowdion), the 110 dumbbell, the tetrahedral and octahedral self-interstitials.

unit area  $A$  and is usually positive, reflecting the energy cost of the broken bonds in the cleaved configuration. In practical calculations, due to periodic boundary conditions, a surface geometry is typically modeled through an infinite series of slabs with finite thickness and separated by finite vacuum regions. The thickness of the slabs and of the vacuum regions are therefore two important geometrical parameters that can influence the final value of the calculation with eq. (6.31). This is due to the possible interactions of the two surfaces of the slab with each other and with their with periodic images. In order to provide reliable results, one should converge the results with respect to these parameters. Examples of characteristic thicknesses for the slab and for the vacuum regions needed to recover a bulk terminated surface like behavior out of a slab configuration in metals are provided in Refs. [149, 166, 167] and amount roughly to 10/12 atomic layers. Another geometrical parameter that should be considered is the cell size in the plane of the surface. It should not affect the value of the formation energy, and should be large enough to allow for possible surface reconstruction and (in a dynamical simulation) to allow for surface vibrations (surface phonons [168]).

The four crystallographic free surface orientations most important for the equilibrium shape and growth of nano crystals in iron are the low index surfaces (100), (110), and (112). In fact, it has been calculated (see Ref. [167, 169]) that  $\min_{hkl}(E^{surf}) = E_{110}^{surf} < E_{100}^{surf} < E_{112}^{surf}$  ( $h, k, l$  being the Miller indexes), with higher values for the other surface energies. For the sake of completeness, the (111) orientation is also considered in this work.

As for the previous sections, the sampling strategy for the terminated surfaces is based on the generation of trajectories from BO AIMD with reduced convergence parameters. The trajectories are generated in a NVE ensemble with controlled (rescaled) average temperature of 300 K and inhibited in-plane motion. Only the out-of-plane motion is allowed thus to sample surface relaxation from the initial unrelaxed structure. The sampling is followed by a second step in which total energies and forces from selected snapshots are recalculated with higher accuracy.

The simulation cells are generated by means of the ASE [170] package, and correspond to supercells that are primitive in the crystallographic plane of interest and elongated in the  $c$  direction to include 12 (6 in the case of the (211) surface) atomic-layers. The vacuum region

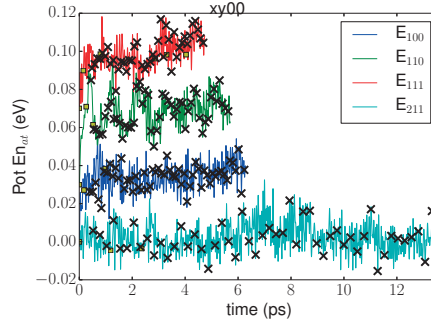


Figure 6.5: Total energies (per atom) of (100), (110), (111) and (112) terminated surfaces as a function of simulated time. The black crosses on top of the total energy curves highlight the snapshots selected for training GAP while the squares correspond to points in which the trajectories have been interrupted and reinitialized with randomized atomic velocities due to hardware/software failure. The (211) curve is much longer of the others due to its different  $k$ -point sampling.

separating the atomic slabs in the  $c$  direction is taken to be  $16 \text{ \AA}$  thick. The primitive in-plane lattice vectors are constructed from an equilibrium bulk geometry (with a lattice spacing of  $2.8336 \text{ \AA}$ ), as if the crystal would infinitely extend in the direction orthogonal to the interface (relaxations for thin slabs are in fact expected [168]). Each run lasts at least  $4.5 \text{ ps}$  (as visible from Fig. 6.5) performed with a  $k$ -point sampling of  $4 \times 4 \times 1$  for the (100), (110), (111) and  $2 \times 2 \times 1$  for the (112)), a reduced step of  $\Delta t = 2 \text{ fs}$  (since we noticed the explosion of the (110) terminated surface with the  $\Delta t = 4 \text{ fs}$  used for the analysis of bulk and mono-vacancies configurations). The other electronic parameters instead are equal to those reported in Tab. 6.5.

The total number of atomic environments generated and recalculated with high accuracy (see Sec. 6.6.6) to train GAP (from total energies and forces) is 2412. These are distributed as 55, 49, 43, 54 configurations, i.e. 660, 588, 516, 648 environments (assuming each atom counts as one surface environment - which is a strong approximation), from the (100), (110), (111) and (112) terminated surfaces.

**Future work DB4:** according to Ref. [169], in order for a more detailed description of nanocrystal equilibrium shapes obtained through Wulff construction, one might want to include in the training-set also information about (310) terminated surfaces which have a surface energy lower than the (111) case. Another important set of configurations that would be worth to include in the training process is given by simulation cells extended in the in-plane dimension in order to sample also surface vibrations, i.e. surface phonons. Finally a trivial extension of such database would consist in generating trajectories similar to the ones described above at different (contracted and expanded) volumes.

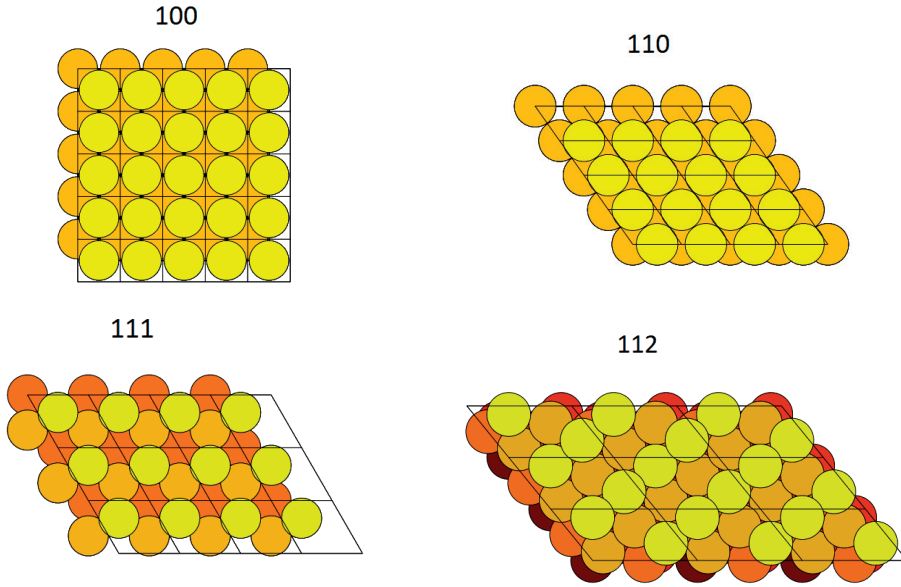


Figure 6.6: Top view of the geometry of the (100), (110), (111) and (112) terminated surfaces.

### 6.6.5 Gamma surfaces

The concept of generalized stacking faults, commonly known as  $\gamma$  surfaces, was introduced by Vitek in late 1960s on bcc metals [171].  $\gamma$  surfaces are two dimensional surfaces describing the energy change due to a displacement of two halves of a crystal with respect to each other across a shear plane (and relaxing the atoms normal to that plane). This energy surface spans the space of all the possible relative shear displacement vectors within a given crystallographic plane. However, since the displacements vector is periodic with the lattice, one obtains a two-dimensional energy surface bound by the lattice vectors of the bulk crystal.  $\gamma$  surfaces were originally introduced as a means of finding potential stacking faults in metals. This because local minima in the  $\gamma$  surface correspond to metastable stacking faults. This concept is somehow orthogonal to that of bulk terminated surfaces obtained by pulling two surfaces apart and provides a further assessment of the quality of the interatomic potentials. An accurate description of  $\gamma$  surfaces is also critical for the description of dislocation structures. The  $\gamma$  surface energy for a given displacement vector can then be calculated according to:

$$E_f^{\gamma surf} = \min_{\mathbf{x}_1^\perp, \dots, \mathbf{x}_N^\perp} (E^{\gamma surf}(N)) - E_0(N). \quad (6.32)$$

The two crystallographic surface orientations of interest are the (110), (112) since they are considered the most important planes to characterize plasticity in bcc crystals. bcc crystals have no truly close-packed planes; slip can occur in the direction of the shortest Burgers vector  $\langle 111 \rangle$  which contains the nearest neighbor atoms. Any plane containing a  $\langle 111 \rangle$  direction is a potential slip plane. In practice, however, heat is required to overcome the activation energy for slip to occur and such activation barrier usually correlates with how densely constituent



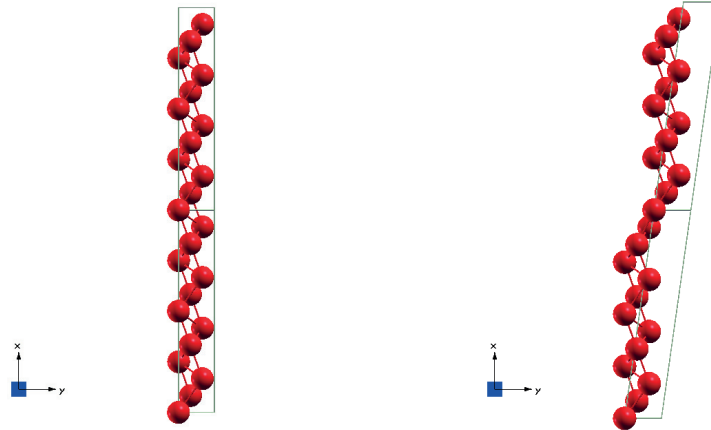


Figure 6.7: Two examples of supercells used in practical calculations for calculating (112)  $\gamma$  surface energies. In the left panel is displayed a perfect bcc structure with no displacement vector applied to the equilibrium cell vectors, i.e. no shear. In the right panel instead is displayed a supercell with a displacement vector corresponding to the 80% of the cell vector pointing in the  $\frac{1}{2}[11\bar{1}]$  applied to the cell vector normal to the surface. In both cases two supercells are stacked along the  $c$  axis to highlight the relative displacement of crystal atoms in adjacent cells.

atoms are packed within the slip plane. The most densely packed planes of the  $\langle 111 \rangle$  zone (those planes containing the  $\langle 111 \rangle$  vector) are the  $\{110\}$  planes with 12 possible slip systems in total. The second most densely packed slip planes are the  $\{112\}$  planes forming another 12 possible slip systems with activation energy usually close to those of the  $\{110\}$  planes. There are also further slip systems like the  $\langle 111 \rangle \{123\}$  and  $\langle 111 \rangle \{134\}$  that are however significantly less densely packed and consequently do not play an important role in the description of plasticity in bcc crystals.

The points of the  $\gamma$  surface are computed by adding the relative displacement vector to the lattice vector used to model the supercell perpendicular to the shear plane, i.e. the gamma surface itself. This effectively shears the simulation cell without shearing directly the atomic positions and one could visualize this as shearing the simulation cell and moving the atoms of adjacent cells so that there is just one gamma surface per cell. This is the most efficient method of computing an arbitrary point on the  $\gamma$  surface as the simulation size can be kept at minimum. As was for the case of terminated surfaces, the cell vector orthogonal to the surface has to be long enough to ensure the two interfaces in the supercell are not interacting. Two examples associated to the two crystallographic orientation of interest are reported in Fig. 6.7.

The sampling of the  $\gamma$  surfaces is obtained again through BO AIMD performed with a 12 atoms (12 layers) simulation cell, in a NVE ensemble with average temperature 300 K and in-plane bulk electronic equilibrium lattice parameter for the (110), (112) orientations. We compute a trajectory per cell deformation, i.e. per displacement vector in steps of 10% of the in-plane cell vectors to span the entire  $\gamma$  surface, for at least 10 ps and starting from atomic positions

## Chapter 6. Gaussian approximation potentials (GAP)

---

relaxed in the out-of-plane direction. The electronic and ionic parameters are reported in Tabs. 6.8, 6.9.

$N_{atoms}$	12
$k$ -points	$4 \times 4 \times 1$
ecutwfc (Ry)	64 (480)
smearing (Ry)	0.01 Marzari-Vanderbilt
$\beta_{mix}$ (Ry)	0.05
conv_thr (Ry)	1-e7

Table 6.8: Parameters of the electronic calculation for sampling of  $\gamma$  surfaces.

$\Delta t$ (fs)	2
ensemble	NVE

Table 6.9: Parameters of the ionic calculation for sampling of  $\gamma$  surfaces.

The total number of atomic environments generated and recalculated with high accuracy (see details in Sec. 6.6.6) to train GAP (from total energies and forces) is estimated around 48000. These are distributed as 2000, 2000 configurations, i.e., 24000, 24000 environments (assuming each atom counts as one surface environment - which is a strong approximation), from the (110) and (112) terminated surfaces.

**Future work DB5:** expanded and contracted lattice vectors, other crystallographic orientations should be considered.

### 6.6.6 Convergence of first-principles calculations for GAP database

In order to generate reliable and accurate databases of total energies, forces and stresses from DFT we use the PWSCF package of the QUANTUM-ESPRESSO distribution [172]. The calculations for  $\alpha$ -iron are spin-polarized and the magnetic moment is free to vary collinearly in order to minimize the total energy. In all calculations the exchange-correlation effects have been treated within the generalized-gradient approximation (GGA) with the PBE functional [98]. We use an ultrasoft pseudopotential [102] (USPP) from *pslibrary.0.3.0*<sup>2</sup> [112], which includes also 3s and 3p semicore states<sup>3</sup> (i.e. 16 valence electrons). The pseudopotential has been chosen among different candidates from the *pslibrary*<sup>4</sup> and *GBRV* library<sup>5</sup> to reproduce, as closely as possible, the all-electron FLAPW equilibrium lattice parameter, bulk modulus at 0 K and local magnetization obtained with different all-electron codes [173, 174] and from independent groups (see Ref. [45]). The results are also compared against those obtained using the VASP code and associated pseudopotentials [175].

---

<sup>2</sup>For iron, this is identical to 0.2.1

<sup>3</sup>This pseudopotential is uniquely labeled as Fe.pbe-spn-rrkjus-ps1.0.2.1.UPF

<sup>4</sup><http://www.qe-forge.org/gf/project/pslibrary>

<sup>5</sup><http://www.physics.rutgers.edu/gbrv/>

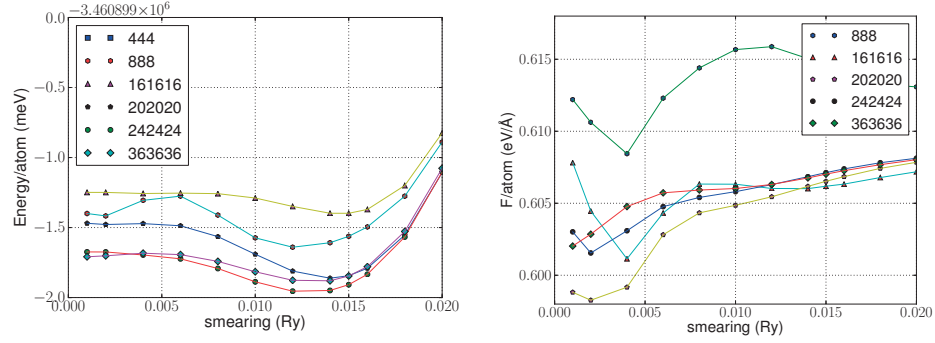


Figure 6.8: Total energy (per atom) and force of bcc ferromagnetic iron of the bcc geometry deformed as in Fig. 6.9 as a function of the Marzari-Vanderbilt smearing value and of the offset Monkhorst-Pack  $k$ -mesh. The kinetic-energy cutoff (dual of 12 for the charge density) is fixed to 90 Ry.

As summarized in Figs. 6.8, 6.10, 6.9, a careful investigation of the input parameters suggests to use a plane-wave basis with two different wavefunction and charge density kinetic-energy cutoffs of 90/1080 Ry and 144/1728 Ry to converge energy differences/forces and stresses to 1 meV/0.01 eV/Å and 0.1 GPa respectively. The BZ is sampled by means of an offset Monkhorst-Pack  $k$ -mesh with an average  $k$ -point spacing for the reference reciprocal vectors of  $\approx 0.032$  ( $2\pi\text{Å}^{-1}$ ) (see Tab. 6.10 for details), using a Marzari-Vanderbilt smearing [109] of 0.01 Ry.

	mesh	$\delta b_1$	$\delta b_2$	$\delta b_3$	Notes
<b>DB_1.b</b>	$20 \times 20 \times 20$	0.0252	0.0252	0.0350	1 atom cells (mean eq/exp)
<b>DB_2.c</b>	$3 \times 3 \times 3$	0.0392	0.0392	0.0392	54 atoms (mean eq/exp)
	$2 \times 2 \times 2$	0.0441	0.0441	0.0441	128 atoms (mean eq/exp)
<b>DB_3.a</b>	$3 \times 3 \times 3$	0.0389	0.0389	0.0389	53 atoms (mean eq/exp)
	$2 \times 2 \times 2$	0.0441	0.0441	0.0441	127 atoms (mean eq/exp)
<b>DB_4.a</b>	$16 \times 16 \times 1$	0.0220	0.0220	0.0316	100 orientation
	$19 \times 22 \times 1$	0.0227	0.0226	0.0262	110 orientation
	$13 \times 13 \times 1$	0.0221	0.0221	0.0400	111 orientation
	$9 \times 14 \times 1$	0.0226	0.0230	0.0264	211 orientation
<b>DB_5.a</b>	$2 \times 10 \times 14$	0.0415	0.0249	0.0252	110 orientation
	$2 \times 14 \times 10$	0.0360	0.0291	0.0249	112 orientation
Average		$\delta b \approx 0.032$ ( $2\pi\text{Å}^{-1}$ )			

Table 6.10: Summary of the Monkhorst-Pack mesh and reciprocal space  $k$ -point spacing ( $\frac{|\mathbf{b}|}{N_k}$ ; in  $2\pi\text{Å}^{-1}$  units) for the different atomic configurations included in the different databases used to train the GAP potential.

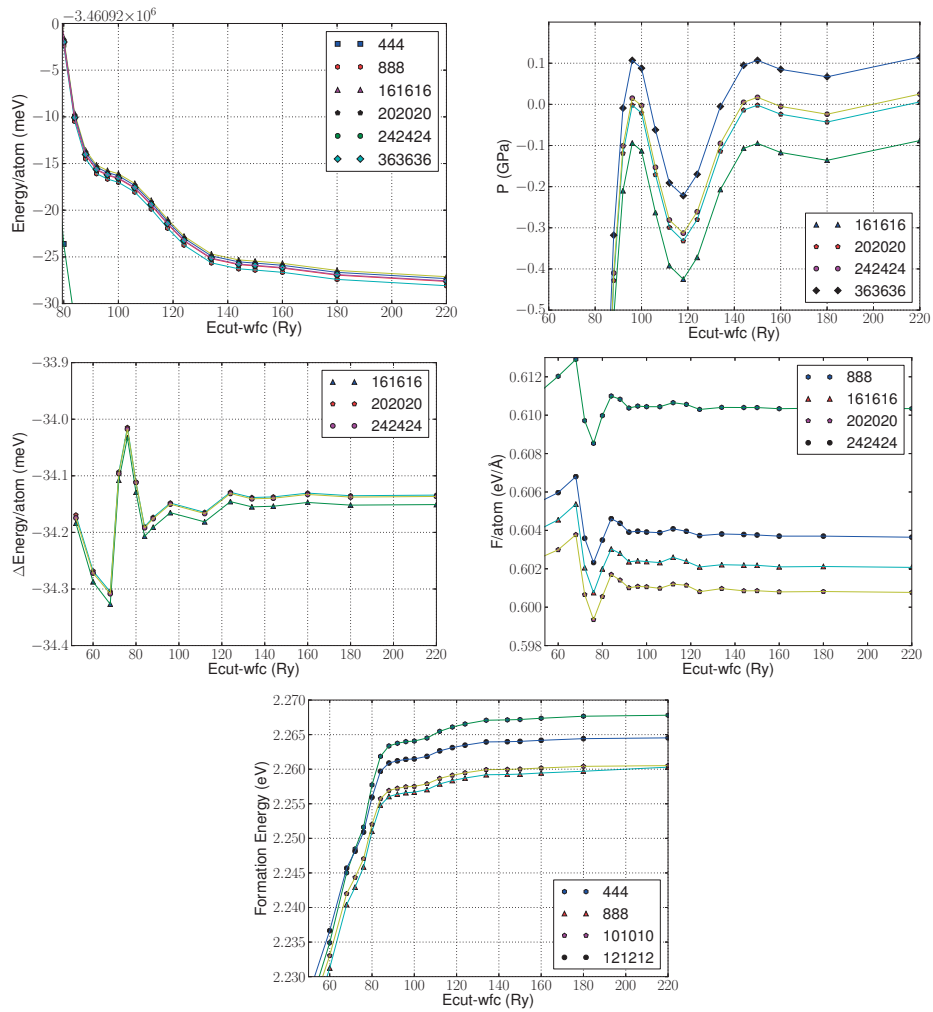


Figure 6.9: Total energy (per atom) and pressure of perfect bcc ferromagnetic iron and energy difference (per atom) between perfect bcc geometry and a deformed bcc geometry and mono-vacancy formation energy as a function of the kinetic-energy cutoff (dual of 12 for the charge density cutoff) and offset Monkhorst-Pack  $k$ -mesh. The smearing is Marzari-Vanderbilt with 0.1 Ry. The deformed geometry is obtained considering a cubic cell with two atoms and the central atom displaced by 5% along the 111 direction towards the atom at the origin. The vacancy formation energy is calculated using a defective  $2 \times 2 \times 2$  cubic supercell with 15 atoms.

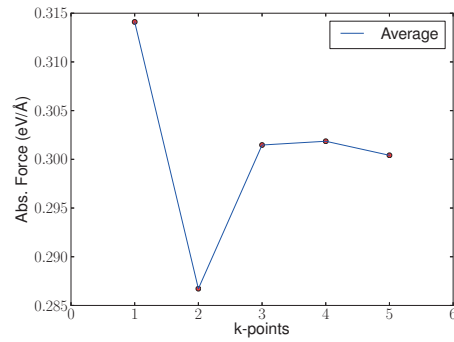


Figure 6.10: Absolute average force of a cubic supercell with 54 atoms having randomly distorted positions around a reference bcc structure as a function on the offset Monkhorst-Pack  $k$ -mesh. The kinetic-energy cutoff (dual of 12 for the charge density) is fixed to 90 Ry and the smearing to 0.01 Ry. The results show that the average absolute force is converged within the assumed tolerance of 0.01 eV/Å for meshes  $\geq 3$ .

## Chapter 6. Gaussian approximation potentials (GAP)

<b>DB_1.b</b> <i>Elastic constants</i> 4000 environments	→ MC sampling in the lattice space MC temperature=300 K Lattice1: +0.36/0.17% wrt $a_0^{el}/a_0^{zpe}$ Lattice2: +1.17/0.98% wrt $a_0^{el}/a_0^{zpe}$ [DB_1.b] • slice sampling algorithm • primitive unit cell • training from energies(low_cutoff) and stresses(high_cutoff)
<b>DB_2.c</b> <i>Phonon spectrum</i> 20538 environments	→ MD, no defects • 54 at. 333 simulation box MD temperature=400/600/1000/1400 K Lattice $a_0^{el}$ , $\pm 0.7\%$ $a_0^{el}$ (-0.88%, +0.51% $a_0^{zpe}$ ) Lattice +1.17% $a_0^{el}$ (+0.98% $a_0^{zpe}$ ) [MD sampling at lower volumes, DB_2.b] • 128 at. 444 simulation box [DB_2.c] MD temperature=800 K Lattice $a_0^{el}$ , $\pm 0.7\%$ $a_0^{el}$ , +1.17% $a_0^{el}$ ( $\pm 0.51\%$ , +0.98% $a_0^{zpe}$ ) • training from energies and forces
<b>DB_3.a</b> <i>Vacancies</i> 32346 environments	→ MD, mono-vacancy + di-vacancy MD temperature=400/600/1000 K • 53 at. 333 simulation box Lattice $a_0^{el}$ , $\pm 0.7\%$ $a_0^{el}$ (-0.88%, +0.51% $a_0^{zpe}$ ) • 127 at. 444 simulation box Lattice $a_0^{el}$ • 126 at. $3nn$ , 444 simulation box Lattice $a_0^{el}$ • training from energies and forces
<b>DB_4.a</b> <i>Surfaces</i> 2412 environments	→ MD, (100) (110) (111) (211) MD temperature=300 K • 12 at. simulation box In-plane Lattice $a_0^{el}$ • training from energies and forces
<b>DB_5.a</b> $\gamma$ <i>Surfaces</i> 75000 environments	→ MD, (110) (211) MD temperature=300 K Lattice $a_0^{el}$ , $\pm 1.0\%$ $a_0^{el}$ • 12 at. simulation box • training from energies and forces

Table 6.11: Summary of training database for *Fe* GAP. For each database, on the left column is reported the reference name with the physical properties that are intended to be trained along with the number of atomic environments included; on the right column are summarized the details of the atomic configurations including how they are obtained and which physical properties are actually used for the training.  $a_0^{el}$  and  $a_0^{zpe}$  stand for electronic and zero-point-energy equilibrium lattice parameter respectively. Nomenclature: DB\_X.x, X indicates the database type denoted by integer numbers, while x indicates the latest version of a database type X in Latin letters.

# 7 Thermodynamic and thermoelastic properties of $\alpha$ -iron

This chapter is dedicated to the results of this thesis that are mainly thermodynamic and thermoelastic properties of  $\alpha$ -iron. They are grouped in three different sections according to the model or framework (quantum, classical or GAP) from which they are obtained. I start from the data obtained with the well established EAM potentials, focusing on a selection of models that are available in the literature. I move then to the results from DFT that are used to provide accurate reference values to compare with and to verify the quality of classical potential models. I also comment on the verification of DFT results in terms of experimental data, when available. Finally, I present the data obtained with preliminary versions of Gaussian approximation potentials, analyzing their performances with respect to both the reference DFT and the EAM potentials.

## 7.1 EAM results

Empirical potentials have been extensively tested and used to study thermodynamic and mechanical properties of iron [176, 177] and its alloys [178, 179], including phase stability, structural martensitic transitions and a vast class of point- or extended defects such as mono-vacancies, interstitials, dislocations or tip-cracks with brittle to ductile transitions [34, 156, 180, 181] both at zero and finite temperature. It is known that extended defects come along with long range residual stresses that can directly influence structure and dynamics of the core-defect region [156, 157] and need to be described in large supercells containing thousands or ten thousands of atoms. It is evident therefore how potentials capable of reproducing accurate plastic, non-elastic and elastic properties are desirable to a reliable description of the mentioned materials properties. Also for this reason, 0 K elastic constants from experiments and ab initio have been explicitly included in the reference data-set of many of the potentials available in the literature on top of other standard 0 K quantities such as lattice parameter, cohesive energy, local defects formation energy. However, only a few works have been carried out to investigate the potential performances for such elastic properties at increasingly high temperature. Since we consider the analysis of thermoelasticity a stringent test for the validation of a potential, we decided to address a survey of the thermodynamic properties and of the

second order elastic constants as a function of temperature by means of classical molecular dynamics (MD) calculations.

In this work we focus our attention on the Mendeleev03 [91], Meyer98 [93], Ouyang12 [94] and Marchese87 [92] EAM potentials which have proven to be successful in the description of a wide range of crystal and defect properties (cohesive energy, 0 K elastic properties, mono-vacancy formation energy) in iron and its alloys. They differ in the details of the EAM functional form of the embedding, pair and effective charge density functions and, also, in the nature of the information included in the data-set used in the training procedure (experimental and first-principles information are used often altogether). It is worth to note, however, that all these potentials have been constructed by including information of the experimental elastic constant of bcc iron at at 0 K (see Tab. 7.1).

### 7.1.1 Thermodynamic results

We first compute the thermal expansion from MD simulations, extracting the volumetric/linear thermal expansion coefficient  $\alpha_V(T)/\alpha_L(T)$ . The results are displayed in Fig. 7.1 starting from 100 K. A simple polynomial extrapolation of the EAM equilibrium volumes at zero temperature, provides values in reasonable agreement with the experimental data (see also Tab. 7.1). Despite the expected zero temperature agreement, as visible from Fig. 7.1, the EAM potentials fail to reproduce the experimental thermal expansion. This is even more clearly evident from the expansion coefficient curves. In fact, both the Marchese87 and Ouyang12 potentials show a tiny to negligible nearly linear temperature dependence with absolute values well below the experimental ones above room temperature. The Meyer98 potential shows a monotonic decreasing coefficient in the whole range of temperature considered, which is in contrast, both quantitatively and qualitatively, with experimental observations. The Mendeleev03, on the other hand, is the only EAM potential that displays a qualitative reasonable behavior, replicating also the low temperature experimental trend. It is known however that such a peculiar trend is dominated by statistical quantum effects that are not present in MD. It is then clear that the Mendeleev03 is fitted to artificially reproduce it, most likely through a careful fitting procedure. Accounting for the proper quantum effects would then introduce corrections to the classical picture of Figs. 7.1 of the order of those due to the zero-point motion. These corrections however are expected to become important only well below the Debye temperature  $\Theta_D$  (experimental measure of  $\approx 500$  K) as the 0 K limit is approached. The neglect of quantum zero-point motion is also evident when comparing the calculated low temperature heat capacity at constant pressure  $C_P(T)$  to the experimental data. The specific heat results are reported in Fig. 7.2 and are obtained from the enthalpy of the system  $H$  according to the relation  $C_P(T) = \left. \frac{\partial H(T,P)}{\partial T} \right|_{P=0}$ . The classical MD calculations yields a value close to  $3R$  ( $24.94 \text{ J mol}^{-1} \text{ K}^{-1}$ ), according to the Dulong-Petit law (strictly speaking, the constant volume heat capacity  $C_V$  follows the Dulong-Petit law), while the experimental data below  $\Theta_D$  go to zero due to the Bose-Einstein distribution that governs the vibrational modes. Furthermore, the calculations deviate from experiments even at high-temperature



	Marchese87	Mendelev03	Meyer98	Ouyang12
$V$ ( $\text{\AA}^3$ )	11.777	11.639	11.797	11.774
$C_{11}$ (GPa)	–	243.4	251.0	233.0
$C'$ (GPa)	–	44.6	60.3	48.8
$C_{44}$ (GPa)	–	116.0	118.7	117.8

Table 7.1: 0 K equilibrium volumes and elastic constants as reported in the original works of the different potentials. The volume value of the Marchese87 potential instead is calculated in this work.

where a divergence is measured around the Curie temperature (1043 K). Such divergence is in fact due to the contribution of the magnetic degrees of freedom to the entropy of the system, and, to a lesser extent, to electronic excitations [69]. As such, since both degrees of freedom are neglected in our classical MD, any deviation from  $3R$  limit can than be ascribed, in first-approximation, to anharmonic contributions to the Helmholtz free energy.

### 7.1.2 Phonons and elastic constants

We then use the thermal expansion information to compute and survey the  $C_{11}$ ,  $C_{44}$  and  $C' = \frac{C_{11}-C_{12}}{2}$  elastic constants as a function of temperature. To this end, we calculate the phonon dispersion at different temperatures and corresponding equilibrium volumes using the method discussed in Sec. 2.4.3. This approach accounts for anharmonic contributions that are naturally present in MD; these are recast into a standard dynamical matrix whose eigenvalues depend explicitly on the temperature. On the other hand, as previously mentioned, quantum effects like zero-point motion and the freezing out of the normal modes at low temperature are neglected due to the classical MD approach. The phonons of the four potentials at 400 K are explicitly compared to room-temperature experimental data in Fig. 7.3, while the softening of the frequencies with the temperature is reported in Figs. 7.4. The results highlight different behaviors in terms of absolute frequency values and softening for the various potentials. Interestingly, the high-temperature (1200 K) Mendelev03 dispersion is closer than the room-temperature one to the reference experimental data.

The  $C_{11}$ ,  $C_{44}$ ,  $C'$  elastic constants are obtained from the sound velocities through the method described in Sec. 7.1.3, making use of eqs. (4.19,7.1), and are reported in Figs. 7.5, 7.6 from 200 K to 1200 K in steps of 200 K. For the sake of completeness, the  $C_{12}$  elastic constant and the bulk modulus  $B$  are also derived from standard relationship for cubic crystals and their values are reported in Figs. 7.7. The good agreement of the (linearly extrapolated) 0 K elastic constants with the experiments is expected, since all these potentials have been generated/fitted by taking into account explicitly some experimental elastic constant values<sup>1</sup>.

<sup>1</sup>Note that the different experimental dataset used for the fitting are responsible for the different zero-temperature values of the various potentials

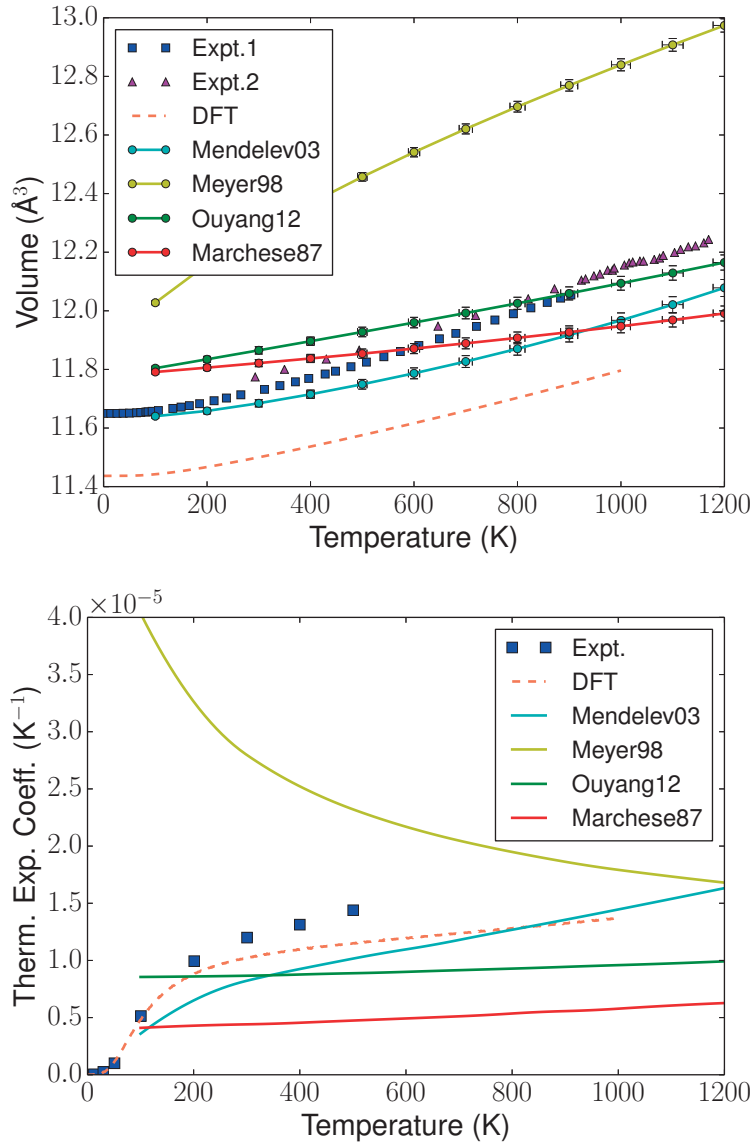


Figure 7.1: (Top panel) Linear thermal expansion in the range of experimental thermodynamic stability of  $\alpha$  and  $\beta$  phases of iron for each of the empirical potential considered in this work. The results are reported along with their standard deviations and compared to experimental data from Ref. [163] (Expt.1 – blue squares), Ref. [164] (Expt.2 – magenta triangles) and to quasi-harmonic ab initio data (dashed line) from Ref. [45] (see also Sec. 7.2.2). (Bottom panel) Linear thermal expansion coefficient  $\alpha_L(T)$  as before in the range of experimental thermodynamic stability of  $\alpha$  and  $\beta$  phases of iron and for each of empirical potential. These results are obtained as numerical derivatives of a cubic spline of the data in the Top panel and are compared to experimental data from Ref. [182] (Expt. – blue squares) and to quasi-harmonic ab initio data (dashed line) from Ref. [45] (see also Sec. 7.2.2).

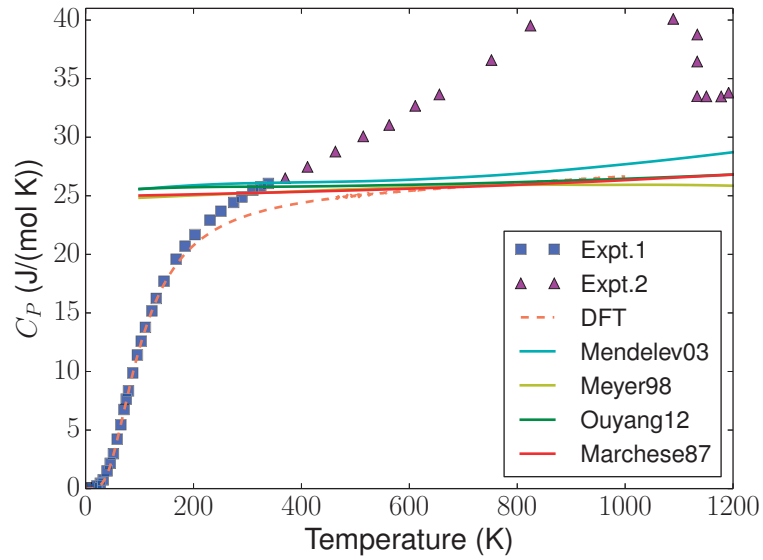


Figure 7.2: Heat capacity at constant pressure as a function of temperature. These results are obtained as numerical derivatives of a cubic spline of the Enthalpy data and are compared to experimental data from Ref. [183] (Expt.1 – blue squares), from Ref. [184] (Expt.2 – magenta triangles) and to quasi-harmonic ab initio data (dashed line) from Ref. [45] (see also Sec. 7.2.2).

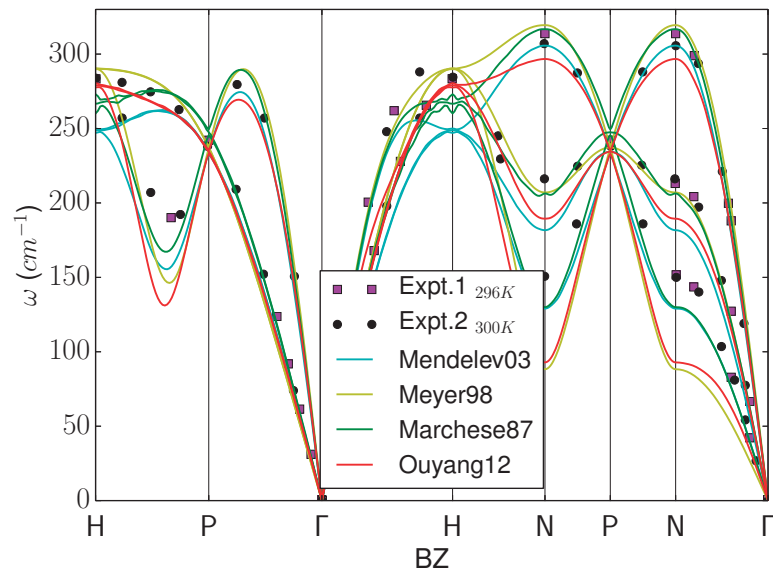


Figure 7.3: Solid lines are the phonon dispersions of the empirical potentials at 400 K. The results are compared to Experiments at 296 K (Expt.1 – squares) from Ref. [185] and at 300 K (Expt.2 – circles) from Ref. [186].

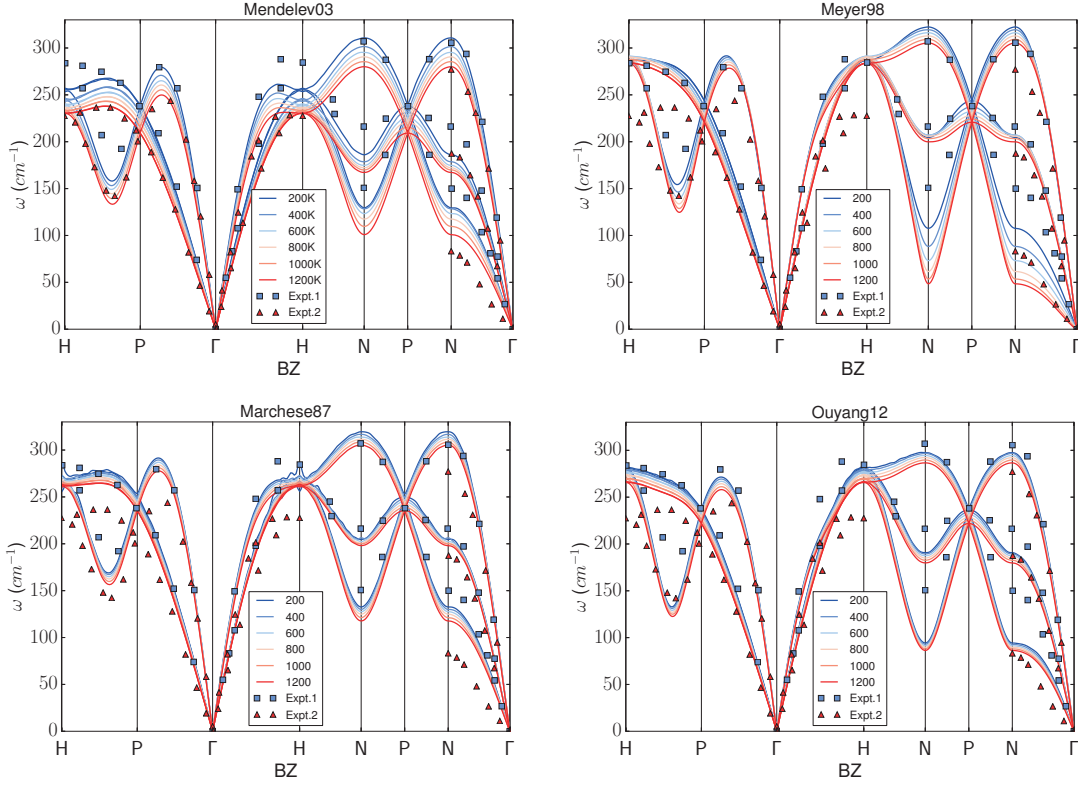


Figure 7.4: Phonon dispersions in the first BZ as a function of temperature for the four EAM potentials considered in this work. The temperature increase in steps of 200 K from 200 K (azure lines) to 1200 K (red lines), spanning the experimental range of stability of the  $\alpha$  and  $\beta$  phases of iron. The calculations are compared with experimental results from Ref. Brockhouse measured at 300 K (Expt.1 – squares) and Ref. Fultz measured at 1158 K (Expt.2 – triangles).

On the other hand, the results show an overall deteriorating ability of the selected potentials in reproducing the experimental data upon increasing the temperature. In the high temperature regime, far from the region in which have been trained, large differences among the potentials themselves and large deviations with respect to experiments arise. On average, the  $C_{11}$ ,  $C'$  and  $B$  curves display the largest deviations from experiments, while better performances are obtained (on average) in reproducing the nearly linear  $C_{44}$  temperature dependence. Interestingly, the  $C_{44}$  elastic constant of the Mendeleev03 displays a rapid unexpected softening with absolute values that are 18% lower than the experiments already at 200 K. A peculiar case is the Meyer98 that shows an unexpected marked stiffening of the  $C_{12}$  and  $B$  accompanied by a  $C'$  that softens rapidly at low  $T$  with a positive curvature. This softening of the shear modulus  $C'$  of the Meyer98 potential suggests a vanishing restoring force for atomic displacements along the  $[1\bar{1}0]$  direction associated to the long wavelength  $T_2[110]$  normal mode, and a consequent possible mechanical/structural instability of the bcc structure towards an fcc through the Bain path transformation [72]. Noticeably, as discussed in Ref. [176], the Meyer98 is one of the few potentials that allows for a thermodynamic stabilization of the fcc phase with

respect to the bcc one upon increasing temperature. In particular the Meyer98 free energy of the fcc phase is lower than the one of the bcc phase already at 600 K and the softening of the  $C'$  can be considered a precursor mechanism for the bcc/fcc transformation.

In the literature, it has been proposed that the high-temperature non-linear behavior of some of the elastic constants of iron is inherently related to magnetic excitations [45, 187–189]. The inability of all these potentials to reproduce such non-linear behavior suggests that fitting an empirical potential solely on experimental data or a mix of experimental and ab initio data which neglect magnetic order/disorder, is not sufficient to describe the magnetic effects on iron properties. This is somehow expected and reassuring, since the standard EAM model does not include any term treating magnetism explicitly. Some of these information can be implicitly included fitting experimental results, but an explicit treatment of the magnetic degrees of freedom remains fundamental, as it is clear from the analysis of the heat capacity behavior [69]. The explicit inclusion of magnetic terms can be achieved through the use of Ising, Heisenberg and generalized Alexander-Anderson [190] model or using generalized magnetic EAM [191], as well as through the use of molecular- coupled to spin-dynamics [192].

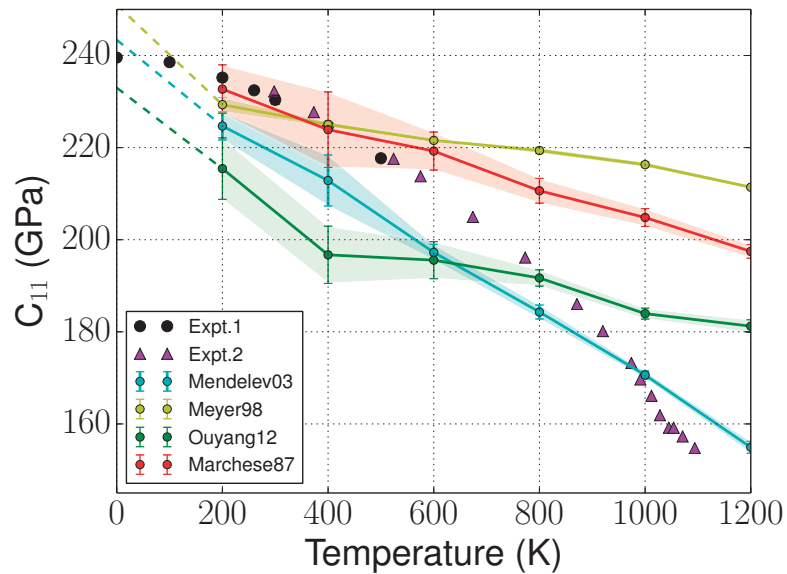


Figure 7.5: thermal dependence of the  $C_{11}$  for different potentials. The experimental results from Ref. [162] (Expt.1 – black circles) and Ref. [189] (Expt.2 – magenta triangles) are included as a reference to compare with. Shaded areas provide a confidence interval connecting the error bars on the elastic constants calculated at discrete values of temperatures. The dashed lines are guides to the eye that connect our curves with the 0 K values reported in the reference works of the different potentials (where available) and collected in Tab. 7.1.

Finally, note that experimental data for the elastic constants are obtained from ultrasonic measurements [162, 189] and are intrinsically adiabatic. However, as discussed in Sec. 4.4, we compute the elastic constant curves from phonon sound velocities, where any distinction between isothermal and adiabatic constants is lost. This is in fact a mechanical approximation to

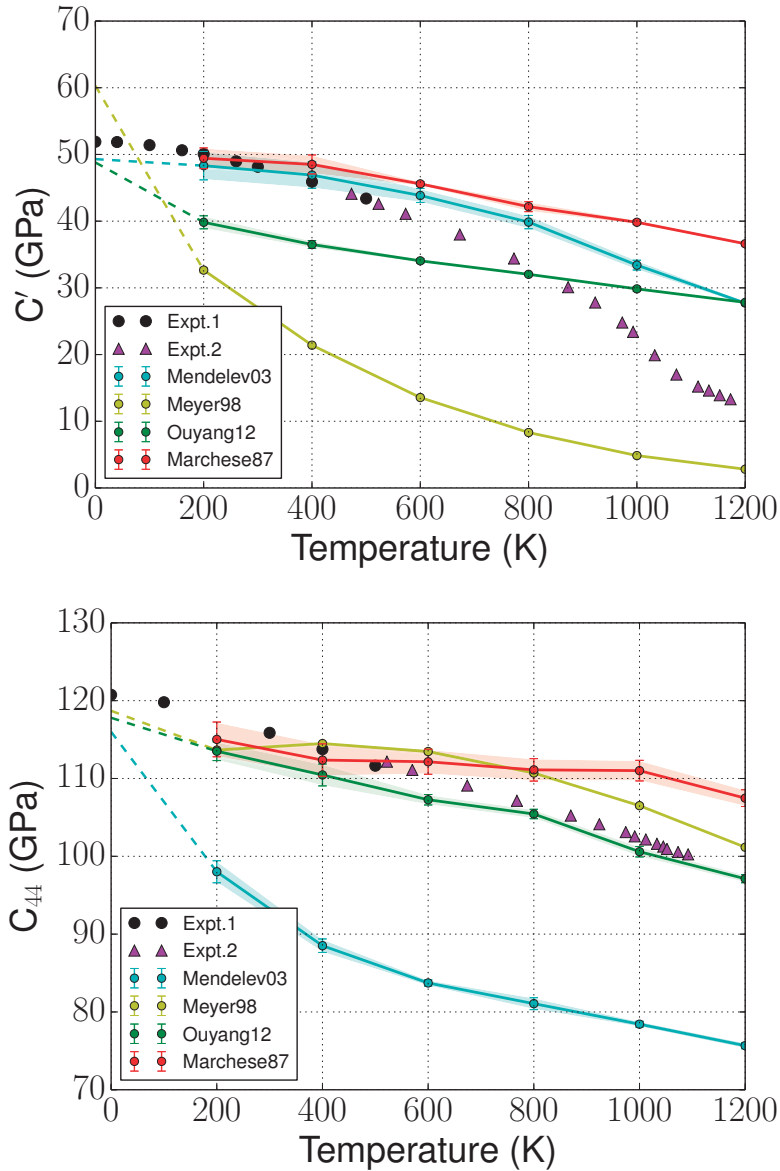


Figure 7.6: (Top panel) Temperature dependence for different potentials of the  $C'$  elastic constant. (Bottom panel) Temperature dependence for different potentials of the  $C_{44}$  elastic constant. The results are compared to ultrasonic experimental values from Ref. [162] (Expt.1 – black circles) and Ref. [189] (Expt.2 – magenta triangles). Shaded areas and dashed lines as in Fig. 7.5.

the thermodynamic elastic constants. We test the validity of this approximation by calculating the isothermal bulk modulus with a standard method used in the literature (see for instance Refs. [193]) based on the computation of the virial stress [194]. The spatial- and time-averaged virial stress is here considered equivalent of the Cauchy defined in eqs. (4.11,4.12). The validity of this statement is debated in Refs. [195] and [196]. for finite cell deformations, and then

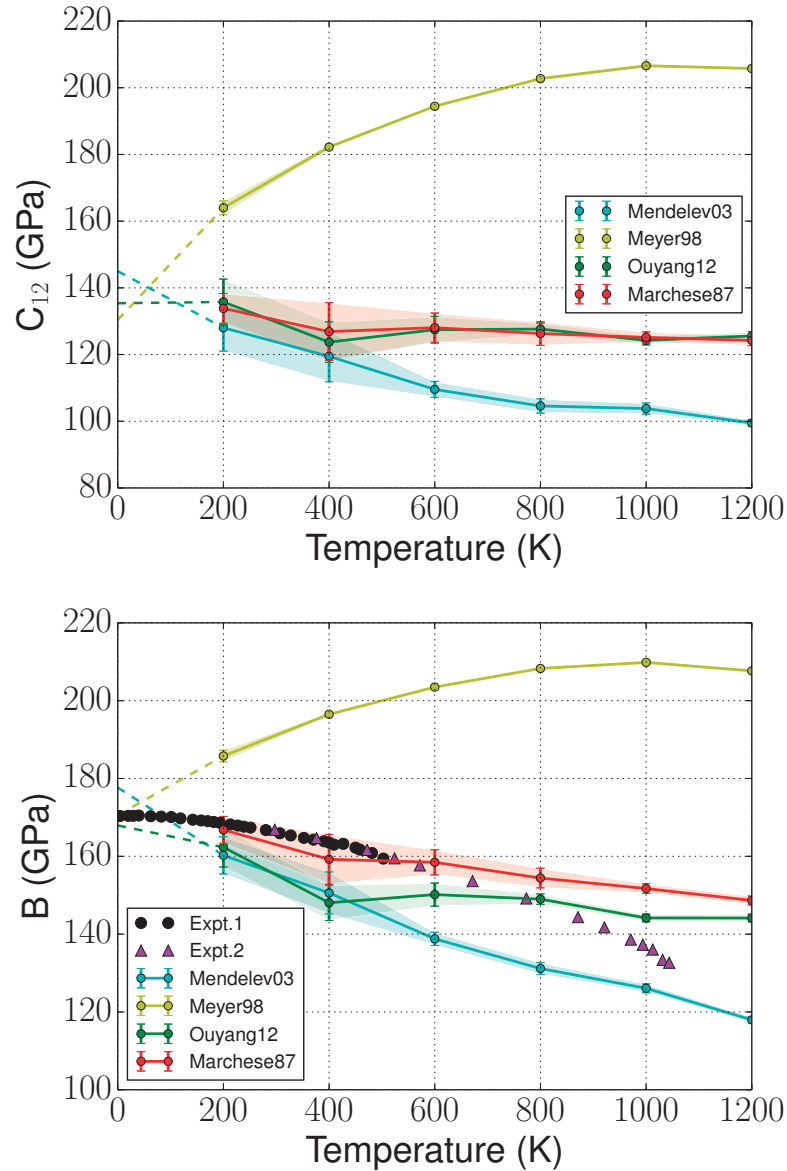


Figure 7.7: Temperature dependence of the  $C_{12}$  (top panel) elastic constant and bulk modulus  $B$  (bottom panel) for different potentials. The results are obtained as a linear combination of those in Figs. 7.5, 7.6 according to the standard relations for cubic crystals. The experimental values from Ref. [162] (Expt.1 – black circles) and Ref. [189] (Expt.2 – magenta triangles) are included only as a reference.

recovering the adiabatic counterpart from usual thermodynamic relations. The results are shown in Fig. 7.8 and validate this approximation for all potentials except for the Meyer98 case, due to an unexpected large difference between isothermal and adiabatic constants. This difference is motivated by the peculiar and unphysical thermal expansion behavior of the potential itself.

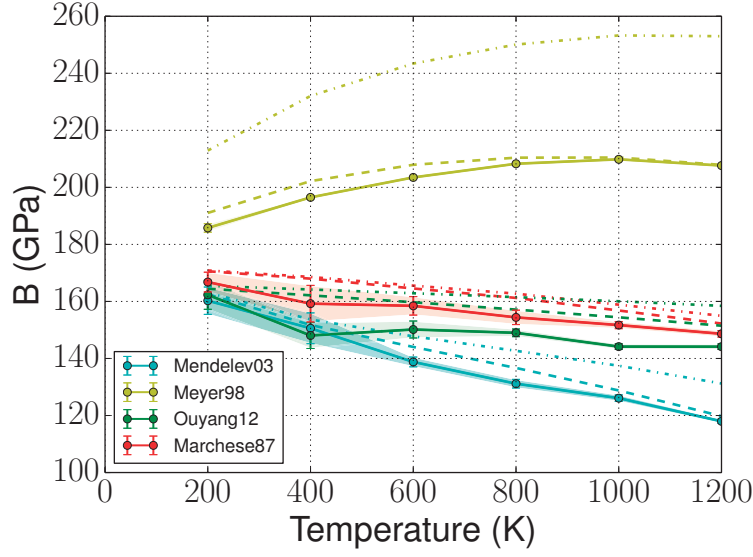


Figure 7.8: Temperature dependence of the bulk modulus  $B$  obtained from the slope of the phonons in  $\Gamma$  compared to the isothermal bulk modulus  $B^{(T)}$  as obtained from the variation of the virial hydrostatic pressure with respect to finite deformations (dashed lines). The results for the four EAM potentials considered show similar temperature trends, while the absolute values of the curves deviate at most of 10 GPa.

### 7.1.3 Computational details

All the results reported in the previous section have been obtained from classical MD runs. The equilibrium volumes are obtained performing a set of constant pressure and temperature (NPT) runs at vanishing external pressure and in the temperature range of stability of  $\alpha$  (0  $\rightarrow$  1043 K) and  $\beta$  (1043  $\rightarrow$  1185 K) phases of iron from 100 to 1200 K with increments of 100 K. The pressure is controlled through a Parrinello-Rahman barostat [197] while a Nose-Hoover chain thermostat [198] is used to keep constant the average temperature as implemented in the LAMMPS [199] package. Each MD run is initialized from a bcc supercell with slightly randomized atomic positions, and with initial velocities from the Maxwell-Boltzmann distribution. During MD simulations, the time-step is fixed at 1 fs, and the relaxation times of the barostat and thermostats are set to be 1 ps and 0.1 ps, respectively. Each simulation is carried out for 10 million steps, equivalent to 10 ns. The first 0.5 ns are used for thermalization and equilibration of the system, while the remaining 9.5 ns are used for accumulating the thermodynamics averages. The system consists of 2000 atoms in a  $10 \times 10 \times 10$  cubic supercell with periodic boundary conditions (PBCs). The simulation length and size are chosen to ensure the convergence of all the average values and standard deviations of the relevant thermodynamic quantities. The volumetric and linear coefficients of thermal expansion are obtained from the temperature derivative of the average equilibrium volumes calculated from the MD runs according to eq. 5.12. Since we have equilibrium volumes only at discrete points, we first compute a cubic spline interpolation of the calculated data, and then get numerical



derivatives of the spline function. Similarly, the specific heat is obtained as a temperature derivative of a cubic spline interpolation of the average enthalpy  $H$  calculated from the MD runs.

The calculation of the phonon dispersion is performed using the constant volume-temperature (NVT) ensemble from 200 K to 1200 K with increments of 200 K. The supercell volumes are adjusted to match those obtained by the thermal expansion curves calculated previously. The temperature was controlled by the Nose-Hoover chain technique, described in the previous paragraphs. In order to access directly the phonon dispersion in the bcc first BZ, we replace here the cubic supercell used above with a  $N \times N \times N$  repetition of a primitive bcc cell. The eigenvalues of the dynamical matrix are computed at  $\mathbf{q} = (\frac{k_1}{N_1} \mathbf{b}_1, \frac{k_2}{N_2} \mathbf{b}_2, \frac{k_3}{N_3} \mathbf{b}_3)$  commensurate with the supercell size, where  $N_i$  is the multiplicity of the primitive reciprocal space vector  $\mathbf{b}_i$ ,  $k_i = 0, \dots, N_i - 1$ . The acoustic sum rules are used to enforce the condition of zero frequency in  $\Gamma$  as required by crystal translational symmetry. The choices of the supercell size, i.e. the  $N$  value, as well as the simulation length are crucial to a good convergence of the phonon frequencies especially around  $\Gamma$  and, as such, need to be discussed. We start fixing the size of our simulation box (we use  $8 \times 8 \times 8$  supercell as a reasonable size to start with) and, after equilibration, we block-average the phonon dispersion and we check the time convergence of the phase velocities  $\omega_L(q_N^{[100]})/q_N^{[100]}$ ,  $\omega_{T_1}(q_N^{[100]})/q_N^{[100]}$ ,  $\omega_{T_2}(q_N^{[110]})/q_N^{[110]}$ , where  $q_N^{[100]}$ ,  $q_N^{[110]}$  are the moduli of the vectors  $\mathbf{q}_N^{[100]} = \frac{(-\mathbf{b}_1 + \mathbf{b}_2 + \mathbf{b}_3)}{N}$ ,  $\mathbf{q}_N^{[110]} = \frac{\mathbf{b}_3}{N}$  associated to the maximum wavelength allowed for the considered supercell in the selected direction. From the analysis of the data, we observed that the autocorrelation time of the calculated phase velocities is long and a simulation time of 100 ns would be necessary to reduce the phase-velocities standard deviation to a few GPa (more critical at low temperature). In order to deal with statistically meaningful quantities and to decrease further their uncertainty, instead of extending our simulations in time, we decide to average all our phase velocities values over seven parallel independent runs (each of them performed at the same conditions but different initial random seed). Next, we consider the supercell size effects. We perform different runs with  $N \times N \times N$  supercells with  $N$  ranging from 4 to 20 in steps of 4. The increase of  $N$  actually corresponds to an improved sampling of the phonon spectrum in the first BZ, so that the  $\mathbf{q}_N$  points associated to the maximum wavelength defined above get closer and closer to  $\Gamma$  and their phase velocity also converge to the group velocity in  $\Gamma$  i.e., the speed of sound, as  $N \rightarrow \infty$ . An example of the convergence of the phase velocity to the speed of sound with respect to  $N$  along the [100] and [110] is displayed in Figs. 7.9.

Since the acoustic phonon branches can be described as a superposition of sines of the wavevector, for large  $N$  (i.e. small  $q_N$ ) they can be expanded in series as:

$$\begin{aligned} \omega(q_N) &\propto q_N - \frac{q_N^3}{3!} + \frac{q_N^5}{5!} + O(q_N^7), \\ &\propto \frac{1}{N} \left[ 1 - \frac{a_1}{N^2} + \frac{a_2}{N^4} \right] + O\left(\frac{1}{N^7}\right). \end{aligned} \quad (7.1)$$

Combining this equation and the definition given above, we find that the phase velocities

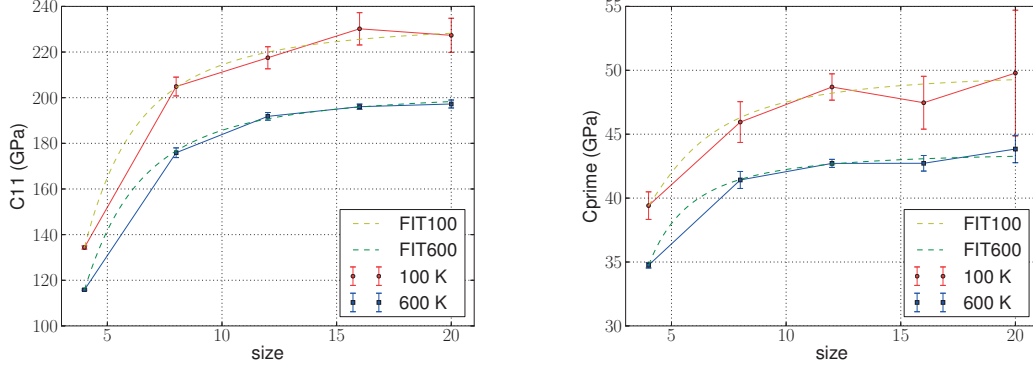


Figure 7.9: Convergence of the Mendeleev03  $C_{11}$ ,  $C'$  with respect to size  $N$  of the supercell at 100 K and 600 K respectively. As discussed in the text, the data are fitted through a function of the form  $A_1 + A_2/N^2 + A_3/N^4$  in order to extrapolate the  $N \rightarrow +\infty$  limit.

obtained by this method converge, in terms of the supercell size  $N$ , as  $A_1 + A_2/N^2 + A_3/N^4$  to the proper sound velocities. This function can then be used to fit the phase velocities calculated at finite sizes to extrapolate the  $N \rightarrow \infty$  limit and to get a clear estimation of the finite size error made on the elastic constants. In our case, as reported in Figs. 7.9, this approach suggests that a  $20 \times 20 \times 20$  supercell can provide phase velocities and, consequently, elastic constants well converged within the uncertainty due to the finite time simulation used in the MD runs.

## 7.2 DFT results

### 7.2.1 Thermodynamics and thermoelasticity

In order to compute finite-temperature properties from DFT we decided to get access to the Helmholtz free energy  $F$ . As discussed in Sec. 5.1 the most important contribution to  $F$  beyond the static energy term is due to the thermally excited vibrations. The QHA [145] provides an analytical expression to account for this term:

$$F(\{\mathbf{a}_i\}, T) = \underbrace{E_{stat}(\{\mathbf{a}_i\})}_{\text{Static}} + \underbrace{\frac{1}{2} \sum_{\mathbf{q}, \lambda} \hbar \omega_{\mathbf{q}, \lambda}(\{\mathbf{a}_i\})}_{\text{ZPE}} + \underbrace{k_B T \sum_{\mathbf{q}, \lambda} \ln \left( 1 - e^{-\frac{\hbar \omega_{\mathbf{q}, \lambda}(\{\mathbf{a}_i\})}{k_B T}} \right)}_{\text{Thermal}}, \quad (7.2)$$

where the sum is performed over all the phonon modes  $\lambda$  and all the phonon wave vectors  $\mathbf{q}$  spanning the Brillouin zone (BZ) and the free energy explicit depends on the geometry of the system via the primitive lattice vectors  $\{\mathbf{a}_i\}$ . The vibrational part, coming directly from the analytic partition function of a Bose-Einstein gas of harmonic oscillators, is split into a zero-point energy term plus a contribution which depends explicitly on the temperature  $T$ . The knowledge of the analytical expression for the free energy and for its partial derivatives

with respect to temperature or to the cell degrees freedom, provides the relevant equilibrium thermodynamic quantities characterizing a material.

Assuming a quasi-harmonic approximation, the thermal electronic effects are completely neglected. We will show later on (see also Refs. [83, 200]) they are small compared to the quasi-harmonic ones in the range of stability of the  $\alpha$  phase. Magnetic effects instead are partially considered, accounting for the longitudinal relaxation of the total magnetic moment as a function of strain on the vibrational properties. It is however known the transverse degrees of freedom of the magnetic moments are increasingly important approaching the Curie point [67, 72, 201]; as such their influence on the elastic properties will be also briefly discussed.

For cubic crystals, like  $\alpha$ -iron, only three elastic constants are needed to completely determine the stiffness tensor and, therefore, fully characterize the mechanical response of the system in the linear elastic regime. As a consequence, if one calculates the elastic constants from small finite cell deformations, only three independent types of deformations are sufficient. In this work we choose the hydrostatic, tetragonal and trigonal deformations (the associated strain matrices are shown in Tab. 7.2) since they uniquely determines the bulk modulus  $B$  and the elastic constants  $C_{11}$ ,  $C_{44}$  respectively. Eq. 4.9 is then used to calculate the isothermal elastic constants at finite temperature. However, in order to compare results with experimental data obtained from resonant ultrasonic spectroscopy [189], we calculate the adiabatic elastic constants, using relation 5.16 by means of the heat capacity at constant volume  $C_V$ , the volumetric thermal expansion coefficient  $\alpha$  and of the isothermal bulk modulus  $B$  calculated from the quasi-harmonic Helmholtz free energy.

$\boldsymbol{\varepsilon}^{(i)}$	$\varepsilon_1$	$\varepsilon_2$	$\varepsilon_3$	$\varepsilon_4$	$\varepsilon_5$	$\varepsilon_6$
$\boldsymbol{\varepsilon}^{(1)}$	$\varepsilon_a$	$\varepsilon_a$	$\varepsilon_a$	0	0	0
$\boldsymbol{\varepsilon}^{(2)}$	0	0	$\varepsilon_c$	0	0	0
$\boldsymbol{\varepsilon}^{(3)*}$	0	0	0	$\varepsilon_d/2$	$\varepsilon_d/2$	$\varepsilon_d/2$

Table 7.2: Deformations and corresponding strain vectors in Voigt notation: <sup>(1)</sup>hydrostatic, <sup>(2)</sup>tetragonal and <sup>(3)</sup>trigonal deformations are governed by a single parameter, namely the magnitude of the deformation. \*Note that the trigonal deformation reported here is the first-order expansion of the full strain tensor  $\boldsymbol{\varepsilon}^{(3)}$  (see eq. (B.1) in the Appendix).

### 7.2.2 Volumetric strain

The volumetric deformation can be described by a strain matrix  $\boldsymbol{\varepsilon}^{(1)}$  with a single parameter  $\varepsilon_a$  (see Tab. 7.2). If we apply such strain matrix to the cell vectors of a cubic crystal with a reference lattice parameter, any strained lattice can be obtained as:

$$a = a_0(1 + \varepsilon_a) \tag{7.3}$$

where we chose  $a_0$  as the theoretical equilibrium lattice parameter without zero-point contribution calculated in this work (see Tab. 7.4 and Sec. 7.2.6 for a discussion about its dependence on the pseudopotential).

Assuming such a strain deformation the QHA Helmholtz free energy is a function of  $T$  and  $\varepsilon_a$  only, and is shown in Fig. 7.11. Its static part is then obtained by fitting a Birch-Murnaghan equation of state [202] to a series of well converged total energy values calculated on a one dimensional regular grid with  $\varepsilon_a$  going from  $-0.02$  to  $+0.03$  in steps of  $0.001$ . The resulting static contribution to the bulk modulus is reported in Tab. 7.4. The vibrational contribution, on the other hand, has been calculated on a coarser grid via integration of the phonon dispersions as from Eq. 7.2.1 (examples for the calculated phonon dispersion and resulting Grüneisen parameters can be found in Fig. 7.10), with  $\varepsilon_a$  ranging from  $-0.012$  to  $+0.020$  in increments of  $0.004$  and fitted at each  $T$  with a second-order polynomial as a function of the strain parameter  $\varepsilon_a$ . The stability of the results has been checked against lower and higher order fitting polynomials (see Supplemental Material B). From the calculated free energy we determine the volumetric thermal expansion  $V(T)$  (Fig. 7.11), the linear thermal expansion coefficient  $\alpha(T) = \beta(T)/3$  (see eq. 5.12 for the definition of the volumetric thermal expansion coefficient and Fig. 7.12), the heat capacity (see eq.( 5.8, 5.11) for the definitions and Fig. 7.12) and the isothermal bulk modulus  $B^{(T)}(T)$  from the analytic second derivative of the free energy as in Eq. 4.9. The adiabatic correction of Eq. 5.14 is used to compute the adiabatic bulk modulus  $B^{(S)}(T)$ . Results are reported in Fig. 7.13 and compared to experimental data from Refs. [162, 189]. The agreement between experiments and calculations in the thermal behavior of the bulk modulus is remarkable, especially below the Debye temperature ( $\Theta_D \simeq 500$  K). Above  $\Theta_D$ , the relatively small deviation from experiments can be ascribed to magnetic contributions [187–189, 201] that become increasingly important approaching the Curie temperature (1043 K), plus contributions from anharmonic (beyond quasi-harmonic) effects and electronic entropy. At 1000 K, the softening of the calculated  $B^{(S)}$  with respect to the 0 K value is nearly 15% even neglecting the effects due to the transverse magnetic fluctuations. The mismatch in the absolute values of the experiments and calculations is due to the XC functional and to the specific pseudopotential chosen for this work, and is largely discussed in Sec. 7.2.6.

### 7.2.3 Tetragonal and trigonal strains – $C_{11}, C_{44}$

In this case the Helmholtz free energy depends upon two strain parameters: the isotropic lattice strain  $\varepsilon_a$  and a second strain parameter  $\varepsilon_c$  or  $\varepsilon_d$  according to the deformation considered (see Tab. 7.2).

The tensor  $\boldsymbol{\varepsilon}^{(2)}$  is associated to a continuous tetragonal deformation that stretches the edge  $c$  of the cubic undistorted structure along the  $z$  axis while leaving unchanged the other edges. The relation between the strain  $\varepsilon_c$  and the distorted edge  $c$  is:

$$c = a(1 + \varepsilon_c). \quad (7.4)$$

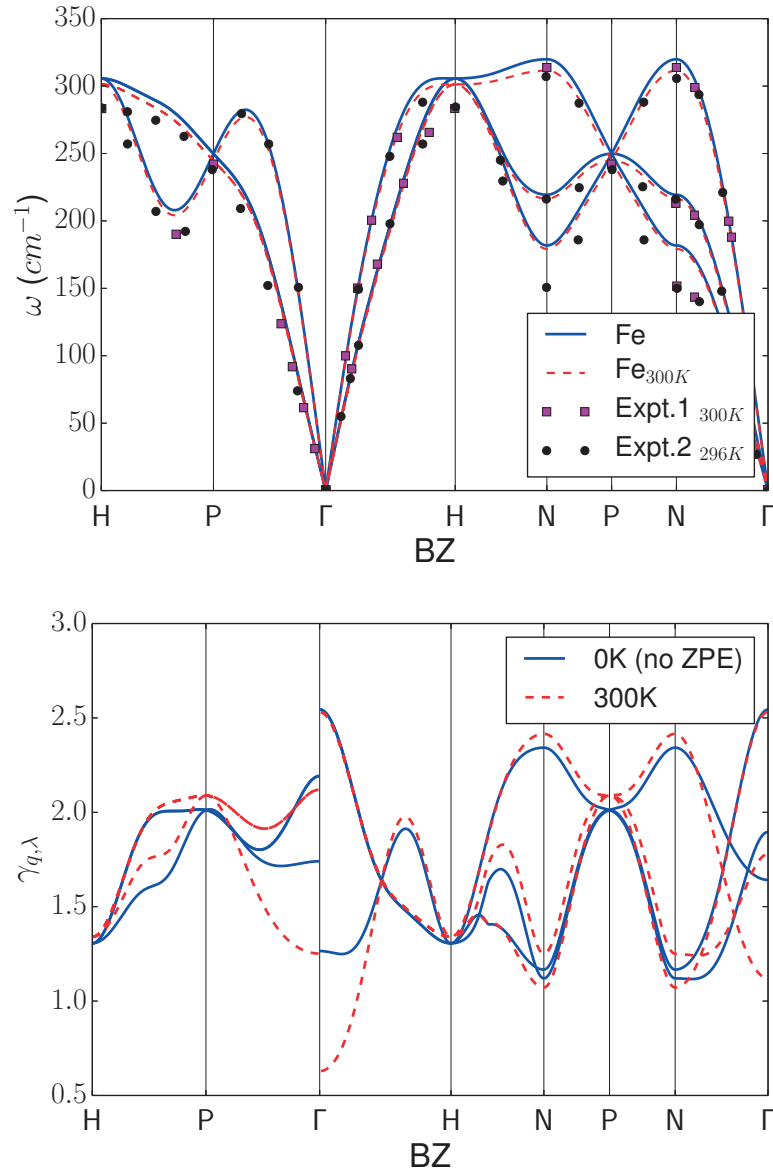


Figure 7.10: Top panel: Phonon dispersions along high-symmetry directions in the BZ calculated at the theoretical electronic equilibrium volume (blue solid line) and at the quasi-harmonic theoretical equilibrium volume at 300 K (red dashed line). The results (see also Fig. B.2 in Supplemental Material B and Ref. [75] or Ref. [74] for comparison with previous theoretical data) are compared to experimental data at room temperature from Ref. [185] (Expt.1 – squares) and Ref. [186] (Expt.2 – circles). Bottom panel: Grüneisen parameters calculated along the same path in the BZ and the same equilibrium volumes used for the phonon dispersion (blue solid line for the 0 K case and red dashed line for the 300 K case). The Grüneisen parameters are obtained computing the first derivative of a cubic fit of the phonon frequencies with respect to the volume.

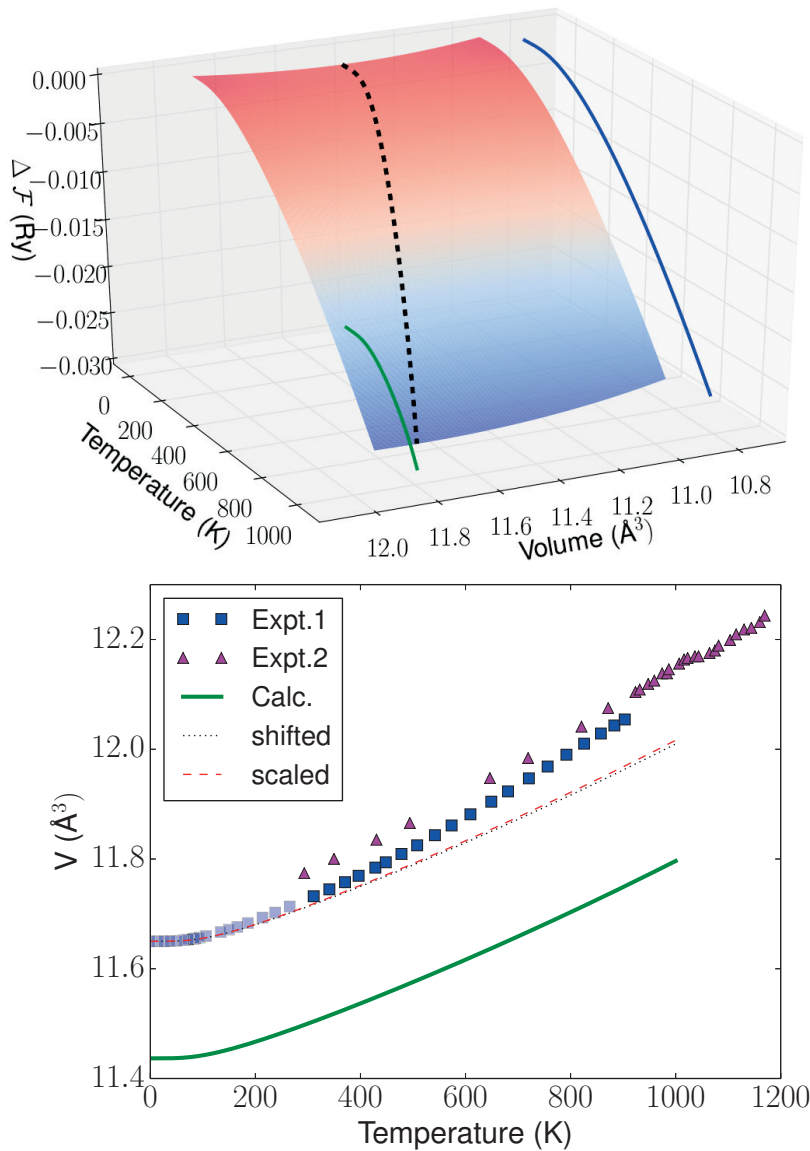


Figure 7.11: Top panel: Free-energy landscape of cubic bcc iron as a function of volume  $V$  and temperature  $T$ . The dashed black line corresponds to the locus of points that minimize the free-energy surface at each temperature. The continuous green and blue lines are the projections of the black dashed line in the  $T$ - $V$  and  $F$ - $T$  planes, thus describing the volumetric thermal expansion and the zero-pressure free energy as a function of  $T$ . Bottom panel: Volumetric thermal expansion (green solid line) compared to experimental data from Ref. [163] (Expt.1 – blue squares; note that below room temperature the data are extrapolated according to the thermal expansion coefficient of Ref. [203]) and Ref. [164] (Expt.2 – magenta triangles). As a guide to the eye, we also report the shifted and scaled curves. The former is obtained via rigid translation of the reference curve on the vertical axis to match the experimental 0 K value, while the latter via multiplication of the reference curve by a constant factor also to match the experimental 0 K value.

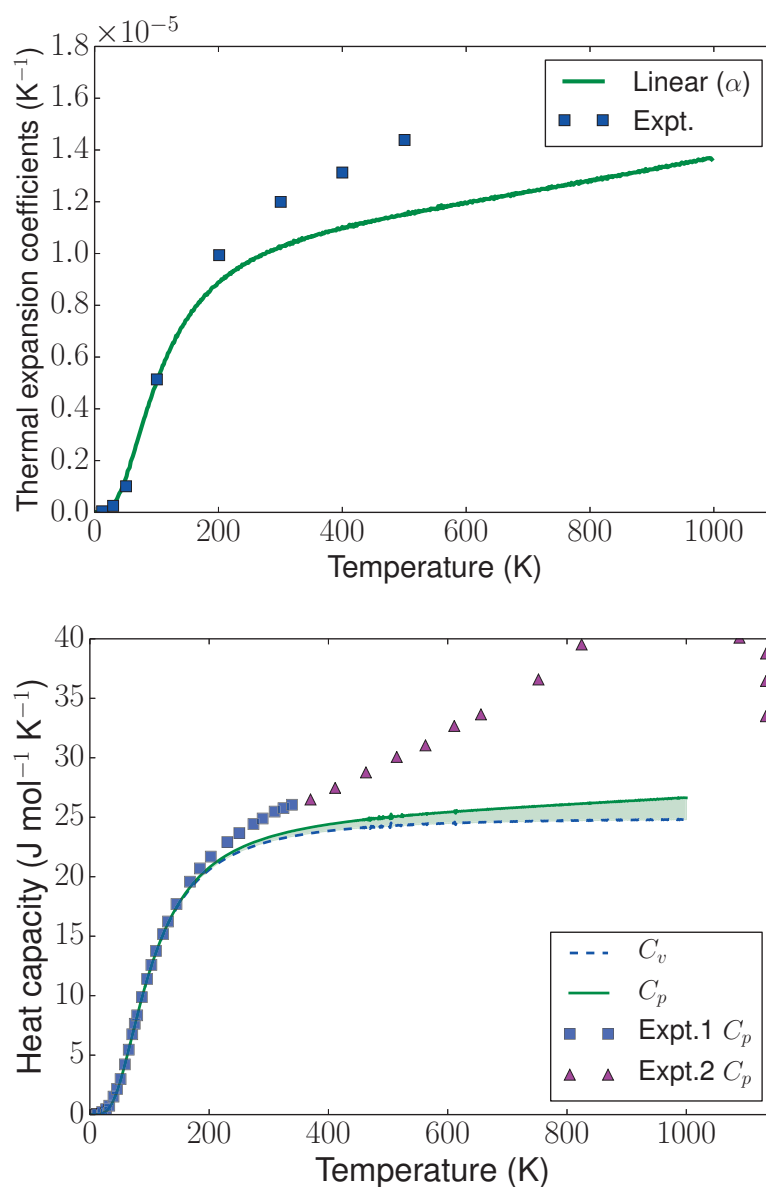


Figure 7.12: Top panel: Coefficient of linear thermal expansion (green solid line) compared to experimental data from Ref. [182] (squares). Bottom panel: Specific heat at constant pressure (green solid line) and at constant volume (blue dashed line), compared to experimental data from Ref. [183] (Expt.1 – squares) and from Ref. [184] (Expt.2 – triangles) .

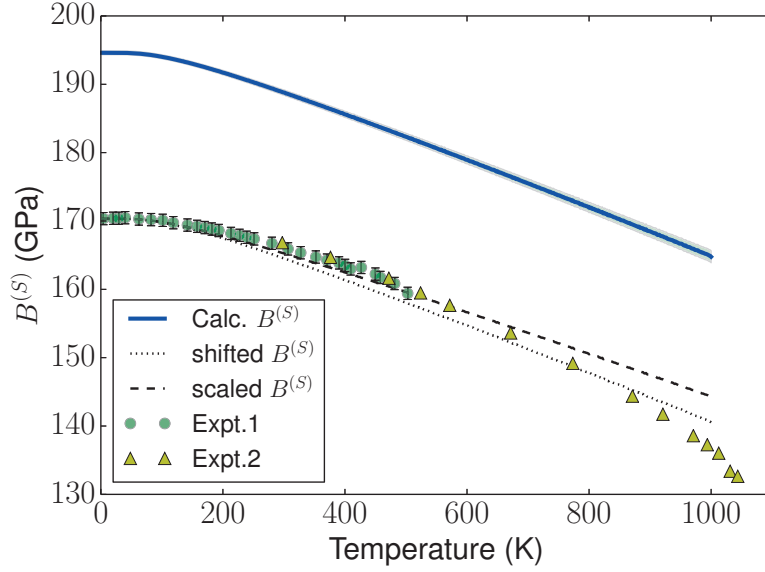


Figure 7.13: Adiabatic bulk modulus as a function of  $T$  (blue continuous line) calculated along with its confidence interval on the fit (shaded green) and compared to experimental data from Ref. [162] (Expt.1 – green circles) and from Ref. [189] (Expt.2 – yellow triangles). As a guide to the eye, we also plot the bulk modulus rigidly shifted (dotted line) and scaled (dashed line) to match the experimental 0 K value.

The tensor  $\boldsymbol{\epsilon}^{(3)}$  is associated to a continuous trigonal deformation that stretches the main diagonal  $d$  of the undistorted cubic structure along the (111) direction while tilting the undistorted edges and preserving their length. In this case, the relation between the strain  $\epsilon_d$  and the distorted main diagonal is

$$d = \sqrt{3}a(1 + \epsilon_d), \quad (7.5)$$

while the relation with the cosine of the angle between the distorted edges is

$$\cos(\alpha) = \frac{1 - \epsilon_d(2 + \epsilon_d)}{(\epsilon_d - 1)(\epsilon_d + 3)}. \quad (7.6)$$

Both deformations do not conserve the volume per atom. In particular, in the tetragonal one the volume increases as a function of  $\epsilon_c$ , while in the trigonal case, the volume decreases as a function of  $\epsilon_d$ . Alternatively, we could have chosen volume-conserving deformations as in Ref. [204], but the advantage of the present scheme is that each deformation determines uniquely one elastic constant at the time, and enables us to determine easily the confidence interval of each elastic constant by error-propagation theory.

In the next sub-sections we describe the calculation of the static and vibrational contributions, separately. The reason is that we want to analyze their contributions to the global energy landscape separately. This also allows us to sample the two contribution landscapes with



two different grids. Indeed, the static term displays a minimum as a function of the strain parameters and has to be sampled with a dense grid, while, on the other hand, the vibrational term is flat, monotonic and can be sampled with a coarse grid.

### Static contribution

To evaluate the static contribution to the elastic constants, we performed a series of well converged total energy calculations on a two dimensional discrete grid  $[\varepsilon_a, \varepsilon_{c/d}]$  (see Fig. 7.14 for details on the grid). The  $\varepsilon_a$  grid is asymmetric with respect to zero and with more points in the positive range of the strain parameter, in order to sample accurately the values of the static contribution to the free energy in the thermal expansion range.

The resulting total energies are fitted with a two-dimensional bivariate polynomials up to 5th degree using a least-square method <sup>2</sup>.

The analysis of the quality of the fit of discrete data points to a two-dimensional energy surface is crucial to resolve the possible sources of error that could affect our elastic constants and, therefore, for a reliable comparison with experiments and the wide range of scattered data available in the literature. Therefore, in addition to the visual inspection of the fit along constant  $\varepsilon_{c/d}$  sections, we evaluated the adjusted coefficient of determination ( $R^2$ ) and the the average absolute error (AAE), defined as:

$$\text{AAE} \equiv \frac{1}{N} \sum_{i,j} \left| P_n(\varepsilon_a^{(i)}, \varepsilon_{c/d}^{(j)}) - E(\varepsilon_a^{(i)}, \varepsilon_{c/d}^{(j)}) \right|, \quad (7.7)$$

where  $N$  is the total number of  $[\varepsilon_a, \varepsilon_{c/d}]$  discrete values and  $P_n$  is the bivariate best fit polynomial of degree  $n$ .  $R^2$  is a measure of the quality of the fitting model, i.e. how well the analytic function approximates the calculated data points. The AAE is a quantitative measure of the distance of the fitted curve from the calculated points. We found that the AAE decreases by increasing the degree  $n$  of the polynomial and  $R^2$  approaches unity, as shown in Tab. 7.3. According to these results, in both cases, we considered the 4th-degree polynomial to provide a sufficiently accurate fit (indeed the AAE is two orders of magnitude smaller than the difference between the highest and the lowest total-energy data points).

Fig. 7.14 shows a plot of the static energy landscape for both the tetragonal and trigonal deformations, with the minimum elongated along the diagonal in the  $[\varepsilon_a, \varepsilon_c]$  space or along constant  $\varepsilon_d$  in the  $[\varepsilon_a, \varepsilon_d]$  space.

<sup>2</sup>We used the least squares method routine `scipy.optimize.leastsq` which is a wrapper around the Fortran routine `lmdif` of MINPACK [205].

Order	AAE (Ry)	$R^2$	AAE (Ry)	$R^2$
	tetragonal		trigonal	
2	$1.894 \times 10^{-5}$	0.997259	$9.163 \times 10^{-5}$	0.971580
3	$1.997 \times 10^{-6}$	0.999975	$7.369 \times 10^{-6}$	0.999819
4	$1.002 \times 10^{-6}$	0.999993	$2.933 \times 10^{-6}$	0.999968
5	$9.150 \times 10^{-7}$	0.999995	$1.693 \times 10^{-6}$	0.999990

Table 7.3: Average absolute error (AAE) and adjusted coefficient of determination ( $R^2$ ) of the two-dimensional fit of the static energy landscape, for the tetragonal and trigonal deformations, as a function of the order of the polynomial.

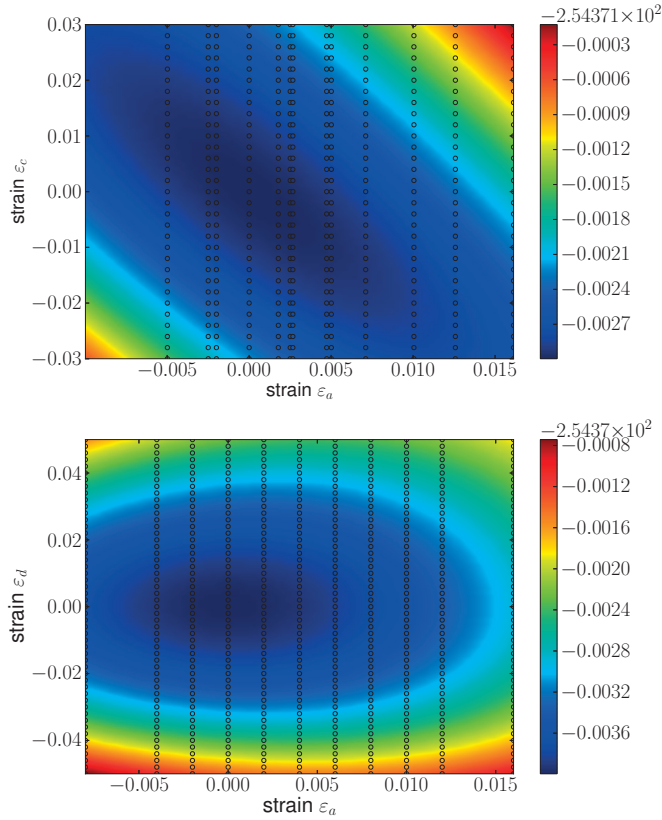


Figure 7.14: Static energy landscape of the tetragonal (top panel) and trigonal (bottom panel) distortions projected on the  $[\epsilon_a, \epsilon_{c/d}]$  plane.

### Vibrational contribution

In order to evaluate the vibrational contributions to the free energy, we perform a series of linear-response phonon calculations on a two dimensional grid in the space of deformation scalars  $\varepsilon_a, \varepsilon_{c/d}$ . Since the lattice dynamics calculations are one order of magnitude more time consuming than the total energy calculations, we used a coarser grid (see Fig. 7.15 for details on the grid).

The eigenvalues of each dynamical matrix are Fourier-interpolated in order to obtain smooth and continuous phonon dispersions. The zero-point energy and the thermal contributions are calculated by numerical integration over  $21 \times 21 \times 21$  points in reciprocal space. This is essential to obtain numerically accurate values of the vibrational contribution.

Like for the case of the static contribution, we determine the best polynomial necessary to fit our data over the entire temperature range from 0 to 1000 K. We use the adjusted  $R^2$  and the AAE as indicators of the quality of the fit. We also check *a posteriori* the convergence of the elastic constant curves obtained by fitting to different polynomial degrees. In the tetragonal case, a quadratic bivariate polynomial (i.e. 6 parameters) is sufficient to accurately reproduce the distribution of data points. On the other hand, for the trigonal deformation, a 4th order bivariate polynomial (i.e. 16 parameters) is needed. Our choice of polynomial is dictated by the need to minimize the AAE, maximize  $R^2$  and minimize the confidence interval as a function of temperature (see Figs. B.3, B.4 B.5 in Supplemental Material for the stability of the results against other polynomials). As an illustration, we report the vibrational energy landscape at 750 K for the tetragonal and for the trigonal distortions (Fig. 7.15).

### Evaluation of the elastic constants

Next, we sum the static and vibrational energy landscapes obtained in the previous sections and compute the Helmholtz free energy. An example of the resulting landscape at 500 K is displayed in Fig. 7.16. The second derivative with respect to strain can be evaluated analytically at the minimum of the free energy as a function of temperature.

Then, in order to understand if the discrepancy between the experimental and calculated elastic constants could be ascribed to the fitting procedure, we have calculated the confidence interval of  $C_{11}$  and  $C_{44}$ . To this end, we have computed the covariance matrix of each best-fit contribution to the free energy, defined as:

$$\text{Cov}[P] = \sigma_r^2 (J^T J)^{-1}, \quad (7.8)$$

where  $P$  is the set of polynomial coefficients,  $\sigma_r^2$  is the squared residual and  $J$  is the Jacobian matrix which is provided in output by the least squares routine. The global variance of each best fit polynomial is then obtained by considering both the diagonal and the off-diagonal elements of the covariance matrix  $\text{Cov}[P]$ . Finally, we used error-propagation theory to obtain the confidence interval of the elastic constants.

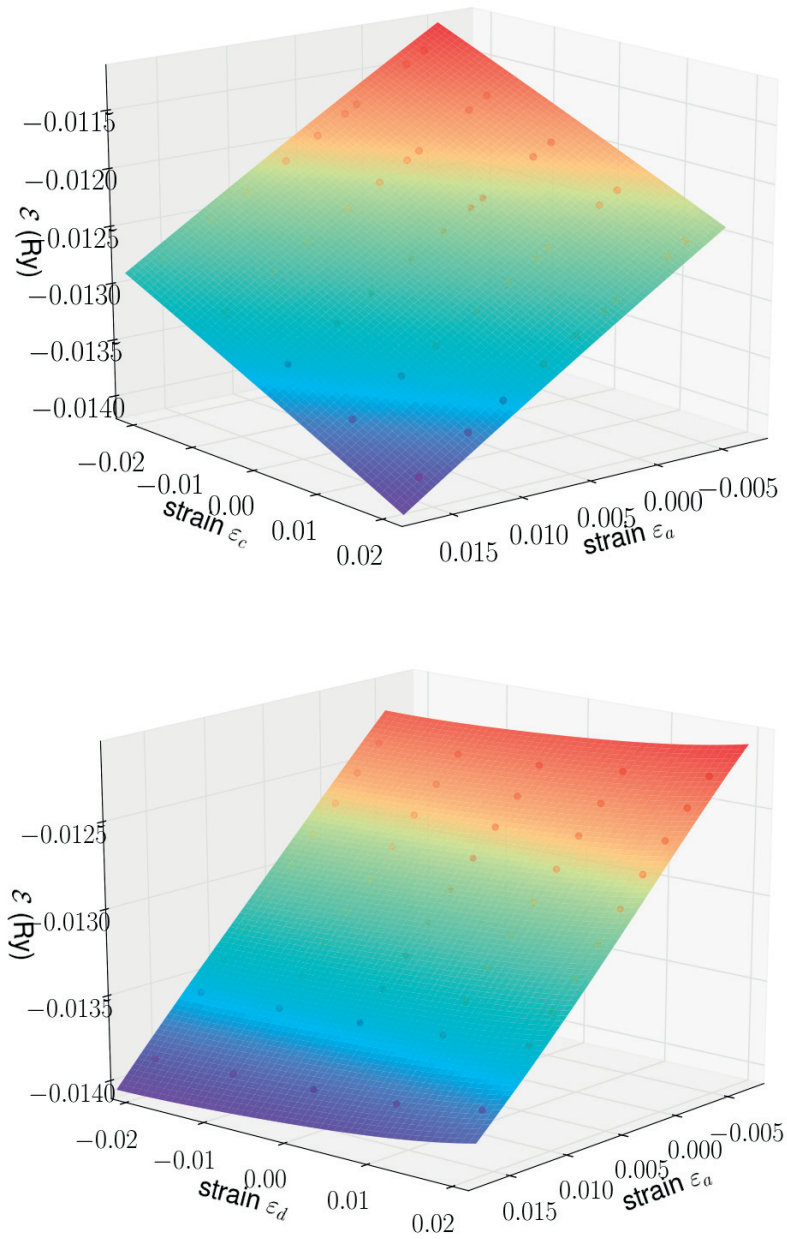


Figure 7.15: Vibrational quasi-harmonic contribution to the Helmholtz free energy at  $T = 750$  K in the  $[\epsilon_a, \epsilon_c]$  space (top panel),  $[\epsilon_a, \epsilon_d]$  space (bottom panel). A 2nd and a 4th order bivariate polynomial are respectively used to fit the tetragonal and trigonal data sets.

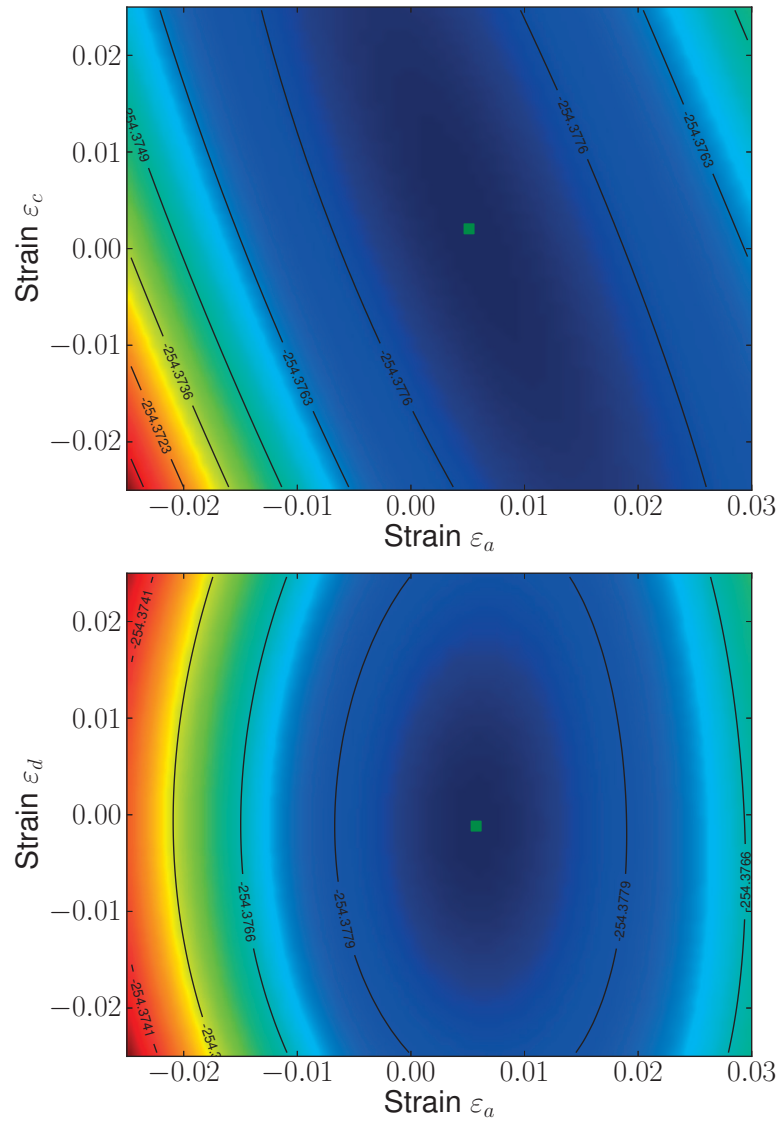


Figure 7.16: Free energy landscape of the tetragonal (top panel) and trigonal (bottom panel) deformations projected on the  $[\epsilon_a, \epsilon_d]$  and  $[\epsilon_a, \epsilon_c]$  plane respectively at 500 K. The green squares represent the minima of the energy landscapes.

## Chapter 7. Thermodynamic and thermoelastic properties of $\alpha$ -iron

The calculated  $C_{11}$  and  $C_{44}$  elastic constants of bcc  $\alpha$ -iron decrease by increasing temperature, as shown in Fig. 7.17. Our results are in reasonable accordance with those calculated in Ref. [83] (the exception is  $C_{44}$  that in our case is fairly underestimated) where, however, a direct detailed comparison with experimental thermal softening is clearly more difficult. In Tab. 7.4, we report our calculated zero temperature values with and without zero-point energy (ZPE) contributions, and compare them to experiments. Also, for sake of completeness, we report in Tab. 7.5 the  $C_{12} = \frac{3B-C_{11}}{2}$ ,  $C' = \frac{1}{2}(C_{11} - C_{12}) = \frac{3}{4}(C_{11} - B)$  and anisotropy ratio  $C_{44}/C'$  obtained from standard theory of elasticity and our calculated  $B$ ,  $C_{11}$  and  $C_{44}$  (see Fig. 7.18 for the temperature dependence of the  $C'$ ). The inclusion of ZPE results in a small decrease of the elastic constants and bulk modulus. The confidence interval at zero temperature is of the order of 0.1 GPa and cannot account for the difference with respect to experiments.

$T$ (K)	$a$ (Å)	$B$ (GPa)	$C_{11}$ (GPa)	$C_{44}$ (GPa)
0 (no ZPE)	2.834	199.8±0.1	296.7±0.3	104.7±0.1
0 (ZPE)	2.839	194.6±0.3	287.9±0.4	102.2±0.5
0 (Expt.) [162, 163]	2.865	170.3±1	239.5±1	120.7±0.1

Table 7.4: Calculated 0 K elastic constants for iron with and without zero-point energy contributions. Results are compared to experimental data extrapolated to 0 K.

$T$ (K)	$C_{12}$ (GPa)	$C'$ (GPa)	$C_{44}/C'$
0 (no ZPE)	151.4±0.2	72.7±0.3	1.44
0 (ZPE)	148.01±0.5	70.0±0.4	1.46
0 (Expt.) [162]	135.7	51.9	2.32

Table 7.5:  $C_{12}$  and  $C'$  elastic constants, and  $C_{44}/C'$  anisotropy ratio, derived from Tab. 7.4 with and without zero-point energy. Results are compared to experimental data extrapolated at 0 K. Errors are obtained according to propagation of uncertainties.

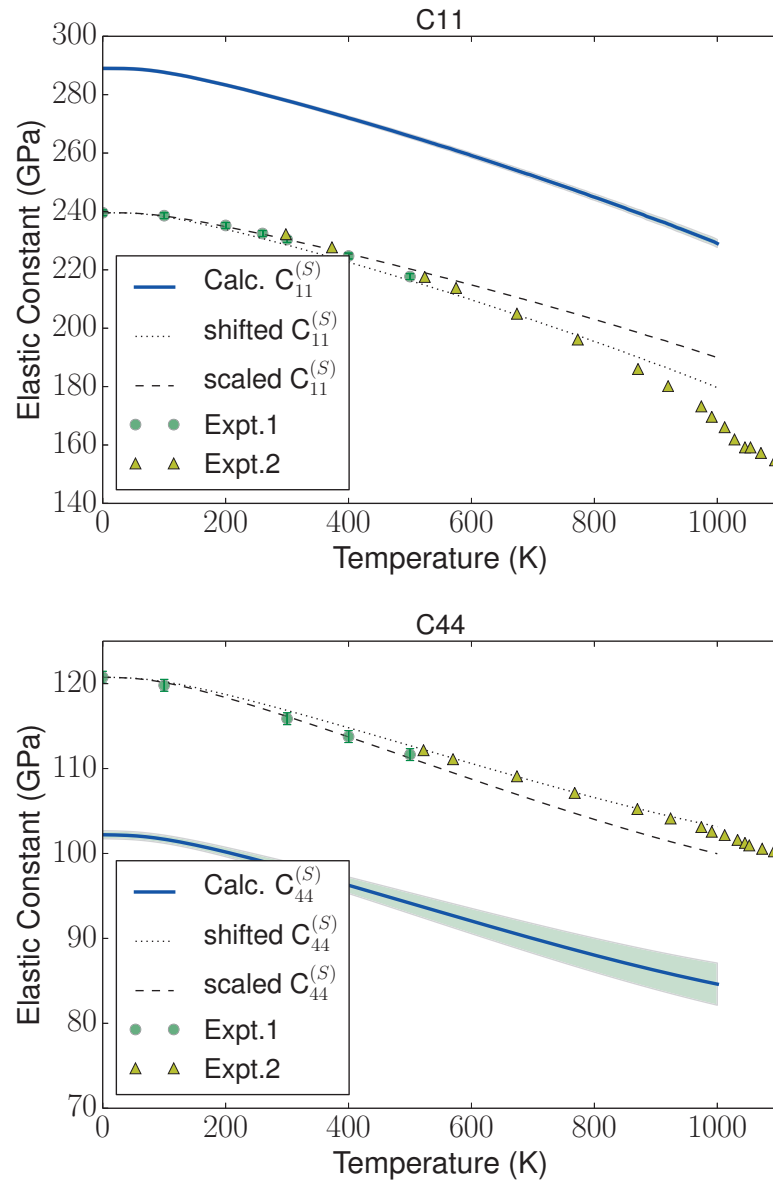


Figure 7.17: Top panel: calculated adiabatic  $C_{11}$  elastic constant (blue solid line). Bottom panel: calculated adiabatic  $C_{44}$  (blue solid line). Two sets of experimental data are reported on each plot – Expt.1 (green circles) from Ref. [162] and Expt.2 (yellow triangles) from Ref. [189]. The calculated interval of confidence is displayed as a shaded area. As a guide to the eye, we also plot the elastic constants rigidly shifted (dotted line) and scaled (dashed line) to match the experimental values at zero temperature.

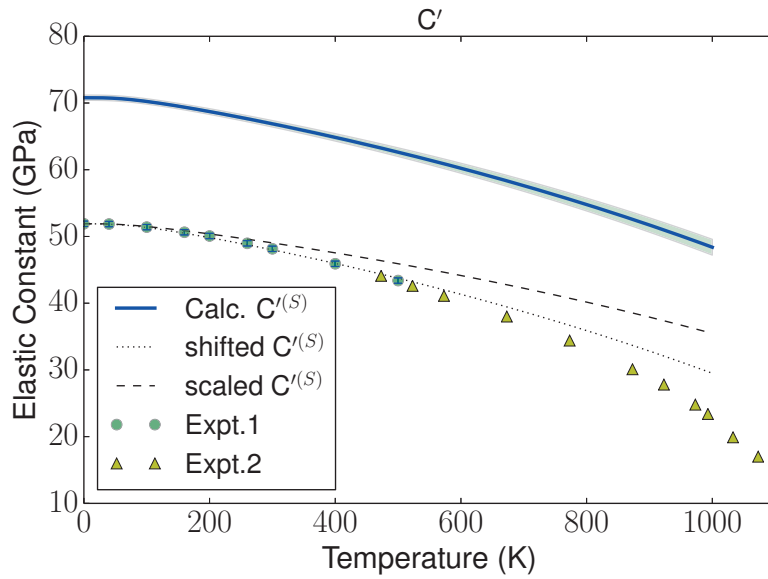


Figure 7.18: Thermal behavior of the  $C'$  elastic constant calculated as a linear combination of  $B(T)$  and  $C_{11}(T)$  (blue continuous line). Two sets of experimental data are reported – Expt.1 (green circles) from Ref. [162] and Expt.2 (yellow triangles) from Ref. [189]. The calculated interval of confidence is displayed as a shaded area. As a guide to the eye, we also plot the elastic constants rigidly shifted (dotted line) and scaled (dashed line) to match the experimental values at zero temperature.



### 7.2.4 Finite temperature electrons

Although the QHA proved to provide a reliable description of thermoelastic properties for a large part of the temperature range of stability of the  $\alpha$ -phase, we are interested in evaluating the effects of the electronic excitations of the system. This can be done according to Sec. 2.3 including in the definition of the Helmholtz free energy the electronic contribution from eq. (2.35) and using Fermi-Dirac occupation function for the ground state KS eigenstates. In particular we compute the electronic contribution to the free energy as a function of the strain for volumetric deformations that preserve the cubic symmetry of the crystal. The same strain matrix  $\boldsymbol{\epsilon}^{(1)} = \{\epsilon_a, \epsilon_a, \epsilon_a, 0, 0, 0\}$  used for the quasi-harmonic case is considered. We start from the zero temperature equilibrium lattice parameter  $a_0$  with steps in the strain of 0.002 from  $-0.020 \rightarrow +0.050$ . For each volume/strain configuration we compute the density of states (DOS)  $D(\epsilon)$  and the spin resolved densities of state  $D_\uparrow(\epsilon), D_\downarrow(\epsilon)$  and we then integrate them to obtain the following quantities:

$$N^{el} = \int_{-\infty}^{+\infty} f(\epsilon, T, V) D(\epsilon) d\epsilon = \int_{-\infty}^{\epsilon_F} D(\epsilon) d\epsilon \quad (7.9)$$

$$U^{el}(T, V) = \int_{-\infty}^{+\infty} \epsilon(V) f(\epsilon, T, V) D(\epsilon) d\epsilon \quad (7.10)$$

$$S^{el}(T, V) = -k_B \int_{-\infty}^{+\infty} [f(\epsilon, T, V) \ln f(\epsilon, T, V) + (1 - f(\epsilon, T, V)) \ln(1 - f(\epsilon, T, V))] D(\epsilon) d\epsilon \quad (7.11)$$

$$M^{el}(T, V) = \mu_B \int_{-\infty}^{+\infty} [D_\uparrow(\epsilon) - D_\downarrow(\epsilon)] f(\epsilon, T, V) d\epsilon \quad (7.12)$$

$$C_v^{el}(T, V) = -k_B T \int_{-\infty}^{+\infty} \frac{\partial f(\epsilon, T, V)}{\partial T} \ln \left[ \frac{f(\epsilon, T, V)}{1 - f(\epsilon, T, V)} \right] D(\epsilon) d\epsilon \quad (7.13)$$

with  $f(\epsilon, T, V)$  the Fermi-Dirac distribution and  $\epsilon(V)$  are the non self-consistent energy-levels of 0 K the calculations that, in the approximation used herein, depend explicitly on the volume  $V$  and not on  $T$ . In order to compute the DOS at the different volumes with the necessary accuracy we use similar parameters used for the QHA results (see Sec. 7.2.6) using a Marzari-Vanderbilt smearing scheme with 0.005 Ry and  $32 \times 32 \times 32$  for the self-consistent calculation which is followed by a non self-consistent calculation with an enhanced  $96 \times 96 \times 96$  sampling. The DOS and its spin-resolved counterparts are then computed with steps of 5 meV and spline interpolated to ensure a improved energy resolution that is beneficial to the numerical integration of the quantities reported above (see Fig. 7.19). In Fig. 7.20 we optimize and validate our integration scheme finding a DOS energy resolution of 1.4 meV (roughly equivalent to 16 K) that gives an error in the integrated number of (valence) electrons below  $\pm 0.0004$  fractions of electron and an integrated Fermi energy converged up to  $\pm 0.4$  meV at a given volume configuration.

After the verification of the implementation of the approach, we compute the chemical potential as a function of  $T$  and  $V$  as reported in Fig. 7.21 by inversion of eq. (7.9). The

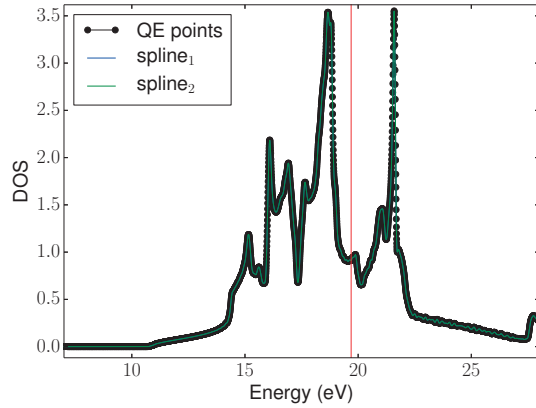


Figure 7.19: Electronic density of states calculated from the QUANTUM-ESPRESSO suite (black circles) at a strain of  $\epsilon_a = -0.020$ . The continuous blue and green lines are respectively a quadratic and a cubic spline used to interpolate the calculated points thus providing an augmented energy resolution. The black vertical line represents the Fermi energy calculated internally by the code.

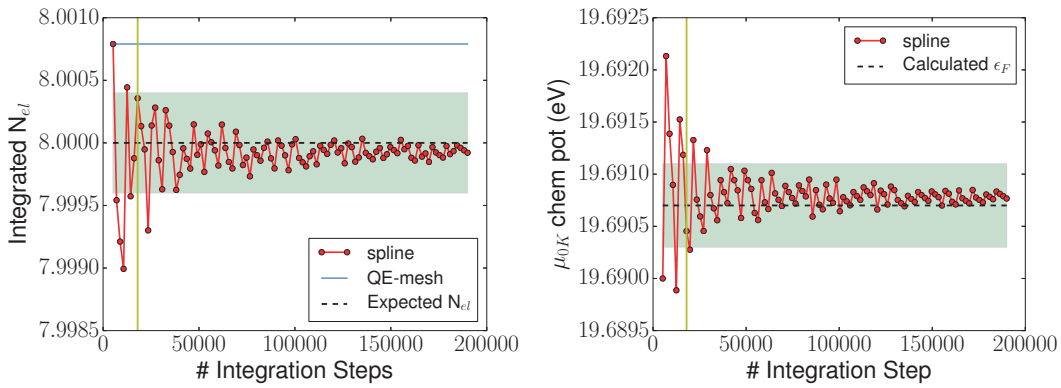


Figure 7.20: Left panel: Convergence of the integrated number of electrons from eq. (7.9) to the expected number of 8 valence electrons for bcc iron (black dashed line) as a function of the number of bins used to sample the DOS. The red circles are the calculated values, the blue line the number of electrons calculated integrating the DOS as it is provided by the code, the green shaded area defines the convergence threshold around the expected integer number of electrons while the vertical yellow line corresponds to the number of bins used in this work. Right panel: Convergence of the Fermi energy as from the panel above. The black dashed line here indicates the value of the Fermi energy as calculated by the code with a tetrahedron method.

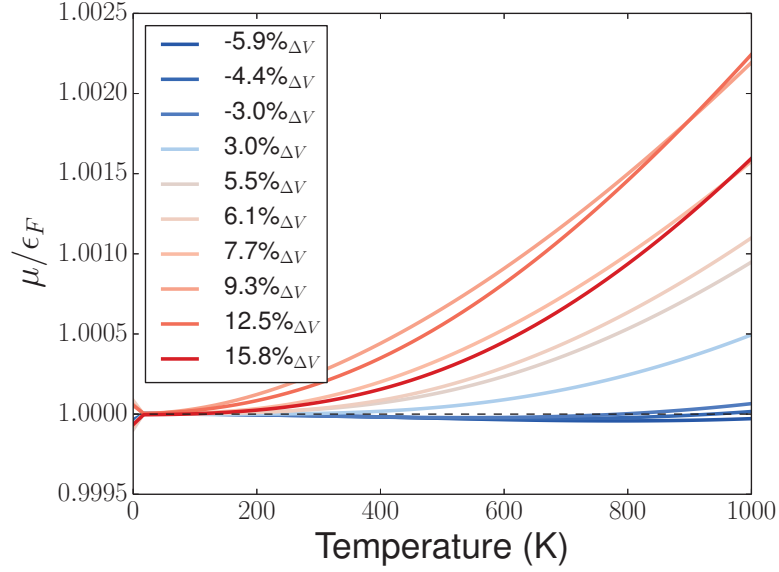


Figure 7.21: Chemical potential renormalized by its Fermi energy as a function of temperature for different volumes. The volume curves are drawn with colors following a heat map from blue to red as the volume increases. The details at very low temperature are an artifact due to the limited energy (and therefore temperature) resolution used in the numerical integration scheme. The chemical potential is obtained by inversion of eq. (7.9) using the exact value 8 electrons.

various thermodynamic quantities are then obtained integrating from  $\sim -8$  eV below the lowest (valence) eigenstate to  $\sim +8$  eV above the highest Fermi energy considered in this work.

We compute the internal energy  $E$ , the entropy  $S$  and consequently the Helmholtz free energy of the non interacting system as a function of volume and temperature. In order to extract the temperature dependence of the internal energy (which, in the approximation used here is due to the different occupation of the temperature independent eigenvalues/energy levels only – see eq. 2.35), we remove entirely the 0 K part of the total energy (actually, to avoid numerical noise we subtract the value at very low temperature  $\sim 16$  K). The numerical results are reported in Figs. 7.22.

Finally, we couple these extra contributions from the electronic excitations to those from QHA to get the more general Helmholtz free energy from which it is possible to calculate also the thermal expansion, the heat capacity and the bulk modulus. These results are reported in Fig. 7.23 and Fig. 7.24.

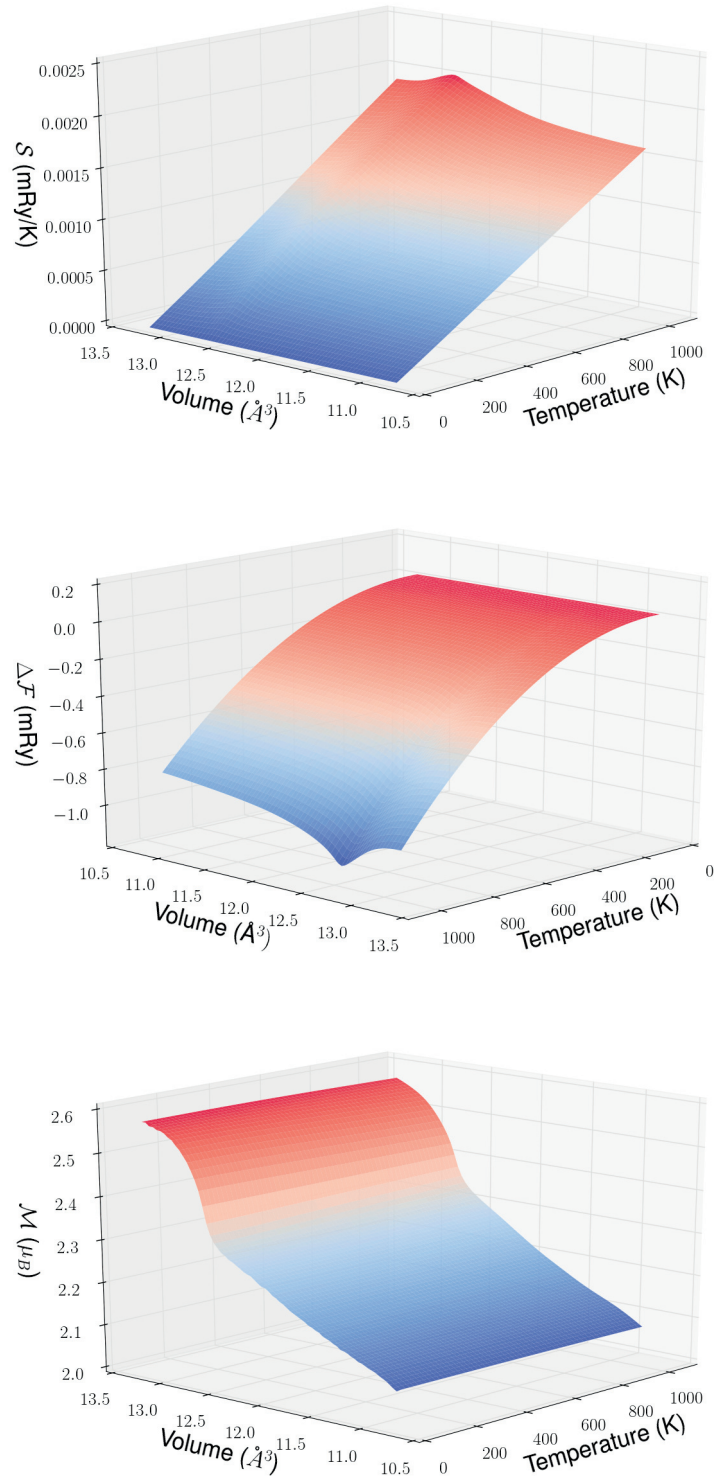


Figure 7.22: From top to bottom are reported the electronic entropy, the Helmholtz free energy at which the 0 K contributions at all the volumes have been subtracted, and magnetization as a function of temperature and volume.

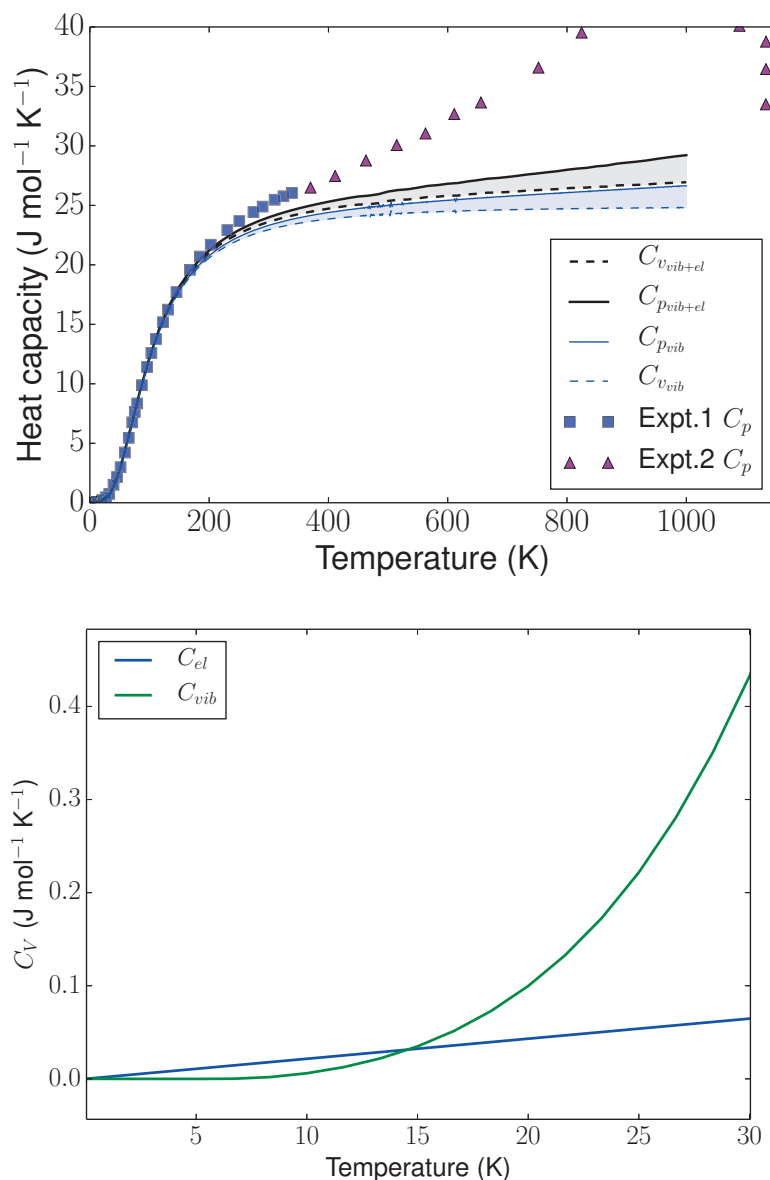


Figure 7.23: Top panel: the blue curves are the vibrational contribution only (dashed is  $C_V$ , solid  $C_P$ ) that scales cubically at low temperature as shown in the zoom-in picture in the bottom panel. The inclusion of electronic contribution is visible in the black lines (dashed is  $C_V$ , solid  $C_P$ ). As expected from the theory (see for instance Ref. [206]) the electrons provide a linear contribution to the total heat capacity that is dominant at very low temperature (below 20 K; see bottom panel) and that become again visible at high temperature (above  $\sim 500$  K), where the vibrational  $C_V$  saturates around  $25 \text{ J mol}^{-1} \text{ K}^{-1}$  ( $3k_B$ ), in agreement with the classical Dulong-Petit limit. Squares and triangles are experimental results as reported in Fig. 7.12.

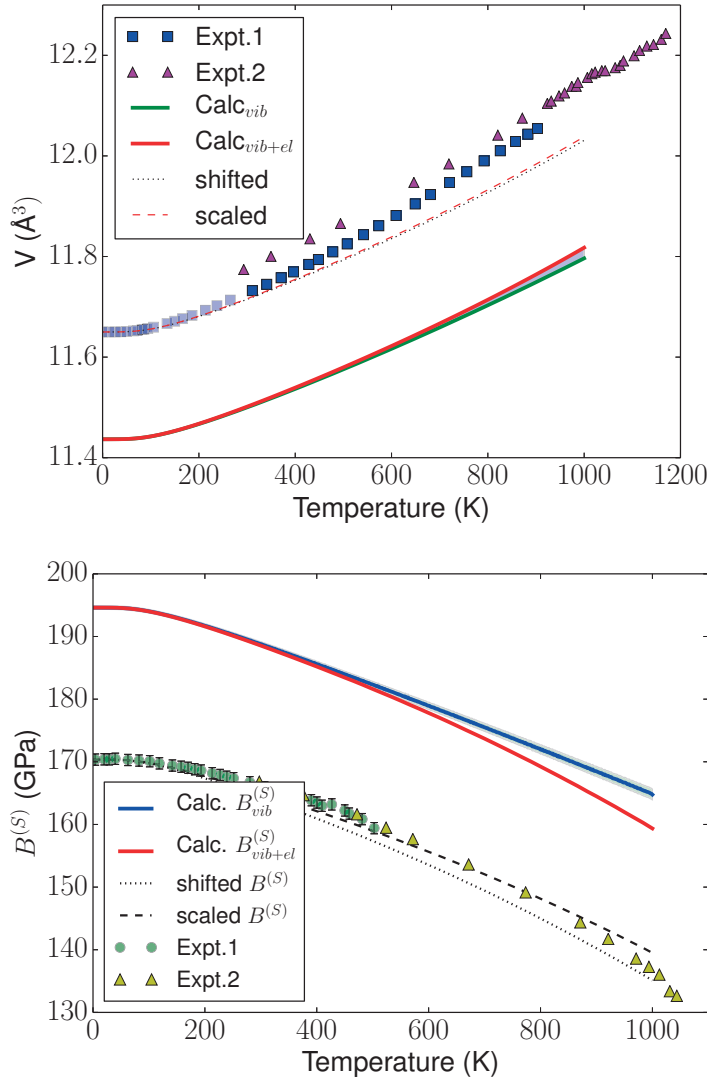


Figure 7.24: Top panel: thermal expansion of bcc  $\alpha$ -iron. Green solid line is the vibrational contribution only, red solid line is the vibrational plus electronic curve (the shaded azure area is the difference). Squares and triangles are Experimental data as in Fig. 7.12. Bottom panel: adiabatic bulk modulus as a function of T. The addition of the electronic correction to the vibrational solid blue line that we obtained from QHA [45] results in the solid red line. Circles and triangles are experimental data as from Fig. 7.13. Interestingly, albeit small in the thermal expansion and in the heat capacity, the electronic correction is relevant to describe properly the bulk modulus thermal behavior especially in its marked bending above  $T_D$  ( $\sim 00$  K from Ref. [115]) that was believed to be primarily due to transverse magnetic fluctuations. This result differently from what expected, suggests how the influence of the transverse magnetic fluctuations on the bulk modulus (not included here), although still present, is prominent only in a very narrow range of temperature around the  $T_C$ . As a guide to the eye, in both panel we also report shifted (dotted) and scaled (dashed) quantities. The former are rigidly translated on the vertical axis, while the latter are multiplied by a constant factor to match the experimental 0 K value.

### 7.2.5 Defects

We also calculate the energetics of some important defects of the perfect bulk  $\alpha$ -iron structure that we would like to be able to reproduce with the GAP potentials. These data, however, are used only to test the quality of the generated potentials and are not explicitly included in the training database. Some examples such as the mono-vacancy formation energy, the di-vacancy formation and binding energies for first, second and third nearest-neighbors and the bulk-terminated surface energies for the crystallographic orientations considered in this work are collected in Tabs. 7.6, 7.10. These data agree qualitatively with those from the literature, suggesting first and second nearest-neighbor vacancies bind together contrarily to third nearest-neighbor vacancies, that have a slightly negative binding energy. The  $\gamma$  surface energies introduced in Sec. 6.6.5 are instead reported in Figs. 7.25, 7.26 for the (110) and (112) crystallographic orientations at the bulk equilibrium lattice parameter, with and without out-of-plane structural relaxation. The results for the (110) interface show a local minimum at mismatch 50-50% of the in-plane lattice vectors both in the unrelaxed and relaxed configurations, thus suggesting a metastable state which is favorable for a stacking fault. The (112) interface instead undergoes a strong energy renormalization upon out-of-plane relaxation of the atoms, eventually displaying a saddle point at a displacement vector 20-50%. These results are in qualitative agreement with those reported for tungsten in Ref. [149], and confirm that the bcc structures of different materials share common trends in the energetics of defects.

	Expt.	DFT (54 atoms)	DFT (128 atoms)	Other Calcs.
$E^v$ (eV)	1.6, 2.2 [207, 208]	2.22	2.22	2.10 [209]
$E_f^{1NNv}$	-	-	4.24	4.01 [209]
$E_f^{2NNv}$	-	-	4.20	3.95 [209]
$E_f^{3NNv}$	-	-	4.45	-
$E_b^{1NNv}$	-	-	0.20	0.14, 0.08 [209, 210]
$E_b^{2NNv}$	-	-	0.24	0.28, 0.15, ~0.2 [35, 209–211]
$E_b^{3NNv}$	-	-	-0.01	-0.02 [210]

Table 7.6: Mono-vacancy  $E^v$  and first, second, third nearest-neighbors di-vacancy formation and binding energies  $E_f^{1NNv}, E_f^{2NNv}, E_f^{3NNv}, E_b^{1NNv}, E_b^{2NNv}, E_b^{3NNv}$ . The formation energies are calculated from eq. (6.28) at the equilibrium volume using two different cells containing 54 and 128 atoms to check for size convergence. The atomic positions are fully relaxed using a force threshold of 1 mRy/Bohr while the input parameters coincide with those reported in Sec. 6.6.6 for the GAP database generation. The results show the mono-vacancy formation energy difference between the two cell sizes is of the order of a few meV. For this reason, we then use a 54-atoms cell to compute the formation energy at two volumes, namely  $\pm 2.1\%$  with respect to the equilibrium. The latter results are displayed in Fig. 7.32.

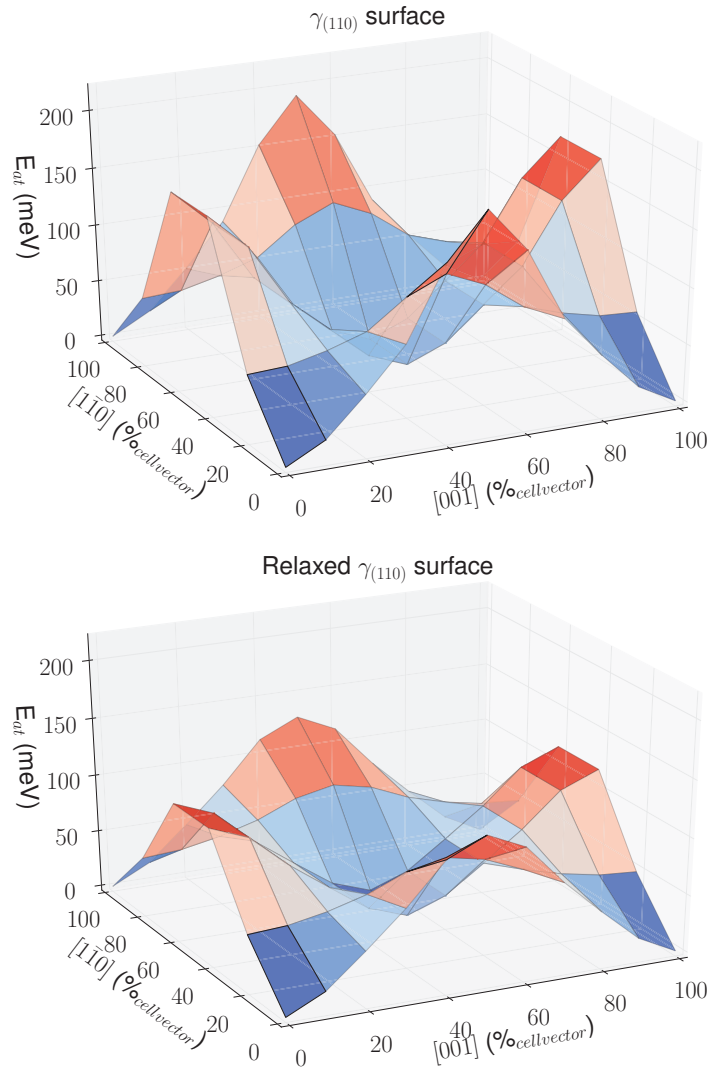


Figure 7.25: Top panel: unrelaxed  $\gamma_{(110)}$  energy surface as a function of the relative mismatch of two stacked bcc crystals along the  $[1\bar{1}0]$  and  $[001]$  directions in a  $(110)$  plane in fractions of the in-plane cell vectors. Bottom panel: same as top panel allowing for out-of plane relaxation of the atomic positions. The sampling of the energy surface is in steps of 10% and 20% of the two in-plane cell vectors.



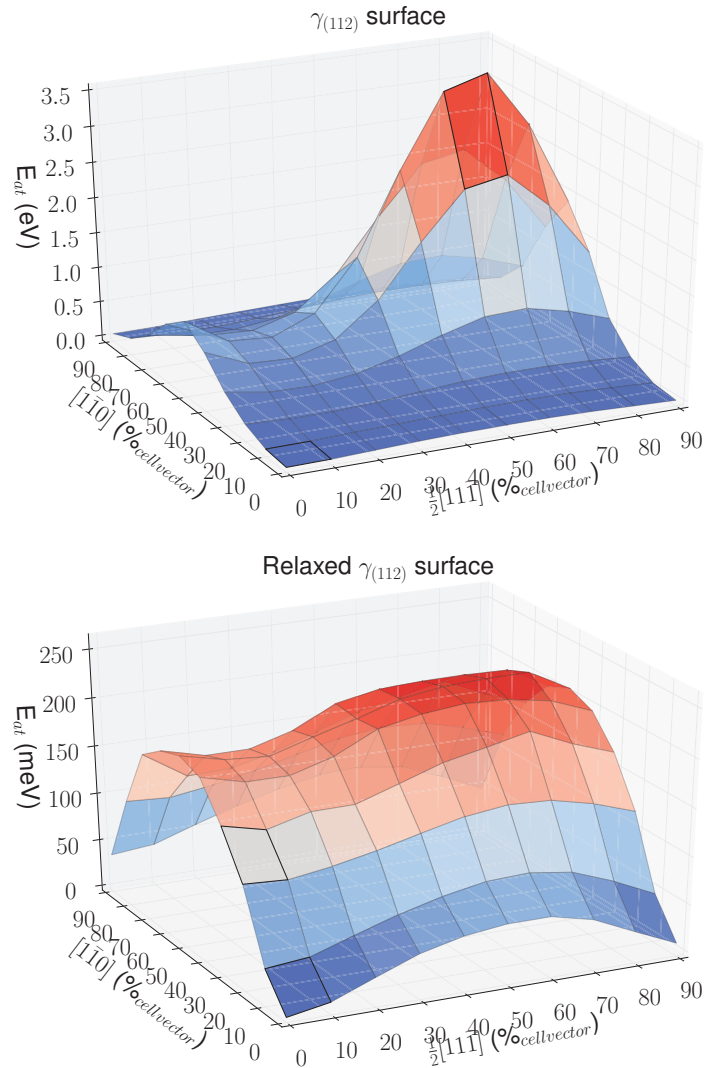


Figure 7.26: Top panel: unrelaxed  $\gamma_{(112)}$  energy surface as a function of the relative mismatch of two stacked bcc crystals along the  $[1\bar{1}0]$  and  $\frac{1}{2}[11\bar{1}]$  directions in a (112) plane in fractions of the in-plane cell vectors. Bottom panel: same as top panel allowing for out-of plane relaxation of the atomic positions. The sampling of the energy surface is in steps of 10% of the two in-plane cell vectors.

### 7.2.6 Computational details and pseudopotential selection

We calculate the first-principles elastic constants from DFT as implemented in the PWSCF and PHONON packages of the QUANTUM-ESPRESSO distribution [172] for the static and lattice dynamical calculations, respectively. The calculations are spin-polarized and the magnetic moment is free to vary collinearly in order to minimize the total energy. In all calculations the exchange-correlation effects have been treated within the generalized-gradient approximation (GGA) with the PBE functional [98]. We use an ultrasoft pseudopotential [102] (USPP) from *pslibrary.0.3.0*<sup>3</sup>, which includes also 3s and 3p semicore states<sup>4</sup> (i.e. 16 valence electrons) along with a plane-wave basis with a wavefunction kinetic-energy cutoff of 90 Ry and a cutoff of 1080 Ry for the charge density. For the calculation of the thermoelastic properties we sampled the BZ with an offset  $24 \times 24 \times 24$  Monkhorst-Pack  $k$ -mesh, with a Marzari-Vanderbilt smearing [109] of 0.005 Ry, while for the calculation of the different defects we use the  $k$  sampling reported in Tab. 6.10 with a smearing of 0.01 Ry.

Phonon calculations were carried out for each deformation within DFPT [87, 119]: the dynamical matrix and its eigenvalues are calculated on a  $4 \times 4 \times 4$  mesh of special points in the BZ and Fourier-interpolated on an extended  $21 \times 21 \times 21$  grid for the integration of thermodynamic quantities. We arrived at this computational setup (cutoff, smearing and BZ sampling) after a careful investigation of the convergence of total energy and individual phonon frequencies for different deformations. Also, we verified that individual total energies and phonon frequencies do change smoothly as a function of strain.

In order to provide reliable data for finite temperature properties we decided to validate and verify our DFT scheme checking different possible pseudopotentials available in the literature. We chose our pseudopotential of reference among different candidates from the *pslibrary*<sup>5</sup> and *GBRV* library<sup>6</sup> to reproduce, as closely as possible, the all-electron FLAPW equilibrium lattice parameter, bulk modulus at 0 K and local magnetization obtained from independent groups [212–214]. Also, for the sake of completeness, we compare against results obtained using the VASP code and associated pseudopotentials [175].

These values, reported in Figs. 7.27, 7.28, are obtained from a Birch-Murnaghan fit of calculated  $E(V)$  data points. Interestingly, we have found that the volume range of validity for fitting a Birch-Murnaghan [202] curve is limited on the expansion side due to anomalies in the  $E(V)$  curve and its derivatives. These anomalies, also reported for all-electron and other calculation methods in Ref. [223], are more clearly visible as “shoulders” in the  $M(V)$  behavior (see Fig. 7.29) and, as visible from Fig. 7.30, can be associated to a smooth magnetic transition from a low to high spin state due to the splitting of the majority and minority spin  $t_{2g}$  electrons upon increasing the volume. However, for the pseudopotential chosen here, the expanded

---

<sup>3</sup>For iron, this is identical to 0.2.1

<sup>4</sup>This pseudopotential is uniquely labeled as Fe.pbe-spn-rrkjus\_ps1.0.2.1.UPF

<sup>5</sup><http://www.qe-forge.org/gf/project/pslibrary>

<sup>6</sup><http://www.physics.rutgers.edu/gbrv/>

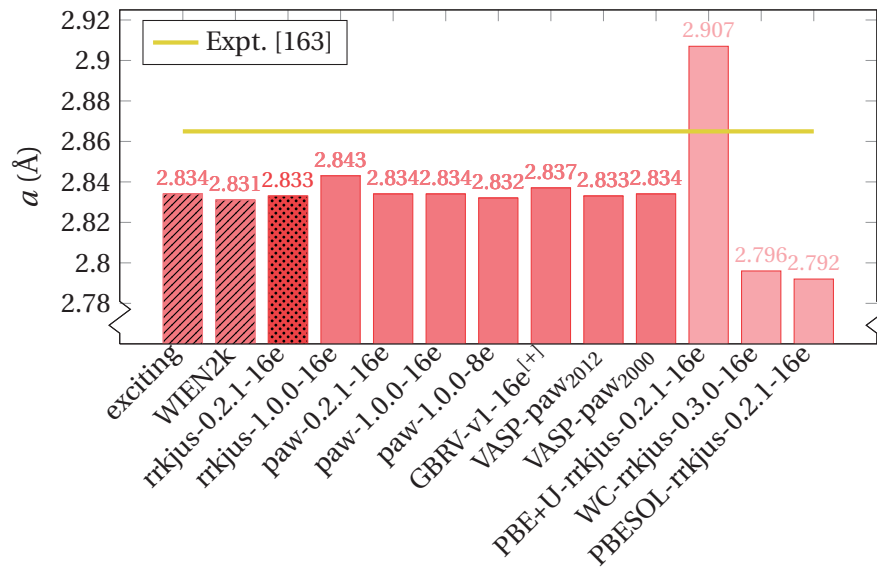


Figure 7.27: Equilibrium lattice parameter at 0 K for the different iron pseudopotentials tested in this work. All the data shown here are obtained with the PBE XC functional except for the last three columns on the right, where we have used PBE+U [215–218], WC [219] and a PBEsol [220] respectively (here we use a Hubbard  $U$  correction with  $U = 3eV$ ). The data come from a Birch-Murnaghan fit, do not include zero-point energy and are compared to all-electron WIEN2K [173], **exciting** [174] and VASP [175] calculations from Ref. [212–214, 221] respectively and experiments [163, 203, 222] (horizontal yellow line). The crosshatch dotted column corresponds to the pseudopotential chosen for the production runs.

volumes at which this anomaly is observed (above 9%<sup>7</sup>) are far beyond the theoretical thermal expansion of the system in the thermodynamic region considered in this work, thus enabling us to fit the energy surface with volume expansions up to  $\sim 9\%$  still using a standard Birch-Murnaghan equation.

<sup>7</sup>For the GBRV and rrkjus-1.0.0 pseudopotentials reported in Fig. 7.29 instead, the anomaly starts around +4/5% of their equilibrium volume and the magnetization is systematically overestimated if compared to all-electron data.

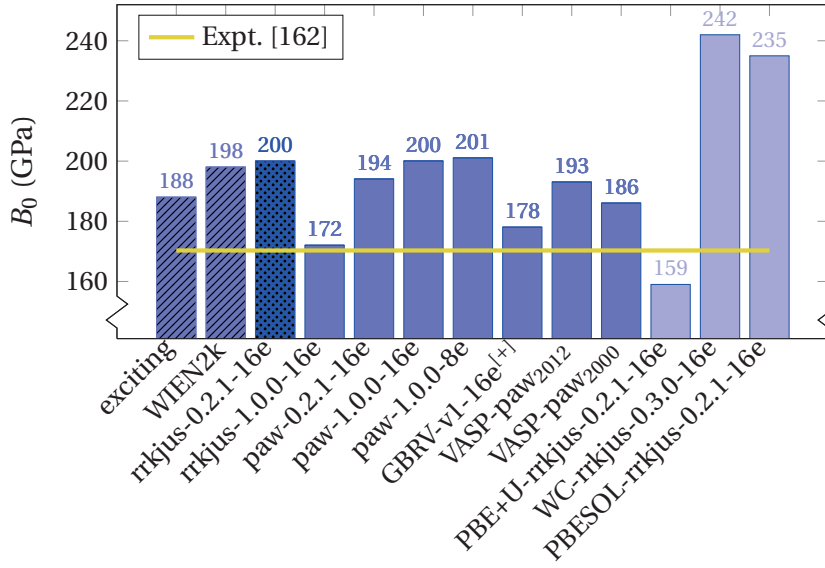


Figure 7.28: Equilibrium bulk moduli at 0 K for the different iron pseudopotentials tested in this work. All the data shown here are obtained with the PBE XC functional except for the last three columns on the right, where we have used PBE+U [215–218], WC [219] and a PBESol [220] respectively (we use here a Hubbard  $U$  correction with  $U = 3eV$ ). The data come from a Birch-Murnaghan fit, do not include zero-point energy and are compared to all-electron WIEN2k [173], **exciting** [174] and VASP [175] calculations from Ref. [212–214] respectively and experiments [162] (horizontal yellow line). The crosshatch dotted column corresponds to the pseudopotential chosen for the production runs.

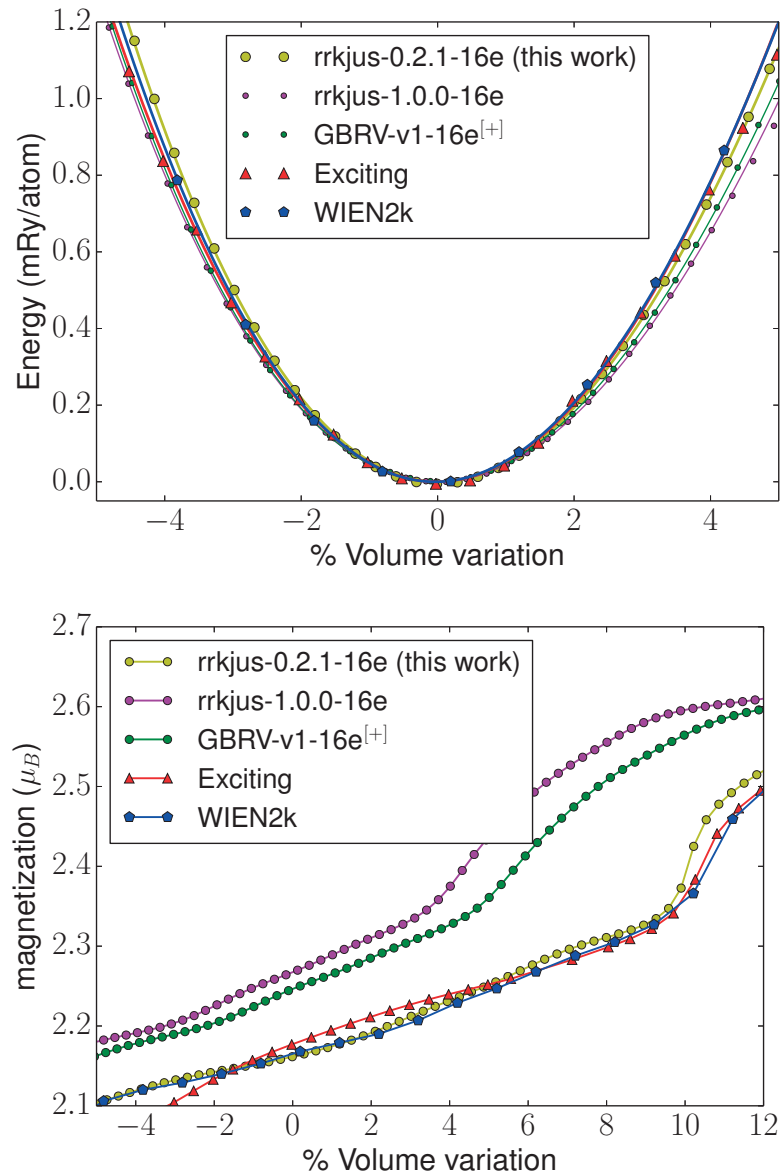


Figure 7.29: Top panel: Equation of state as a function of percent volume change with respect to the theoretical equilibrium configurations for three of the selected PBE pseudopotentials considered in this work (circles). The yellow circles best match the all-electron WIEN2k [173] (pentagons) and `exciting` [174] (triangles) results from Ref. [213,221] and correspond to the `rrkjus-0.2.1-16e` pseudopotential used in this work. Continuous lines are the best fit of the Birch-Murnaghan equation. Bottom panel: Total magnetization as a function of percent volume change. The soft magnetic transition discussed in the text is visible as a clear change in the average slope of the different curves.

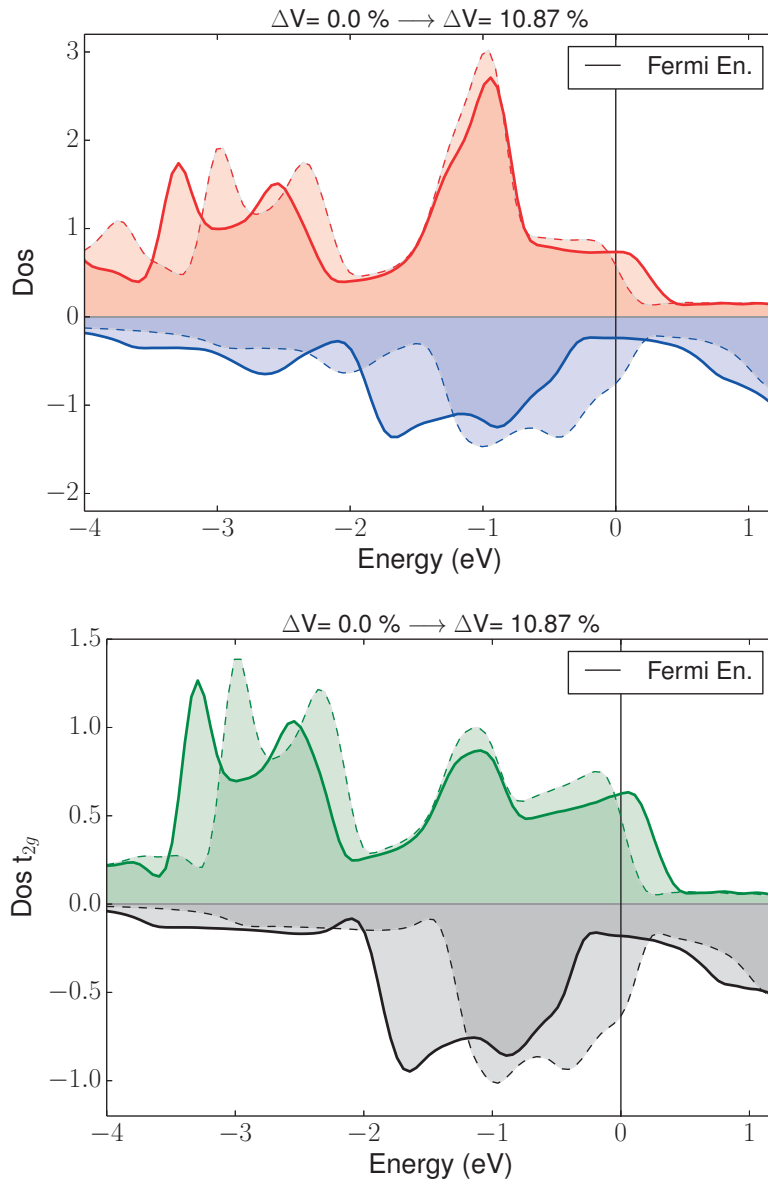


Figure 7.30: Top panel: DOS of majority/minority (red/blue) spin channels at the equilibrium (solid line) and  $\Delta V \approx 11\%$  (dashed line) where, for the pseudopotential used in production run, the magnetic transition takes place. Bottom panel: The contribution of the  $t_{2g}$  electrons to the majority/minority DOS (green/black) is also reported. To obtain a smooth DOS, a non-self-consistent calculation with an offset  $60 \times 60 \times 60$  Monkhorst-Pack  $k$ -mesh is performed on top of a scf loop.

## 7.3 GAP results

Various versions of the potential have been trained to model bcc  $\alpha$ -iron. In what follows, these are identified through the  $GAP_x$  nomenclature,  $x$  being a progressive integer. The higher its value, the larger the number of reference databases (see Sec. 6.6 and Tab 6.11) included in the training process. Through this chapter we analyze the performances of such potentials in terms of selected mechanical and thermal properties and we verify their expected systematic improvement as the database is extended. For clarity reasons, we focus only on a few representative candidate potentials, namely the  $GAP_3$ ,  $GAP_5$  and  $GAP_6$ .

### 7.3.1 Setting of the hyper-parameters and verification

The convergence of the  $GAP_3$  lattice parameter and elastic constants at the equilibrium (no  $zpe$ ) with respect to the hyper-parameters is first considered. The convergence in terms of the cutoff radius  $r_{cut}$  and radial and angular resolution  $n_{max}$ ,  $l_{max}$  of the spherical harmonic expansion of the atomic density, as described in eq. 6.22, is displayed in Tab. 7.7. In these convergence tests the  $n_{max}, l_{max}$  ratio is set to 1 for simplicity; other different ratios are possible and will be investigated with successive potentials with the aim to minimize the computational cost of the GAP prediction while preserving a high predictive accuracy. The results of Tab. 7.7, suggest  $r_{cut} = 5.0 \text{ \AA}$  and  $n/l_{max} = 14$  as good values for  $GAP_3$ . These values are used as a starting point for the generation of successive potential models as  $GAP_5$  and  $GAP_6$ . For all the generated models, the specific values of other (hyper-)parameters are fixed and listed in Tab. 7.8. The selection of these values is based mainly on the experience gained on the Tungsten potentials [152], and their transferability to similar systems is ensured by the GAP framework, which is designed so that its parameters are easy to set and the final potential is not very sensitive to the exact values.

## Chapter 7. Thermodynamic and thermoelastic properties of $\alpha$ -iron

$r_{cut}$ (Å) ( $n/l_{max}=14$ )	$a_0^{el}$ (Å)	$C_{11}^{el}$ (GPa)	$C_{12}^{el}$	$C_{44}^{el}$
4.0	2.833	294	162	101
5.0	2.834	288	155	104
6.0	2.834	289	157	102
7.0	2.834	286	154	105
$n, l_{max}$ ( $r_{cut}=5.0$ )				
10	2.834	288	157	104
12	2.834	288	155	104
14	2.834	288	155	104

Table 7.7: Convergence of the equilibrium lattice parameter and elastic constants as a function of radial cutoff  $r_{cut}$  and radial/angular dependence  $n_{max}, l_{max}$  of the SOAP kernel used in the GAP\_3 fitting procedure. In this tests the  $n_{max}/l_{max}$  ratio is set to 1 for simplicity, future detailed analysis will be performed on the new potentials.

	GAP_3	GAP_5	GAP_6
$r_{cut}$ (Å)	5.0	5.0	5.0
$r_{\Delta}$ (Å)	1.0	1.0	1.0
$\zeta$	4	4	4
$t$	2	2	2
$\sigma_{atom}$ (Å)	0.5	0.5	0.5
$n_{max}$	14	14	14
$l_{max}$	14	14	14
$\sigma_w$ (eV)	1.0	1.0	1.0
$\sigma_{v_{Eifl\sigma}}$ (eV <sub>at</sub> , eV/Å, eV <sub>at</sub> *)	[0.001, 0.1, 0.1]	[0.001, 0.1, 0.1]	[0.001, 0.1, 0.1]
Sparse atomic envir.	5000	8000	8000
Training database	DB1.a,DB2.a	DB1.b,DB2.b,DB3,DB4	DB1.b,DB2.c,DB3.a,DB4.a

Table 7.8: List of parameters and hyper-parameters for the generation of GAPs with a SOAP kernel. The symbols  $\sigma_{v_{Eifl\sigma}}$  refer to the different errors assumed on the total energy, the atomic forces and the stresses respectively. \*The virial stress is provided in eV. The databases DB1.a/DB2.a and DB1.b/DB2.b differ by the presence in the  $b$  version of extra configurations (54 atoms for the DB2 case) at an expanded volume corresponding roughly to +3% of volume expansion (+1.17%  $a_0^{el}$ , 0.98%  $a_0^{zpe}$ ). The DB2.c includes extra configurations (128 atoms with +1.17% and  $\pm 0.7\%$   $a_0^{el}$ ) on top of the DB2.b data.



### 7.3.2 Validation

#### Equilibrium lattice constant, bulk modulus and equation of state

All the potential models are validated comparing against DFT data not included in the training set. The equilibrium lattice parameter and the energy vs. volume curve are first considered; the calculated values are reported in Tab. 7.9 and in Fig. 7.31 respectively. The equilibrium lattice parameter, bulk modulus and pressure derivative of the bulk modulus  $B'$  are extracted from a Birch-Murnaghan [202], Vinet [224] fit (and compared to a Gaussian Process (GP) fit – see Appendix A) of the energy/volume curves. The results for the lattice and bulk modulus are stable with respect to the different fitting procedures, with respect to the potential models and in accordance with the DFT data. As visible from Fig. 7.31, the maximum energy differences in the DFT and GAP curves are within the 0.5 meV across the range of volumes considered [-3%:+6%]  $a_0^{el}$ . This is consistent with the 1 meV error assumed on the total energy DFT data in the training process. The elastic constants of GAP\_5 and GAP\_6 do not differ from those of GAP\_3 and are in reasonable agreement with the the DFT data in Tab. 7.10 [45].

	$a_{BM/V/GP}^{el}$ (Å)	$B_{0(BM/V/GP)}^{el}$ (GPa)	$B'_{BM/V/GP}$	$\Delta_{BM}$ (meV/at)
GAP_3	2.834/2.834/2.830	199.5/199.5/200.2	2.8/2.8/-	1.10
GAP_5	2.834/2.834/2.833	198.0/198.0/197.4	3.7/3.7/-	1.24
GAP_6	2.834/2.834/2.833	198.0/198.0/197.5	3.7/3.7/-	1.24
QE	2.834/2.834/2.834	202.8/202.8/204.1	7.0/7.0/-	-

Table 7.9: Optimized equation of state parameters from Birch-Murnaghan (BM), Vinet (V), and Gaussian Process (GP) fit (see Appendix A — Squared exponential kernel and hyper-parameters  $\theta = 1e-04$ ,  $\lambda = 0.24$ ,  $\sigma = 4e-06$ ). The  $\Delta$  value is calculated following Ref. [212] with respect to Quantum Espresso DFT data. The DFT parameters are those specified in Sec. 6.6.6. The reference volume range on which both the QE and GAP equations are fitted is [-3%,+3%].

#### Point defects: mono-, di- vacancies and self-interstitials

In Tab. 7.10 we report the computed equilibrium mono-vacancy formation energy for GAP\_3, GAP\_5, GAP\_6 and we note that, while the GAP\_3 gives a wrong value, the other models are in good agreement with DFT. We also compute the same quantity for the GAP\_5, GAP\_6 potentials at different volumes to compare with available DFT data (see Fig. 7.32) and, again, we find good reasonable values for the GAP models. For the sake of completeness, the mono-vacancy formation enthalpy for the GAP\_5 is also reported in Fig. 7.33. Then we compute the minimum energy path for a first and second-nearest neighbor vacancy diffusion through a nudged elastic band (NEB) [225] calculation. The curves are reported in Fig. 7.34 for the GAP\_6 model and provide also the migration energy barrier (taken as the maximum height energy value) for the considered mechanism. The migration energy data, including a third nearest-neighbor case, are reported in Tab. 7.10. Next, the first, second and third nearest-neighbor di-vacancy formation energies and associated binding energies are calculated at the equilibrium volume for the GAP\_5 and GAP\_6 models, according to eqs. (6.28, 6.30). The GAP\_5, GAP\_6 results

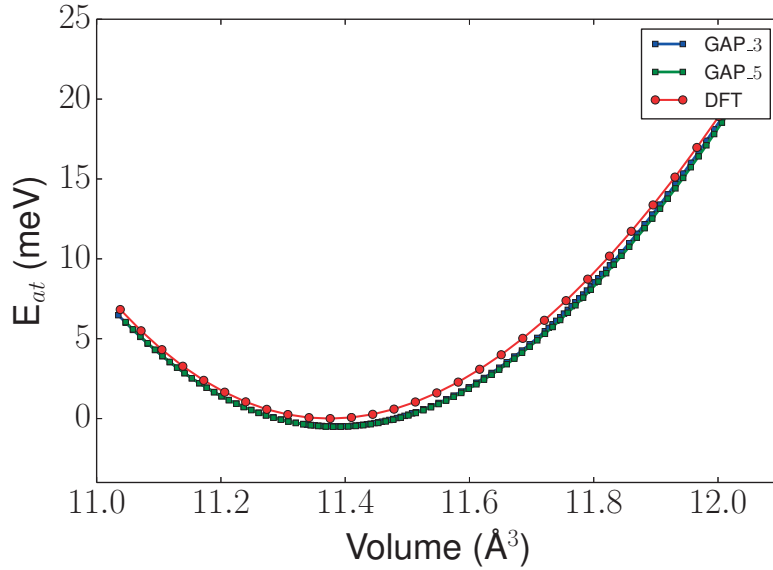


Figure 7.31: Energies as a function of volume of bcc iron obtained from GAP\_3 and GAP\_5 compared to DFT data (The GAP\_6 curve is not reported since is essentially equivalent to the GAP\_5 case). The energy difference between the GAP curves and the DFT one across the volume range herein considered is within 0.5 meV/at. The volume spanned is roughly equivalent to [-3%,+6%] of the ground state equilibrium lattice.

are reported in Tab. 7.10 and agree qualitatively only with the DFT data for the second and third nearest-neighbor di-vacancy configurations (although slightly underestimated). This result is not surprising since only few third nearest-neighbor di-vacancy configurations has been included in the training of these models. As discussed in Sec. 6.6.3, a future extension of the database is planned to take into account second and first nearest-neighbors di-vacancies. Other defects that we have considered are the self-interstitials, considering in particular the octahedral, tetrahedral, dumbbell<sub>100</sub>, dumbbell<sub>110</sub>, dumbbell<sub>111</sub> configurations. These are in fact considered the most important simple interstitials in iron [34]. The bulk equilibrium formation energies of GAP\_6 are reported in Tab. 7.10 and also in Fig. 7.35. The absolute values of the self-interstitial formation energies are roughly 1 eV larger than DFT from this work and 1.5 eV larger than DFT values available in the literature. Interestingly, however, the dumbbell<sub>110</sub> configuration has the lowest energy as predicted by DFT studies, and the energy landscape in the space of the selected self-interstitial defects agrees nicely with the one from DFT despite the absence of any self-interstitial configuration included in the training database.

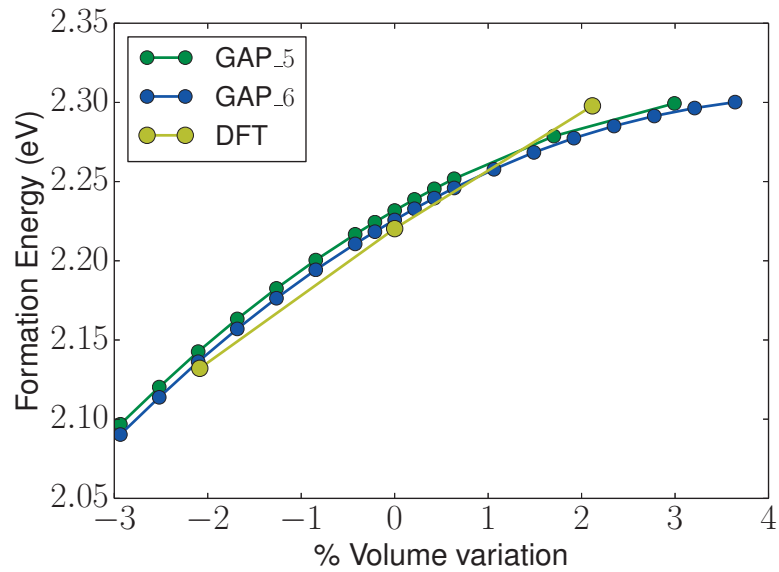


Figure 7.32: Vacancy formation energy of GAP\_5, GAP\_6 and DFT from Quantum espresso calculated at different volumes (here we use the variation with respect to the electronic equilibrium case). The GAP results are obtained from a reference bulk supercell containing 2000 atoms while the DFT data are extracted from a reference 54 atoms cell. See Tab. 7.6 for the convergence with respect to the cell size.

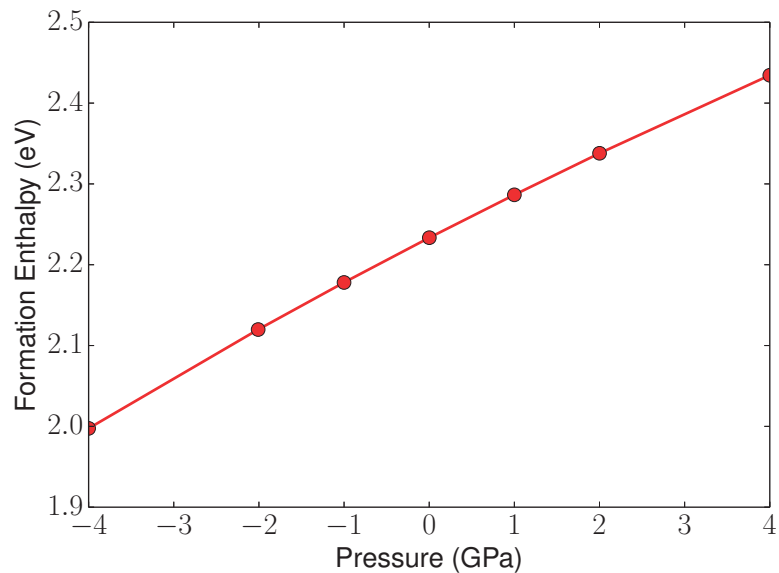


Figure 7.33: Vacancy formation enthalpy of GAP\_5 at different pressures. The calculations are performed with a reference bulk supercell containing 2000 atoms.

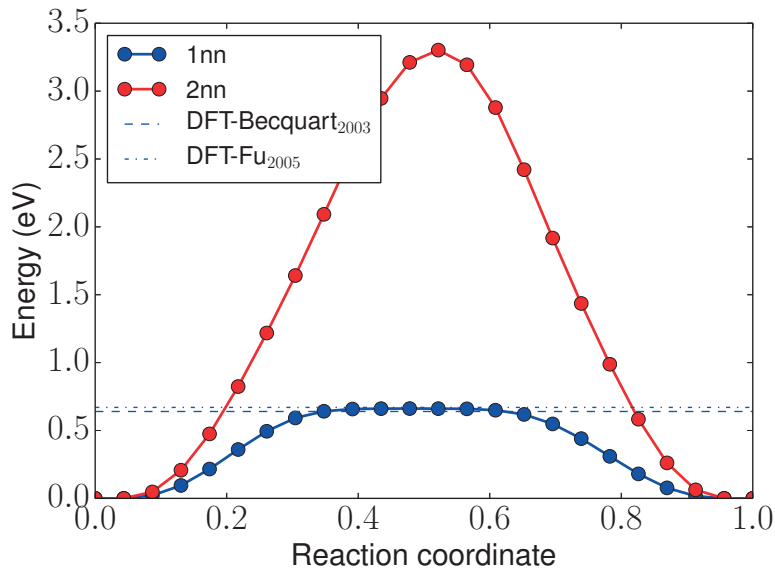


Figure 7.34: Minimum energy path from NEB calculation for the diffusion of a mono-vacancy to a first- and second-nearest neighbor sites for the GAP\_6 potential. The calculation are performed with a 53 atoms supercell using atoms-relaxed initial and final replicas. The associated migration energy barriers are reported in Tab. 7.10. Differently from other EAM potentials like de Mendeleev03, and in accordance with DFT results from the literature [34], no double hump is found for the first-nearest neighbor migration profile. The DFT migration energy barriers from Refs. [210, 226] are also reported for comparison.

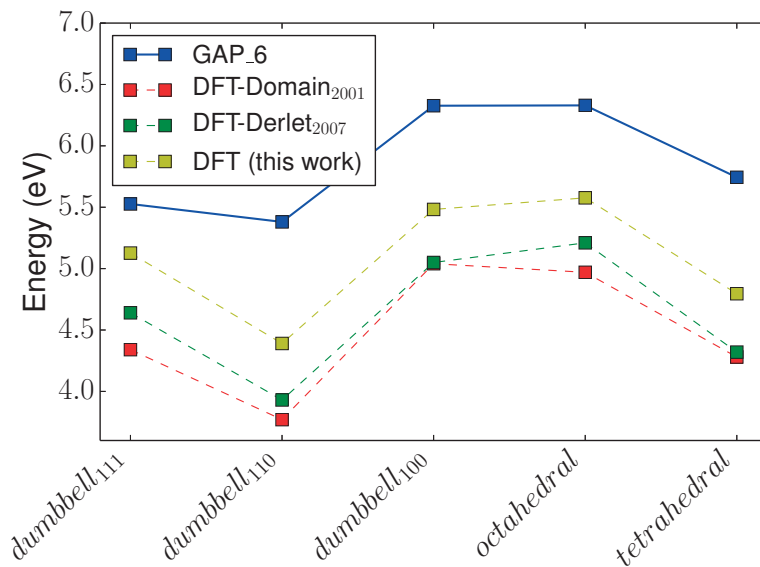


Figure 7.35: Selected self-interstitial formation energies obtained for the GAP\_6 potential. The calculations are performed in a  $10 \times 10 \times 10$  cubic supercell containing 2001 atoms to minimize the residual stress associated to this kind of defects. The data are compared to DFT values calculated in this work, from Ref. [34] (DFT<sub>1</sub>) and Ref. [227] (DFT<sub>2</sub>).

### Phonons

The phonon dispersion is also calculated for the three potential models along high symmetry directions in the first BZ at different volumes spanning the region of thermodynamic stability of  $\alpha$ -iron predicted by DFT quasi-harmonic theory [45]). For each volume, the dynamical matrices of the GAP potentials are obtained with a frozen phonon method using a  $10 \times 10 \times 10$  supercell and finite displacement of  $0.1 \text{ \AA}$ . These are then interpolated on a denser  $22 \times 22 \times 22$  mesh to give the phonon frequencies. According to the literature and some tests, these parameters provide well converged frequency values. The phonon dispersion calculated at the equilibrium volume and at a reference expanded volume corresponding approximately to the QHA equilibrium volume at 1000 K data, are compared to DFT results (obtained with a DFPT approach as described in Sec. 7.2) in Figs. 7.36. The overall agreement between GAP and DFT is good, although, especially for the GAP\_3 case, it tends to deteriorate as the volume is expanded. At the  $N$  point, for instance, GAP\_3 predicts much lower frequency values than DFT. This deterioration can be explained with the fact that the GAP\_3 potential has not been trained to deal with very expanded volumes (see Tab. 7.8). In fact, as expected, this behavior can be systematically corrected through the inclusion of new training environments (*in primis* the bulk expanded-volume configurations of DB2.b and DB2.c), as visible looking at the GAP\_3  $\rightarrow$  GAP\_5  $\rightarrow$  GAP\_6 evolution of the phonon dispersions upon volume expansion. The extension of the database introduces also second order effects that affect locally the phonon dispersion accuracy. An example is the decrease of the GAP\_5/6 frequency around  $H$  compared to GAP\_3 (and DFT). These effects can be however controlled with the sparsification procedure by reducing or increasing relative weights of different types of atomic environments that compose the full database. A further quantity that is important to the thermal expansion is the phonon softening. For this reason, we also report the difference in the phonon frequencies at the electronic equilibrium volume and at the +3.0% electronic volume for the three GAP models in Figs. 7.39. The curves show the improved softening of the GAP dispersions as the potential model is refined by inclusion of extra databases.

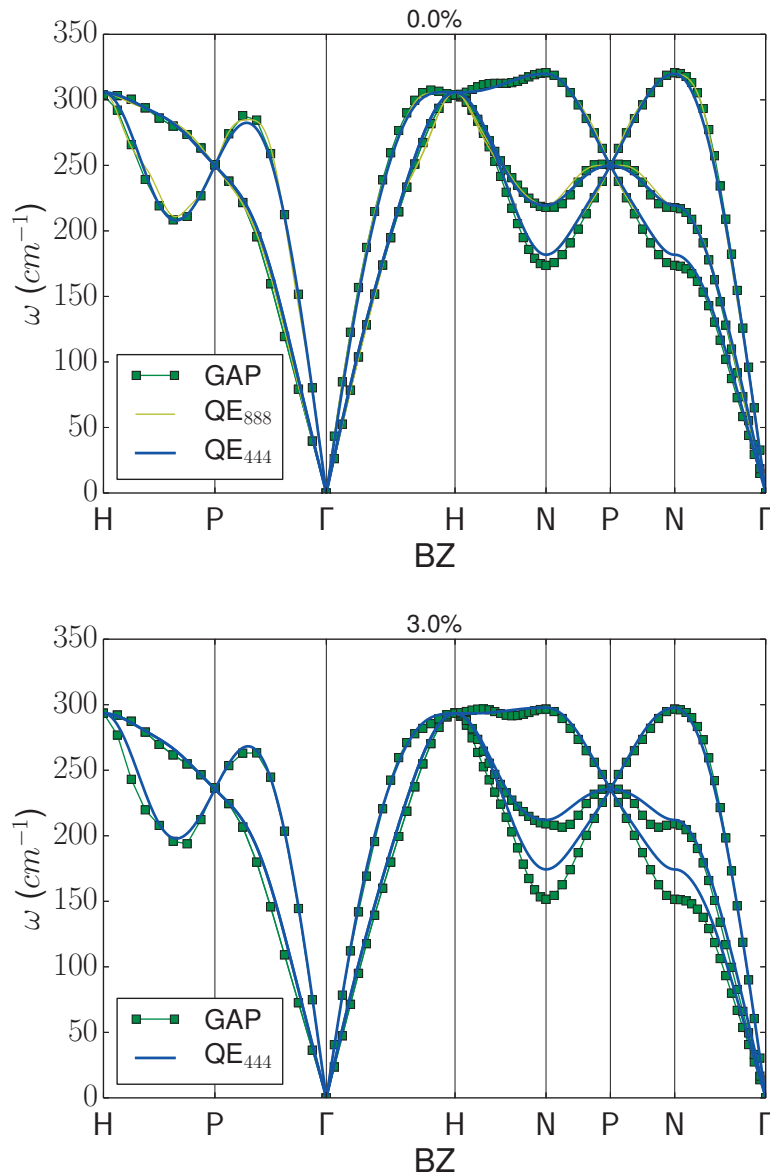


Figure 7.36: Phonon dispersions from frozen phonon GAP\_3 and Quantum Espresso DFPT calculated at the electronic equilibrium volume (Top panel – +0.0%) and at an expanded volume corresponding roughly to the equilibrium value at 1000 K (Bottom panel – +3.0%). The GAP\_3 data (green squares) are obtained computing the dynamical matrix on a  $10 \times 10 \times 10$  and interpolating it on a denser  $22 \times 22 \times 22$  grid to get the phonon frequencies along high symmetry directions. The results are compared to Quantum Espresso DFPT values obtained from a Fourier interpolation on a  $21 \times 21 \times 21$  mesh (blue continuous line) of the phonon frequencies calculated explicitly on a  $4 \times 4 \times 4$  mesh (and  $8 \times 8 \times 8$  at the equilibrium – yellow continuous line).

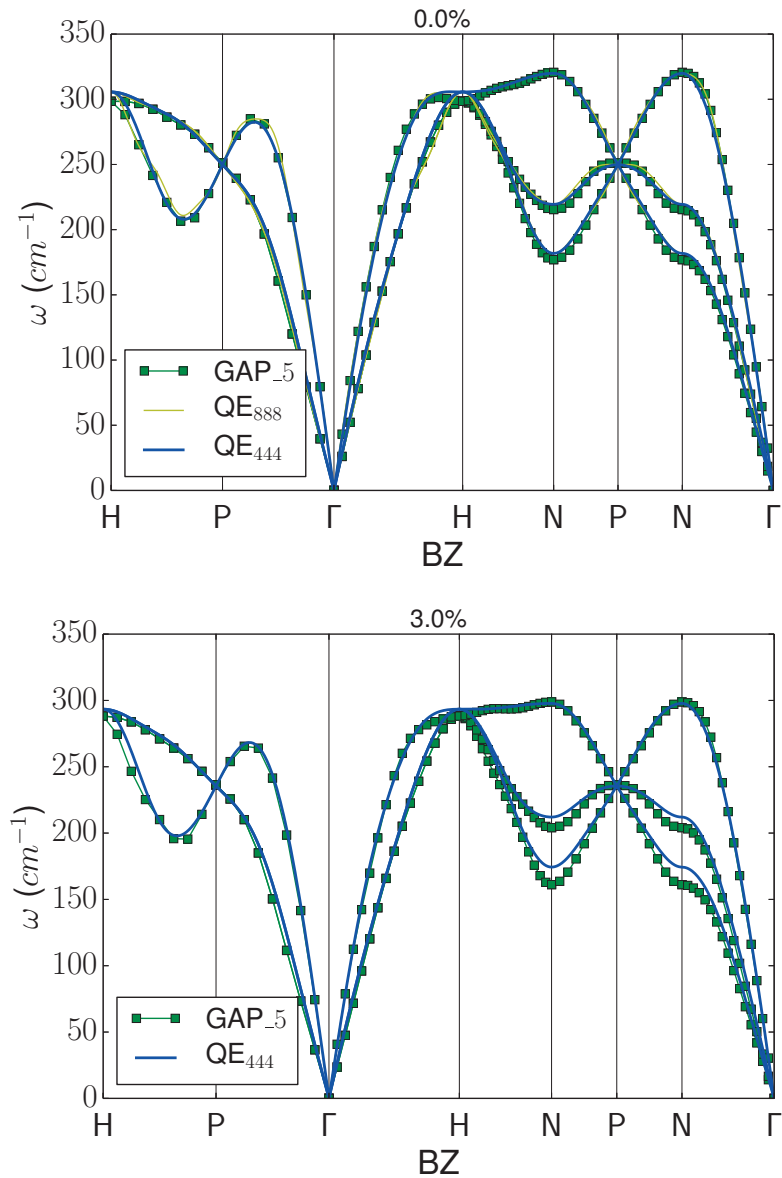


Figure 7.37: Phonon dispersions from frozen phonon GAP\_5 and Quantum Espresso DFPT calculated at the electronic equilibrium volume ( Top panel – +0.0%) and at an expanded volume corresponding roughly to the equilibrium value at 1000 K (Bottom panel – +3.0%). Calculation details same as Figs. 7.36.

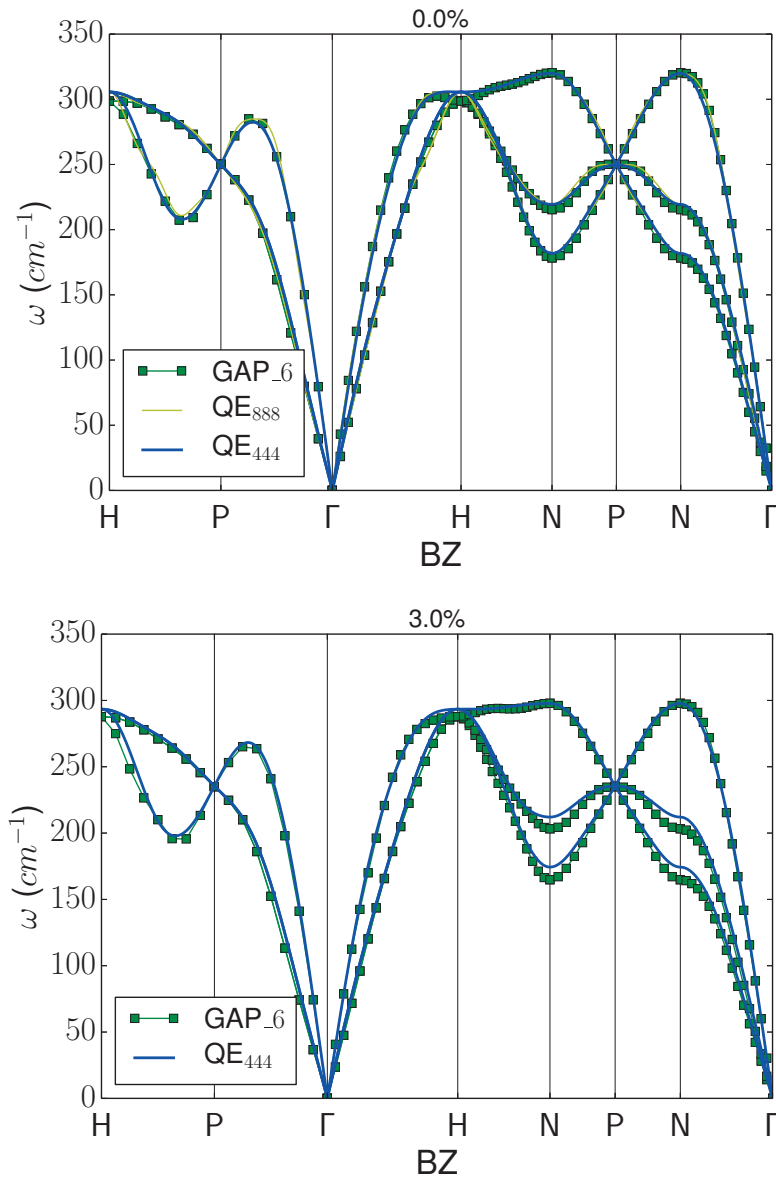


Figure 7.38: Phonon dispersions from frozen phonon GAP\_6 and Quantum Espresso DFPT calculated at the electronic equilibrium volume ( Top panel – +0.0%) and at an expanded volume corresponding roughly to the equilibrium value at 1000 K (Bottom panel – +3.0%). Note the improved behavior at  $N$  especially in the expanded configuration compared to the GAP\_3 case. Calculation details same as Figs. 7.36.



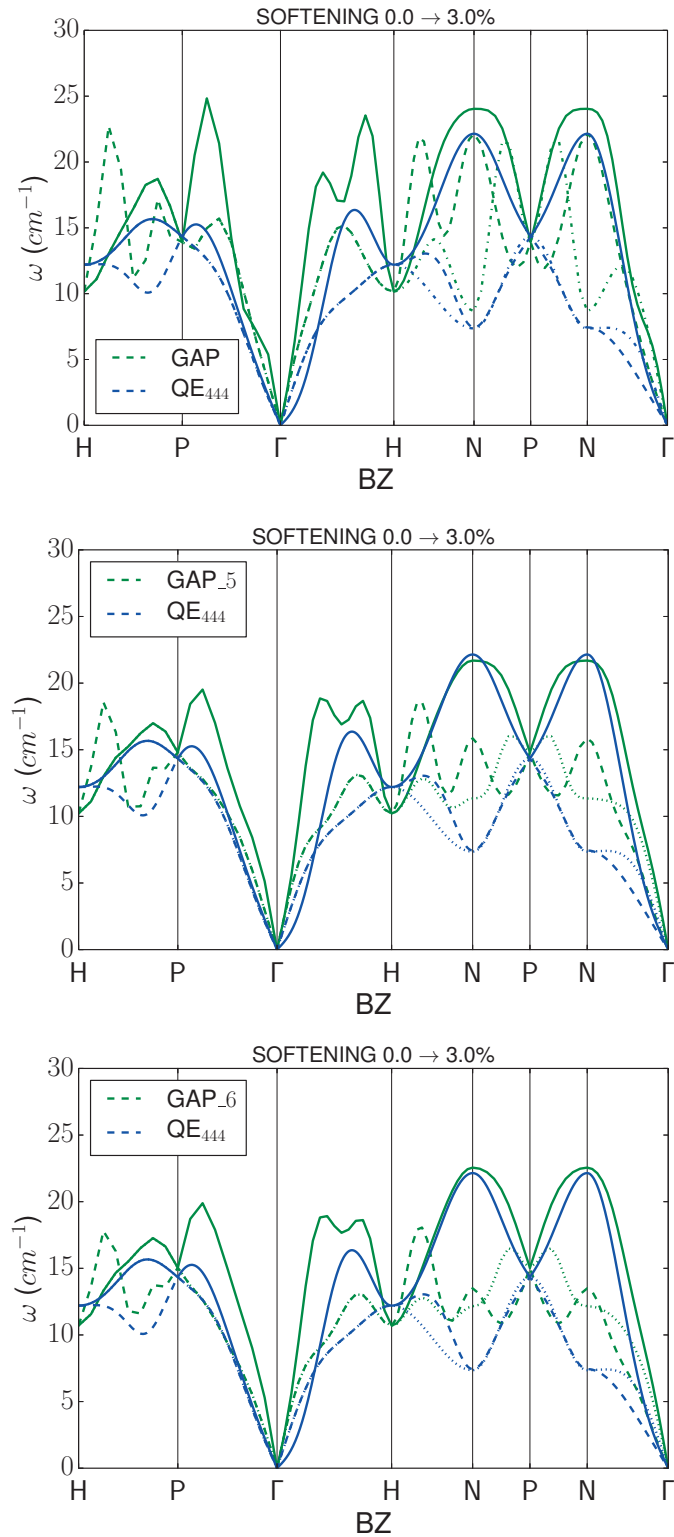


Figure 7.39: Phonon dispersion softening of the GAP models compared to Quantum Espresso DFPT data. The softening is computed as the frequencies difference between the electronic equilibrium volume and the +3.0% electronic volume. Calculation details same as Figs. 7.36.

### Thermal properties from MD

In order to analyze the thermal properties of the GAP models we first compute the thermal expansion curves. These are obtained from NPT MD simulations relaxing the cell volume at its zero pressure equilibrium configuration for a given temperature. The pressure is controlled through a Parrinello-Rahman barostat [197] while a Nose-Hoover chain thermostat [198] is used to keep constant the average temperature as implemented in the LAMMPS [199] package. Each MD run is initialized from a bcc supercell with slightly randomized atomic positions, and with initial velocities from a Maxwell-Boltzmann distribution. During MD simulations, the time-step is fixed at 1 fs, and the relaxation times of the barostat and thermostats are set to be 1 ps and 0.1 ps, respectively. Each simulation is carried out for 100 thousand steps, equivalent to 100 ps. The first 2.0 ps are used for thermalization and equilibration of the system, while the remaining are used for accumulating the thermodynamics averages. The system consists of 2000 atoms in a  $10 \times 10 \times 10$  cubic supercell with PBCs.

The results are displayed in Fig. 7.40 showing good agreement with QHA DFT data in terms of temperature dependence and absolute values. The agreement in the thermal behavior is also remarkable if compared to the experimental data. On the other hand, as exhaustively discussed in the DFT chapter, the absolute values differ from the experimental ones due to the choice of the DFT functional used in generating the training set. The GAP curves slowly diverge only at high temperature, thus suggesting the potentials are able to describe a stable bcc-phase up to the experimental melting point. For sake of completeness, the (linear) coefficient of thermal expansion is also reported in Fig. 7.42.

The temperature-volume relation allows also to calculate the temperature dependence of other relevant thermodynamic equilibrium quantities like the heat capacity. The results in this case are shown in Figs. 7.43 and are obtained as derivative of a spline interpolation of the Enthalpy as a function of temperature obtained, in turn, from NVT runs with same supercell size, time step, thermostat details, and simulation length as before.

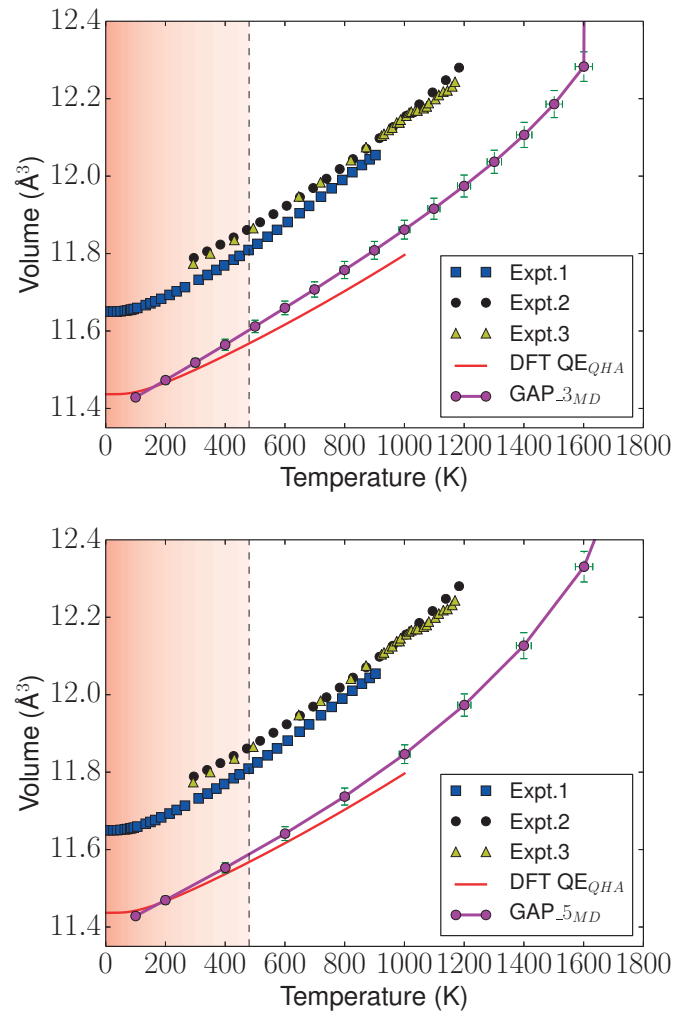


Figure 7.40: Thermal expansion curves of the GAP models obtained from NPT MD simulations with a zero target pressure (solid magenta curves). The standard deviation is also reported for each calculated point both in temperature and in volume. The results are compared to QHA DFT values [45] (solid red curves) and experiments – Expt.1 [163] (blue squares), Expt.2 [228] (black circles), Expt.3 [164] (yellow triangles). The red-shaded region highlights the temperature range below the Debye point where statistical quantum effects, that are not included in classical MD, become increasingly important. The low temperature linear behavior of the MD curve, as opposed to the quadratic QHA result, is a direct consequence of such wrong statistics.

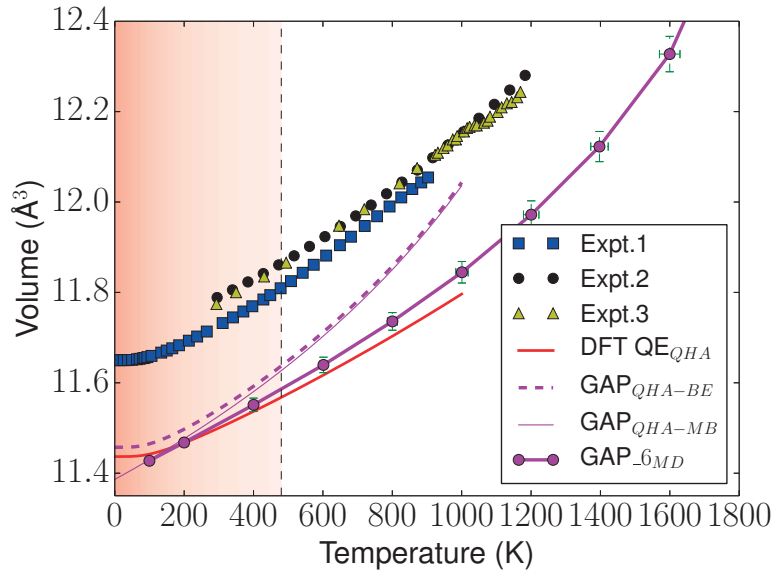


Figure 7.41: Thermal expansion of the GAP\_6 model as from Fig. 7.40. The solid magenta curve is obtained from NPT MD simulations with a zero target pressure and is reported with its standard deviation in temperature and volume at each calculated point. The dashed magenta curve is the GAP\_6 QHA expansion with the proper quantum Bose-Einstein (BE) occupation function, while the thin solid line is obtained using a classical Maxwell-Boltzmann (MB) occupation function. Note that the BE curve reproduces the expected experimental “quadratic” behavior at low temperature converging to the ZPE corrected equilibrium volume at  $T = 0$ , while the MB curve displays a linear behavior converging at low temperature to the MD result and, finally, to the ZPE uncorrected electronic equilibrium volume at  $T = 0$ . Note also that at low temperature, within the Debye point, the GAP\_6 QHA BE result agrees with the solid red curve, namely the QE QHA BE result from Ref. [45] (except for a small mismatch stemming from the slightly different electronic equilibrium volumes) while, above is, deviates from both the QE QHA and the GAP\_6 MD curve. This mismatch originates from the apparently small differences in the softening of the phonons with the volume (see Fig. 7.39) and highlights the sensitivity of this method with respect to the details of the phonon dispersion. The results are also compared to experiments – Expt.1 [163] (blue squares), Expt.2 [228] (black circles), Expt.3 [164] (yellow triangles). As above, the red-shaded region highlights the temperature range below the Debye point where statistical quantum effects, that are not included in classical MD, become increasingly important.

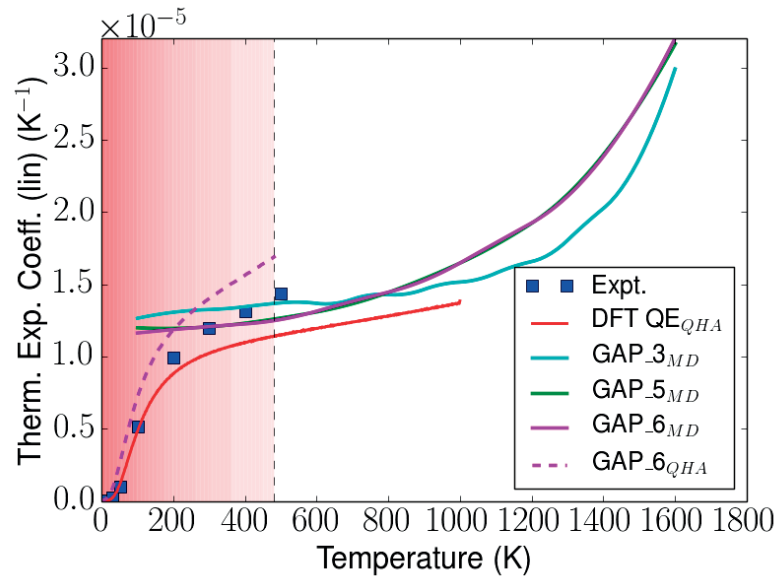


Figure 7.42: Linear thermal expansion coefficient curves of the GAP models obtained from NPT MD simulations with a zero target pressure (solid magenta curves). The results are compared to QHA DFT values [45] (solid red curves) and experiments – Expt.1 [182] (blue squares). The red-shaded region highlights the temperature range below the Debye point where statistical quantum effects, that are not included in classical MD, become increasingly important.

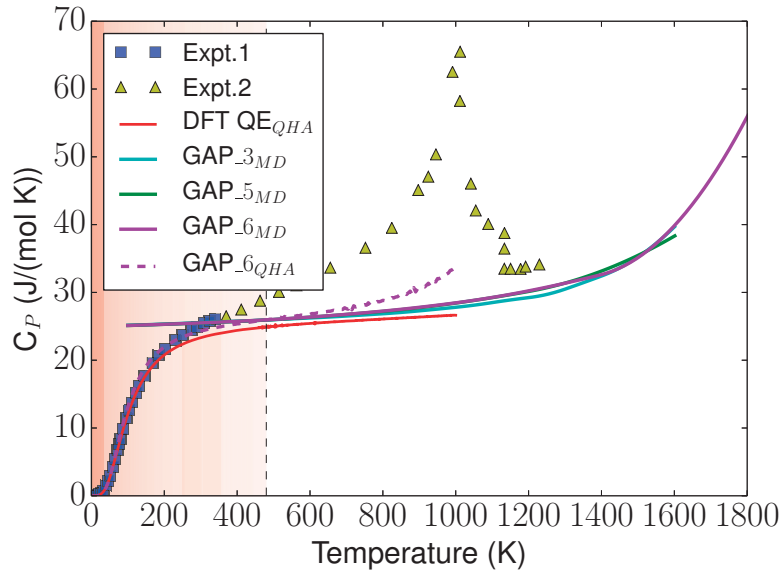


Figure 7.43: Heat capacity of the GAP models obtained as cubic spline derivative of the Enthalpy as a function of temperature from NVT MD simulations at the equilibrium volumes (green solid lines). The results are compared to QHA DFT values [45] (solid red curves) and experiments – Expt.1 [183] (blue squares), Expt.2 [184] (yellow triangles). The red-shaded region highlights the temperature range below the Debye point where statistical quantum effects, that are not included in classical MD, become increasingly important. The heat capacity of the potential from classical MD converges as expected to the Petit-Dulong limit rather than approaching the zero value predicted by a proper quantum Bose-Einstein statistics. Moreover, as described in Ref. [69] instead, the divergence at the Curie point of 1043 K is related to magnetic disorder effects and magnetic degrees of freedom that are not explicitly taken into account neither in classical MD nor in QHA data from Ref. [45].

### Thermal properties from quasi-harmonic theory

We have also computed some of the relevant thermodynamic quantities of the GAP\_6 model from quasi-harmonic theory in a fashion similar to Sec. 7.2. The QHA naturally describes the low temperature behavior of the thermodynamic properties considered by accounting for the statistical quantum Bose-Einstein effects. As such it should be the reference to consider for a comparison with experiments at low temperature. On the other hand, at variance with MD simulations, it takes into account phonon-phonon anharmonic effects only partially. From the vibrational QHA Helmholtz free energy we compute thermal expansion, its (linear) expansion coefficient, the heat capacity at constant volume and constant pressure, and the bulk modulus. The results are reported in Figs. 7.41, 7.42, 7.43, 7.44 and show essentially the GAP\_6 displays a DFT accuracy below the Debye point. Above it, the results deviate both from the QHA DFT and GAP MD ones. This deviation can be traced back to the details of the GAP phonon softening and their differences with respect to the DFT case. In particular, the over-expansion of the equilibrium lattice parameter as a function of temperature influences the values of all the other calculated thermodynamic quantities.

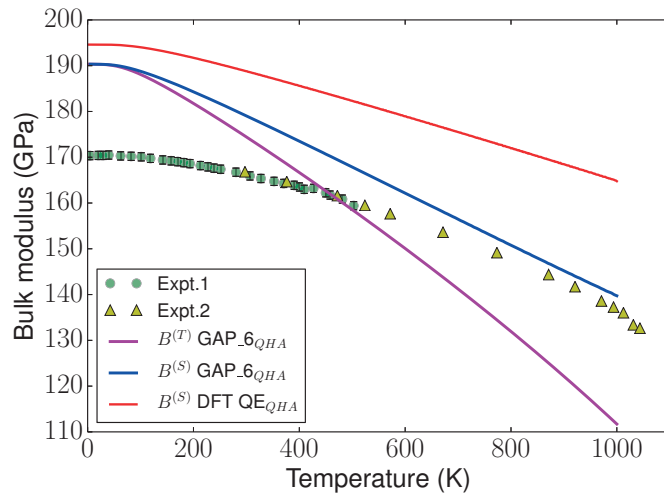


Figure 7.44: Isothermal  $B^{(T)}$  (blue continuous line) and adiabatic  $B^{(S)}$  (magenta continuous line) bulk moduli from quasi-harmonic theory of GAP\_6. The GAP\_6 adiabatic bulk modulus is compared to same quantity obtained from DFT QE QHA and is also compared ultrasonic measurements from Ref. [162] (Expt.1 – green circles) and from Ref. [189] (Expt.2 – yellow triangles). The GAP\_6 results start to deviate significantly from the QE results already from 200 K. However, as already seen from the previous graphs, a comparison between GAP\_6 and QE data is questionable above the Debye point.

## Chapter 7. Thermodynamic and thermoelastic properties of $\alpha$ -iron

	Expt.	DFT (this work)	GAP_3	GAP_5	GAP_6	Other Calcs.
$a_0^{el}$ (Å)	2.856 [163]	2.834	2.834	2.834	2.834	-
$B^{el}$ (GPa)	170.3 [162]	199.8	199.8	198.6	198.6	-
$C_{11}^{el}$	239.5 [162]	296.7	288.8	288.3	288.3	-
$C_{12}^{el}$	135.7 [162]	151.4	155.2	153.8	153.8	-
$C_{44}^{el}$	120.7 [162]	104.7	105.0	104.5	104.5	-
$E_f^v$ (eV)	1.6, 2.2 [207,208]	2.22	0.829	2.23	2.23	2.10 [209]
$E_{m1NN}^v$	-	-	-	-	0.66	0.64 [210],0.67 [226]
$E_{m2NN}^v$	-	-	-	-	3.20	-
$E_{m3NN}^v$	-	-	-	-	6.82	-
$E_f^{1NNv}$	-	4.24	1.289	4.503	4.491	4.01 [209]
$E_f^{2NNv}$	-	4.20	1.642	4.284	4.271	3.95 [209]
$E_f^{3NNv}$	-	4.45	1.667	4.495	4.481	-
$E_b^{1NNv}$	-	0.20	0.362	-0.037	-0.035	0.14, 0.08 [209,210]
$E_b^{2NNv}$	-	0.24	0.010	0.182	0.185	0.28, 0.15,~0.2 [35,209–211]
$E_b^{3NNv}$	-	-0.01	-0.015	-0.029	-0.026	-0.02 [210]
$E_{f(110)}^{SIA}$	-	4.37	-	-	5.38	3.93 [227]
$E_{f(111)}^{SIA}$	-	5.13	-	-	5.53	4.64
$E_{f(100)}^{SIA}$	-	5.48	-	-	6.327	5.05
$E_{f_{tet}}^{SIA}$	-	4.79	-	-	5.744	4.32
$E_{f_{oct}}^{SIA}$	-	5.58	-	-	6.329	5.21
$E^{110}$ (J/m <sup>2</sup> )	-	2.495	-0.088	2.514	2.513	-
$E^{100}$	-	2.543	0.147	2.538	2.539	-
$E^{211}$	-	2.629	-0.172	2.604	2.604	-
$E^{111}$	-	2.752	0.222	2.750	2.750	-

Table 7.10: Electronic (no zpe) lattice parameter  $a_0^{el}$ , electronic bulk modulus  $B^{el}$ ,  $C_{11}^{el}$ ,  $C_{12}^{el}$ ,  $C_{44}^{el}$  elastic constants, mono-vacancy formation energy  $E_f^v$ , first, second, third nearest-neighbor migration energy barriers  $E_{m1NN}^v$ ,  $E_{m2NN}^v$ ,  $E_{m3NN}^v$ , first, second, third nearest-neighbors divacancy formation and binding energies (enthalpies)  $E_f^{1NNv}$ ,  $E_f^{2NNv}$ ,  $E_f^{3NNv}$ ,  $E_b^{1NNv}$ ,  $E_b^{2NNv}$ ,  $E_b^{3NNv}$  (using 128 atoms DFT data), the  $\langle 110 \rangle$ ,  $\langle 100 \rangle$ ,  $\langle 111 \rangle$  dumbbell, tetrahedral and octahedral self-interstitial formation energies  $E_{f(110)}^{SIA}$ ,  $E_{f(100)}^{SIA}$ ,  $E_{f(111)}^{SIA}$ ,  $E_{f_{tet}}^{SIA}$ ,  $E_{f_{oct}}^{SIA}$ , and the [100], [110], [111], [211] free surface formation energies  $E^{100}$ ,  $E^{100}$ ,  $E^{211}$ ,  $E^{111}$  (per unit area) computed from DFT and successive versions of GAP models.



## 8 Conclusions and future directions

We started this work surveying a selection of EAM potentials for bcc-iron in order to understand their strengths and limitations in terms of vibrational and elastic properties at finite temperature. To this end, we have used a classical MD approach that accounts for phonon-phonon anharmonic contributions while neglecting quantum statistical effects. Our calculations show that all the potentials, on average, deviate from experimental results at high temperature. Moreover, in more detail, we found anomalies in the  $C_{44}$  of the Mendeleev03 potential and in the  $C'$ ,  $C_{12}$  and  $B$  of the Meyer98 potential that one should be aware of when studying finite temperature mechanical properties of either elemental iron or iron alloys with these potentials. Despite the anomaly in the  $C_{44}$  shear elastic constant, the Mendeleev03 potential appears to be on average the most accurate EAM parameterizations analyzed. This result conforms to that of other studies available in the literature [34, 176, 177] where different EAM potentials for iron have been studied in terms of other fundamental properties.

As a second step, we computed the thermodynamic and thermoelastic properties and the energetics of defects at zero temperature from density-functional theory (DFT). Due to the notorious difficulties of DFT in describing the combined metallic and magnetic nature of iron, we decided to accurately verify and validate our plane-wave spin-polarized pseudopotential-based implementation against selected zero temperature all-electron calculations. According to this analysis, DFT-GGA provides a reasonable description of the zero temperature equilibrium properties, although revealing discrepancies with experiments that are larger than what is typically found for semiconductors, insulators or nonmagnetic metals. We found GGA to underestimate the experimental lattice parameter (about 1% for GGA-PBE, 2% for the GGA-PBEsol), while overestimating the bulk modulus (about 16% for GGA-PBE, 38% for GGA-PBEsol). Recent results on iron and non-magnetic metals [229, 230], suggest that RPA correlations might improve considerably the agreement with the experiments. It would therefore be interesting to extensively investigate the zero temperature geometric and elastic properties of iron by means of RPA, or other beyond-GGA schemes as DFT+U(+J). An extensive analysis of the elastic properties with the latter approach shall be addressed in a future work. The finite temperature analysis has been carried out making use of the quasi-harmonic approximation,

## Chapter 8. Conclusions and future directions

---

assuming a ferromagnetic configuration, and allowing for the relaxation of the longitudinal part of the magnetic moment. We neglected as a whole the transverse degrees of freedom although these proved to be fundamental for the description of ferro- to para-magnetic transition and for a correct description of the relative stability of the different structural phases of iron at high temperature [66, 69, 187, 189, 231]. Despite this approximation, the results of the quasi-harmonic analysis show that the thermal trend of the elastic and selected thermodynamical properties are well described up to a large fraction of the Curie point. Finally, we showed the band electronic excitations improve the description of the high temperature bending of the bulk modulus while producing only marginal effects on the calculated thermal expansion and heat capacity.

The last part of the thesis was devoted to the development of GAP models for the  $\alpha$ -phase of iron. The Gaussian approximation potentials are introduced as an attempt to create inter-atomic potentials that are systematically improvable upon extension of the training database. At variance with semi-empirical potentials where a simple parametrized functional form is used for the atomic energy function, the GAPs are based on a non-linear, non-parametric Gaussian-process regression which maximizes the flexibility of the model requiring however an extensive dataset to ensure transferability. We constructed a database of total energies, stresses and forces taken from first-principles molecular dynamics simulations of pristine and defected bulk systems, and of surfaces with different crystallographic orientations, covering roughly  $10^5$  local atomic environments. We then developed and tested different GAP models. The latest model, namely the GAP\_6, proved to be able to reproduce the equilibrium electronic lattice parameter, the elastic constants, the mono-vacancy formation energy at different volumes, the first nearest-neighbor migration energy barrier, partially the di-vacancy formation and binding energies, and the (100), (110), (111), (112) bulk terminated surface formation energies. Interestingly, the energy landscape of selected self-interstitials agrees qualitatively with DFT results despite the absence of any self-interstitial information in the training set. The phonon dispersion and its volume softening are also reasonably well reproduced. The thermal expansion, the thermal expansion coefficient and the heat capacity from MD also reproduce the DFT results up to the experimental Curie point. The potential also displays a stable bcc structure up to 1800 K, i.e., the experimental melting temperature. This work provides therefore a robust starting point for the generation of refined GAP potentials for iron that can continue well beyond the end of this doctoral project. In fact, further atomic environments such as multi-vacancies, voids, self-interstitials, and further  $\gamma$ -surfaces that have been already pointed out in Sec. 6.6, will be also included in future databases in order to train potentials that can be used to tackle problems of current scientific and technological relevance. In particular, we are extremely interested in the study of the energetics and kinetics of dislocations and their interaction with other defects, of crack-tip evolution, as well as in the study of radiation damage effects in bcc iron and ultimately in high strength, low carbon ferritic steels that are used in plasma fusion tokamak reactors. To this end, it would be important to extend the GAP models to include hydrogen and carbon thus allowing also the study of hydrogen embrittlement or cementite segregation and precipitation in ferritic steel.

---

It is important to note that any potential fitted to first-principles will suffer from the same limitations of the first-principles scheme used to generate the training database. As such, the GAP models that we generated in this work are bound to the GGA-PBE exchange and correlation performances and to the collinear spin-polarized approach where no transverse magnetic moment relaxation is allowed. Furthermore, since the potentials is built to depend on the configurational space of atomic positions only, all the effects associated to electronic and/or magnetic degrees of freedom are not captured. As a consequence, for instance, the phonon softening at the  $N$  point in the reciprocal space, the anomalous softening of the  $C'$  shear constant, and the specific heat divergence around the Curie point are not expected to be reproduced. In order to go towards a more realistic description of high temperature ferromagnetic (and paramagnetic) phases of iron one should generalize the method to account for noncollinearity and to deal with magnetic degrees of freedom. The inclusion of Heisenberg-like terms, or a magnetic cluster expansion terms [80], (including second and third nearest-neighbor interactions and/or possibly three- and higher-order-body interactions) might be suited for this purpose. Care should be taken in the parametrization of such magnetic terms in order to avoid double counting of the exchange energy already included in the model due to the fitting of spin-polarized DFT data. An alternative possible line of research, would be the generalization of the non-parametric closed-form of the GAP atomic energy to depend explicitly on magnetic local environments, thus allowing for the navigation of the magnetic PES.

The results of this thesis show that GAP potentials are very powerful tools to reproduce reference potential energy surfaces. However, the price for this ability is a computational cost that scales linearly with the number of training environments, on top of the standard linear scaling with the number of atoms considered in the simulation. Albeit the sparsification procedure considerably alleviates this problem, the intrinsic dependence of the Gaussian process prediction on the training set size poses a limitation towards speed up comparable to that of other semi-empirical potentials. On the other side, the linear scaling with the number of radial/angular resolution terms used for the atomic density expansion in the SOAP kernel can be considered a strength of GAP, since it can be reduced or increased at ease as necessitates. Another issue that is common to machine learning potentials is their limited transferability. A method that was proposed to solve this problem within a GAP framework, was to fit models starting from existing potentials available in the literature, thus taking advantage of the GAP flexibility and of the baseline moderate transferability at the same time. This approach was tested for tungsten making use of simple FS potentials. However, the outcome was unsatisfactory due to the inability of GAP to correct for non-smooth regions that were unexpectedly found in the FS PES (indeed the smoothness of the PES is one of the requirements for GAP to be applied). A possible alternative to this approach would be the generation of a GAP baseline attempting to capture the average trends of the PES without aiming at full accuracy. Such GAP baseline would be smooth and would not require a dense sampling (that is especially difficult to achieve for particular configurations such as those with atoms very close by). The full accuracy of the GAP model would then be retrieved through a

## **Chapter 8. Conclusions and future directions**

---

second fitting procedure taking advantage of the GAP baseline and a dense training database.

Finally, it is clear that the generation of a potential solely on massive DFT databases is both computationally expensive and time consuming. Hence, the automation of the database generation as well of the potential training and testing should be considered for speeding up the production of future potentials. The reorganization of all the scripts created during this work would provide a robust starting point for the generation of potentials for bcc metals.

# A Gaussian processes for EOS fitting: a basic 1D Python implementation

```
1  #!/usr/bin/env python
2  # Daniele Dragoni 07/02/2015
3  # Fit with Gaussian process - FUNCTION
4  ##### INPUT PARAMS LOAD #####
5  #####
6  BtoAA = 0.529177249
7  eVtoRy = 0.073498618
8  RyAtoGPa = 4.5874e-4
9
10 import numpy as np
11 #data=np.genfromtxt("/home/dragoni/daint.rsinc/data/dragoni/test/EOS_tight/Edef.
12 dat")
13
14 data=np.genfromtxt("/home/dragoni/bellatrix.rsinc/data/dragoni/elastic-DAN-FM/
15 isotropic/REdo/Edef.dat")
16
17
18 x_training=data[:,2]*(BtoAA**3)
19 t_training=data[:,3]
20 x_prediction=np.linspace(10.6,12.1,101) # test set
21
22 print "Define correlation length, hight and error of training set"
23 Theta = 0.0002 # Amplitude of oscillations
24 Lambda = 0.08 # Correlation length
25 Sigma = 0.00008 # standard deviation, not variance !!!
26 #####
27 #####
28 ##### MAIN FUNCTION #####
29 #####
30 def GP_fit(x_prediction, x_training, t_training, Theta, Lambda, Sigma):
31     import numpy as np
32     import scipy
33     import sys
34     from scipy import optimize
35     import scipy.interpolate
36     import matplotlib.pyplot as plt
37     from matplotlib import rc
38     import warnings
39     from datetime import datetime
40     from tabulate import tabulate
41
42     startTime=datetime.now()
```

## Appendix A. Gaussian processes for EOS fitting: a basic 1D Python implementation

```

41     #print "Use eV, AA for energy and distance !!"
42     #print
43     ##### DEFINE SUB-FUNCTIONS #####
44     #####
45     def covariance_DER00(x,y,amplitude,length_scale):      # Covariance function-
46         function
47         return amplitude**2*np.exp(-(x-y)**2/(4*length_scale**2))
48     ## Definition of covariance/kernel between first derivative function and
49     function or vice-versa
50     def covariance_DER10(x,y,amplitude,length_scale):      # Covariance 1
51         st_derivative-function
52         return ((-x+y)/(2*length_scale**2))*amplitude**2*np.exp(-(x-y)**2/(4*
53         length_scale**2))
54     def covariance_DER01(x,y,amplitude,length_scale):      # Covariance function-1
55         st_derivative: equivalent to covariance_DER10
56         return ((x-y)/(2*length_scale**2))*amplitude**2*np.exp(-(x-y)**2/(4*
57         length_scale**2))
58     ## Definition of covariance/kernel between first derivative function and first
59     derivative function
60     def covariance_DER11(x,y,amplitude,length_scale):
61         return ((2*length_scale**2-(x-y)**2)/(4*length_scale**4))*amplitude**2*np.
62         exp(-(x-y)**2/(4*length_scale**2))
63     ## Definition of covariance/kernel between second derivative function
64     def covariance_DER20(x,y,amplitude,length_scale):
65         return amplitude**2 * (-2*length_scale**2 +(x-y)**2)/(4*length_scale**4) *
66         np.exp(-(x-y)**2/(4*length_scale**2))
67     ## Definition of covariance/kernel between second derivative function and
68     second derivative function
69     def covariance_DER22(x,y,amplitude,length_scale):
70         return amplitude**2 * (12*length_scale**4 -12*length_scale**2 *(x-y)**2 + (x
71         -y)**4)/(16*length_scale**8) * np.exp(-(x-y)**2/(4*length_scale**2))
72     #####
73     #####
74     ##### FIT quadratic polynomial #####
75     #####
76     degpoly          = 4          # QUadratic fit to start with
77     pol              = np.polyfit(x_training,t_training,degpoly)
78     polder1         = np.polyder(pol,1)
79     polder2         = np.polyder(pol,2)
80     poly_func       = np.poly1d(pol)
81     poly_func_der1  = np.poly1d(polder1)
82     poly_func_der2  = np.poly1d(polder2)
83     t_training      = t_training-poly_func(x_training)
84     #####
85     #####
86     ##### LOAD COVARIANCE MATRICES #####
87     #####
88     Kov_train_train      =np.zeros((x_training.size,x_training.size))
89     Kov_train_train_noisy =np.zeros((x_training.size,x_training.size))
90     Kov_predict_predict  =np.zeros((x_prediction.size,x_prediction.size))
91     Kov_predict_train    =np.zeros((x_prediction.size,x_training.size))
92     Kov_train_predict    =np.zeros((x_training.size,x_prediction.size))
93     Kov_predict_train_DER10 =np.zeros((x_prediction.size,x_training.size))
94     Kov_predict_train_DER20 =np.zeros((x_prediction.size,x_training.size))
95     Kov_predict_predict_DER11 =np.zeros((x_prediction.size,x_prediction.size))
96     Kov_predict_predict_DER22 =np.zeros((x_prediction.size,x_prediction.size))
97
98     for line,lvalue in enumerate(x_training):
99         for column,cvalue in enumerate(x_training):
100             Kov_train_train[line,column] = covariance_DER00(lvalue,cvalue,

```

---

```

    Theta, Lambda)
90     if line==column:
91         Kov_train_train_noisy[line, column] = Kov_train_train[line, column] + (
            Sigma**2)
92     else:
93         Kov_train_train_noisy[line, column] = Kov_train_train[line, column]
94
95     for line, lvalue in enumerate(x_prediction):
96         for column, cvalue in enumerate(x_prediction):
97             Kov_predict_predict[line, column] = covariance_DER00(lvalue, cvalue,
            Theta, Lambda)
98             Kov_predict_predict_DER11[line, column]= covariance_DER11(lvalue, cvalue,
            Theta, Lambda) #derivata1 incrociata:
99             Kov_predict_predict_DER22[line, column]= covariance_DER22(lvalue, cvalue,
            Theta, Lambda) #derivata2 incrociata:
100
101     for line, lvalue in enumerate(x_prediction):
102         for column, cvalue in enumerate(x_training):
103             Kov_predict_train[line, column] = covariance_DER00(lvalue, cvalue,
            Theta, Lambda)
104             #Kov_train_predict[line, column] = Kov_predict_train[column, line]
            #trasposta
105             Kov_predict_train_DER10[line, column] = covariance_DER10(lvalue, cvalue,
            Theta, Lambda) #derivata1 su prediction
106             Kov_predict_train_DER20[line, column] = covariance_DER20(lvalue, cvalue,
            Theta, Lambda) #derivata2 su prediction
107     Kov_train_predict=Kov_predict_train.T
108     #####
109     #####
110     ##### CALCULATE #####
111     #####
112     # Prior (unconditioned) distribution in function space
113     prior_mean = np.zeros(x_prediction.size)
114     prior_covariance = Kov_predict_predict
115     # POSTERIOR (conditioned) distribution in function space
116     Inverted_Kov_train_train = np.linalg.inv(Kov_train_train)
117     posterior_mean = np.dot(np.dot(Kov_predict_train,
            Inverted_Kov_train_train), t_training)
118     posterior_covariance = Kov_predict_predict - np.dot(Kov_predict_train,
            np.dot(Inverted_Kov_train_train, Kov_train_predict))
119     posterior_mean_der1 = np.dot(np.dot(Kov_predict_train_DER10,
            Inverted_Kov_train_train), t_training)
120     posterior_covariance_der1 = Kov_predict_predict_DER11 - np.dot(
            Kov_predict_train_DER10, np.dot(Inverted_Kov_train_train, -1 *
            Kov_predict_train_DER10.T))
121     posterior_mean_der2 = np.dot(np.dot(Kov_predict_train_DER20,
            Inverted_Kov_train_train), t_training)
122     posterior_covariance_der2 = Kov_predict_predict_DER22 - np.dot(
            Kov_predict_train_DER20, np.dot(Inverted_Kov_train_train, -1 *
            Kov_predict_train_DER20.T))
123     # POSTERIOR (conditioned) NOISY distribution in function space with Gaussian
            error on training data
124     Inverted_Kov_train_train_noisy = np.linalg.inv(Kov_train_train_noisy)
125     posterior_mean_noisy = np.dot(np.dot(Kov_predict_train,
            Inverted_Kov_train_train_noisy), t_training)
126     posterior_covariance_noisy = Kov_predict_predict - np.dot(Kov_predict_train,
            np.dot(Inverted_Kov_train_train_noisy, Kov_train_predict))
127     posterior_mean_der1_noisy = np.dot(np.dot(Kov_predict_train_DER10,
            Inverted_Kov_train_train_noisy), t_training)
128     posterior_covariance_der1_noisy= Kov_predict_predict_DER11 - np.dot(

```

## Appendix A. Gaussian processes for EOS fitting: a basic 1D Python implementation

```

    Kov_predict_train_DER10,np.dot(Inverted_Kov_train_train_noisy,-1 *
    Kov_predict_train_DER10.T))
129 posterior_mean_der2_noisy      = np.dot(np.dot(Kov_predict_train_DER20 ,
    Inverted_Kov_train_train_noisy),t_training)
130 posterior_covariance_der2_noisy= Kov_predict_predict_DER22-np.dot(
    Kov_predict_train_DER20,np.dot(Inverted_Kov_train_train_noisy,-1 *
    Kov_predict_train_DER20.T))
131 # ERRORS on predictions
132 check_negative=np.where(np.diag(posterior_covariance)<0.)
133 if check_negative[0] is not None:
134     warnings.warn("Negative variance elements ... std ?!!!")
135     #sys.exit("Negative variance elements -- std not possibile")
136 devstd      =np.sqrt(np.diag(posterior_covariance))
137 devstd_noisy =np.sqrt(np.diag(posterior_covariance_noisy))
138 devstd_der1  =np.sqrt(np.diag(posterior_covariance_der1))
139 devstd_der1_noisy =np.sqrt(np.diag(posterior_covariance_der1_noisy))
140 devstd_der2  =np.sqrt(np.diag(posterior_covariance_der2))
141 devstd_der2_noisy =np.sqrt(np.diag(posterior_covariance_der2_noisy))
142 #####
143 #####
144 ##### RECONSTRUCT ORIGINAL FUNCTION #####
145 #####
146 # Reconstruct the optimized function
147 posterior_mean      = posterior_mean+poly_func(x_prediction)
148 posterior_mean_der1 = posterior_mean_der1+poly_func_der1(x_prediction)
149 posterior_mean_der2 = posterior_mean_der2+poly_func_der2(x_prediction)
150 posterior_mean_noisy = posterior_mean_noisy+poly_func(x_prediction)
151 posterior_mean_der1_noisy = posterior_mean_der1_noisy+poly_func_der1(
    x_prediction)
152 posterior_mean_der2_noisy = posterior_mean_der2_noisy+poly_func_der2(
    x_prediction)
153
154
155 return posterior_mean,posterior_mean_der1,posterior_mean_der2 ,
    posterior_mean_noisy,posterior_mean_der1_noisy,posterior_mean_der2_noisy ,
    devstd_der2_noisy
156 print 'Execution time: ',(datetime.now()-startTime)
157
158 #####
159 #####
160
161
162
163
164 ##### 1-D OUTPUT #####
165 #####
166 def GP_fit_func(x_prediction ,x_training ,t_training ,Theta ,Lambda ,Sigma):
167     return GP_fit(x_prediction ,x_training ,t_training ,Theta ,Lambda ,Sigma)[0]
168
169 def GP_fit_der1(x_prediction ,x_training ,t_training ,Theta ,Lambda ,Sigma):
170     return GP_fit(x_prediction ,x_training ,t_training ,Theta ,Lambda ,Sigma)[1]
171
172 def GP_fit_der2(x_prediction ,x_training ,t_training ,Theta ,Lambda ,Sigma):
173     return GP_fit(x_prediction ,x_training ,t_training ,Theta ,Lambda ,Sigma)[2]
174
175 def GP_fit_func_noisy(x_prediction ,x_training ,t_training ,Theta ,Lambda ,Sigma):
176     return GP_fit(x_prediction ,x_training ,t_training ,Theta ,Lambda ,Sigma)[3]
177
178 def GP_fit_der1_noisy(x_prediction ,x_training ,t_training ,Theta ,Lambda ,Sigma):
179     return GP_fit(x_prediction ,x_training ,t_training ,Theta ,Lambda ,Sigma)[4]

```



---

```

180
181 def GP_fit_der2_noisy(x_prediction,x_training,t_training,Theta,Lambda,Sigma):
182     return GP_fit(x_prediction,x_training,t_training,Theta,Lambda,Sigma)[5]
183
184 def GP_fit_der2_devstd_noisy(x_prediction,x_training,t_training,Theta,Lambda,
185     Sigma):
186     return GP_fit(x_prediction,x_training,t_training,Theta,Lambda,Sigma)[6]
187
188 #####
189 #####
190
191
192 ##### CHECK CONVERGENCE HYPERPARAMETERS WHEN POSSIBLE #####
193 #####
194
195 def check_hyperparams_convergence(x_training,t_training,Theta,Lambda,Sigma):
196
197     def covariance_DER00(x,y,amplitude,length_scale):        # Covariance function-
198         function
199         return amplitude**2*np.exp(-(x-y)**2/(4*length_scale**2))
200
201     def Kov_train_train_noisy_func(x_training,t_training,Theta,Lambda,Sigma):
202         Kov_train_train_noisy = []
203         for line in x_training:
204             for column in x_training:
205                 if line==column:
206                     Kov_train_train_noisy.append(covariance_DER00(line,column,Theta,Lambda)
207                         +(Sigma**2))
208                 else:
209                     Kov_train_train_noisy.append(covariance_DER00(line,column,Theta,Lambda))
210         return np.array(Kov_train_train_noisy).reshape(len(x_training),len(x_training)
211             ))
212
213     def logP(x_training,t_training,Theta,Lambda,Sigma):
214         K=Kov_train_train_noisy_func(x_training,t_training,Theta,Lambda,Sigma)
215         return -0.5*np.log(np.linalg.det( K )) - 0.5*np.dot(np.dot(t_training,np.
216             linalg.inv(K)),t_training )-len(x_training)/2.*np.log(np.pi*2)
217
218     Theta_values = np.arange(0.05,0.2,0.01)
219     Lambda_values = np.arange(0.01,0.16,0.004)
220     Parameters_function=[]
221
222     for Theta_ in Theta_values:
223         for Lambda_ in Lambda_values:
224             Parameters_function.append(logP(x_training,t_training,Theta_,Lambda_,Sigma)
225                 )
226
227     Parameters_f_matrix=np.array(Parameters_function).reshape(len(Theta_values),len
228         (Lambda_values))
229     Parameters_f_matrix[Parameters_f_matrix==inf]=-8e8
230
231     #from pylab import *
232     from mpl_toolkits.mplot3d.axes3d import Axes3D
233     X,Y=np.meshgrid(Lambda_values,Theta_values)
234     fig,ax=plt.subplots()
235     p=ax.pcolor(X,Y,Parameters_f_matrix,cmap=cm.coolwarm)
236     cb=fig.colorbar(p,ax=ax)
237     plt.ylabel(r'Amplitude $\theta$', fontsize=20)
238     plt.xlabel(r'Length scale $\lambda$', fontsize=20)

```

## Appendix A. Gaussian processes for EOS fitting: a basic 1D Python implementation

---

```
233 plt.tight_layout()
234 show()
235 plt.close()
236 fig=plt.figure()
237 ax=fig.add_subplot(1,1,1,projection='3d')
238 p=ax.plot_surface(X,Y,Parameters_f_matrix*1e-8,rstride=1,cstride=1,cmap=cm.
    coolwarm,linewidth=0.)
239 cb=fig.colorbar(p)
240 plt.ylabel(r'Amplitude  $\theta$ ',fontsize=20)
241 plt.xlabel(r'Length scale  $\lambda$ ',fontsize=20)
242 plt.tight_layout()
243 show()
244 plt.close()
245
246 #####
247 #####
```

## B Supplemental material

Full stiffness tensor associated to the trigonal deformation  $\boldsymbol{\epsilon}^{(3)}$  used in the main text:

$$\boldsymbol{\epsilon}^{(3)} = \begin{pmatrix} \frac{1+\epsilon_d}{3} + \frac{2}{3}\sqrt{1-\frac{1}{2}\epsilon_d(2+\epsilon_d)} & \frac{1+\epsilon_d}{3} - \frac{1}{3}\sqrt{1-\frac{1}{2}\epsilon_d(2+\epsilon_d)} & \frac{1+\epsilon_d}{3} - \frac{1}{3}\sqrt{1-\frac{1}{2}\epsilon_d(2+\epsilon_d)} \\ \frac{1+\epsilon_d}{3} - \frac{1}{3}\sqrt{1-\frac{1}{2}\epsilon_d(2+\epsilon_d)} & \frac{1+\epsilon_d}{3} + \frac{2}{3}\sqrt{1-\frac{1}{2}\epsilon_d(2+\epsilon_d)} & \frac{1+\epsilon_d}{3} - \frac{1}{3}\sqrt{1-\frac{1}{2}\epsilon_d(2+\epsilon_d)} \\ \frac{1+\epsilon_d}{3} - \frac{1}{3}\sqrt{1-\frac{1}{2}\epsilon_d(2+\epsilon_d)} & \frac{1+\epsilon_d}{3} - \frac{1}{3}\sqrt{1-\frac{1}{2}\epsilon_d(2+\epsilon_d)} & \frac{1+\epsilon_d}{3} + \frac{2}{3}\sqrt{1-\frac{1}{2}\epsilon_d(2+\epsilon_d)} \end{pmatrix}, \quad (\text{B.1})$$

and associated determinant, also reported in Fig. B.1:

$$\det(\boldsymbol{\epsilon}^{(3)}) = 1 - \frac{3\epsilon_d^2}{2} - \frac{\epsilon_d^3}{2} \quad (\text{B.2})$$

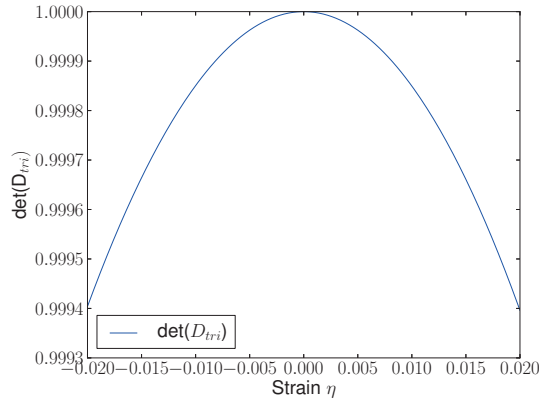


Figure B.1: Determinant of the trigonal deformation  $\boldsymbol{\epsilon}^{(3)}$  herein used as a function of the strain  $\epsilon_d$ .

## Appendix B. Supplemental material

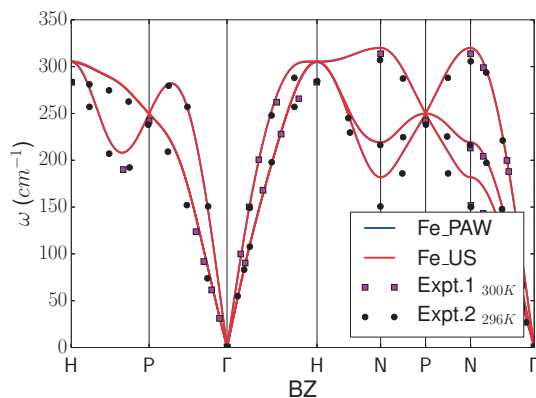


Figure B.2: Comparison between phonon dispersions obtained with the ultrasoft pseudopotential chosen in the article (`rrkjus-0.2.1-16e`) and another PAW pseudopotential from the *pslibrary*, namely the `paw-0.2.1-16e` one (see the article for equilibrium lattice parameter and bulk modulus). The two phonon dispersions are nearly indistinguishable on the scale of the plot and are in good to very good agreement with experimental data (Expt.1 – squares [185] and Expt.2 – circles [186]).

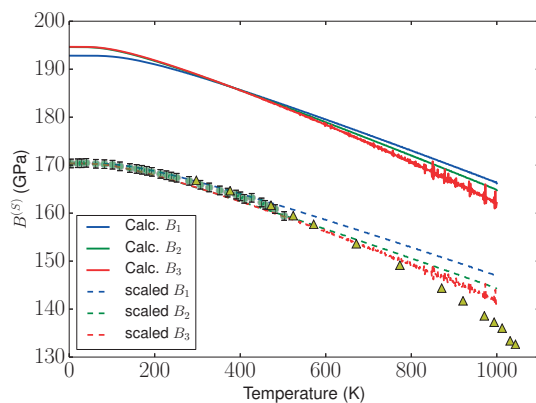


Figure B.3: Temperature dependence of the adiabatic bulk modulus –  $B^{(S)}(T)$  – for different polynomial fits of the one-dimensional vibrational contribution to the Helmholtz free energy. All the polynomials (first, second and third order) provide quite similar results. In particular, second- and third- order polynomials are almost equivalent below 500 K, while they tend to slightly differ at higher temperatures where, however, the third order shows numerical noise. For the sake of clarity, we also reported the scaled curves (see the article) and experimental data (Expt.1 – circles [162] and Expt.2 – triangles [189]). From this analysis we chose to adopt the second order polynomial to compute thermodynamic properties.

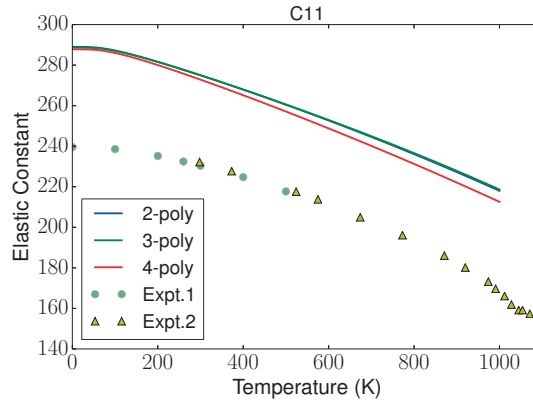


Figure B.4: Temperature dependence of the  $C_{11}$  elastic constant for different polynomial fits of the two-dimensional vibrational contribution to the Helmholtz free energy. Even in this case, all the bivariate polynomials (second, third and fourth order) provide comparable results. The difference between all curves is relatively small compared to the absolute theoretical or experimental (Expt.1 – circles [162] and Expt.2 – triangles [189]) softening observed. As a consequence, we chose the second order bivariate polynomial as optimal for the description of the  $C_{11}$  thermal dependence.

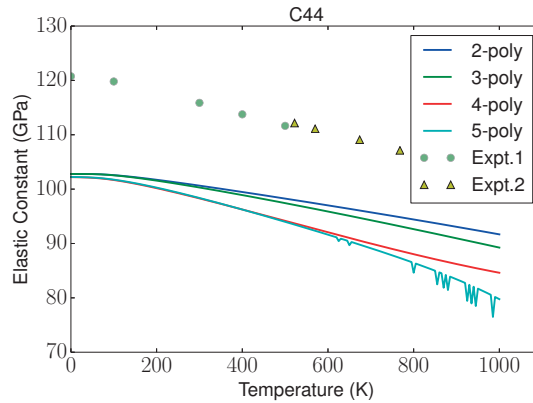


Figure B.5: Temperature dependence of the  $C_{44}$  elastic constant for different polynomial fits of the two-dimensional vibrational contribution to the Helmholtz free energy. The difference between these fit is of the same order of magnitude as in the  $C_{11}$  case. However, due to the relatively small thermal softening (compared to the  $C_{11}$  case), this difference appears more prominent and the choice for an optimal polynomial less clear. We note that, despite the numerical instability at high temperature, the fourth and fifth order polynomials match closely up to 700 K. These data, compared to experimental observations (Expt.1 – circles [162] and Expt.2 – triangles [189]), suggest that we can consider the fourth order polynomial as optimal for the description of the  $C_{44}$  thermal dependence.



# Bibliography

- [1] P. Hohenberg and W. Kohn, "Inhomogeneous electron gas," *Phys. Rev.*, vol. 136, pp. B864–B871, Nov 1964.
- [2] W. Kohn and L. J. Sham, "Quantum density oscillations in an inhomogeneous electron gas," *Phys. Rev.*, vol. 137, pp. A1697–A1705, Mar 1965.
- [3] W. Kohn and L. J. Sham, "Self-consistent equations including exchange and correlation effects," *Phys. Rev.*, vol. 140, pp. A1133–A1138, Nov 1965.
- [4] J. P. Perdew, K. Burke, and Y. Wang, "Generalized gradient approximation for the exchange-correlation hole of a many-electron system," *Phys. Rev. B*, vol. 54, pp. 16533–16539, Dec 1996.
- [5] J. P. Perdew and A. Zunger, "Self-interaction correction to density-functional approximations for many-electron systems," *Phys. Rev. B*, vol. 23, pp. 5048–5079, May 1981.
- [6] I. Lindgren, "A statistical exchange approximation for localized electrons," *International Journal of Quantum Chemistry*, vol. 5, no. S5, pp. 411–420, 1971.
- [7] M. d’Avezac, M. Calandra, and F. Mauri, "Density functional theory description of hole-trapping in SiO<sub>2</sub>: A self-interaction-corrected approach," *Phys. Rev. B*, vol. 71, p. 205210, May 2005.
- [8] J. P. Perdew, R. G. Parr, M. Levy, and J. L. Balduz, "Density-functional theory for fractional particle number: Derivative discontinuities of the energy," *Phys. Rev. Lett.*, vol. 49, pp. 1691–1694, Dec 1982.
- [9] E. Kraisler and L. Kronik, "Piecewise linearity of approximate density functionals revisited: Implications for frontier orbital energies," *Phys. Rev. Lett.*, vol. 110, p. 126403, Mar 2013.
- [10] A. Tkatchenko and M. Scheffler, "Accurate molecular van der waals interactions from ground-state electron density and free-atom reference data," *Phys. Rev. Lett.*, vol. 102, p. 073005, Feb 2009.

## Bibliography

---

- [11] S. Grimme, "Semiempirical GGA-type density functional constructed with a long-range dispersion correction," *Journal of computational chemistry*, vol. 27, no. 15, pp. 1787–1799, 2006.
- [12] O. A. Vydrov and T. Van Voorhis, "Nonlocal van der Waals density functional: The simpler the better," *The Journal of chemical physics*, vol. 133, no. 24, p. 244103, 2010.
- [13] H. Hellmann, "A new approximation method in the problem of many electrons," *The Journal of Chemical Physics*, vol. 3, no. 1, 1935.
- [14] V. Heine, "The pseudopotential concept," vol. 24 of *Solid State Physics*, pp. 1 – 36, Academic Press, 1970.
- [15] W. E. Pickett, "Pseudopotential methods in condensed matter applications," *Computer Physics Reports*, vol. 9, no. 3, pp. 115 – 197, 1989.
- [16] D. Vanderbilt, "Optimally smooth norm-conserving pseudopotentials," *Phys. Rev. B*, vol. 32, pp. 8412–8415, Dec 1985.
- [17] C.-K. Skylaris, P. D. Haynes, A. A. Mostofi, and M. C. Payne, "Introducing ONETEP: Linear-scaling density functional simulations on parallel computers," *The Journal of Chemical Physics*, vol. 122, no. 8, p. 084119, 2005.
- [18] J. M. Soler, E. Artacho, J. D. Gale, A. García, J. Junquera, P. Ordejón, and D. Sánchez-Portal, "The SIESTA method for ab initio order-N materials simulation," *Journal of Physics: Condensed Matter*, vol. 14, no. 11, p. 2745, 2002.
- [19] C. M. Bishop, *Neural networks for pattern recognition*. Oxford university press, 1995.
- [20] S. S. Haykin, S. S. Haykin, S. S. Haykin, and S. S. Haykin, *Neural networks and learning machines*, vol. 3. Pearson Education Upper Saddle River, 2009.
- [21] S. Lorenz, A. Groß, and M. Scheffler, "Representing high-dimensional potential-energy surfaces for reactions at surfaces by neural networks," *Chemical Physics Letters*, vol. 395, no. 4–6, pp. 210 – 215, 2004.
- [22] J. Behler and M. Parrinello, "Generalized neural-network representation of high-dimensional potential-energy surfaces," *Phys. Rev. Lett.*, vol. 98, p. 146401, Apr 2007.
- [23] A. P. Bartók, M. C. Payne, R. Kondor, and G. Csányi, "Gaussian approximation potentials: The accuracy of quantum mechanics, without the electrons," *Phys. Rev. Lett.*, vol. 104, p. 136403, Apr 2010.
- [24] D. A. Young, *Phase diagrams of the elements*. University of California, Lawrence Livermore Laboratory, 1975.
- [25] C.-A. Gandin and M. Rappaz, "A coupled finite element-cellular automaton model for the prediction of dendritic grain structures in solidification processes," *Acta Metallurgica et Materialia*, vol. 42, no. 7, pp. 2233–2246, 1994.



- 
- [26] M. Asta, C. Beckermann, A. Karma, W. Kurz, R. Napolitano, M. Plapp, G. Purdy, M. Rappaz, and R. Trivedi, "Solidification microstructures and solid-state parallels: Recent developments, future directions," *Acta Materialia*, vol. 57, no. 4, pp. 941–971, 2009.
- [27] M. Rappaz and C.-A. Gandin, "Probabilistic modelling of microstructure formation in solidification processes," *Acta metallurgica et materialia*, vol. 41, no. 2, pp. 345–360, 1993.
- [28] S. Taira, K. Tanaka, and M. Hoshina, "Grain size effect on crack nucleation and growth in long-life fatigue of low-carbon steel," *ASTM STP*, vol. 675, pp. 135–173, 1979.
- [29] M. Tanaka, E. Tarleton, and S. Roberts, "The brittle–ductile transition in single-crystal iron," *Acta Materialia*, vol. 56, no. 18, pp. 5123–5129, 2008.
- [30] J. P. Hirth, "Effects of hydrogen on the properties of iron and steel," *Metallurgical Transactions A*, vol. 11, no. 6, pp. 861–890, 1980.
- [31] J. Song and W. Curtin, "Atomic mechanism and prediction of hydrogen embrittlement in iron," *Nature materials*, vol. 12, no. 2, pp. 145–151, 2013.
- [32] D. Hardie, E. Charles, and A. Lopez, "Hydrogen embrittlement of high strength pipeline steels," *Corrosion Science*, vol. 48, no. 12, pp. 4378–4385, 2006.
- [33] A. Ramasubramaniam, M. Itakura, M. Ortiz, and E. Carter, "Effect of atomic scale plasticity on hydrogen diffusion in iron: Quantum mechanically informed and on-the-fly kinetic monte carlo simulations," *Journal of Materials Research*, vol. 23, no. 10, pp. 2757–2773, 2008.
- [34] L. Malerba, M. Marinica, N. Anento, C. Björkas, H. Nguyen, C. Domain, F. Djurabekova, P. Olsson, K. Nordlund, A. Serra, *et al.*, "Comparison of empirical interatomic potentials for iron applied to radiation damage studies," *Journal of Nuclear Materials*, vol. 406, no. 1, pp. 19–38, 2010.
- [35] S. Dudarev, "Density functional theory models for radiation damage\*," *Materials Research*, vol. 43, no. 1, p. 35, 2013.
- [36] D. Alfe, G. Price, and M. Gillan, "Iron under earth's core conditions: liquid-state thermodynamics and high-pressure melting curve from ab initio calculations," *Phys. Rev. B*, vol. 65, no. 16, p. 165118, 2002.
- [37] L. Vočadlo, D. Alfè, M. Gillan, I. Wood, J. Brodholt, and G. D. Price, "Possible thermal and chemical stabilization of body-centred-cubic iron in the earth's core," *Nature*, vol. 424, no. 6948, pp. 536–539, 2003.
- [38] D. J. Stevenson, T. Spohn, and G. Schubert, "Magnetism and thermal evolution of the terrestrial planets," *Icarus*, vol. 54, no. 3, pp. 466–489, 1983.

## Bibliography

---

- [39] H. Wende, M. Bernien, J. Luo, C. Sorg, N. Ponpandian, J. Kurde, J. Miguel, M. Piantek, X. Xu, P. Eckhold, *et al.*, “Substrate-induced magnetic ordering and switching of iron porphyrin molecules,” *Nature materials*, vol. 6, no. 7, pp. 516–520, 2007.
- [40] S. Han, K. Cho, and J. Ihm, “Ab initio study on the molecular recognition by metallo-porphyrins: Co interaction with iron porphyrin,” *Phys. Rev. E*, vol. 59, no. 2, p. 2218, 1999.
- [41] A. Dedieu, M. Rohmer, and A. Veillard, “Ab initio calculations of metalloporphyrins,” *Adv. Quantum Chem*, vol. 16, pp. 43–95, 1982.
- [42] U. Ryde and K. Nilsson, “Quantum chemistry can locally improve protein crystal structures,” *Journal of the American Chemical Society*, vol. 125, no. 47, pp. 14232–14233, 2003.
- [43] E. G. Moroni, G. Kresse, J. Hafner, and J. Furthmüller, “Ultrasoft pseudopotentials applied to magnetic Fe, Co, and Ni: From atoms to solids,” *Phys. Rev. B*, vol. 56, pp. 15629–15646, Dec 1997.
- [44] H. Herper, E. Hoffmann, and P. Entel, “Ab initio full-potential study of the structural and magnetic phase stability of iron,” *Phys. Rev. B*, vol. 60, no. 6, p. 3839, 1999.
- [45] D. Dragoni, D. Ceresoli, and N. Marzari, “Thermoelastic properties of  $\alpha$ -iron from first-principles,” *Phys. Rev. B*, vol. 91, p. 104105, Mar 2015.
- [46] G. Steinle-Neumann, L. Stixrude, and R. E. Cohen, “First-principles elastic constants for the hcp transition metals Fe, Co, and Re at high pressure,” *Phys. Rev. B*, vol. 60, pp. 791–799, Jul 1999.
- [47] M. Friák and M. Šob, “Ab initio study of the bcc-hcp transformation in iron,” *Phys. Rev. B*, vol. 77, p. 174117, May 2008.
- [48] R. Lizárraga, L. Nordström, O. Eriksson, and J. Wills, “Noncollinear magnetism in the high-pressure hcp phase of iron,” *Phys. Rev. B*, vol. 78, p. 064410, Aug 2008.
- [49] P. Söderlind, J. A. Moriarty, and J. M. Wills, “First-principles theory of iron up to earth-core pressures: Structural, vibrational, and elastic properties,” *Phys. Rev. B*, vol. 53, pp. 14063–14072, Jun 1996.
- [50] P. Giles, M. Longenbach, and A. Marder, “High-pressure  $\alpha \rightleftharpoons \epsilon$  martensitic transformation in Iron,” *Journal of Applied Physics*, vol. 42, no. 11, pp. 4290–4295, 1971.
- [51] F. Bundy, “Pressure—temperature phase diagram of iron to 200 kbar, 900 C,” *Journal of Applied Physics*, vol. 36, no. 2, pp. 616–620, 1965.
- [52] J. Liu and D. Johnson, “Bcc-to-hcp transformation pathways for iron versus hydrostatic pressure: coupled shuffle and shear modes,” *Phys. Rev. B*, vol. 79, no. 13, p. 134113, 2009.

- [53] R. Cohen and S. Mukherjee, "Non-collinear magnetism in iron at high pressures," *Physics of the Earth and Planetary Interiors*, vol. 143, pp. 445–453, 2004.
- [54] G. Cort, R. Taylor, and J. Willis, "Search for magnetism in hcp  $\epsilon$ -Fe," *Journal of Applied Physics*, vol. 53, no. 3, pp. 2064–2065, 1982.
- [55] S. Nasu, T. Sasaki, T. Kawakami, T. Tsutsui, and S. Endo, "Mössbauer study of  $\epsilon$ -Fe under an external magnetic field," *Journal of Physics: Condensed Matter*, vol. 14, no. 44, p. 11167, 2002.
- [56] J.-P. Rueff, M. Mezouar, and M. Acet, "Short-range magnetic collapse of Fe under high pressure at high temperatures observed using X-ray emission spectroscopy," *Phys. Rev. B*, vol. 78, no. 10, p. 100405, 2008.
- [57] O. Mathon, F. Baudelet, J. Itié, A. Polian, M. d'Astuto, J. Chervin, and S. Pascarelli, "Dynamics of the magnetic and structural  $\alpha$ - $\epsilon$  phase transition in iron," *Phys. Rev. Lett.*, vol. 93, no. 25, p. 255503, 2004.
- [58] S. Ono, T. Kikegawa, N. Hirao, and K. Mibe, "Letter. high-pressure magnetic transition in hcp-Fe," *American Mineralogist*, vol. 95, no. 5-6, pp. 880–883, 2010.
- [59] S. Merkel, A. F. Goncharov, H.-k. Mao, P. Gillet, and R. J. Hemley, "Raman spectroscopy of iron to 152 gigapascals: Implications for earth's inner core," *Science*, vol. 288, no. 5471, pp. 1626–1629, 2000.
- [60] A. Monza, A. Meffre, F. Baudelet, J.-P. Rueff, M. d'Astuto, P. Munsch, S. Huotari, S. Lachaize, B. Chaudret, and A. Shukla, "Iron under pressure: "kohn tweezers" and remnant magnetism," *Phys. Rev. Lett.*, vol. 106, no. 24, p. 247201, 2011.
- [61] K. Shimizu, T. Kimura, S. Furomoto, K. Takeda, K. Kontani, Y. Onuki, and K. Amaya, "Superconductivity in the non-magnetic state of iron under pressure," *Nature*, vol. 412, no. 6844, pp. 316–318, 2001.
- [62] J. Bardeen, L. N. Cooper, and J. R. Schrieffer, "Theory of superconductivity," *Phys. Rev.*, vol. 108, pp. 1175–1204, Dec 1957.
- [63] S. Saxena and P. B. Littlewood, "Superconductivity: Iron cast in exotic role," *Nature*, vol. 412, no. 6844, pp. 290–291, 2001.
- [64] T. Jarlborg, "Ferromagnetic and antiferromagnetic spin fluctuations and superconductivity in the hcp-phase of Fe," *Physics Letters A*, vol. 300, no. 4, pp. 518–523, 2002.
- [65] L. V. Pourovskii, J. Mravlje, M. Ferrero, O. Parcollet, and I. A. Abrikosov, "Impact of electronic correlations on the equation of state and transport in  $\epsilon$ -Fe," *Phys. Rev. B*, vol. 90, p. 155120, Oct 2014.
- [66] H. Hasegawa and D. Pettifor, "Microscopic theory of the temperature-pressure phase diagram of iron," *Phys. Rev. Lett.*, vol. 50, no. 2, p. 130, 1983.

## Bibliography

---

- [67] F. Körmann, A. Dick, B. Grabowski, B. Hallstedt, T. Hickel, and J. Neugebauer, “Free energy of bcc iron: Integrated ab initio derivation of vibrational, electronic, and magnetic contributions,” *Phys. Rev. B*, vol. 78, p. 033102, Jul 2008.
- [68] A. Dick, F. Körmann, T. Hickel, and J. Neugebauer, “Ab initio based determination of thermodynamic properties of cementite including vibronic, magnetic, and electronic excitations,” *Phys. Rev. B*, vol. 84, p. 125101, Sep 2011.
- [69] F. Körmann, A. Dick, T. Hickel, and J. Neugebauer, “Rescaled monte carlo approach for magnetic systems: Ab initio thermodynamics of bcc iron,” *Phys. Rev. B*, vol. 81, p. 134425, Apr 2010.
- [70] A. Zunger, S.-H. Wei, L. G. Ferreira, and J. E. Bernard, “Special quasirandom structures,” *Phys. Rev. Lett.*, vol. 65, pp. 353–356, Jul 1990.
- [71] E. M. Haines, R. Clauberg, and R. Feder, “Short-range magnetic order near the Curie temperature iron from spin-resolved photoemission,” *Phys. Rev. Lett.*, vol. 54, pp. 932–934, Mar 1985.
- [72] F. Körmann, A. Dick, B. Grabowski, T. Hickel, and J. Neugebauer, “Atomic forces at finite magnetic temperatures: Phonons in paramagnetic iron,” *Phys. Rev. B*, vol. 85, p. 125104, Mar 2012.
- [73] Y. Ikeda, A. Seko, A. Togo, and I. Tanaka, “Phonon softening in paramagnetic bcc Fe and its relationship to the pressure-induced phase transition,” *Phys. Rev. B*, vol. 90, no. 13, p. 134106, 2014.
- [74] A. Dal Corso and S. de Gironcoli, “Ab initio phonon dispersions of Fe and Ni,” *Phys. Rev. B*, vol. 62, pp. 273–277, Jul 2000.
- [75] A. J. Hatt, B. C. Melot, and S. Narasimhan, “Harmonic and anharmonic properties of Fe and Ni: Thermal expansion, exchange-correlation errors, and magnetism,” *Phys. Rev. B*, vol. 82, p. 134418, Oct 2010.
- [76] S. Okatov, A. Kuznetsov, Y. N. Gornostyrev, V. Urtsev, and M. Katsnelson, “Effect of magnetic state on the  $\gamma$ - $\alpha$  transition in iron: First-principles calculations of the bain transformation path,” *Phys. Rev. B*, vol. 79, no. 9, p. 094111, 2009.
- [77] I. Leonov, A. Poteryaev, V. Anisimov, and D. Vollhardt, “Calculated phonon spectra of paramagnetic iron at the  $\alpha$ - $\gamma$  phase transition,” *Phys. Rev. B*, vol. 85, no. 2, p. 020401, 2012.
- [78] B. Gyorffy, A. Pindor, J. Staunton, G. Stocks, and H. Winter, “A first-principles theory of ferromagnetic phase transitions in metals,” *Journal of Physics F: Metal Physics*, vol. 15, no. 6, p. 1337, 1985.

- [79] A. V. Ruban and I. Abrikosov, "Configurational thermodynamics of alloys from first principles: effective cluster interactions," *Reports on Progress in Physics*, vol. 71, no. 4, p. 046501, 2008.
- [80] M. Y. Lavrentiev, D. Nguyen-Manh, and S. Dudarev, "Magnetic cluster expansion model for bcc-fcc transitions in Fe and Fe-Cr alloys," *Phys. Rev. B*, vol. 81, no. 18, p. 184202, 2010.
- [81] R. Singer, F. Dietermann, and M. Fähnle, "Spin Interactions in bcc and fcc Fe beyond the Heisenberg Model," *Phys. Rev. Lett.*, vol. 107, p. 017204, Jun 2011.
- [82] F. G. Eich and E. K. U. Gross, "Transverse spin-gradient functional for noncollinear spin-density-functional theory," *Phys. Rev. Lett.*, vol. 111, p. 156401, Oct 2013.
- [83] X. Sha and R. E. Cohen, "Lattice dynamics and thermodynamics of bcc iron under pressure: First-principles linear response study," *Phys. Rev. B*, vol. 73, p. 104303, Mar 2006.
- [84] R. Martin, *Electronic Structure: Basic Theory and Practical Methods*. Cambridge University Press, 2004.
- [85] F. Giustino, *Materials Modelling using Density Functional Theory: Properties and Predictions*. OUP Oxford, 2014.
- [86] R. G. Parr and Y. Weitao, *Density-Functional Theory of Atoms and Molecules*. Oxford University Press, May 1994.
- [87] S. Baroni, S. de Gironcoli, A. Dal Corso, and P. Giannozzi, "Phonons and related crystal properties from density-functional perturbation theory," *Rev. Mod. Phys.*, vol. 73, pp. 515–562, Jul 2001.
- [88] <http://www.fisica.uniud.it/ercolessi/md/md/>.
- [89] M. P. Allen and D. J. Tildesley, *Computer simulation of liquids*. Oxford university press, 1989.
- [90] D. Frenkel and B. Smit, *Understanding molecular simulation: from algorithms to applications*, vol. 1. Academic press, 2001.
- [91] M. I. Mendeleev, S. Han, D. J. Srolovitz, G. J. Ackland, D. Y. Sun, and M. Asta, "Development of new interatomic potentials appropriate for crystalline and liquid iron," *Philosophical Magazine*, vol. 83, pp. 3977–3994, Dec 2003.
- [92] M. Marchese, G. Jacucci, and C. P. Flynn, "Isotope effect of vacancy diffusion in b.c.c.-Fe," *Philosophical Magazine Letters*, vol. 57, pp. 25–30, Jan 1988.
- [93] R. Meyer and P. Entel, "Martensite-austenite transition and phonon dispersion curves of  $\text{Fe}_{1-x}\text{Ni}_x$  studied by molecular-dynamics simulations," *Phys. Rev. B*, vol. 57, no. 9, p. 5140, 1998.

## Bibliography

---

- [94] Y. Ouyang, X. Tong, C. Li, H. Chen, X. Tao, T. Hickel, and Y. Du, “Thermodynamic and physical properties of FeAl and Fe<sub>3</sub>Al: an atomistic study by EAM simulation,” *Physica B: Condensed Matter*, vol. 407, pp. 4530–4536, Dec 2012.
- [95] <http://physics.nist.gov/cgi-bin/cuu/Value?mpsme>.
- [96] O. Gunnarsson and B. I. Lundqvist, “Exchange and correlation in atoms, molecules, and solids by the spin-density-functional formalism,” *Phys. Rev. B*, vol. 13, pp. 4274–4298, May 1976.
- [97] M. Levy, “Universal variational functionals of electron densities, first-order density matrices, and natural spin-orbitals and solution of the v-representability problem,” *Proceedings of the National Academy of Sciences*, vol. 76, no. 12, pp. 6062–6065, 1979.
- [98] J. P. Perdew, K. Burke, and M. Ernzerhof, “Generalized gradient approximation made simple,” *Phys. Rev. Lett.*, vol. 77, pp. 3865–3868, Oct 1996.
- [99] U. von Barth and L. Hedin, “A local exchange-correlation potential for the spin polarized case. i,” *Journal of Physics C: Solid State Physics*, vol. 5, no. 13, p. 1629, 1972.
- [100] W. H. Press and G. B. Rybicki, “Fast algorithm for spectral analysis of unevenly sampled data,” , vol. 338, pp. 277–280, Mar 1989.
- [101] D. R. Hamann, M. Schlüter, and C. Chiang, “Norm-conserving pseudopotentials,” *Phys. Rev. Lett.*, vol. 43, pp. 1494–1497, Nov 1979.
- [102] D. Vanderbilt, “Soft self-consistent pseudopotentials in a generalized eigenvalue formalism,” *Phys. Rev. B*, vol. 41, pp. 7892–7895, Apr 1990.
- [103] P. E. Blöchl, “Projector augmented-wave method,” *Phys. Rev. B*, vol. 50, pp. 17953–17979, Dec 1994.
- [104] N. D. Mermin, “Thermal properties of the inhomogeneous electron gas,” *Phys. Rev.*, vol. 137, pp. A1441–A1443, Mar 1965.
- [105] E. Wasserman, L. Stixrude, and R. E. Cohen, “Thermal properties of iron at high pressures and temperatures,” *Phys. Rev. B*, vol. 53, pp. 8296–8309, Apr 1996.
- [106] S. de Gironcoli, “Lattice dynamics of metals from density-functional perturbation theory,” *Phys. Rev. B*, vol. 51, pp. 6773–6776, Mar 1995.
- [107] C. L. Fu and K. M. Ho, “First-principles calculation of the equilibrium ground-state properties of transition metals: Applications to Nb and Mo,” *Phys. Rev. B*, vol. 28, pp. 5480–5486, Nov 1983.
- [108] M. Methfessel and A. T. Paxton, “High-precision sampling for Brillouin-zone integration in metals,” *Phys. Rev. B*, vol. 40, pp. 3616–3621, Aug 1989.

- 
- [109] N. Marzari, D. Vanderbilt, A. De Vita, and M. C. Payne, "Thermal contraction and disordering of the Al(110) surface," *Phys. Rev. Lett.*, vol. 82, pp. 3296–3299, Apr 1999.
- [110] A. De Vita, "The energetics of defects and impurities in metals and ionic materials from first principles," 1992.
- [111] M. Verstraete and X. Gonze, "Smearing scheme for finite-temperature electronic-structure calculations," *Phys. Rev. B*, vol. 65, p. 035111, Dec 2001.
- [112] <http://www.quantum-espresso.org/pseudopotentials/pslibrary/>.
- [113] R. P. Feynman, "Forces in molecules," *Phys. Rev.*, vol. 56, pp. 340–343, Aug 1939.
- [114] N. Ashcroft and N. Mermin, *Solid State Physics*. HRW international editions, Holt, Rinehart and Winston, 1976.
- [115] C. Kittel, *Introduction to Solid State Physics*. Wiley, 2004.
- [116] I. Errea, M. Calandra, C. J. Pickard, J. Nelson, R. J. Needs, Y. Li, H. Liu, Y. Zhang, Y. Ma, and F. Mauri, "High-pressure hydrogen sulfide from first principles: A strongly anharmonic phonon-mediated superconductor," *Phys. Rev. Lett.*, vol. 114, p. 157004, Apr 2015.
- [117] I. Errea, M. Calandra, and F. Mauri, "First-principles theory of anharmonicity and the inverse isotope effect in superconducting palladium-hydride compounds," *Phys. Rev. Lett.*, vol. 111, p. 177002, Oct 2013.
- [118] A. Glensk, B. Grabowski, T. Hickel, and J. Neugebauer, "Breakdown of the arrhenius law in describing vacancy formation energies: The importance of local anharmonicity revealed by *Ab initio* thermodynamics," *Phys. Rev. X*, vol. 4, p. 011018, Feb 2014.
- [119] X. Gonze, "Adiabatic density-functional perturbation theory," *Phys. Rev. A*, vol. 52, pp. 1096–1114, Aug 1995.
- [120] M. T. Yin and M. L. Cohen, "Microscopic theory of the phase transformation and lattice dynamics of Si," *Phys. Rev. Lett.*, vol. 45, pp. 1004–1007, Sep 1980.
- [121] K. M. Ho, C. L. Fu, B. N. Harmon, W. Weber, and D. R. Hamann, "Vibrational frequencies and structural properties of transition metals via total-energy calculations," *Phys. Rev. Lett.*, vol. 49, pp. 673–676, Aug 1982.
- [122] L. T. Kong, "Phonon dispersion measured directly from molecular dynamics simulations," *Computer Physics Communications*, vol. 182, no. 10, pp. 2201 – 2207, 2011.
- [123] F. Ercolessi and J. B. Adams, "Interatomic potentials from first-principles calculations: The force-matching method," *EPL (Europhysics Letters)*, vol. 26, no. 8, p. 583, 1994.
- [124] N. Artrith and J. Behler, "High-dimensional neural network potentials for metal surfaces: A prototype study for copper," *Phys. Rev. B*, vol. 85, p. 045439, Jan 2012.

## Bibliography

---

- [125] P. P. Ewald, "Die berechnung optischer und elektrostatischer gitterpotentiale," *Annalen der Physik*, vol. 369, no. 3, pp. 253–287, 1921.
- [126] P. J. Steinhardt, D. R. Nelson, and M. Ronchetti, "Bond-orientational order in liquids and glasses," *Phys. Rev. B*, vol. 28, pp. 784–805, Jul 1983.
- [127] A. P. Bartók, *Gaussian Approximation Potential: an interatomic potential derived from first principles Quantum Mechanics*. PhD thesis, Cavendish Laboratory, University of Cambridge, 2009.
- [128] A. P. Bartók, R. Kondor, and G. Csányi, "On representing chemical environments," *Phys. Rev. B*, vol. 87, p. 184115, May 2013.
- [129] M. S. Daw, S. M. Foiles, and M. I. Baskes, "The embedded-atom method: a review of theory and applications," *Materials Science Reports*, vol. 9, no. 7, pp. 251–310, 1993.
- [130] F. Ercolessi, M. Parrinello, and E. Tosatti, "Au (100) reconstruction in the glue model," *Surface Science*, vol. 177, no. 2, pp. 314–328, 1986.
- [131] M. Finnis and J. Sinclair, "A simple empirical n-body potential for transition metals," *Philosophical Magazine A*, vol. 50, no. 1, pp. 45–55, 1984.
- [132] M. I. Baskes, "Modified embedded-atom potentials for cubic materials and impurities," *Phys. Rev. B*, vol. 46, pp. 2727–2742, Aug 1992.
- [133] M. I. Baskes, J. S. Nelson, and A. F. Wright, "Semiempirical modified embedded-atom potentials for silicon and germanium," *Phys. Rev. B*, vol. 40, pp. 6085–6100, Sep 1989.
- [134] D. G. Pettifor and I. I. Oleinik, "Analytic bond-order potentials beyond Tersoff-Brenner. I. Theory," *Phys. Rev. B*, vol. 59, pp. 8487–8499, Apr 1999.
- [135] D. G. Pettifor and I. I. Oleinik, "Bounded analytic bond-order potentials for  $\sigma$  and  $\pi$  bonds," *Phys. Rev. Lett.*, vol. 84, pp. 4124–4127, May 2000.
- [136] M. Mrovec, D. Nguyen-Manh, C. Elsässer, and P. Gumbsch, "Magnetic bond-order potential for iron," *Phys. Rev. Lett.*, vol. 106, p. 246402, Jun 2011.
- [137] R. Drautz and D. G. Pettifor, "Valence-dependent analytic bond-order potential for magnetic transition metals," *Phys. Rev. B*, vol. 84, p. 214114, Dec 2011.
- [138] M. E. Ford, R. Drautz, T. Hammerschmidt, and D. G. Pettifor, "Convergence of an analytic bond-order potential for collinear magnetism in Fe," *Modelling and Simulation in Materials Science and Engineering*, vol. 22, no. 3, p. 034005, 2014.
- [139] A. A. Shabana, *Computational Continuum Mechanics*. Cambridge University Press, 2008. Cambridge Books Online.
- [140] D. Wallace, *Thermodynamics of Crystals*. Dover books on physics, Dover Publications, 1998.



- 
- [141] R. N. Thurston and K. Brugger, “Third-order elastic constants and the velocity of small amplitude elastic waves in homogeneously stressed media,” *Phys. Rev.*, vol. 133, pp. A1604–A1610, Mar 1964.
- [142] G. Srivastava, *The Physics of Phonons*. Taylor & Francis, 1990.
- [143] K. Huang, *Statistical mechanics*. Wiley, 1987.
- [144] D. Chandler, *Introduction to Modern Statistical Mechanics*. Oxford University Press, 1987.
- [145] S. Baroni, P. Giannozzi, and E. Isaev, “Thermal properties of materials from ab-initio quasi-harmonic phonons,” *arXiv preprint arXiv:1112.4977*, 2011.
- [146] D. Marx and J. Hutter, *Ab initio molecular dynamics: basic theory and advanced methods*. Cambridge University Press, 2009.
- [147] C. Rasmussen and C. Williams, *Gaussian Processes for Machine Learning*. Adaptive computation and machine learning series, University Press Group Limited, 2006.
- [148] D. J. C. MacKay, *Information Theory, Inference & Learning Algorithms*. New York, NY, USA: Cambridge University Press, 2002.
- [149] W. J. Szlachta, *First principles interatomic potential for tungsten based on Gaussian process regression*. PhD thesis, University of Cambridge, 2013.
- [150] J. Skilling, “Nested sampling for general Bayesian computation,” *Bayesian Anal.*, vol. 1, pp. 833–859, Dec 2006.
- [151] S. E. Ahnert, *Implementations of information theory in molecular dynamics, quantum measurement and genetic data analysis*. PhD thesis, University of Cambridge, 2005.
- [152] W. J. Szlachta, A. P. Bartók, and G. Csányi, “Accuracy and transferability of Gaussian approximation potential models for tungsten,” *Phys. Rev. B*, vol. 90, p. 104108, Sep 2014.
- [153] J. Quiñonero-Candela and C. E. Rasmussen, “A unifying view of sparse approximate Gaussian process regression,” *The Journal of Machine Learning Research*, vol. 6, pp. 1939–1959, 2005.
- [154] E. Snelson and Z. Ghahramani, “Sparse Gaussian processes using pseudo-inputs,” in *Advances in neural information processing systems*, pp. 1257–1264, 2005.
- [155] K. Kaufmann, W. Baumeister, and M. Jungen, “Universal Gaussian basis sets for an optimum representation of Rydberg and continuum wavefunctions,” *Journal of Physics B: Atomic, Molecular and Optical Physics*, vol. 22, no. 14, p. 2223, 1989.
- [156] G. Singh, J. R. Kermode, A. De Vita, and R. W. Zimmerman, “Validity of linear elasticity in the crack-tip region of ideal brittle solids,” *International Journal of Fracture*, vol. 189, no. 1, pp. 103–110, 2014.

## Bibliography

---

- [157] C. Woodward and S. I. Rao, "Flexible *Ab Initio* boundary conditions: Simulating isolated dislocations in bcc Mo and Ta," *Phys. Rev. Lett.*, vol. 88, p. 216402, May 2002.
- [158] R. M. Neal, "Slice sampling," *Annals of statistics*, pp. 705–741, 2003.
- [159] W. L. Jorgensen and J. Tirado-Rives, "Monte carlo vs molecular dynamics for conformational sampling," *The Journal of Physical Chemistry*, vol. 100, no. 34, pp. 14508–14513, 1996.
- [160] A. Debernardi, M. Alouani, and H. Dreysse, "Ab initio thermodynamics of metals: Al and W," *Phys. Rev. B*, vol. 63, no. 6, p. 064305, 2001.
- [161] F. H. Featherston and J. Neighbours, "Elastic constants of tantalum, tungsten, and molybdenum," *Phys. Rev.*, vol. 130, no. 4, p. 1324, 1963.
- [162] J. J. Adams, D. S. Agosta, R. Leisure, and H. Ledbetter, "Elastic constants of monocrystal iron from 3 to 500 K," *Journal of Applied Physics*, vol. 100, pp. 113530–113530–7, Dec 2006.
- [163] Z. S. Basinski, W. Hume-Rothery, and A. L. Sutton, "The lattice expansion of iron," *Proceedings of the Royal Society of London. Series A. Mathematical and Physical Sciences*, vol. 229, no. 1179, pp. 459–467, 1955.
- [164] N. Ridley and H. Stuart, "Lattice parameter anomalies at the curie point of pure iron," *J. Phys. D: Appl. Phys.*, vol. 1, p. 1291, 1968.
- [165] A. Laio and M. Parrinello, "Escaping free-energy minima," *Proceedings of the National Academy of Sciences*, vol. 99, no. 20, pp. 12562–12566, 2002.
- [166] P. Błoński and A. Kiejna, "Calculation of surface properties of bcc iron," *Vacuum*, vol. 74, no. 2, pp. 179–183, 2004.
- [167] M. J. Spencer, A. Hung, I. K. Snook, and I. Yarovsky, "Density functional theory study of the relaxation and energy of iron surfaces," *Surface Science*, vol. 513, no. 2, pp. 389–398, 2002.
- [168] J. Łażewski, J. Korecki, and K. Parlinski, "Phonons of (100) and (110) iron surfaces from first-principles calculations," *Phys. Rev. B*, vol. 75, p. 054303, Feb 2007.
- [169] P. Błoński and A. Kiejna, "Structural, electronic, and magnetic properties of bcc iron surfaces," *Surface science*, vol. 601, no. 1, pp. 123–133, 2007.
- [170] S. R. Bahn and K. W. Jacobsen, "An object-oriented scripting interface to a legacy electronic structure code," *Computing in Science & Engineering*, vol. 4, no. 3, pp. 56–66, 2002.
- [171] V. Vitek, "Intrinsic stacking faults in body-centred cubic crystals," *Philosophical Magazine*, vol. 18, no. 154, pp. 773–786, 1968.

- [172] P. Giannozzi, S. Baroni, N. Bonini, M. Calandra, R. Car, C. Cavazzoni, D. Ceresoli, G. L. Chiarotti, M. Cococcioni, I. Dabo, A. Dal Corso, S. de Gironcoli, S. Fabris, G. Fratesi, R. Gebauer, U. Gerstmann, C. Gougoussis, A. Kokalj, M. Lazzeri, L. Martin-Samos, N. Marzari, F. Mauri, R. Mazzarello, S. Paolini, A. Pasquarello, L. Paulatto, C. Sbraccia, S. Scandolo, G. Schlauser, A. P. Seitsonen, A. Smogunov, P. Umari, and R. M. Wentzcovitch, “Quantum espresso: a modular and open-source software project for quantum simulations of materials,” *Journal of Physics: Condensed Matter*, vol. 21, no. 39, p. 395502 (19pp), 2009.
- [173] P. Blaha, K. Schwarz, P. Sorantin, and S. Trickey, “Full-potential, linearized augmented plane wave programs for crystalline systems,” *Computer Physics Communications*, vol. 59, no. 2, pp. 399 – 415, 1990.
- [174] A. Gulans, S. Kontur, C. Meisenbichler, D. Nabok, P. Pavone, S. Rigamonti, S. Sagmeister, U. Werner, and C. Draxl, “exciting: a full-potential all-electron package implementing density-functional theory and many-body perturbation theory,” *Journal of Physics: Condensed Matter*, vol. 26, no. 36, p. 363202, 2014.
- [175] G. Kresse and J. Furthmüller, “Efficient iterative schemes for ab initio total-energy calculations using a plane-wave basis set,” *Phys. Rev. B*, vol. 54, pp. 11169–11186, Oct 1996.
- [176] C. Engin, L. Sandoval, and H. M. Urbassek, “Characterization of Fe potentials with respect to the stability of the bcc and fcc phase,” *Modelling and Simulation in Materials Science and Engineering*, vol. 16, p. 035005, Apr 2008.
- [177] M. Müller, P. Erhart, and K. Albe, “Analytic bond-order potential for bcc and fcc iron—comparison with established embedded-atom method potentials,” *Journal of Physics: Condensed Matter*, vol. 19, p. 326220, Aug 2007.
- [178] E. M. Lopasso, M. Caro, A. Caro, and P. E. A. Turchi, “Phase diagram of an empirical potential: The case of Fe-Cu,” *Phys. Rev. B*, vol. 68, p. 214205, Dec 2003.
- [179] G. Bonny, R. Pasianot, E. Zhurkin, and M. Hou, “Determination of the phase diagram from interatomic potentials: The iron–chromium case,” *Computational materials science*, vol. 50, no. 7, pp. 2216–2220, 2011.
- [180] E. Bitzek, J. Kermode, and P. Gumbsch, “Atomistic aspects of fracture,” *International Journal of Fracture*, vol. 191, no. 1-2, pp. 13–30, 2015.
- [181] K. S. Cheung and S. Yip, “A molecular-dynamics simulation of crack-tip extension: the brittle-to-ductile transition,” *Modelling and Simulation in Materials Science and Engineering*, vol. 2, no. 4, p. 865, 1994.
- [182] I. S. Grigoriev and E. Z. Melikhov, *Handbook of Physical Quantities*. Boca Raton: CRC Press, 1997.

## Bibliography

---

- [183] P. D. Desai, “Thermodynamic properties of iron and silicon,” *Journal of Physical and Chemical Reference Data*, vol. 15, no. 3, pp. 967–983, 1986.
- [184] D. C. Wallace, P. H. Sidles, and G. C. Danielson, “Specific heat of high purity iron by a pulse heating method,” *Journal of Applied Physics*, vol. 31, no. 1, pp. 168–176, 1960.
- [185] S. Klotz and M. Braden, “Phonon dispersion of bcc iron to 10 GPa,” *Phys. Rev. Lett.*, vol. 85, pp. 3209–3212, Oct 2000.
- [186] B. Brockhouse, H. Abou-Helal, and E. Hallman, “Lattice vibrations in iron at 296 K,” *Solid State Communications*, vol. 5, no. 4, pp. 211 – 216, 1967.
- [187] H. Hasegawa, M. W. Finnis, and D. G. Pettifor, “A calculation of elastic constants of ferromagnetic iron at finite temperatures,” *J. Phys. F: Met. Phys.*, vol. 15, p. 19, 1985.
- [188] J. Yin, M. Eisenbach, D. M. Nicholson, and A. Rusanu, “Effect of lattice vibrations on magnetic phase transition in bcc iron,” *Phys. Rev. B*, vol. 86, p. 214423, Dec 2012.
- [189] D. J. Dever, “Temperature dependence of the elastic constants in  $\alpha$ -iron single crystals: relationship to spin order and diffusion anomalies,” *J. Appl. Phys.*, vol. 43, p. 3293, 1972.
- [190] P. F. Bessarab, V. M. Uzdin, and H. Jónsson, “Calculations of magnetic states and minimum energy paths of transitions using a noncollinear extension of the Alexander-Anderson model and a magnetic force theorem,” *Phys. Rev. B*, vol. 89, p. 214424, Jun 2014.
- [191] S. Dudarev and P. Derlet, “A ‘magnetic’ interatomic potential for molecular dynamics simulations,” *Journal of Physics: Condensed Matter*, vol. 17, no. 44, p. 7097, 2005.
- [192] P.-W. Ma and S. L. Dudarev, “Longitudinal magnetic fluctuations in langevin spin dynamics,” *Phys. Rev. B*, vol. 86, p. 054416, Aug 2012.
- [193] P. Steneteg, O. Hellman, O. Y. Vekilova, N. Shulumba, F. Tasnádi, and I. A. Abrikosov, “Temperature dependence of tin elastic constants from *ab initio* molecular dynamics simulations,” *Phys. Rev. B*, vol. 87, p. 094114, Mar 2013.
- [194] [http://lammps.sandia.gov/doc/compute\\_pressure.html](http://lammps.sandia.gov/doc/compute_pressure.html).
- [195] J. A. Zimmerman, E. B. WebbIII, J. Hoyt, R. E. Jones, P. Klein, and D. J. Bammann, “Calculation of stress in atomistic simulation,” *Modelling and Simulation in Materials Science and Engineering*, vol. 12, no. 4, p. S319, 2004.
- [196] M. Zhou, “A new look at the atomic level virial stress: on continuum-molecular system equivalence,” in *Proceedings of the Royal Society of London A: Mathematical, Physical and Engineering Sciences*, vol. 459, pp. 2347–2392, The Royal Society, 2003.
- [197] M. Parrinello and A. Rahman, “Polymorphic transitions in single crystals: A new molecular dynamics method,” *Journal of Applied Physics*, vol. 52, no. 12, 1981.

- 
- [198] W. G. Hoover, "Canonical dynamics: Equilibrium phase-space distributions," *Phys. Rev. A*, vol. 31, pp. 1695–1697, Mar 1985.
- [199] S. Plimpton, "Fast parallel algorithms for short-range molecular dynamics," *Journal of Computational Physics*, vol. 117, no. 1, p. 1–19, 1995.
- [200] M. J. Verstraete, "Ab initio calculation of spin-dependent electron–phonon coupling in iron and cobalt," *Journal of Physics: Condensed Matter*, vol. 25, p. 136001, 2013.
- [201] L. Mauger, M. S. Lucas, J. A. Muñoz, S. J. Tracy, M. Kresch, Y. Xiao, P. Chow, and B. Fultz, "Nonharmonic phonons in  $\alpha$ -iron at high temperatures," *ArXiv e-prints*, Apr 2014.
- [202] F. Birch, "Finite elastic strain of cubic crystals," *Phys. Rev.*, vol. 71, pp. 809–824, Jun 1947.
- [203] F. C. Nix and D. MacNair, "The thermal expansion of pure metals: Copper, gold, aluminum, nickel, and iron," *Phys. Rev.*, vol. 60, pp. 597–605, Oct 1941.
- [204] Z. Wu and R. M. Wentzcovitch, "Quasiharmonic thermal elasticity of crystals: An analytical approach," *Phys. Rev. B*, vol. 83, p. 184115, May 2011.
- [205] J. J. Moré, B. S. Garbow, and K. E. Hillstrom, "User guide for MINPACK-1," Tech. Rep. ANL-80-74, Aug 1980.
- [206] R. E. Hummel, *Electronic properties of materials*. Springer Science & Business Media, 2011.
- [207] H. Matter, J. Winter, and W. Triftshäuser, "Phase transformations and vacancy formation energies of transition metals by positron annihilation," *Applied physics*, vol. 20, no. 2, pp. 135–140, 1979.
- [208] L. De Schepper, D. Segers, L. Dorikens-Vanpraet, M. Dorikens, G. Knuyt, L. Stals, and P. Moser, "Positron annihilation on pure and carbon-doped  $\alpha$ -iron in thermal equilibrium," *Phys. Rev. B*, vol. 27, no. 9, p. 5257, 1983.
- [209] Y. Tateyama and T. Ohno, "Stability and clusterization of hydrogen-vacancy complexes in  $\alpha$ -Fe: An ab initio study," *Phys. Rev. B*, vol. 67, no. 17, p. 174105, 2003.
- [210] C. Becquart and C. Domain, "Ab initio contribution to the study of complexes formed during dilute FeCu alloys radiation," *Nuclear Instruments and Methods in Physics Research Section B: Beam Interactions with Materials and Atoms*, vol. 202, pp. 44–50, 2003.
- [211] J. Christian, *The Theory of Transformations in Metals and Alloys*. The Theory of Transformations in Metals and Alloys, Elsevier Science, 2002.
- [212] K. Lejaeghere, V. Van Speybroeck, G. Van Oost, and S. Cottenier, "Error estimates for solid-state density-functional theory predictions: An overview by means of the ground-state elemental crystals," *Critical Reviews in Solid State and Materials Sciences*, vol. 39, no. 1, pp. 1–24, 2014.

## Bibliography

---

- [213] P. Pavone private communication. `exciting` code ('boron' version), PBE functional,  $rmt=2.00$  Bohr,  $rgkmax=9.0$  Bohr,  $24\times 24\times 24$   $k$ -mesh, Gaussian smearing, smearing width= $0.002$  Ha,  $nempty=15$ ,  $gmaxvr=12$ , 2014.
- [214] <https://molmod.ugent.be/deltacodesdft>.
- [215] V. I. Anisimov and O. Gunnarsson, "Density-functional calculation of effective Coulomb interactions in metals," *Phys. Rev. B*, vol. 43, pp. 7570–7574, Apr 1991.
- [216] V. I. Anisimov, J. Zaanen, and O. K. Andersen, "Band theory and Mott insulators: Hubbard  $U$  instead of Stoner  $I$ ," *Phys. Rev. B*, vol. 44, pp. 943–954, Jul 1991.
- [217] V. I. Anisimov, F. Aryasetiawan, and A. I. Lichtenstein, "First-principles calculations of the electronic structure and spectra of strongly correlated systems: the LDA+ $U$  method," *Journal of Physics: Condensed Matter*, vol. 9, no. 4, p. 767, 1997.
- [218] B. Himmetoglu, A. Floris, S. de Gironcoli, and M. Cococcioni, "Hubbard-corrected DFT energy functionals: The LDA+ $U$  description of correlated systems," *International Journal of Quantum Chemistry*, vol. 114, no. 1, pp. 14–49, 2014.
- [219] Z. Wu and R. E. Cohen, "More accurate generalized gradient approximation for solids," *Phys. Rev. B*, vol. 73, p. 235116, Jun 2006.
- [220] J. P. Perdew, A. Ruzsinszky, G. I. Csonka, O. A. Vydrov, G. E. Scuseria, L. A. Constantin, X. Zhou, and K. Burke, "Restoring the density-gradient expansion for exchange in solids and surfaces," *Phys. Rev. Lett.*, vol. 100, p. 136406, Apr 2008.
- [221] S. Cottenier private communication. WIEN2K code (13.1 version), PBE functional,  $rmt=1.8$ ,  $rkmax=10.0$ ,  $36\times 36\times 36$   $k$ -mesh, Fermi-Dirac smearing, smearing width= $0.001$  Ry, 2014.
- [222] H. Ebert, "Ausdehnungsmessungen bei tiefen temperaturen," *Zeitschrift für Physik*, vol. 47, pp. 712–722, 1928.
- [223] H. L. Zhang, S. Lu, M. P. J. Punkkinen, Q.-M. Hu, B. Johansson, and L. Vitos, "Static equation of state of bcc iron," *Phys. Rev. B*, vol. 82, p. 132409, Oct 2010.
- [224] P. Vinet, J. R. Smith, J. Ferrante, and J. H. Rose, "Temperature effects on the universal equation of state of solids," *Phys. Rev. B*, vol. 35, pp. 1945–1953, Feb 1987.
- [225] G. Henkelman, G. Jóhannesson, and H. Jónsson, "Methods for finding saddle points and minimum energy paths," in *Theoretical Methods in Condensed Phase Chemistry*, pp. 269–302, Springer, 2002.
- [226] C.-C. Fu, J. Dalla Torre, F. Willaime, J.-L. Bocquet, and A. Barbu, "Multiscale modelling of defect kinetics in irradiated iron," *Nature materials*, vol. 4, no. 1, pp. 68–74, 2005.

- [227] P. M. Derlet, D. Nguyen-Manh, and S. Dudarev, “Multiscale modeling of crowdion and vacancy defects in body-centered-cubic transition metals,” *Phys. Rev. B*, vol. 76, no. 5, p. 054107, 2007.
- [228] I. Seki and K. Nagata, “Lattice constant of iron and austenite including its supersaturation phase of carbon,” *ISIJ international*, vol. 45, no. 12, pp. 1789–1794, 2005.
- [229] L. Schimka, R. Gaudoin, J. c. v. Klimeš, M. Marsman, and G. Kresse, “Lattice constants and cohesive energies of alkali, alkaline-earth, and transition metals: Random phase approximation and density functional theory results,” *Phys. Rev. B*, vol. 87, p. 214102, Jun 2013.
- [230] B. Grabowski, S. Wippermann, A. Glensk, T. Hickel, and J. Neugebauer, “Random phase approximation up to the melting point: Impact of anharmonicity and nonlocal many-body effects on the thermodynamics of Au,” *Phys. Rev. B*, vol. 91, p. 201103, May 2015.
- [231] F. Körmann, B. Grabowski, B. Dutta, T. Hickel, L. Mauger, B. Fultz, and J. Neugebauer, “Temperature dependent magnon-phonon coupling in bcc Fe from theory and experiment,” *Phys. Rev. Lett.*, vol. 113, p. 165503, Oct 2014.





## PERSONAL INFORMATION

### Daniele Dragoni

Sex M | Date of birth 25/06/1985 | Nationality Italian

Address: Ch. du Martinet 27, Lausanne, 1007, CH  
Cell-Phone: +41 79 88 92450  
+39 328 566 73 71  
Email: daniele.dragoni.job@gmail.com  
Webpage: <https://it.linkedin.com/in/danieledragoni>  
Languages: Italian, English, French  
Date of availability: 01/05/2016

## EDUCATION

2011 - 2015 Ph.D. candidate in Materials Science École Polytechnique Fédérale de Lausanne (CH)

Subjects covered ▪ **Machine learning**, materials design & **modelling**, quantum and classical **simulations**, solid state physics, iron, steels, magnetism, metals, thermo-mechanics.

Skills acquired ▪ **Data management** and **Statistical analysis of data** gained through scripting and coding.  
▪ **Self-organization, autonomy** in decision-making, proactive participation to **group** dynamics gained through discussions with collaborators and colleagues.  
▪ Good communication skills gained through team discussions, presentation of scientific work in seminars, conferences and schools on scientific communication (see Awards below).

Extra experiences ▪ Co-organizer of the WinsCool 2015 Winter school in materials science; "*New materials from Physics to Applications*" <https://sites.google.com/site/winscool2015/>  
▪ Teaching assistant in *Quantum Simulations of Materials: Properties and Spectroscopies* at EPFL.  
▪ Participation to the *Modelling of Interface Evolution in Advanced Welding* (Mintweld) European Commission Seventh Framework Programme (FP7)  
▪ External collaborations with the engineering department of *Cambridge University* and *Centro Nazionale delle Ricerche* (C.N.R.) in Milano

February 2011 Master degree - *cum laude* - Università degli Studi di Milano (IT)  
December 2007 Bachelor degree Università degli Studi di Milano (IT)

Subjects covered ▪ Solid state physics, electronic structure, Plasma physics, Ionic liquids, electrochemistry, computer simulations

## PERSONAL SKILLS

Computer skills ▪ **Unix, Windows** and **OS** environments  
▪ **Python**, bash, awk, **Mathematica**, gnuplot scripting  
▪ **Microsoft Office & LibreOffice** tools, **Latex**  
▪ Most of web browsers  
▪ Basic **Fortran90/95** coding

## TRAINING

---

### List of Publications

- *Interfacial layering of a room-temperature ionic liquid thin film on mica: A computational investigation*, ChemPhysChem, 2012. DOI: 10.1002/cphc.201100947
- *Thermoelastic properties of  $\alpha$ -iron from first-principles*, Physical Review B, 2015. DOI: <http://dx.doi.org/10.1103/PhysRevB.91.104105>

### List of International Conferences

- EDMX research day, Lausanne (Switzerland), November 2015. Poster contribution
- Euromat conference, Warsaw (Poland), September 2015. Poster contribution
- Psi-k conference, Donostia/San Sebastian (Spain), September 2015. Poster contribution
- CCMX Technology aperitif, Lausanne (Switzerland), May 2015.
- CCMX annual meeting, Bern (Switzerland), May 2015. Poster contribution
- International Workshop on Computational Physics and Materials Science: Total Energy and Force Methods, Trieste (Italy), January 2015. Poster contribution
- Earth and Space Symposium, Lausanne (Switzerland), November 2014. Poster contribution
- Ab-initio Description of Iron and Steel: Multiples Impacts of Magnetism, Ringberg Castle – Tegernsee (Germany), October 2014. Poster contribution
- Junior Euromat, Lausanne (Switzerland), July 2014. Poster and oral contribution
- DPG-Frühjahrstagung, Dresden (Germany), April 2014. Oral contribution
- International Workshop on Computational Physics and Materials Science: Total Energy and Force Methods, Trieste (Italy), January 2014. Poster contribution
- PASC Junior Retreat, Boldern-Mannedorf (Switzerland), July 2013. Poster contribution
- DPG-Frühjahrstagung, Regensburg (Germany), April 2013. Oral contribution
- International Workshop on Computational Physics and Materials Science: Total Energy and Force Methods, Trieste (Italy), January 2013. Poster contribution
- Mintweld consortium meeting, Cambridge (UK), September 2012. Oral contribution
- CCMX Summer Course - Multiscale Modelling of Materials, Lausanne (Switzerland), September 2012
- Mintweld consortium meeting, Delft (The Netherlands), April 2012. Oral contribution
- DPG-Frühjahrstagung, Berlin (Germany), March 2012. Oral contribution
- Mintweld consortium meeting, Gliwice (Poland), September 2011. Oral contribution

### List of International Schools

- WinsCool Winter School, Champéry (Switzerland), March 2015. **Organizer** of the school
- CCMX Summer School - Atomistic Scale Modeling of Materials, Lausanne (Switzerland), September 2014. Poster contribution and exam
- CAMD Summer School on Electronic Structure Theory and Materials Design, Copenhagen (Denmark), August 2014. Poster contribution
- Psi-k/CECAM/CCP9 Biennial Graduate School in Electronic-Structure Methods, Oxford (UK), September 2013. Poster contribution
- Mintweld Summer School – Leading Edges in Welding, Cambridge (UK), July 2012.
- Hermes Summer School, Windsor (UK), July 2012

### Awards

2<sup>nd</sup> place – Best Science & Communication Video Award (Hermes Summer School 2012)

## ADDITIONAL INFORMATION

---

### Other interests

Photography, Oriental cultures, Karate (1<sup>st</sup> DAN black belt), Architecture, Transportation networks.

### Driving licence

Italian driving license: A (motorbike), B (car)

